

THÈSE DE DOCTORAT
DE L'UNIVERSITÉ PSL

Préparée à l'Institut de Mécanique Céleste et de Calcul des Éphémérides,
Observatoire de Paris

Architecture et stabilité des systèmes planétaires

Architecture and stability of planetary systems

Soutenue par
Antoine C. Petit
Le 28 juin 2019

École doctorale n°127
École Doctorale Astronomie et Astro-
physique en Ile de France

Spécialité
Astronomie et Astrophysique

Composition du jury :

Françoise Roques
Astronome, Observatoire de Paris *Présidente*

Konstantin Batygin
Assistant Professor, California Institute of Technology *Rapporteur*

Alessandro Morbidelli
Directeur de recherche, Observatoire de la Côte d'Azur *Rapporteur*

Anders Johansen
Professor, Lund University *Examinateur*

Jacques Laskar
Directeur de recherche, Observatoire de Paris *Directeur de thèse*

Gwenaël Boué
Maitre de conférences, Sorbonne Université *Co-directeur de thèse*

Remerciements

Je tiens tout d'abord à remercier mes directeurs de thèses, Jacques Laskar et Gwenaël Boué, de m'avoir permis d'effectuer cette thèse. Lors de notre première rencontre, Jacques a su me proposer un sujet riche, qui m'a passionné immédiatement. Puis tout au long de la thèse, ses remarques et conseils avisés m'ont permis de clarifier et mettre en valeur mes travaux. J'ai conscience aussi de toute l'aide qu'il m'a apporté pour la diffusion de nos résultats. Merci à Gwenaël qui a toujours été là pour écouter mes idées – bonnes ou mauvaises (!). La cohérence et la rigueur de cette thèse lui doivent beaucoup.

I would like to kindly thank Konstantin Batygin, Anders Johansen, Alessandro Morbidelli and Françoise Roques for accepting to participate to my defense committee. For their careful and insightful review of the manuscript, I particularly thank Konstantin and Alessandro. Thank you, Françoise for your help to implement the AMD analysis in the database exoplanet.eu. Anders, I am grateful for the opportunity you gave me to present my works in Lund and I am excited to join your team in September.

Merci à Mickaël Gastineau sans qui tout aurait pris beaucoup plus de temps pour ta capacité à résoudre immédiatement mes problèmes informatiques mais aussi pour tes conseils afin de m'améliorer en programmation. Je remercie également les membres de l'équipe ASD et en particulier Philippe Robutel pour toutes les discussions informelles sur mes recherches ou non.

Au sein de l'IMCCE je tiens à remercier Lusine Amirkhanyan, Rachida Amidhez, Amélie Muslewski, Nevada Mendez et Agnès Patu pour toute leur aide concernant l'organisation des voyages ou les tâches administratives. Merci en particulier à Lusine avec qui j'ai apprécié de partager notre bureau. Merci également à Géraldine Gaillant et Jacqueline Plancy pour leur aide à l'école doctorale.

Je remercie également les stagiaires, doctorants et post-doctorants du laboratoire pour les séminaires informels et les discussions entre deux portes. Merci en particulier à Nathan Hara pour l'initiation aux statistiques, à Federico Mogavero et Éric Woillez qui ont rafraîchi mes notions de physique statistique, à Léo Bernus et à Melaine Saillenfest pour des discussions tout aussi riches sur des sujets variés.

Thanks to Alexandre Correia, Aurélien Crida, Sam Hadden, David Hernandez, Michiel Lambrechts, Adrien Leleu, Anne-Sophie Libert, Gabriele Picchierri, Hanno Rein and Dan Tamayo for their questions and the interest they showed for my work in conferences, I look forward to meet you again.

I also would like to thank Doug Lin and Mark Krumholz for the opportunity

they gave me in 2014 to discover the research in astronomy at UC Santa Cruz. Merci également à Jacques Féjoz pour la possibilité de travailler avec lui sur le problème à trois corps d'un point de vue plus mathématique. Dans mon cursus scolaire, je remercie également mes professeurs de prépa de mathématiques et de physique Denis Choimet, Jacques Renault, Franz Ridde et Cécile Vince ainsi que ma professeur d'histoire de Terminale, Céline Fruchart pour m'avoir orienté vers la recherche. Merci en particulier à Jacques Renault pour m'avoir fait découvrir la beauté des *Principia*.

Merci à Claire de me supporter quand je rêve de planètes la nuit et quand je ne mange pas de fromage le jour. Merci à mes colocataires Olivier, Emilie, Delphin, Yaël et bien sûr Corentin qui résolvait mes bugs à domicile (et faisait de mauvaises blagues). Merci à tou·te·s mes ami·e·s pour les moments passés à parler de tout et de rien, à jouer, à randonner, à Paris, à Arèches, ou n'importe où. Merci en particulier à Xavier pour nos déjeuners rue Daguerre, à Vincent et Robin pour tout et rien, à Aurore, Laure et Arno pour leurs conseils toujours avisés, à Vero et Laura pour le club Petit·e·s, à Cyrille pour les discussions musique et ses templates¹.

Finalement, je remercie du fond du cœur mes parents pour leurs encouragements, pour avoir cultivé ma curiosité et tenté de répondre à mes questions quand j'étais Petit. Merci à Arthur et Chloé, à mes oncles et tantes, mes cousins et cousines. Enfin merci à mes quatre grands-parents pour tout ce qu'ils m'ont transmis et qui sont sûrement encore plus fiers que moi aujourd'hui.

¹La mise en page du manuscrit devrait te dire quelque chose... .

Contents

Remerciements	i
Contents	iii
1 Introduction	1
1.1 The diversity of exoplanetary systems	1
1.2 Planet formation theories	7
1.2.1 Classical view of planet formation	7
1.2.2 New paradigms	8
1.3 Stability in planetary systems	9
1.3.1 Stability of the Solar System, from Kepler to chaos	10
1.3.2 Current understanding of the Solar System dynamics	12
1.3.3 Challenges in exoplanet stability analysis	15
1.4 Organization of the manuscript	16
2 Introduction to planetary dynamics	19
2.1 Two-body problem	20
2.2 Planetary system Hamiltonian	25
2.3 Conserved quantities in planet dynamics	27
2.4 Secular dynamics	28
2.4.1 Lie series averaging	28
2.4.2 First order secular Hamiltonian	29
2.4.3 Lagrange-Laplace solution	31
2.5 Mean motion resonances	32
3 AMD-stability and the classification of planetary systems	33
3.1 Introduction	33
3.2 Angular Momentum Deficit (AMD)	34
3.3 AMD-stability	35
3.3.1 Collisional condition	36
3.3.2 Critical AMD $C_c(\alpha, \gamma)$	37
3.3.3 Behaviour of the critical AMD	38
3.4 AMD-classification of planetary systems	39
3.4.1 Sample studied and methods of computation	40
3.4.2 Propagation of uncertainties	42

3.4.3	AMD-stable systems	43
3.4.4	AMD-unstable systems	44
3.5	Conclusion	50
4	AMD-stability in presence of first order MMR overlap	53
4.1	Introduction	53
4.2	Resonant Hamiltonian	54
4.2.1	Averaged Hamiltonian in the vicinity of a resonance	55
4.2.2	Computation of the perturbation coefficients	57
4.2.3	Renormalization	58
4.2.4	Integrable Hamiltonian	59
4.2.5	Andoyer Hamiltonian	61
4.3	Overlap criterion	62
4.3.1	Width of the libration island	63
4.3.2	Minimal AMD of a resonance	64
4.3.3	Implicit overlap criterion	66
4.3.4	Overlap criterion for circular orbits	67
4.3.5	Overlap criterion for high-eccentricity orbits	68
4.3.6	Overlap criterion for low-eccentricity orbits	68
4.3.7	General order MMR overlap criterion	70
4.4	Critical AMD and MMR	71
4.4.1	Critical AMD in a context of resonance overlap	71
4.4.2	Comparison with the collision criterion	73
4.5	Effects of the MMR overlap on the AMD-classification of planetary systems	74
4.5.1	Sample and methodology	75
4.5.2	Results	76
4.6	Conclusions	78
5	Hill stability in the AMD framework	81
5.1	Introduction	81
5.2	Hill stability in the three-body problem	83
5.2.1	Generalized Hill curves	83
5.2.2	AMD condition for Hill stability	86
5.2.3	Close planets approximation	87
5.2.4	Comparison of the Hill criteria	88
5.3	Comparison with the AMD-stability	88
5.4	Numerical simulations	90
5.4.1	Numerical setup	90
5.4.2	Results	91
5.4.3	Influence of the masses	93
5.5	Conclusions	96
6	High order regularized symplectic integrator for collisional planetary systems	97
6.1	Introduction	97
6.2	Splitting symplectic integrators	99

6.3	The regularised Hamiltonian	100
6.3.1	Choice of the regularization function	102
6.4	Order of the scheme	104
6.4.1	Non integrable perturbation Hamiltonian	106
6.5	Error analysis near the close encounter	106
6.5.1	Time step and scheme comparison	106
6.5.2	Behaviour at exact collision	109
6.6	Pericenter regularization	110
6.6.1	Kepler step	111
6.6.2	The case of heliocentric coordinates	112
6.6.3	Combining both regularizations	113
6.7	Long-term integration performance	113
6.7.1	Initially circular and coplanar systems	113
6.7.2	Planet scattering on inclined and eccentric orbits	114
6.8	Comparison with existing integrators	117
6.9	Discussion	118
7	Architecture of planetary systems	121
7.1	Introduction	121
7.2	AMD and planet collisions	122
7.2.1	Collision in the secular case	122
7.2.2	General collision case	124
7.3	AMD model of planet formation	128
7.3.1	Dynamical assumption	128
7.3.2	AMD-Stable Planetary distribution	129
7.3.3	Scaling laws with initial mass distribution $\rho(a) \propto a^p$	130
7.4	Planetary system population synthesis	131
7.4.1	AMD-driven models in the context of modern planet formation	132
7.4.2	Numerical implementation	133
7.4.3	Results	135
7.4.4	Final remarks	138
8	Conclusions	141
A	Jacobi coordinates	145
B	AMD-stability appendices	149
B.1	Intersection of planar orbits	149
B.2	AMD in the averaged equations	150
B.3	Special values of $C_c(\alpha, \gamma)$	151
C	Details on the computation of the MMR overlap criterion	155
C.1	Expression of the first-order resonant Hamiltonian	155
C.2	Development of the Keplerian part	159
C.3	Width of the resonance island	159
C.4	Influence of γ on the limit α_{MMR}	161

C.5 AMD-stability coefficients of the system affected by the MMR overlap criterion	162
D Complements on Hill stability	165
D.1 Computation of R at the Lagrange points	165
D.2 Expansion of C_c^{Ex} and h_1	166
E Details on the adaptive integrator	169
E.1 Implementation	169
E.2 MacLachlan high order schemes	171
Bibliography	173

Chapter 1

Introduction

1.1 The diversity of exoplanetary systems

The question of the organization of the Solar System is one of the oldest of astronomy and celestial mechanics. Indeed, the eight planets of the Solar System orbit around the Sun along near coplanar and near circular orbits. There is also a clear difference between the inner Solar System, composed of four rocky planets and the outer Solar System composed of 4 gaseous planets.

Early in the history of modern astronomy, laws have been proposed to explain the distances of the planets to the Sun. The most famous attempts are Kepler's Platonic solid model (Kepler, 1596, see fig. 1.1) and the Titius-Bode law (Titius, 1766; Bode, 1772, see table 1.1). Titius and Bode proposed that the distance of the planet follows an arithmetic-geometric progression. At the time, only 6 planets were known and the subsequent discovery of Uranus and Ceres¹ seemed to confirm the law. However, the discovery of Neptune away from the predicted position made astronomers disregard it.

Nevertheless, the current organisation of the Solar System, in particular the orbit properties, is considered as a major clue in the development of any theory of the Solar System formation. Indeed, the Solar System is more ordered than required by the laws of gravitation. The almost coplanar and circular orbits have led the theorists to consider that planet formation takes place in a flat disk around the nascent star. While the details of the planet formation model have evolved since Laplace theories (Laplace, 1796), the flat disk hypothesis is still at the heart of the modern scenarii.

Planetary systems architecture has regained a lot of interest since the discovery of the first exoplanet (Mayor and Queloz, 1995). Indeed, the discovered planet, 51 Pegasi b is a hot Jupiter (*i.e.* a Jupiter-mass planet orbiting very close to the star in less than a few days) was the first hint of the diversity of existing planetary

¹While the combined asteroid belt mass is smaller than any planet mass, its position filled a gap between Mars and Jupiter in Titius-Bode law.

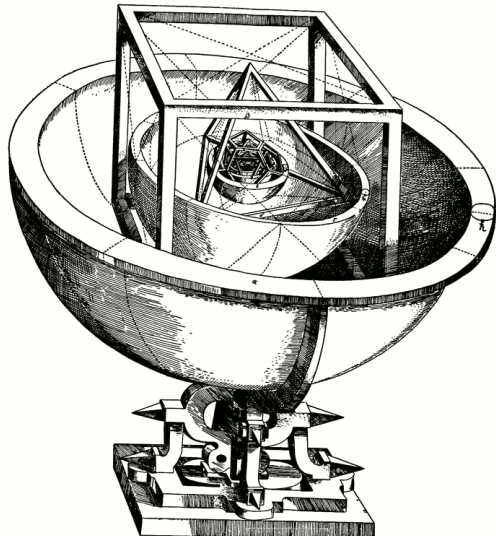


Figure 1.1 – Kepler’s Platonic solid model of the Solar System, from *Mysterium Cosmographicum*. Each of the six known planet’s orbit is contained in a shell that is inscribed and circumscribed by one of the five Platonic solid

n	Planet	a (AU)	Error (%)
$-\infty$	Mercury	0.39	-3.2
0	Venus	0.72	3.3
1	Earth	1.0	0.0
2	Mars	1.52	-4.8
3	Ceres	2.77	-1.2
4	Jupiter	5.2	0.1
5	Saturn	9.55	-4.5
6	Uranus	19.2	-2.0
7	Neptune	30.1	-22.4

Table 1.1 – Titius-Bode law predicts the semi-major axis of the Solar System planets as an arithmetic-geometric progression $a[\text{AU}] = 0.4 + 0.3 \times 2^n$. We give here the actual semi-major axis and the relative errors. Note that n begins at $-\infty$ and $n = 3$ corresponds to the asteroid belt.

systems.

Since then, we learnt that the Solar system architecture is far from representative of the observed exoplanetary systems. In April 2019, the database The Extrasolar Planets Encyclopædia² (Schneider *et al.*, 2011) counts 4003 planets. Among them, 1647 are in one of the 657 multiplanetary systems. The masses and orbital periods of these planets are shown in figure 1.2.

In the past 25 years, exoplanet observations programs has raised and started to answers the main questions about planetary systems and their architecture:

- Are exoplanets common ?
- What are their mass and orbital parameters distributions ?
- What is the multiplicity of multiplanetary systems and their orbital spacing ?
- Are there distinct exoplanet populations ?

In their review about the exoplanetary systems architecture, Winn and Fabrycky (2015) compile the currently known properties of the observed planetary.

Exoplanets appear to be almost ubiquitous. Indeed, the majority of stars host planets. Surveys have shown that about 50% of FGK stars host at least a planet of mass comprised between Earth’s and Neptune’s with period shorter than a year

²<http://www.exoplanet.eu/>

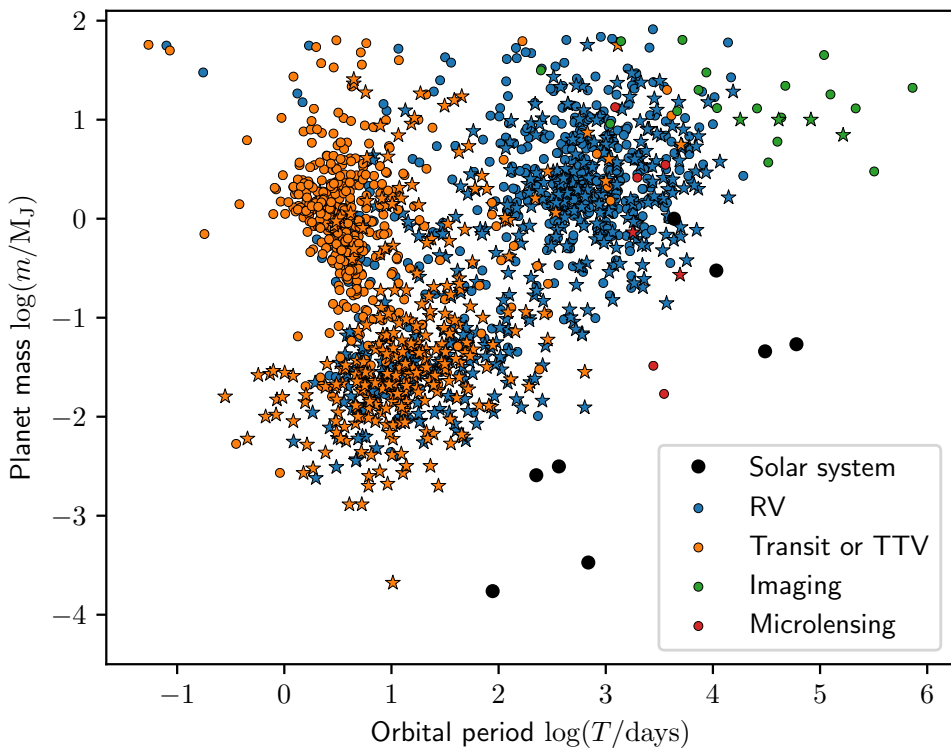


Figure 1.2 – Masses and semi-major axes of discovered exoplanets from a query on exoplanet.eu. The color gives the detection method, planets noted with a star indicates a multiplanetary system. The black dot indicates the positions of the eight planets of the solar system. The positions are approximate.

(Mayor *et al.*, 2011; Petigura *et al.*, 2013; Fressin *et al.*, 2013) and Kopparapu (2013) found a similar occurrence rate for M dwarves.

We see in figure 1.2 that the range of masses and periods of the discovered planets spans several orders of magnitude. For the masses, we observed planets with a mass similar to Mars’, *e.g.* Kepler-138 (Jontof-Hutter *et al.*, 2015), up to several Jupiter masses planets that could even be considered as brown dwarves. Discovered exoplanets have periods between a fraction of day *e.g.* 55 Cancri e (Dawson and Fabrycky, 2010) to tens of years for some young planets observed through direct imaging such as β Pictoris b (Lagrange *et al.*, 2009). These results are even more striking when we realize the biases that affect the detection methods. Indeed, the two most efficient detection methods, based on primary transit or radial velocities (RV) measurements, are heavily biased towards high mass and short period methods.

We see that the majority of known planets have a period smaller than 100 days. In the Solar System, only Mercury has such a short period. Longer period planets have been observed as well (mostly thanks to RV measurements), these planets are almost all gas giants. In particular, we see in figure 1.2 that the only planets of the Solar System that could have been observed as exoplanets are Jupiter and Saturn.

Microlensing allows to probe smaller planets at larger separations, and do help to correct the RV and transit biases. However, the method is not as efficient as

the two previously mentioned. Besides, the observed host star are often too faint for a follow-up study. Similarly, direct imaging is making stunning progresses and we have even observed multiplanetary systems (Marois *et al.*, 2010). It is however limited to very few large mass and luminous planets orbiting very young stars.

If we try to identify different types of planets in figure 1.2, we can roughly separates them in three categories. The first one is composed of planets with masses greater than $0.1 M_J$ and orbital period shorter than 10 days that are referred as Hot Jupiters. Because transit and RV efficiently detect those, they are over-represented in the sample. When biases are taken into account, the frequency of Hot Jupiters is of about 1% (Wright *et al.*, 2012; Fressin *et al.*, 2013). Several scenarios have been developed to explain the formation of the Hot Jupiters (see Dawson and Johnson, 2018, for a review). They could form far away from the star and then migrate within the protoplanetary disk or because of tidal dissipation (Wu and Lithwick, 2011); but the in-situ formation is also consistent (Batygin *et al.*, 2016). The other large planets have been commonly named cold Jupiters. Most of them have orbits with period of about 1 to 10 years. RV studies found that around 10% of FGK star host a giant planet with an orbit within 10 years (Cumming *et al.*, 2008; Mayor *et al.*, 2011).

The last category of observed exoplanets consists in planets with masses smaller than $0.1 M_J$ and typically periods smaller than 100 days. These planets are commonly referred as Super-Earth because most of them have a mass comprised between Earth's and Neptune's mass. As already said, about 50% of the stars host at least one Super-Earth. Nevertheless this type of planet is not represented in the Solar System. Super-Earths are particularly interesting because they compose most of the known multiplanetary systems and some of them may be at the right distance from their host star to have liquid water.

Both RV and transit methods give a good estimate of exoplanets period. From there, we can get an estimate of their semi-major axis thanks to Kepler third law and the estimation of the star mass. However, the other available orbital parameters depend on the method. For RV, we have a good estimate of the minimum mass of a planet $m \sin I$ that is the planet's mass multiplied by the sine of the inclination of the orbit with respect to the sky plane. The two quantities are degenerated and it is not possible to directly obtain an independent measure of the mass and inclination from the RV signal (Cumming *et al.*, 1999). Such a measurement can be made in the case where it is possible to fit the planets mutual perturbations in addition to their Keplerian motion.

When the signal to noise ratio is good enough, RV measurements can provide an estimate of the planet's eccentricity. The range of eccentricities in RV planetary systems goes from almost circular orbits with an upper limit eccentricity of about 10^{-3} to giant planets with a measured eccentricity 0.9. In population studies (Wright *et al.*, 2009; Mayor *et al.*, 2011), it was remarked that planets in multiplanetary systems tends to be on more circular orbits.

In the case of planets discovered by transit, the mass is not easily measurable. Indeed, the observable quantity is the planet to star radius ratio. While it is in principle possible to compute the mass of transiting planet assuming a bulk density, the mass uncertainty remains very large. Similarly, eccentricity measurement are

difficult from transit observations. In cases where RV follow-up can be done, we can obtain information on transiting planets (Marcy *et al.*, 2014). However, the majority of the stars observed by the *Kepler* mission are too faint for such subsequent studies.

Whenever a system contains multiple planets (co-transiting or not), it is possible to fit the effect of planet interactions on the transit timing. This method, called Transit Timing Variation (TTV; Holman and Murray, 2005) allows to determine masses and eccentricities of transiting planets (*e.g.* Lissauer *et al.*, 2013) and even to reveal non transiting planets in the system (*e.g.* Nesvorný *et al.*, 2013). However, this method is only efficient when plenty of transits have been observed and whenever planet perturbations are the more significant *i.e.* close to mean motion resonances (MMR).

While constraining individual transiting planet eccentricity is challenging, it has been possible to study the eccentricity distribution of transiting planets as a whole. Indeed, the transit duration T is related to the eccentricity e through

$$T = \left(\frac{R_* P}{\pi a} \sqrt{1 - b^2} \right) \frac{\sqrt{1 - e^2}}{1 + e \sin \omega}, \quad (1.1)$$

where R_* is the star radius, P the period, a the semi-major axis, b the impact parameter *i.e.* the minimum planet to star distance projected in the sky plane and measured in stellar radius and ω the argument of pericenter.

b and ω are not known in general, because they depend on the observation direction. Nevertheless, it is possible to make assumptions on this distribution and therefore to constrain the eccentricity distribution from the global transit duration distribution. Such studies (Moorhead *et al.*, 2011; Shabram *et al.*, 2016; Xie *et al.*, 2016) have found that the multiple transiting planets tend to have eccentricity smaller than single transit planets. In particular, (Xie *et al.*, 2016) studied a subset of the *Kepler* planet and found that the single transiting planet cannot be all part of the same population that the multi-transiting planets. The eccentricity distribution is best fitted a two-populations model, one with almost circular orbits ($\lesssim 0.05$) and one with moderate eccentricities ($\simeq 0.2$).

Similar studies are possible on the mutual inclinations in multiple transiting planet systems (Fang and Margot, 2012; Xie *et al.*, 2016). They tend to show that multi transiting systems have low mutual inclinations (of a few degrees). The discrepancy between single and multiple transit systems has been called the *Kepler* dichotomy (Johansen *et al.*, 2012).

Another important feature in exoplanetary system architecture are the planet period ratios. We plot in figure 1.3, the distribution of the period ratios for the adjacent pairs of planet in the catalogue `exoplanet.eu`. Additionally we plot the main MMR as dotted lines.

We see that the majority of the period ratios are comprised between 1.5 and 3, which is consistent with the Solar System (1.7 to 2.8). We note also that the distribution is not smooth. In particular we observe deficits at the exact MMR, *e.g.* around period ratios of 2 or 1.5. On the other hand there is an accumulation of planets just outside of the same MMR. This feature has been interpreted as a signpost of tidal dissipation from systems originally into MMR (Terquem and Papaloizou, 2007; Delisle *et al.*, 2012; Batygin and Morbidelli, 2013).

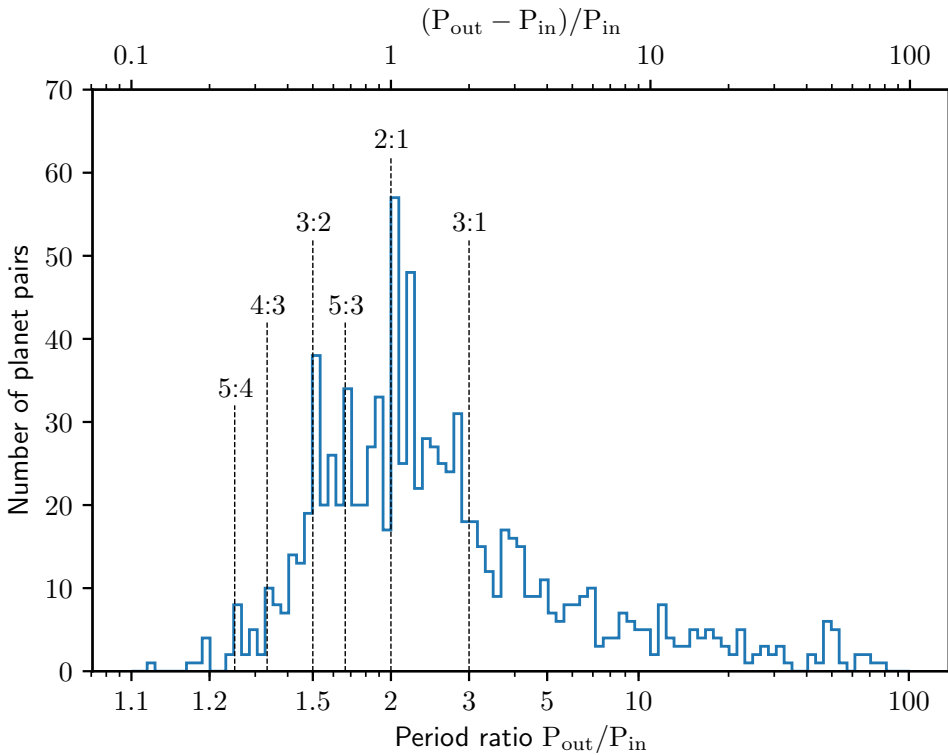


Figure 1.3 – Distribution of the period ratios of the adjacent pair of planets in the catalogue `exoplanet.eu`. The 100 bins are equally spaced in function of $\log_{10}(P_{\text{out}} - P_{\text{in}})/P_{\text{out}}$. The main MMR are plotted as dotted vertical lines.

To conclude this part on the diversity of exoplanetary systems, we should mention briefly that not all discovered planets belong to systems with a single star. Indeed, planets have been observed in binary star systems. In these systems, planets can orbit a single star, in this case the dynamics are almost similar to the case of a single star system if the binary system is wide enough (semi-major axis larger than 20 AU; Eggenberger *et al.*, 2010).

On the other hand, we have also observed much more exotic systems with planet orbiting around a binary star system. These planets are called circumbinaries. Most of the circumbinary planets are single, but there exist an example, Kepler-47, of a three planet system (Orosz *et al.*, 2012; Orosz *et al.*, 2019)³. All planets in such systems seems to cluster at the outer edge of the instability zone of the binary. The pile-up has been explained as a consequence of the migration of the planet into the circumbinary disc (Pierens and Nelson, 2008).

³Kepler-47 d has been discovered very recently. The system was previously the only two circumbinary planet system.

1.2 Planet formation theories

The architecture of planetary systems principally depends on the way they form. It appears important to at least make a short introduction to the state of the art in this domain. A complete overview of the field is beyond the scope of this introduction. This section is based on several reviews (Morbidelli *et al.*, 2012; Johansen and Lambrechts, 2017; Chiang and Youdin, 2010; Raymond *et al.*, 2014; Morbidelli and Raymond, 2016).

The clearest influence of the formation on currently observed systems is the low mutual inclination in multiplanetary systems. Indeed, it is now widely accepted that planet formation starts during the host star formation in the protoplanetary disc.

Stars form during the gravitational collapse of a molecular cloud. Initially, the material (composed principally of gas) falling onto the newly formed star has a high angular momentum and tends to regroup into an accretion disk perpendicular to the total angular momentum direction. Due to viscosity (Shakura and Sunyaev, 1973), the disk tends to spread and as a result transports angular momentum outward while the star is accreting mass inward.

The gas is mixed with a small proportion of solids, principally ices and silicate dusts. In solar abundances, the ratio of the mass of solid to gas is about 1% (Chiang and Youdin, 2010). These solids form the building blocks of the future terrestrial planets and giant planet cores. The protoplanetary disk has a lifetime of a few million year before the star completely photoevaporates the gas (Hartmann *et al.*, 1998). Therefore, the giant planet cores must form within this timescale in order to accrete gas. On the other hand, constraints from cosmochemistry indicates that the Solar System terrestrial planets formed after the dispersion of the disk (Morbidelli *et al.*, 2012, and references therein).

1.2.1 Classical view of planet formation

In the classical theory of planet formation (Safronov, 1972), the solids within the disk sediment in the horizontal plane and eventually aggregates into a swarm of planetesimals of a few tens to hundred of kilometers. At this point, if the dynamics become dominated by planetesimal interactions, the planetesimals start accreting each other to form planet embryos of about Mars size. The biggest objects tend to grow faster than the smaller one due to gravitational focusing (Greenberg *et al.*, 1978). This process has been call the runaway growth.

When embryos contains the majority of the solids, they start merging. This process have been extensively modeled (Chambers *et al.*, 1996; Chambers, 2001; O'Brien *et al.*, 2006; Raymond *et al.*, 2006). The collisions are most of the time assumed to result in perfect merging, but simulations have also been carried out with other assumptions (Kokubo and Genda, 2010; Mustill *et al.*, 2018). This phase of so called giant impacts appear to give satisfactory results for the formation of terrestrial planets.

For giant planets, if the planet core mass reaches several Earth masses within the lifetime of the disk, the planet starts accreting an atmosphere. This scenario, called the core accretion model (Pollack *et al.*, 1996), can lead to the formation of

giant planets but requires the initial mass of the disk to be much larger than the commonly used disk model, the minimum mass solar nebula (Weidenschilling, 1977). Moreover large cores tend to scatter instead of accreting planetesimal, which make the growth very inefficient (Tanaka and Ida, 1999).

In addition, planet embryos interact with the disk and migrate through it (Ward, 1986; Ward, 1997). Indeed, a planet embryo raises waves into the disk that creates a gravitational torque acting on the planet. If the planet is small enough, it will not completely deplete its orbit from the gas. Such a mechanism is called type I migration (Goldreich and Tremaine, 1979; Paardekooper and Mellema, 2006). Jupiter mass planets tend to open gaps in the disk (Lin and Papaloizou, 1986). The migration nature changes and this phenomenon is denominated type II migration. A single embryo generally migrates inward while resonances between embryos can invert the migration (Masset and Snellgrove, 2001).

Planet migration stops at the inner edge of the disk and when multiple embryos migrate together, they naturally end up in mean motion resonances (*e.g.* Terquem and Papaloizou, 2007; Raymond *et al.*, 2008). The observation by the *Kepler* mission of numerous compact systems of super Earth close to their star, with a significant gaseous H/He envelope for many of them, is an observational evidence for their formation within the disk lifetime. During the gas disk phase, the planet eccentricities and inclinations are tidally damped, which help keeping the the planets into resonant chains (Papaloizou and Larwood, 2000). However, as the disk dissipates, the system can enter a scattering phase destroying the resonant chain (Izidoro *et al.*, 2019). Such a scenario have been proposed to explain why most of the *Kepler* systems were found out of MMRs.

1.2.2 New paradigms

As pointed out in (Morbidelli and Raymond, 2016), the planet formation models presented above raise many questions. The first one concerns the growth of planetesimal for which the classical theory provides no mechanism. Indeed, due to the pressure gradient, the gas rotates at sub-Keplerian speed while the solids are unaffected. It results that the building blocks of planetesimals feel a headwind that makes them migrate inward very rapidly (Weidenschilling, 1977). This effect is maximal for typical size of the order of the meter. Moreover, collisions between bodies of this size are more likely to result in a fragmentation rather than in an accretion (Benz, 2000).

A solution to the formation of 100 km size objects has been proposed in the form of streaming instability (Youdin and Goodman, 2005; Johansen *et al.*, 2007). In this model, solids stop their migration and concentrate around pressure bumps. The solid to gas density is then further increased by the solids back reaction onto the gas. It results that the solid concentration become large enough to allow the gravitational collapse of the solids directly into 100 km size bodies.

The timescale of formation is observationally well constrained by the lifetime of the disk. However, the classical model forming planets and giant cores by recursive merging is too slow in order to form massive enough cores able to accrete a gaseous envelope in the imparted time. Moreover, the process tend to become inefficient as

the core grows due to the planetesimal scattering by the massive cores.

In order to solve these problems, Lambrechts and Johansen (2012) proposed a new growth mechanism called pebble accretion. Due to the gaseous disk headwind, pebbles of few cm size migrate inward much faster than planet embryos. They show that the embryo efficiently accretes the pebbles crossing its sphere of influence thanks to the gas drag. Since the feeding zone increases with the embryo mass and the pebble reservoir is replenished by material coming from the outer disk, the growth is exponential. This mechanism allows to form a planet core within the disk lifetime and permits the accretion of a massive gaseous envelope.

Furthermore, the pebbles are mostly refractory inside the snowline while they are bigger and more ice rich beyond it. As a result, the mechanism could explain the differences of nature between the inner and the outer Solar System (Morbidelli *et al.*, 2015; Morbidelli *et al.*, 2016).

The pebble accretion scenario has recently been tested in all aspect of planet formation, with realistic disk prescription and post disk phase evolution in a recent series of papers (Lambrechts *et al.*, 2019; Izidoro *et al.*, 2019; Bitsch *et al.*, 2019). It appears that the difference between pebble fluxes plays a significant role in the nature of the formed system. Indeed, similar embryos can either form terrestrial planets or giant core with a difference of less than an order of magnitude in the pebble flux.

To conclude let note that the system architecture that emerges from the disk (or even after the few first 100 Myr) can significantly differ from the observed exoplanet systems architecture. Indeed, orbital rearrangement is at play along the history of a planetary system. In particular, scattering among systems of giant planet can lead to ejections and generate large mutual inclinations and eccentricities among the surviving planet (Jurić and Tremaine, 2008). Similarly, chain of resonant super Earths may break because of stability constraints.

Outside of purely Newtonian dynamics, tidal dissipation can also change the architecture of planetary systems. Indeed, it is thought that Hot Jupiter form by circularization of highly eccentric orbits thanks to tidal damping in the envelope (Wu and Lithwick, 2011). Another example is the category of ultra short period planets that most likely experience tidal damping as well (Pu and Lai, 2019).

The observed architecture can thus only be understood by considering the whole history of planetary systems. In particular, the orbital rearrangement due to unstable initial conditions.

1.3 Stability in planetary systems

Giving a precise definition of a stable planetary system is a difficult task. From a mathematical point of view, a dynamical system is considered stable if two solutions with very close initial condition remain close at all times. This definition is too restrictive for planetary dynamics. Another definition inspired by KAM theory (Kolmogorov, 1954; Arnold, 1963; Möser, 1962) is to consider stable quasi-periodic orbits. Once again this definition is too restrictive for a practical point of view.

A more practical definition could be obtained by applying the previous math-

ematical definitions on a fixed time interval (longer than the age of the system). However, given the uncertainties on exoplanet orbital elements, we will end up considering every system unstable.

In this thesis, I will consider stable a system that will not experience large modifications of its architecture over its expected life time. In other words, I consider unstable system where planets interactions can lead to planet collision or ejections for the lifetime of the host star (typically 10 Gyr for Sun-like stars).

1.3.1 Stability of the Solar System, from Kepler to chaos

Historically, the answer to the question whether the Solar System is stable has changed multiple times. I begin this section by recalling the progresses made over the last four centuries in the understanding of celestial mechanics. Beyond its intrinsic interest, this presentation allows to introduce a lot of theoretical concepts still used in the study of planetary systems evolution. This part will closely follow the presentation made in (Laskar, 2013) that I strongly recommend to the reader interested in a more in-depth presentation of this question.

Before the Copernican revolution, the description of the motion of the planets that prevailed was that the planet were moving along epicycles (a sum of circular motions at different periods) according to the ideas of Ptolemy. Early in the XVIIth century, Kepler observed the motion of the planets and based on Copernicus ideas, he proposed that the planets were orbiting the Sun on close elliptical trajectories. In both cases, the Solar System was seen as immutable and perfectly stable.

When Newton proposed the universal law of gravitation in 1687, the interaction between the Sun and the planets explained the phenomenology proposed by Kepler. However, Newton's theory predicts interactions between planets, *i.e.* the orbits around the Sun can no longer be considered fixed. Since the planet masses are small, on short timescales their effects can be neglected. But in principle, these perturbations could add up on longer time and provoke close encounters or planet collisions. Eventually, he imagined that the intervention of God was necessary to keep the system in order.

Such an unstable behaviour seemed to be confirmed by Halley that compared his observations of Jupiter and Saturn to some transmitted by Ptolemy. He reported that the orbits of Jupiter and Saturn were moving away. In the XVIIIth century, observations had become precise enough that it was necessary to introduce empirical secular terms into the ephemeris to accurately predict the planet positions.

The planet motion irregularity was such an important problem, that the European Academies of Sciences proposed several prizes related to it. In order to solve Newton's equations, mathematicians such as Euler formulated the basis of perturbation theory. The continuation of Euler's work by Lagrange and then Laplace led to the first successes of such this approach when Laplace proved the secular invariance of the semi-major axis and then successfully solved the question of the great inequality between Jupiter and Saturn.

At the same time, Lagrange (1774) developed the first secular theory for the motion of the inclination and longitudes of the node. Inspired by Lagrange's memoir, Laplace (1775) quickly published a similar theory on the variation of the eccentricities

and precession of the perihelia. Today known as the Lagrange-Laplace theory (see section 2.4.3), these works are the first appearance of the linear differential equations with constant coefficients that represent to the first order the averaged motion of the planetary orbits.

After these works, the stability seemed to be granted. The semi-major axes have only short term variations while the eccentricities and inclinations have a quasi-periodic motion, thus bounded and small enough to forbid collisions. These success led Laplace and the whole scientific community during the XIXth century to believe into a deterministic science. With an accurate enough model, it is in principle possible to reach arbitrary precision on the predictions.

The works of Poincaré (1892) changed our understanding of celestial mechanics. By rewriting in Hamiltonian formalism the problem, he showed that the three-body problem is not integrable and that it is not possible to find an analytical solution representing the planetary motion. Worse, he showed that the series development used by astronomers to go beyond the Lagrange-Laplace theory actually diverges after a certain order. However, the truncated series is still a good approximation for finite times.

The main concept introduced by Poincaré in celestial mechanics is the notion of chaos. Newton's equations admit a unique solution for a given initial condition. However, the difference between two arbitrary close initial conditions will grow exponentially. Laskar (1989) showed that the Lyapunov exponent of the inner Solar System is of about $1/5 \text{ Myr}^{-1}$. As explained in (Laskar, 1990b), if we assume that two initial conditions are initially separated by a distance d_0 , the separation after a time T is $d(T) = d_0 10^{(T/10 \text{ Myr})}$. Typically, an initial error of 15 m (that is of the order of what is possible to measure today) will lead to an error of 1 AU after 100 Myr.

After Poincaré, the instability of the planetary dynamics appeared certain. But in the 50s, the Russian mathematician Kolmogorov (1954) demonstrated that in perturbed integrable systems, some initial quasi-periodic tori were preserved. It means that some initial conditions lead to solutions that are forever stable. This statement does not contradict Poincaré's since such tori are isolated. Arnold (1963) demonstrated a similar result for the planar three-body problem. These results are today known as KAM theorems because of the work of Möser (1962) to generalize them. On the vicinity of KAM tori, it was shown that the actions change only on very long timescales (Nekhoroshev, 1977; Giorgilli *et al.*, 1989; Morbidelli and Giorgilli, 1995). For the Solar System, it is sufficient to prove the stability for the next 5 Gyr, as it is the estimated lifetime of the Sun.

The masses in the Solar System are too large to directly apply the KAM theory. It is however assumed that these mathematical results still apply well beyond the validity of their demonstrations. In particular, it is thought that the outer Solar System is almost quasi-periodic and stable for the remaining lifetime of the Sun (*e.g.* Giorgilli *et al.*, 2017). However, these results do not apply to the inner Solar System due to the secular chaos created by secular resonances.

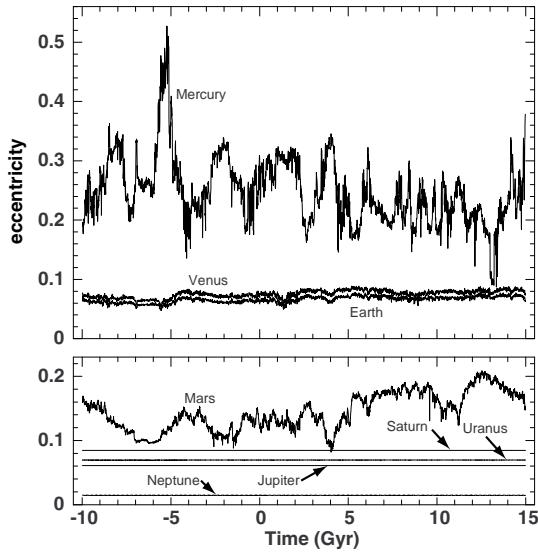


Figure 1.4 – Maximum eccentricity by slices of 10 Myr in a secular integration of the Solar System. Outer planets are almost quasi periodic while inner planets have a chaotic motion. Adapted from (Laskar, 1994).

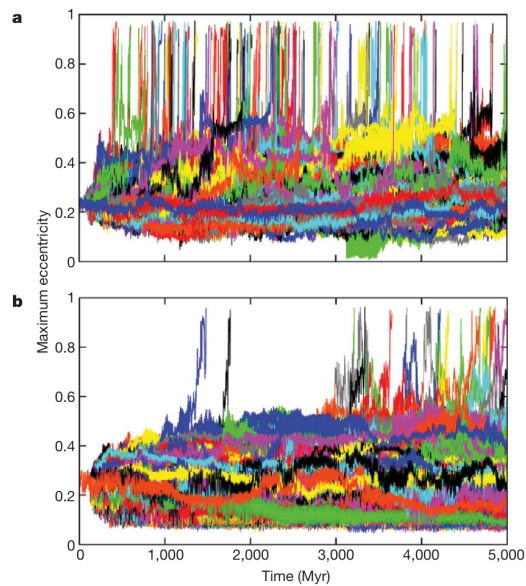


Figure 1.5 – Mercury eccentricity in direct integrations of the Solar System without (a) and with (b) post-Newtonian corrections and the influence of the Moon. Adapted from (Laskar and Gastineau, 2009).

1.3.2 Current understanding of the Solar System dynamics

In the last 30 years, numerical simulations have given us a very good description of the Solar System future. The numerical integration of the Solar System is very challenging and the progresses that allowed it are both technical and theoretical. Indeed, because of Mercury short period, the time-step in direct integration should be smaller than the day while the simulation must be conducted over billions of years. Besides, because the Solar System is chaotic, several thousands of integrations with slight changes in the initial conditions are necessary to highlight the diversity of the outcomes. Moreover, the numerical method should stay as close as possible to the exact trajectory. The development of symplectic integrators (see chapter 6) and in particular the Keplerian splitting (Kinoshita *et al.*, 1991; Wisdom and Holman, 1991) allowed the first integration of the entire Solar System longer 100 Myr (Sussman and Wisdom, 1992).

An alternative to direct integration consists in integrating the secular system developed at high degree in eccentricities, inclinations and masses. Since secular dynamics are much slower the time-step is of the order of sever centuries. Laskar demonstrated the chaotic nature of the inner Solar System and shown evidence that Mercury could eventually become unstable (Laskar, 1989; Laskar, 1990b; Laskar, 1994; Laskar, 2008). On the other hand, the outer System is very stable with an almost quasi-periodic behaviour. In figure 1.4 from (Laskar, 1994), we see the fundamental difference of behaviour between the inner and the outer System.

The first direct integrations over the lifetime of the Solar System (Batygin and

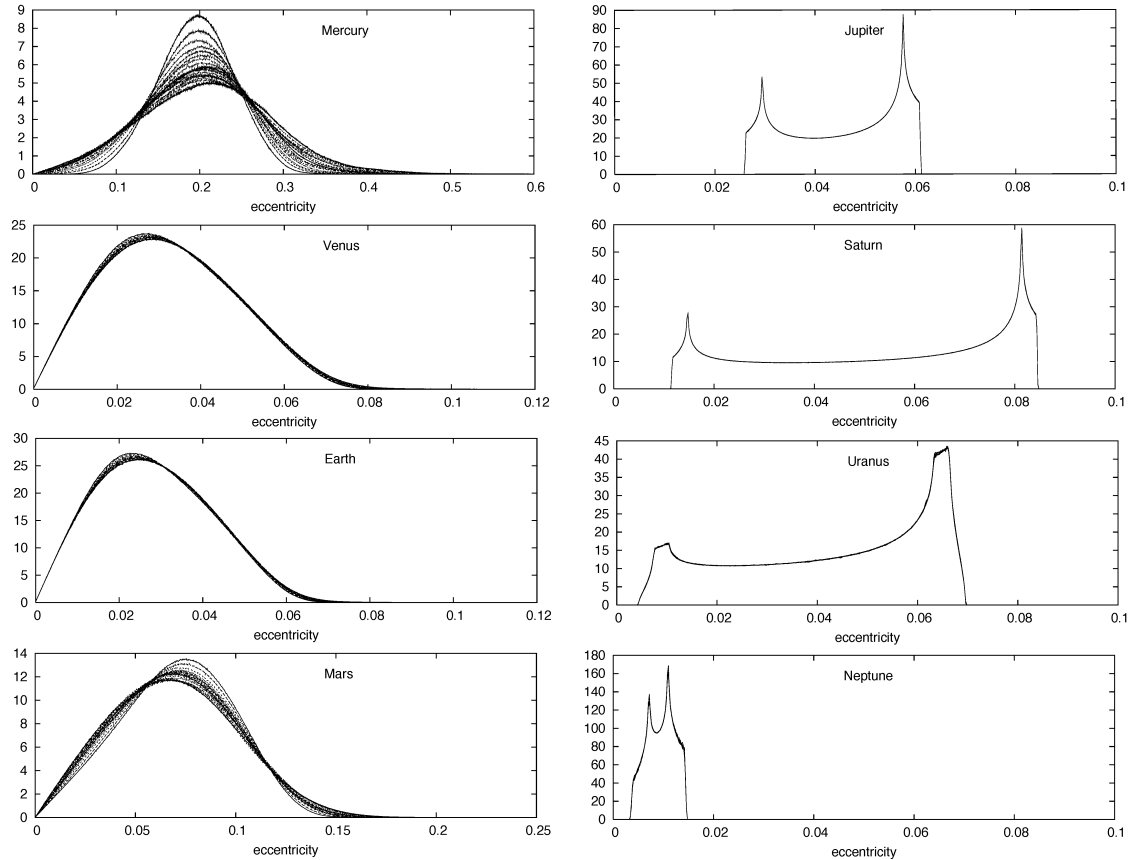


Figure 1.6 – Probability distribution functions of the Solar System planet eccentricities. Each curve represents the evolution along 250 Myr. The average is made over 1001 almost similar initial conditions. The variation of the curves reflects the chaotic diffusion. Adapted from (Laskar, 2008).

Laughlin, 2008; Laskar and Gastineau, 2009) confirmed the results of the secular integrations. Moreover, Laskar and Gastineau (2009) estimated the probability of destabilization of the inner Solar System to 1% over 5 Gyr. Interestingly, the same integrations made without the post-Newtonian corrections resulted in a much more unstable system with about half of the realizations becoming unstable within 5 Gyr (see figure 1.5).

The destabilization of the Solar System is mainly due to a resonance between the frequency associated with the precession of Mercury's perihelion g_1 and the frequency associated with Jupiter's g_5 (Laskar, 2008, see section 2.4.3 for a precise definition of g_k). The destabilization has been studied theoretically on simplified models that reproduce qualitatively the phenomenon (Boué *et al.*, 2012; Batygin *et al.*, 2015; Woillez, 2018).

Since the Solar System can be considered secular, the planet semi-major axes are constant on average. It remains to describe the evolution of the eccentricities and mutual inclinations on the billion year timescales. Laskar (2008) showed the probability distribution functions (PDFs) of the eccentricities and inclinations computed over 1001 initial conditions by bin of 250 Myr.

The PDFs of eccentricities are reproduced in figure 1.6. For the outer planets,

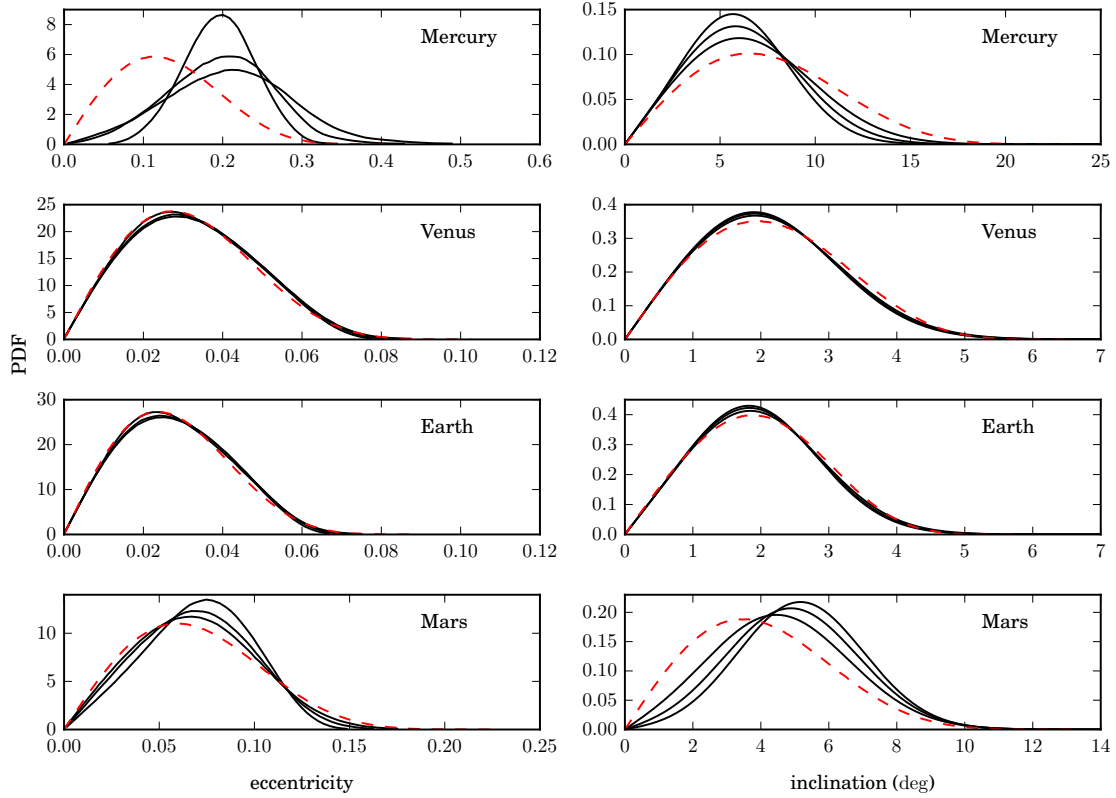


Figure 1.7 – Comparison of the PDFs of the eccentricities and inclinations of the inner planets from (Laskar, 2008) at 500 Myr, 2.5 Gyr and 5 Gyr (black curves) with the PDFs obtained by assuming the ergodicity of the secular dynamics in the part of the phase space guaranteeing the conservation of the inner Solar System’s AMD (dashed red curves). Adapted from (Mogavero, 2017).

the PDFs curves of the different time intervals are almost identical. Moreover they are typical of a quasi-periodic motion (Laskar, 2008). On the other hand, the inner planets PDFs show that there is a chaotic diffusion of the eccentricity, particularly for Mercury. This is another illustration of the difference of dynamical behaviour between the outer and the inner system. The phenomenology is similar for the inclinations.

Since the inner Solar System is chaotic, it is tempting to approximate its dynamics by assuming ergodicity. A dynamical system is said ergodic⁴ if averaging over time is equivalent to average over the accessible phase space. A consequence is that at any time, the system has an equal probability to be in any accessible point of the phase space. With this assumption, it is possible to compute a theoretical PDF that can be compare to the results of numerical simulations.

In the case of the secular problem, a very natural quantity to consider is the Angular Momentum Deficit (AMD, see chapter 3). This constant of the secular problem is a weighted sum of the eccentricities and inclinations that act as a

⁴The definition given here is not the mathematical one. My goal is to describe qualitatively the characteristics that an ergodic system should present.

measure of the non-linearity of the system. In particular, the total AMD bounds the eccentricities and inclinations. By assuming that the eccentricities and inclinations of the inner Solar System can take any value compatible with the conservation of the inner Solar System's AMD, Mogavero (2017) computed the theoretical PDFs of the eccentricities and inclinations.

His results are reproduced in figure 1.7 and compared to (Laskar, 2008). We see that, the assumption is very good for the Earth and Venus but not for Mercury and Mars. However, it should be taken into account that the assumption made was very rough. Moreover, for Mars' eccentricity and inclination and Mercury's inclination, it seems that Mogavero's result is the equilibrium PDFs towards which the numerical results seems to tend.

When one assume the conservation of the inner Solar System's AMD, the underlying assumption is that the outer and the inner Solar System are two different AMD reservoirs that do not communicate in general. However, when a transfer from the outer system to the inner system occurs, it results in a quick destabilization (Laskar, 1997). This phenomenology is confirmed by the numerical simulations.

The example of the Solar System is very rich from a dynamical point of view. Moreover we can see that the difference between the inner and the outer planets is not only a difference in composition and size of the planets. We have seen that the two parts of the Solar System fundamentally differ from a dynamical point of view. It should also be noted that the stability is only marginal. In the future, the inner Solar System could enter into an unstable phase that would lead to a reorganization of the system and even the collision or the ejection of one of the inner planet (Laskar, 1994; Laskar, 1996; Laskar, 2008; Laskar and Gastineau, 2009).

1.3.3 Challenges in exoplanet stability analysis

It is illusory to make a stability analysis as detailed as that performed for the Solar System for each discovered exoplanet system. Individual stability analysis have been carried out with success on a few iconic system such as HD10180 (Lovis *et al.*, 2010) or TRAPPIST-1 (Tamayo *et al.*, 2017; Grimm *et al.*, 2018). These studies are particularly interesting because the system are at the limit of being unstable and their existence look like a challenge to celestial mechanics. Most of the time these stability analysis act as an indirect confirmation of the observations. While the numerical simulations provide a lot of information on the systems, they are only based on short integrations compared to the system lifetime (10 Myr in Grimm *et al.*, 2018, for the TRAPPIST-1 system that orbits a red dwarf). Moreover, unlike in the Solar System where initial conditions are known with extreme precision, it is not the case for exoplanets. It results that numerical simulation must span large part of the phase space to accurately represent all probable states of the systems. Analytical studies provide an alternative to extensive numerical integrations. However, as explained earlier, the typical architecture of exoplanetary systems is very different from the Solar System's. Indeed, in a lot of observed systems, the planets have much more compact orbits than the Solar System's. Moreover, a significant part of the systems seems to be into or close to mean motion resonances (MMR).

Mean motion resonant dynamics are now well understood thanks to the de-

velopment of simplified models (*e.g.*, Henrard and Lemaître, 1983; Ferraz-Mello, 2007). Models have also been developed on the interactions between resonances and dissipative effects (Delisle *et al.*, 2012; Delisle *et al.*, 2014; Batygin and Morbidelli, 2013). The overlap of MMR may lead to very chaotic dynamics (Chirikov, 1979). Stability criteria can be defined based on this condition (Wisdom, 1980; Deck *et al.*, 2013; Petit *et al.*, 2017; Hadden and Lithwick, 2018, see chapter 4). Similarly the secular chaos has been studied in the context of exoplanetary systems (Wu and Lithwick, 2011).

For closely-packed systems, some empirical criteria have been developed based on numerical simulations (Chambers *et al.*, 1996; Smith and Lissauer, 2009; Pu and Wu, 2015; Obertas *et al.*, 2017). These studies consider theoretical systems composed of equal masses planets on evenly spaced circular and coplanar orbits. They show numerically that systems enter an instability phase after a time T_{ins} that depends on the spacing and the Hill radius

$$\log_{10} T_{\text{ins}}/T_{\text{orb}} = b\Delta + c, \quad (1.2)$$

where b and c are numerical constant, T_{orb} is the typical orbital period, Δ the orbital spacing measured in Hill radii. The Hill radius (Gladman, 1993; Petit *et al.*, 2018, see chapter 5) can be roughly defined as the distance where a planet has a stronger influence than the star it is orbiting. b and c depend weakly on the planetary masses and the number of planets. For lifetime of the order of $10^9 T_{\text{orb}}$, a typical separation of 8 to 10 Hill radii seems a good fit. The model has also proven to be robust to some randomization in the initial spacing, masses, and the addition of moderate eccentricity. However, this model still lacks a theoretical understanding even if some attempts have been made (Quillen, 2011). Another approach to this problem has been proposed by Tamayo *et al.* (2016) using machine learning to characterize the stability of 3 planet systems.

1.4 Organization of the manuscript

In this thesis, I present another approach to the question of planetary systems stability. Based on the study of the Solar System, we see that a simplified dynamical model can constrain the accessible region of the phase space and thus the system organization. In chapter 3, I develop in detail the concept of AMD-stability. Assuming a system can be considered secular, we show that the total AMD determines the accessible orbit configurations, and thus can forbid close encounters and collisions, ensuring long-term stability.

The model developed on chapter 3 is based on the critical hypothesis that the system can be considered secular. In chapters 4 and 5, I complete the concept of AMD-stability by studying how non-secular dynamics can affect a system. To do so I revisit and adapt to the AMD framework, the two main stability criteria for the two planet problem. In chapter 4, I discuss the MMR overlap criterion (Wisdom, 1980). In chapter 5, I improve the notion of Hill stability introduced by (Marchal and Bozis, 1982) and popularized by (Gladman, 1993).

During this thesis, it appeared necessary to study a system at the limit of instability, where collisions eventually happen. In those case, numerical simulations are

necessary because of the complexity of the trajectories. However, classical symplectic integrators fail to accurately integrate such systems. Symplectic integrators keep their good geometrical properties only when used with fixed time-step. However, when a system experience a close encounter, it is necessary to reduce the time-step to be able to resolve the encounter. To do so, I developed a new time regularization in order to create a symplectic integrator that can accurately integrate system experiencing close encounters. The development of the integrator and an analysis of its performances are detailed in chapter 6.

The various stability constraints presented above show that stability consideration play a key role in the organization of planetary systems. In chapter 7, I derive the constraints on planetary system architecture that emerge from the AMD-based models. The results are based on (Laskar, 2000) but I present some justifications of the assumptions made by Laskar and show that this theoretical model is compatible with results from modern planet formation theories.

The chapter 2 introduces most of the notations and classical results of planet dynamics that will be used in the following chapters.

Chapter 2

Introduction to planetary dynamics

The goal of this chapter is to introduce various classical notations and results from the study of the planet dynamics. I will not make an extensive introduction to Hamiltonian mechanics beyond this first paragraph. For the reader interested in the basis of Hamiltonian dynamics and its application to celestial mechanics, refer to (Goldstein, 1950; Arnold, 1979; Morbidelli, 2002).

For the practical development of the introduction, let just recall that if a Hamiltonian $\mathcal{H}(\mathbf{p}, \mathbf{q})$ depends on canonical conjugated variables (\mathbf{p}, \mathbf{q}) , the equations of motion are given by

$$\begin{aligned}\frac{d\mathbf{q}}{dt} &= \frac{\partial \mathcal{H}}{\partial \mathbf{p}}, \\ \frac{d\mathbf{p}}{dt} &= -\frac{\partial \mathcal{H}}{\partial \mathbf{q}}.\end{aligned}\tag{2.1}$$

Additionally, the evolution of any function $f(\mathbf{p}, \mathbf{q})$ is determined by the differential equation

$$\frac{df}{dt} = \{\mathcal{H}, f\} = \frac{\partial \mathcal{H}}{\partial \mathbf{p}} \cdot \frac{\partial f}{\partial \mathbf{q}} - \frac{\partial \mathcal{H}}{\partial \mathbf{q}} \cdot \frac{\partial f}{\partial \mathbf{p}},\tag{2.2}$$

where the operator $\{\cdot, \cdot\}$ is the Poisson bracket. Two functions f and g are said to be in involution if $\{f, g\} = 0$. We also define the Lie derivative associated with \mathcal{H} by $L_{\mathcal{H}} = \{\mathcal{H}, \cdot\}$. $L_{\mathcal{H}}$ is a linear operator on the Lie algebra of functions of variables (\mathbf{p}, \mathbf{q}) . The formal solution of (2.2) with initial conditions $(\mathbf{p}_0, \mathbf{q}_0)$ is given by

$$f(t) = \exp(tL_{\mathcal{H}})(f)(\mathbf{p}_0, \mathbf{q}_0) = \sum_{k=0}^{+\infty} \frac{t^k}{k!} L_{\mathcal{H}}^k(f)(\mathbf{p}_0, \mathbf{q}_0).\tag{2.3}$$

The flow of a Hamiltonian preserves the symplectic form $d\mathbf{p} \wedge d\mathbf{q}$, thus the diffeomorphism $(\mathbf{p}, \mathbf{q}) \rightarrow \exp(tL_{\mathcal{H}})(\mathbf{p}, \mathbf{q})$ is a canonical transformation.

2.1 Two-body problem

Due to the mass ratio between the planets and their host stars, planet dynamics are dominated by the planet-star interaction. In this thesis, I will use extensively the tools developed for the two-body problem. It seems important to start by this problem and its resolution. The solution presented here is inspired by J. Laskar lectures notes.

We consider two point-like bodies P_0, P_1 with masses m_0, m_1 and O the origin of an inertial frame. Let $\mathbf{u}_k = \overrightarrow{OP_k}$ and $\tilde{\mathbf{u}}_k = m_k \dot{\mathbf{u}}_k$ the conjugated momentum. The Hamiltonian of the system in presence of gravitational interaction is

$$\mathcal{H}_{\text{2bp}} = \frac{\|\tilde{\mathbf{u}}_0\|^2}{2m_0} + \frac{\|\tilde{\mathbf{u}}_1\|^2}{2m_1} - \frac{\mathcal{G}m_0m_1}{|\mathbf{u}_0 - \mathbf{u}_1|}, \quad (2.4)$$

where \mathcal{G} is the constant of gravitation. We first make a change of coordinates to separate the centre of mass motion from the relative motion. We define

$$\begin{aligned} \mathbf{r}_b &= \frac{m_0\mathbf{u}_0 + m_1\mathbf{u}_1}{m_0 + m_1}, & \mathbf{r} &= \mathbf{u}_1 - \mathbf{u}_0, \\ \tilde{\mathbf{r}}_b &= \tilde{\mathbf{u}}_0 + \tilde{\mathbf{u}}_1, & \tilde{\mathbf{r}} &= \tilde{\mathbf{u}}_1 - \frac{m_1}{m_0 + m_1}\tilde{\mathbf{r}}_b = \frac{m_0\tilde{\mathbf{u}}_1 - m_1\tilde{\mathbf{u}}_0}{m_0 + m_1}. \end{aligned} \quad (2.5)$$

The change of coordinates (2.5) is canonical and \mathcal{H}_{2bp} becomes

$$\mathcal{H}_{\text{2bp}} = \frac{\|\tilde{\mathbf{r}}_b\|^2}{2(m_0 + m_1)} + \frac{\|\tilde{\mathbf{r}}\|^2}{2m} - \frac{\mu m}{r}, \quad (2.6)$$

where $m = m_0m_1/(m_0 + m_1)$ is the reduced mass and $\mu = \mathcal{G}(m_0 + m_1)$ is the gravitational coupling parameter. In these coordinates, \mathcal{H}_{2bp} does not depends on \mathbf{r}_b so $\tilde{\mathbf{r}}_b$ is conserved and the barycentre motion is inertial. Moreover, the barycentre dynamics has no influence on the relative motion described by the variables $(\mathbf{r}, \tilde{\mathbf{r}})$. We drop the barycentric kinetic energy and we end up with the Hamiltonian describing the Keplerian motion

$$\mathcal{K} = \frac{\|\tilde{\mathbf{r}}\|^2}{2m} - \frac{\mu m}{r}, \quad (2.7)$$

The Hamiltonian (2.7) describes the motion of a body P of mass m around a fixed center O with a gravitational coupling parameter μ . The mass m of the body plays no role in the two-body problem and we could remove it by scaling \mathcal{K} and $\tilde{\mathbf{r}}$ by m . Nevertheless, I choose to keep it in order to directly use the results of this section for the N -body problem. \mathcal{K} is integrable and the trajectory of \mathbf{r} follows the Kepler laws:

- The trajectory is a conic section and the centre of force O is one of the foci,
- A line segment joining P and O sweeps out equal areas during equal intervals of time,

- If $\mathcal{K} < 0$, the orbit is an ellipse and the period is linked to its semi-major axis¹

$$\frac{a^3}{T^2} = \frac{\mu}{4\pi^2}. \quad (2.8)$$

These empirical laws proposed by Kepler in *Astronomia Nova* (1609) and *Harmonices Mundi* (1619) were later proved by Newton in its *Principia Mathematica* (1687). We give here a modern demonstration (Laskar, 2017) based on a canonical transformation to a set of coordinates adapted to the problem, the Delaunay coordinates (Delaunay, 1860).

We first remark that \mathcal{K} conserves the angular momentum defined as

$$\mathbf{G} = \mathbf{r} \times \tilde{\mathbf{r}}. \quad (2.9)$$

Indeed, we have

$$\frac{d\mathbf{G}}{dt} = \dot{\mathbf{r}} \times \tilde{\mathbf{r}} + \mathbf{r} \times \dot{\tilde{\mathbf{r}}} = \frac{\tilde{\mathbf{r}}}{m} \times \tilde{\mathbf{r}} - \mathbf{r} \times \frac{\mu m}{r^3} \mathbf{r} = 0. \quad (2.10)$$

Since \mathbf{G} is orthogonal to both \mathbf{r} and $\tilde{\mathbf{r}}$, the motion takes place in the plane orthogonal to \mathbf{G} passing through the origin. Let $\mathbf{u} = \mathbf{r}/r$ the unit vector in the direction of P . We define the Laplace-Runge vector as

$$\mathbf{e} = \frac{\tilde{\mathbf{r}} \times \mathbf{G}}{\mu m^2} - \mathbf{u}. \quad (2.11)$$

\mathbf{e} is a constant of motion and is within the orbital plane, indeed

$$\frac{d\mathbf{e}}{dt} = -\frac{\partial \mathcal{K}}{\partial \mathbf{r}} \times \frac{\mathbf{G}}{\mu m^2} - \dot{\mathbf{u}} = -\frac{\mu m \mathbf{r}}{r^3} \times \frac{(\mathbf{r} \times m r \dot{\mathbf{u}})}{\mu m^2} - \dot{\mathbf{u}} = 0. \quad (2.12)$$

We note e the norm of \mathbf{e} and v , the angle between \mathbf{e} and \mathbf{u} . We have

$$\mathbf{e} \cdot \mathbf{u} = e \cos(v) = \frac{\mathbf{r} \cdot (\tilde{\mathbf{r}} \times \mathbf{G})}{\mu m^2 r} - 1 = \frac{G^2}{\mu m^2 r} - 1. \quad (2.13)$$

We note $p = \frac{G^2}{\mu m^2}$ and from (2.13), we obtain the trajectory as

$$r = \frac{p}{1 + e \cos(v)}, \quad (2.14)$$

that is the polar equation of a conic. If $e < 1$, the orbit is an ellipse, if $e = 1$, a parabola and if $e > 1$, a branch of hyperbola. The first Kepler law is therefore proved. The direction of \mathbf{e} indicates the periapsis of the orbit and v is called the true anomaly. If the orbit is an ellipse², we note a its semi-major axis. Since G is constant of the motion, we can evaluate it at any point of the orbit. At the pericentre, we have $r = a(1 - e)$ and $v = 0$. From (2.13), we deduce

$$G = m \sqrt{\mu a (1 - e^2)}. \quad (2.15)$$

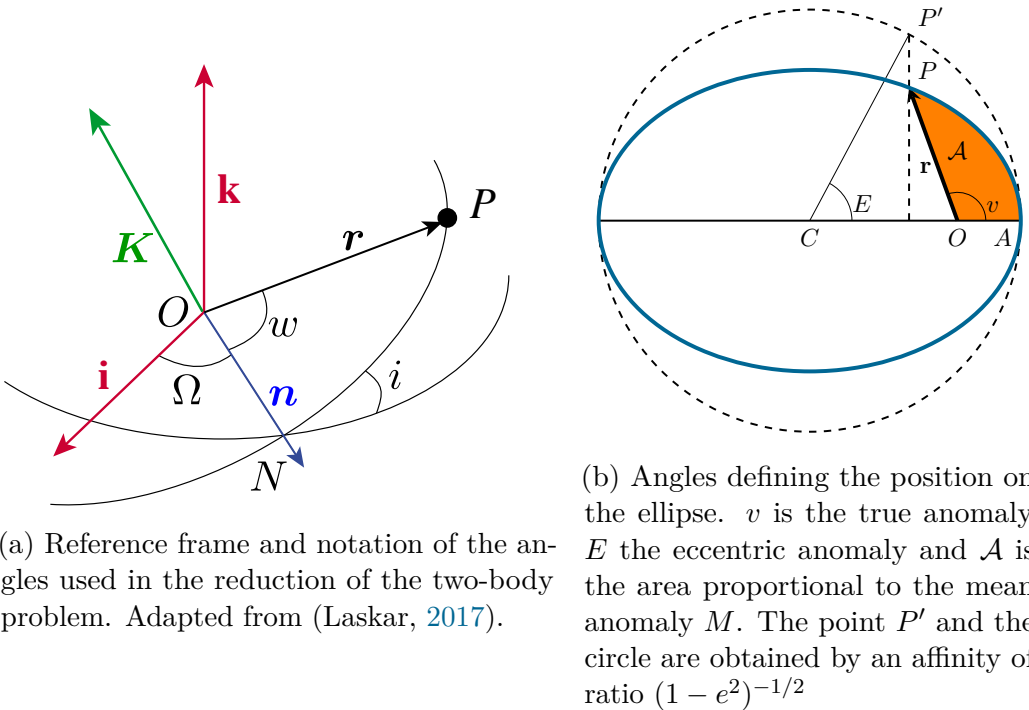


Figure 2.1 – Frame and notation for the resolution of the two-body problem.

Let us note $(\mathbf{i}, \mathbf{j}, \mathbf{k})$ the frame basis, $\mathbf{K} = \mathbf{G}/G$, the direction of angular momentum. The orbital plane is defined by its inclination i with respect to the horizontal plane (\mathbf{i}, \mathbf{j}) and its longitude of the node Ω that is the angle between \mathbf{i} and \mathbf{n} , the unit vector along the intersection of the orbital plane and the horizontal plane. We also note w , the angle between \mathbf{n} and \mathbf{r} . The configuration is illustrated in figure 2.1a. We also define the argument of the periapsis ω as the angle between \mathbf{n} and \mathbf{e} . Since \mathbf{n} , \mathbf{r} and \mathbf{e} are coplanar, it results that $w = v + \omega$.

The position of P , \mathbf{r} , is thus determined by the variables (r, w, i, Ω) . As explained in (Laskar, 2017), the transformation $(\tilde{\mathbf{r}}; \mathbf{r}) \rightarrow (r, w, i, \Omega)$ can be extended into a canonical change of variables using Andoyer's criterion for canonicity (Andoyer, 1923):

$$(\tilde{\mathbf{r}}; \mathbf{r}) \rightarrow (\tilde{r}, G, G \cos i; r, w, \Omega), \quad (2.16)$$

where $\tilde{r} = m\dot{r}$ is the radial component of the momentum. With these new symplectic coordinates, also known as the Hill variables (Hill, 1913), the Hamiltonian becomes

$$\mathcal{K} = \frac{1}{2m} \left(\tilde{r}^2 + \frac{G^2}{r^2} \right) - \frac{\mu m}{r}. \quad (2.17)$$

We note that the Hamiltonian no longer depends on $w, G \cos i$ and Ω which means that respectively G, Ω and $G \cos i$ are conserved. This result is a consequence of the

¹The expression of the constant $\frac{\mu}{4\pi^2}$ is due to Newton. Kepler only remarked the relation between a and T .

²Actually, the relation (2.15) holds for hyperbolic orbits with $-|a|$ instead of $|a|$. For parabolic orbits, $e = 1$ and a is ill-defined so G can only be expressed as a function of the parameter p .

conservation of \mathbf{G} . Written in this new form, \mathcal{K} only have one degree of freedom $(\tilde{r}; r)$ and is thus integrable. The motion of w is given by

$$\frac{dw}{dt} = \frac{\partial \mathcal{K}}{\partial G} = \frac{G}{mr^2}. \quad (2.18)$$

Equation (2.18) is a reformulation of Kepler's second law. Indeed, the infinitesimal element of area $d\mathcal{A}$ swept during an interval dt is a triangle of base r and height rdw , such that

$$d\mathcal{A} = \frac{1}{2}r^2 dw \Leftrightarrow \frac{d\mathcal{A}}{dt} = \frac{1}{2}r^2 \frac{dw}{dt} = \frac{G}{2m}. \quad (2.19)$$

For now on, we will assume that the orbit is an ellipse. Because the trajectory is closed the motion is periodic. Over a period T , the area spanned will be the total area of the ellipse, from (2.19), we compute

$$\mathcal{A} = \pi a^2 \sqrt{1 - e^2} = \int_0^T \frac{d\mathcal{A}}{dt} dt = \frac{GT}{2m} = \frac{\sqrt{\mu a(1 - e^2)} T}{2}. \quad (2.20)$$

After simplification, we obtain Kepler's third law (2.8). The mean motion along the orbit is defined as

$$n = \frac{2\pi}{T} = \sqrt{\frac{\mu}{a^3}}. \quad (2.21)$$

At the pericenter, the radial velocity and thus \tilde{r} is null, we can therefore evaluate the value of \mathcal{K} as a function of the elliptic elements

$$\mathcal{K} = \frac{G^2}{2ma^2(1 - e)^2} - \frac{\mu m}{a(1 - e)} = -\frac{\mu m}{2a}. \quad (2.22)$$

We remark that the Hamiltonian as well as the mean motion only depend on the semi-major axis of the orbit. As a result, the semi-major axis and the area spanned are natural candidates for the determination of action-angle coordinates to describe the motion along the orbit.

We define the mean anomaly M as the angle that is proportional to the area spanned by \mathbf{r} starting at the pericentre; by definition, $\dot{M} = n$ and $\mathcal{A} = a^2 \sqrt{1 - e^2} M / 2$. We also define the eccentric anomaly, that is the angle OCP' , where C is the center of the ellipse and P' the inverse image of P by the affinity defining the ellipse from a circle of center C . The different angles are shown on figure 2.1b.

The area enclosed into the arc of circle ACP' is $a^2 E / 2$. We can also compute this area by adding the area of the triangle COP' and $\mathcal{A}/\sqrt{1 - e^2} = a^2 M / 2$, the area enclosed between the angle ACP' and the circle. After simplification, we obtain the Kepler equation that links M to E

$$M = E - e \sin(E). \quad (2.23)$$

The Kepler equation is transcendental and cannot be solved analytically. However, it allows to write a transformation between the Hill coordinates and the set of orbital elements $(\tilde{r}, G, G \cos(i); r, w, \Omega) \rightarrow (a, e, i; M, \omega, \Omega)$. While the orbital elements are not canonical variables, one can use the Andoyer's method (Andoyer, 1923; Laskar,

2017) to get a set of canonical variables, the Delaunay coordinates (Delaunay, 1860). These coordinates are defined as

$$\begin{aligned} L &= m\sqrt{\mu a}; & M, \\ G &= L\sqrt{1-e^2}; & \omega, \\ H &= G \cos(i); & \Omega, \end{aligned} \quad (2.24)$$

and the Keplerian Hamiltonian takes the form

$$\mathcal{K} = -\frac{\mu^2 m^3}{2L^2}. \quad (2.25)$$

L is the only function of a (up to an additive constant) such that

$$\frac{dM}{dt} = n = \frac{\partial \mathcal{K}}{\partial L} = \frac{\mu^2 m^3}{L^3}. \quad (2.26)$$

The coordinates $(L, G, H; M, \omega, \Omega)$ are called action-angles coordinates because the Hamiltonian only depends on the actions (L, G, H) and is thus trivially integrable. Indeed, the actions are constant and the angle variables evolve at a constant frequency. Besides, the Keplerian Hamiltonian is said to be degenerated because it does not depend on all actions and thus the angles ω and Ω are also constant.

The coordinates (2.24) are ill-defined in the case of a null inclination or circular orbit because we cannot define the angles M, ω and Ω in such a configuration. To solve this issue, we introduce the modified Delaunay coordinates

$$\begin{aligned} \Lambda &= L = m\sqrt{\mu a}; & \lambda &= M + \varpi, \\ C &= L - G = \Lambda \left(1 - \sqrt{1 - e^2}\right); & -\varpi &= -\omega - \Omega, \\ D &= G - H = G(1 - \cos(i)); & -\Omega. \end{aligned} \quad (2.27)$$

The advantage is that now, the mean longitude, λ , is always well-defined and the longitude of the perihelion ϖ and the longitude of the node Ω are only ill defined when respectively C and D are null. As a result, the tuples $(C, -\varpi)$ and $(D, -\Omega)$ constitute polar coordinate systems. The associated canonical cartesian coordinates are called the Poincaré coordinates (Poincaré, 1905), and are defined by

$$\begin{aligned} \xi &= \sqrt{2C} \cos(\varpi); & \eta &= -\sqrt{2C} \sin(\varpi), \\ p &= \sqrt{2D} \cos(\Omega); & q &= -\sqrt{2D} \sin(\Omega). \end{aligned} \quad (2.28)$$

We also introduce the associated canonical complex coordinates that we will call the complex Poincaré coordinates (Laskar, 1991)

$$\begin{aligned} x &= \sqrt{C}e^{\iota\varpi}; & -\iota\bar{x} &= -\iota\sqrt{C}e^{-\iota\varpi}, \\ y &= \sqrt{D}e^{\iota\Omega}; & -\iota\bar{y} &= -\iota\sqrt{D}e^{-\iota\Omega}, \end{aligned} \quad (2.29)$$

where $\iota = \sqrt{-1}$. Note that there is a factor $\sqrt{2}$ between x and $\xi - \iota\eta$ (resp. y and $p - \iota q$). For small eccentricities and inclinations the Poincaré coordinates are proportional to the complex eccentricity and inclination. Indeed, we have

$$x = \sqrt{\frac{\Lambda}{2}}ee^{\iota\varpi} + O(e^3) \quad \text{and} \quad y = \sqrt{\frac{\Lambda}{2}}ie^{\iota\Omega} + O(e^3, i^3). \quad (2.30)$$

2.2 Planetary system Hamiltonian

The planetary $N+1$ body problem consists in studying the motion of $N+1$ point-like particles P_0, P_1, \dots, P_N of masses m_0, m_1, \dots, m_N under gravitational interactions. Here, P_0 represents the star and $(P_k)_{1 \leq k \leq N}$ the planets, thus the mass m_0 is much larger than any planet mass m_k . The dynamics are dominated by the interaction between the star and each of the planets and the planet-planet interactions act as perturbations. The scale of the perturbation is given by the planets-to-star mass ratio. Throughout this manuscript, we will denote ε this parameter with

$$\varepsilon = \frac{m_1 + \dots + m_N}{m_0}. \quad (2.31)$$

We define O , the origin of an inertial frame and consider $(\tilde{\mathbf{u}}_k, \mathbf{u}_k)_{k=0, \dots, N}$, the canonical coordinates in this frame. Here, $\mathbf{u}_k = \overrightarrow{OP_k}$ is the position of the k -th body with respect to O and $\tilde{\mathbf{u}}_k = m_k \dot{\mathbf{u}}_k$ is body k linear momentum. Newton's equations of motion form a differential system of order $6(N+1)$ and can be written in Hamiltonian form using Hamiltonian

$$\mathcal{H}_{\text{inert}} = \frac{1}{2} \sum_{k=0}^N \frac{\|\tilde{\mathbf{u}}_k\|^2}{m_k} - \sum_{0 \leq j < k \leq N} \frac{\mathcal{G} m_j m_k}{\Delta_{jk}} \quad (2.32)$$

where $\Delta_{jk} = \|\mathbf{u}_j - \mathbf{u}_k\|$, and \mathcal{G} is the constant of gravitation.

The $N+1$ body problem is not integrable for $N > 1$. However, a change of coordinates allows to write $\mathcal{H}_{\text{inert}}$ as an integrable Hamiltonian composed of a sum of independent Keplerian Hamiltonians (2.7) and a perturbation of relative order ε with respect to $\mathcal{H}_{\text{inert}}$. The exact expressions of the integrable part and of the perturbation depends on the particular coordinate transformation that is applied.

Several choices are possible, we here use the canonical heliocentric coordinates $(\tilde{\mathbf{r}}_k, \mathbf{r}_k)_{1 \leq k \leq N}$ (Poincaré, 1905) – see also (Laskar, 1990a; Laskar and Robutel, 1995) – defined as

$$\begin{aligned} \mathbf{r}_0 &= \sum_{k=0}^N \frac{m_k}{m_{\text{tot}}} \mathbf{u}_k, & \mathbf{r}_k &= \mathbf{u}_k - \mathbf{u}_0 & 1 \leq k \leq N \\ \tilde{\mathbf{r}}_0 &= \sum_{k=0}^N \tilde{\mathbf{u}}_k, & \tilde{\mathbf{r}}_k &= \tilde{\mathbf{u}}_k - \frac{m_k}{m_{\text{tot}}} \tilde{\mathbf{r}}_0 & 1 \leq k \leq N \end{aligned} \quad (2.33)$$

where $m_{\text{tot}} = \sum_{k=0}^N m_k$ is the total mass of the system. Note that while the positions are heliocentric, the momenta still derive from the barycentric velocities. Here \mathbf{r}_0 represents the position of the barycenter of the system. Using (2.33), the Hamiltonian $\mathcal{H}_{\text{inert}}$ (2.32) becomes

$$\mathcal{H}_{\text{helio}} = \underbrace{\frac{\|\tilde{\mathbf{r}}_0\|^2}{2m_{\text{tot}}}}_{\mathcal{H}_{\text{cm}}} + \underbrace{\sum_{k=1}^N \frac{\|\tilde{\mathbf{r}}_k\|^2}{2m_k} - \frac{\mathcal{G} m_0 m_k}{r_k}}_{\mathcal{H}_0} + \underbrace{\frac{\|\sum_{k=1}^N \tilde{\mathbf{r}}_k\|^2}{2m_0} - \sum_{1 \leq j < k \leq N} \frac{\mathcal{G} m_j m_k}{\Delta_{jk}}}_{\varepsilon \mathcal{H}_1}. \quad (2.34)$$

Note that the Hamiltonian no longer depends on \mathbf{r}_0 so $\tilde{\mathbf{r}}_0$ is conserved *i.e.* the barycentre keeps its inertial motion. Since $\tilde{\mathbf{r}}_0$ only appears in the term \mathcal{H}_{cm} , the

dynamics of the barycentre and the planet dynamics are independent. We can thus take $\tilde{\mathbf{r}}_0 = 0$ without loss of generality.

\mathcal{H}_0 is a sum of the Hamiltonians of disjoint Kepler problems of a single planet of mass m_k around a fixed star of mass m_0 . A set of adapted canonical variables for \mathcal{H}_0 will thus be given by the Delaunay coordinates (see section 2.1) associated with the elliptical elements, $(a_k, e_k, i_k, \lambda_k, \varpi_k, \Omega_k)$, where a_k is the semi major axis, e_k the eccentricity, i_k the inclination, λ_k the mean longitude, ϖ_k the longitude of the perihelion, and Ω_k the longitude of the node. They are defined as the elliptical elements associated with the Hamiltonian

$$\mathcal{K}_k = \frac{\|\tilde{\mathbf{r}}_k\|^2}{2m_k} - \frac{\mu m_k}{r_k} = -\frac{\mu m_k^3}{2\Lambda_k^2} \quad (2.35)$$

with $\mu = Gm_0$.

Using this particular splitting of $\mathcal{H}_{\text{helio}}$ (sometimes called democratic heliocentric), has the advantage that the Keplerian Hamiltonians (2.35) share the same central mass m_0 and the two-body planet masses are the real planet masses. As a consequence they are particularly convenient for an analytical and theoretical work. However, $\varepsilon\mathcal{H}_1$ does not vanish when considering the problem of a single planet, which means that \mathcal{H}_0 does not corresponds to the Keplerian Hamiltonian for a single planet.

It is possible to change definition of \mathcal{H}_0 and $\varepsilon\mathcal{H}_1$ such that \mathcal{H}_0 corresponds to the planets motion if there were not interacting. Indeed, one can develop the kinetic term $\|\sum_1^N \tilde{\mathbf{r}}_k\|^2$ in (2.34) such that we have

$$\mathcal{H}_{\text{helio}} = \underbrace{\sum_{k=1}^N \frac{\|\tilde{\mathbf{r}}_k\|^2}{2\beta_k} - \frac{\mu_k \beta_k}{r_k}}_{\mathcal{H}_0^{\text{Classical}}} + \underbrace{\sum_{1 \leq j < k \leq N} \frac{\tilde{\mathbf{r}}_j \cdot \tilde{\mathbf{r}}_k}{m_0} - \frac{Gm_j m_k}{\Delta_{jk}}}_{\varepsilon\mathcal{H}_1^{\text{Classical}}}, \quad (2.36)$$

where $\mu_k = G(m_0 + m_k)$ and $\beta_k = m_0 m_k / (m_0 + m_k)$. The first sum $\mathcal{H}_0^{\text{Classical}}$ in (2.36) corresponds to the N two-body problems composed of the star and planet k . I emphasize that the same set of canonical coordinates (2.33) are used in both (2.34) and (2.36). However, since the choice of the Keplerian part is different, we obtain different orbital elements and Delaunay coordinates. I will hereafter refer to the orbital elements deduced from the splitting (2.36) as the classical heliocentric coordinates.

It should be noted that in both cases, the perturbation part is not integrable (for $N > 1$). Another set of coordinates, the Jacobi variables, allows to write the Hamiltonian as sum of independent Keplerian terms and a perturbation that only depends of the positions. Therefore the perturbation term is integrable as well. We give the details of the construction of the Jacobi coordinates in appendix A, see also (Laskar, 1990a).

We stick with the Delaunay coordinates that result from the democratic heliocentric splitting (2.34). We have 6 coordinates for each planet, using (2.24), we

have

$$\begin{aligned}\Lambda_k &= m_k \sqrt{\mu a_k}; & \lambda_k, \\ C_k &= \Lambda_k \left(1 - \sqrt{1 - e_k^2} \right); & -\varpi_k, \\ D_k &= \Lambda_k \sqrt{1 - e_k^2} (1 - \cos(i_k)); & -\Omega_k.\end{aligned}\quad (2.37)$$

We also define the associated complex Poincaré coordinates $(x_k, y_k; -\iota \bar{x}_k, -\iota \bar{y}_k)$ as in (2.29).

There is no analytical expression for the interaction term $\varepsilon \mathcal{H}_1$ in function of the coordinates (2.37). However, we can develop $\varepsilon \mathcal{H}_1$ in Fourier series of the mean longitudes λ_k and power series of $(x_k, y_k; -\iota \bar{x}_k, -\iota \bar{y}_k)$. The series takes the form

$$\varepsilon \mathcal{H}_1 = \sum_{\mathbf{k}, \mathbf{l}, \bar{\mathbf{l}}, \mathbf{l}', \bar{\mathbf{l}'}} \mathcal{C}_{\mathbf{k}, \mathbf{l}, \bar{\mathbf{l}}, \mathbf{l}', \bar{\mathbf{l}'}}(\boldsymbol{\Lambda}) \left(\prod_{i=1}^N x_i^{l_i} \bar{x}_i^{\bar{l}_i} y_i^{l'_i} \bar{y}_i^{\bar{l}'_i} \right) e^{\iota \mathbf{k} \cdot \boldsymbol{\lambda}}, \quad (2.38)$$

where $\mathbf{k} \in \mathbb{Z}^N$, $\mathbf{l}, \bar{\mathbf{l}}, \mathbf{l}', \bar{\mathbf{l}'} \in \mathbb{N}^N$, and more generally the bold letters represents vectors of size N . The indices $\mathbf{l}, \bar{\mathbf{l}}, \mathbf{l}', \bar{\mathbf{l}'}$ are positive since $\varepsilon \mathcal{H}_1$ is in general not singular for circular or planar orbits. The expression of the coefficients $\mathcal{C}_{\mathbf{k}, \mathbf{l}, \bar{\mathbf{l}}, \mathbf{l}', \bar{\mathbf{l}'}}(\boldsymbol{\Lambda})$ depend on $\boldsymbol{\Lambda}$ and on the planet masses and can be computed using the method described in (Laskar, 1991; Laskar and Robutel, 1995). Besides, the coefficient \mathcal{C} are real and $\mathcal{C}_{\mathbf{k}, \mathbf{l}, \bar{\mathbf{l}}, \mathbf{l}', \bar{\mathbf{l}'}}(\boldsymbol{\Lambda}) = \mathcal{C}_{-\mathbf{k}, \bar{\mathbf{l}}, \mathbf{l}, \bar{\mathbf{l}'}, \mathbf{l}'}(-\boldsymbol{\Lambda})$.

Since all terms in $\varepsilon \mathcal{H}_1$ only contain contributions from two planets, most of the coefficients in the previous sum are null. Nevertheless, it is convenient to define the more general expression. We can also write the previous development for the modified Delaunay coordinates

$$\varepsilon \mathcal{H}_1 = \sum_{\mathbf{k}, \mathbf{l}, \bar{\mathbf{l}}, \mathbf{l}', \bar{\mathbf{l}'}} \mathcal{C}_{\mathbf{k}, \mathbf{l}, \bar{\mathbf{l}}, \mathbf{l}', \bar{\mathbf{l}'}}(\boldsymbol{\Lambda}) \left(\prod_{i=1}^N C_i^{\frac{l_i + \bar{l}_i}{2}} D_i^{\frac{l'_i + \bar{l}'_i}{2}} \right) e^{\iota (\mathbf{k} \cdot \boldsymbol{\lambda} + (\mathbf{l} - \bar{\mathbf{l}}) \cdot \boldsymbol{\varpi} + (\mathbf{l}' - \bar{\mathbf{l}'}) \cdot \boldsymbol{\Omega})}, \quad (2.39)$$

2.3 Conserved quantities in planet dynamics

Just as in the case of the two-body problem, the total linear momentum and the total angular momentum are conserved in the $N+1$ body problem. We already used the conservation of the total linear momentum in the previous section to reduce the problem to heliocentric coordinates and only consider the relative motion of the planets with respect to the star.

We now prove the conservation of angular momentum and its implications on the form of the series expansion of $\varepsilon \mathcal{H}_1$. The total angular momentum of the system is defined as

$$\mathbf{G} = \sum_{k=0}^N \mathbf{u}_k \times \tilde{\mathbf{u}}_k. \quad (2.40)$$

A straightforward computation shows that \mathbf{G} keeps the same form in canonical heliocentric coordinates

$$\mathbf{G} = \mathbf{r}_0 \times \tilde{\mathbf{r}}_0 + \sum_{k=1}^N \mathbf{r}_k \times \tilde{\mathbf{r}}_k = \sum_{k=1}^N \mathbf{r}_k \times \tilde{\mathbf{r}}_k, \quad (2.41)$$

where the last equality comes from the assumption that we placed ourselves in the barycentric frame. We see that the total angular momentum is the sum of the Keplerian angular momenta

$$\mathbf{G} = \sum_{k=1}^N G_k \mathbf{K}_k = \sum_{k=1}^N m_k \sqrt{\mu a_k (1 - e_k^2)} \mathbf{K}_k. \quad (2.42)$$

From section 2.1, we have $\{\mathcal{H}_0, \mathbf{G}\} = 0$. Therefore,

$$\frac{d\mathbf{G}}{dt} = \{\varepsilon \mathcal{H}_1, \mathbf{G}\} = \frac{1}{m_0} \sum_{j,k} \tilde{\mathbf{r}}_k \times \tilde{\mathbf{r}}_j - \sum_{j \neq k} \frac{G m_j m_k}{\Delta_{jk}^3} \mathbf{r}_j \times \mathbf{r}_k = 0. \quad (2.43)$$

The conservation of \mathbf{G} leads to a natural choice for the orientation of the frame because we can always choose our coordinates such that \mathbf{G} is along the z -axis. With this choice, the coplanar motion takes place in the horizontal plane *i.e.* when the orbit inclinations are null. Moreover, the norm of \mathbf{G} becomes

$$G = \mathbf{G} \cdot \mathbf{k} = \sum_{k=1}^N m_k \sqrt{\mu a_k (1 - e_k^2)} \cos(i_k) = \sum_{k=1}^N \Lambda_k - C_k - D_k. \quad (2.44)$$

With the choice of the vertical axis along G we have not fully exploited the symmetries of the problem. Indeed, the dynamics should be invariant by a rotation along the z -axis of an arbitrary angle. It corresponds to add a constant angle to all angles λ_k, ϖ_k and Ω_k . From equation (2.39) we deduce that the only non-zeros coefficients verifies the relation

$$\sum_{i=1}^N k_i + (l_i - \bar{l}_i) + (l'_i - \bar{l}'_i) = 0. \quad (2.45)$$

The relation (2.45) is the first d'Alembert rule. Using Noether's theorem, the invariance of \mathcal{H} by a rotation along the z -axis is a consequence of the conservation of $\mathbf{G} \cdot \mathbf{k}$. Indeed, the computation of the Poisson bracket $\{\varepsilon \mathcal{H}_1, G\} = 0$ in Delaunay coordinates using the expressions (2.39) and (2.44), gives directly the relation (2.45).

Additionally, the system is invariant by the reflection along the horizontal plane. In Poincaré coordinates, this transformation corresponds to $(\mathbf{y}; -\iota \bar{\mathbf{y}}) \rightarrow (-\mathbf{y}, \iota \bar{\mathbf{y}})$. We deduce that for the non-zeros terms in the formal expansion $\varepsilon \mathcal{H}_1$ (2.38), the sum $\sum_{i=0}^N l'_i + \bar{l}'_i$ should have an even value. In other words, the Hamiltonian is even in the inclinations. This second constraint on the indices is the second d'Alembert rule.

2.4 Secular dynamics

2.4.1 Lie series averaging

In Poincaré coordinates, it is obvious that the motion along the orbits is much faster than the evolution of the other variables. Indeed, we have

$$\mathcal{H}_{\text{helio}} = \mathcal{H}_0(\Lambda_k) + \varepsilon \mathcal{H}_1(\Lambda_k, C_k, D_k; \lambda_k, \varpi_k, \Omega_k), \quad (2.46)$$

so the variation of the λ_k is of the order ε^{-1} faster than the other variables. A Hamiltonian $\mathcal{H}(\mathbf{p}, \mathbf{q})$ that takes the form

$$\mathcal{H}(\mathbf{p}, \mathbf{q}) = \mathcal{H}_0(\mathbf{p}) + \varepsilon \mathcal{H}_1(\mathbf{p}, \mathbf{q}), \quad (2.47)$$

is said to be quasi-integrable. Indeed \mathcal{H}_0 is integrable as it only depends on the actions \mathbf{p} and at the zeroth order in ε , the motion can be approximated by the flow of \mathcal{H}_0 alone and \mathcal{H}_1 will be considered as the perturbation of the system.

The general theory of quasi-integrable Hamiltonian is beyond the scope of this introduction so I will only focus on the determination of the first order secular Hamiltonian while highlighting the challenges that arise from the N -body problem.

The main idea of the perturbation theory is to search for a canonical change of variables ε -close to the identity

$$(\mathbf{p}, \mathbf{q}) = (\mathbf{p}^1, \mathbf{q}^1) + \varepsilon(\mathbf{P}_1(\mathbf{p}^1, \mathbf{q}^1), \mathbf{Q}_1(\mathbf{p}^1, \mathbf{q}^1)), \quad (2.48)$$

such that when substituting (2.48) into the Hamiltonian (2.47) we have

$$\mathcal{H}^1(\mathbf{p}^1, \mathbf{q}^1) = \mathcal{H}_0(\mathbf{p}^1) + \varepsilon \bar{\mathcal{H}}_1(\mathbf{p}^1) + \varepsilon^2 \mathcal{H}_2(\mathbf{p}^1, \mathbf{q}^1), \quad (2.49)$$

where $\bar{\mathcal{H}}_1$ and \mathcal{H}_2 are function of the same order as \mathcal{H}_0 . $\bar{\mathcal{H}}_1$ is integrable and is generally the average of \mathcal{H}_1 over the angles \mathbf{q}^1 . The dynamics after this regularization is given by $\mathbf{q}^1(t) = \nabla_{\mathbf{p}}^1(\mathcal{H}_0 + \varepsilon \bar{\mathcal{H}}_1)t + \mathbf{q}^1(0) + O(\varepsilon^2)$. The motion of the original coordinates (\mathbf{p}, \mathbf{q}) is then obtained by the relation (2.48). In particular the motion of \mathbf{p} presents oscillations of order ε .

If this first step is successful, the perturbation is now of order ε^2 and it is in principle possible to iterate the process in order to approximate the dynamics up to a perturbation of arbitrarily small order ε^{r+1} . The resulting Hamiltonian is called a Birkhoff normal form of order r . In the case of (2.49), \mathcal{H}^1 is a first order normal form. However, in general there exists an optimal order where the process diverges beyond. Just as in the first order case, the original variables dynamics is recovered by composing the successive coordinates transformations from the optimal order approximation.

In the method detailed above, the challenge is in finding a canonical transformation verifying the desired properties. We here illustrate the method of the Lie series (Deprit, 1969) on the determination of the first order secular Hamiltonian.

2.4.2 First order secular Hamiltonian

We want to find a transformation of the Delaunay coordinates such that in the new coordinates $(\Lambda^1, \mathbf{C}^1, \mathbf{D}^1; \boldsymbol{\lambda}^1, -\boldsymbol{\varpi}^1, -\boldsymbol{\Omega}^1)$, the Hamiltonian takes the form

$$\mathcal{H}^1 = \mathcal{H}_0(\Lambda^1) + \varepsilon \bar{\mathcal{H}}_1(\Lambda^1, \mathbf{C}^1, \mathbf{D}^1; \boldsymbol{\varpi}^1, \boldsymbol{\Omega}^1) + \varepsilon^2 \mathcal{H}_2(\Lambda^1, \mathbf{C}^1, \mathbf{D}^1; \boldsymbol{\lambda}^1, \boldsymbol{\varpi}^1, \boldsymbol{\Omega}^1). \quad (2.50)$$

Note that contrarily to the case (2.49), here $\bar{\mathcal{H}}_1$ is not integrable but no longer depends on the mean longitudes. Indeed, we only aim to get rid of the rapid evolution by averaging it from the perturbation. We look for a transformation of the form

$$(\Lambda, \boldsymbol{\lambda}, \mathbf{C}, \mathbf{D}, \boldsymbol{\varpi}, \boldsymbol{\Omega}) = \phi_{\varepsilon W}^1(\Lambda^1, \mathbf{C}^1, \mathbf{D}^1, \boldsymbol{\lambda}^1, \boldsymbol{\varpi}^1, \boldsymbol{\Omega}^1), \quad (2.51)$$

where $\phi_{\varepsilon W}^1 = \exp(L_{\varepsilon W})$ is the the flow at time 1 of a function εW to be determined. This transformation is canonical because a Hamiltonian flow preserves the symplectic form. We have

$$\begin{aligned}\mathcal{H}(\Lambda, \mathbf{C}, \mathbf{D}, \boldsymbol{\lambda}, \boldsymbol{\varpi}, \boldsymbol{\Omega}) &= \mathcal{H}(\phi_{\varepsilon W}^1(\Lambda^1, \mathbf{C}^1, \mathbf{D}^1, \boldsymbol{\lambda}^1, \boldsymbol{\varpi}^1, \boldsymbol{\Omega}^1)) \\ &= \mathcal{H}^1(\Lambda^1, \mathbf{C}^1, \mathbf{D}^1, \boldsymbol{\lambda}^1, \boldsymbol{\varpi}^1, \boldsymbol{\Omega}^1).\end{aligned}\quad (2.52)$$

The new Hamiltonian \mathcal{H}^1 is determined as the evolution of \mathcal{H} along the flow of L_W

$$\mathcal{H}^1 = \exp(L_{\varepsilon W})\mathcal{H}|_{(\Lambda, \mathbf{C}, \mathbf{D}, \boldsymbol{\lambda}, \boldsymbol{\varpi}, \boldsymbol{\Omega})=(\Lambda^1, \mathbf{C}^1, \mathbf{D}^1, \boldsymbol{\lambda}^1, \boldsymbol{\varpi}^1, \boldsymbol{\Omega}^1)}.\quad (2.53)$$

Let us expand \mathcal{H}^1 at the second order in ε

$$\mathcal{H}^1 = \mathcal{H}_0 + \varepsilon \mathcal{H}_1 + \varepsilon \{W, \mathcal{H}_0\} + \varepsilon^2 \{W, \mathcal{H}_1\} + \frac{\varepsilon^2}{2} \{W, \{W, \mathcal{H}_0\}\} + \mathcal{O}(\varepsilon^3),\quad (2.54)$$

where every term is evaluated with the new variables. \mathcal{H}^1 is equal to the averaged Hamiltonian at first order in ε if the first terms of (2.50) and (2.54) are equal

$$\varepsilon \bar{\mathcal{H}}_1 = \varepsilon \mathcal{H}_1 + \varepsilon \{W, \mathcal{H}_0\}.\quad (2.55)$$

Equation (2.55) is called the homologic equation. In order to solve it, we develop in Fourier series of the angles $\boldsymbol{\lambda}^1$, the Hamiltonians W and \mathcal{H}_1 . We write

$$W(\Lambda^1, \boldsymbol{\lambda}^1, \mathbf{C}^1, \mathbf{D}^1, \boldsymbol{\varpi}^1, \boldsymbol{\Omega}^1) = \sum_{\mathbf{k} \in \mathbb{Z}^N} w^{(\mathbf{k})}(\Lambda^1, \mathbf{C}^1, \mathbf{D}^1, \boldsymbol{\varpi}^1, \boldsymbol{\Omega}^1) e^{i\mathbf{k} \cdot \boldsymbol{\lambda}^1},\quad (2.56)$$

and

$$\mathcal{H}_1(\Lambda^1, \boldsymbol{\lambda}^1, \mathbf{C}^1, \mathbf{D}^1, \boldsymbol{\varpi}^1, \boldsymbol{\Omega}^1) = \sum_{\mathbf{k} \in \mathbb{Z}^N} h_1^{(\mathbf{k})}(\Lambda^1, \mathbf{C}^1, \mathbf{D}^1, \boldsymbol{\varpi}^1, \boldsymbol{\Omega}^1) e^{i\mathbf{k} \cdot \boldsymbol{\lambda}^1}.\quad (2.57)$$

Since $\bar{\mathcal{H}}_1$ does not depend on the mean longitudes, for every $\mathbf{k} \in \mathbb{Z}^N \setminus \{0\}$, the equation (2.55) becomes

$$h_1^{(\mathbf{k})} - \iota(\mathbf{k} \cdot \mathbf{n}^1) w^{(\mathbf{k})} = 0,\quad (2.58)$$

where $\mathbf{n}^1 = \nabla_{\Lambda^1} \mathcal{H}_0$ are the mean motion computed in the new coordinates. We therefore obtain the Fourier coefficients of W as

$$w^{(\mathbf{k})} = \frac{h_1^{(\mathbf{k})}}{\iota(\mathbf{k} \cdot \mathbf{n}^1)}.\quad (2.59)$$

If $(\mathbf{k} \cdot \mathbf{n}^1) > \varepsilon$, the new variables are ε -close to the original ones and can be computed by the transformation $\phi_{\varepsilon W}^1$. At first order in ε , the coordinates $(\Lambda^1, \mathbf{C}^1, \mathbf{D}^1, \boldsymbol{\varpi}^1, \boldsymbol{\Omega}^1)$ correspond to their average value over the mean longitudes. If we neglect the terms of order ε^2 , the Hamiltonian (2.50) no longer depends on the mean longitudes. Therefore, the Λ_k^1 are conserved. This approximation is called the secular approximation and allows to study the long term evolution of the orbit's parameters $(C_k, D_k, \varpi_k, \Omega_k)$. In order to avoid complicated notations, I will no longer use explicitly the averaged variables $(\Lambda^1, \mathbf{C}^1, \mathbf{D}^1, \boldsymbol{\varpi}^1, \boldsymbol{\Omega}^1)$ whenever I

study the secular system I will instead simply use the original notation without the superscript 1.

In the term of order ε^2 of (2.50), there are products of W and H_1 . As a result, the development of \mathcal{H}_2 contains terms with contributions from up to three planets contrarily to \mathcal{H}_1 . However, due to the expression of W , the d'Alembert relations still hold. While at first order in ε , the Lie series method is equivalent to directly using the averaged dynamics, new terms will appear at higher order.

2.4.3 Lagrange-Laplace solution

There is no analytical expression in Poincaré coordinates for the averaged Hamiltonian $\bar{\mathcal{H}}_1$. However, it is possible to study analytically the truncated expansion in power series of (x_k, y_k) of (2.38). The development of the solution of degree two in (x_k, y_k) was initially proposed by Lagrange for the development in inclinations and Laplace for the development in eccentricities.

Since the semi-major axes are constant, the Keplerian part can be dropped and the Λ_k appear only as parameters. From the second d'Alembert relation, we know that $\bar{\mathcal{H}}_1$ is even in the inclination degrees of freedom in the sense that $\sum_{i=1}^N l'_i - \bar{l}'_i$ is an even integer. Because we only consider the secular term, we have $k_i = 0$ in (2.45) so we deduce that the secular Hamiltonian is also even in the eccentricity degrees of freedom since $\sum_{i=1}^N l_i - \bar{l}_i = -\sum_{i=1}^N l'_i - \bar{l}'_i$. The Lagrange-Laplace Hamiltonian can be written as (*e.g.* Laskar and Robutel, 1995)

$$\varepsilon \mathcal{H}_{LL} = \bar{\mathbf{x}}^T \cdot \mathbf{Q}_x \cdot \mathbf{x} + \bar{\mathbf{y}}^T \cdot \mathbf{Q}_y \cdot \mathbf{y}, \quad (2.60)$$

where \mathbf{Q}_x and \mathbf{Q}_y are two symmetric matrices that depend on the masses and semi-major axes. The coefficients of \mathbf{Q}_x and \mathbf{Q}_y have for expression

$$\mathbf{Q}_x^{k,l} = \begin{cases} -\frac{Gm_k m_l}{a_l} \frac{C_1(\alpha_{k,l})}{\sqrt{\Lambda_k \Lambda_l}} & \text{for } k \neq l \\ \sum_{j \neq k} -\frac{Gm_k m_j}{a_j} \frac{C_2(\alpha_{k,j})}{\Lambda_k} & \text{for } k = l \end{cases} \quad (2.61)$$

and

$$\mathbf{Q}_y^{k,l} = \begin{cases} -\frac{Gm_k m_l}{a_l} \frac{C_2(\alpha_{k,l})}{\sqrt{\Lambda_k \Lambda_l}} & \text{for } k \neq l \\ \sum_{j \neq k} \frac{Gm_k m_j}{a_j} \frac{C_2(\alpha_{k,j})}{\Lambda_k} & \text{for } k = l \end{cases}, \quad (2.62)$$

where $\alpha_{k,l} = a_k/a_l$ and

$$\begin{aligned} C_1(\alpha) &= \frac{3}{4} \alpha b_{3/2}^{(0)}(\alpha) - \frac{\alpha^2 + 1}{2} b_{3/2}^{(1)}, \\ C_2(\alpha) &= \frac{1}{4} \alpha b_{3/2}^{(0)}(\alpha), \end{aligned} \quad (2.63)$$

where $b_s^{(k)}(\alpha)$ are the Laplace coefficients (see chapter 4). It should be noted that $C_{1,2}(\alpha^{-1}) = \alpha C_{1,2}(\alpha)$ so the coefficients in (2.61) and (2.62) are symmetric.

The equations of motion are

$$\begin{aligned}\frac{d\mathbf{x}}{dt} &= \iota \frac{\partial \varepsilon \mathcal{H}_{LL}}{\partial \bar{\mathbf{x}}} = \iota \mathbf{Q}_x \cdot \mathbf{x}, \\ \frac{d\mathbf{y}}{dt} &= \iota \frac{\partial \varepsilon \mathcal{H}_{LL}}{\partial \bar{\mathbf{y}}} = \iota \mathbf{Q}_y \cdot \mathbf{y}.\end{aligned}\quad (2.64)$$

They are a linear system of ordinary differential equations (ODE). The solution is a sum of periodic terms of frequencies given by the eigenvalues of the two matrices. The frequencies of the motion of \mathbf{x} are usually called g_k and those associated with the motion of \mathbf{y} are noted s_k . Due to the conservation of angular momentum, one of the s_k frequency should be zero. In the Solar System this is traditionally s_5 . While at first order, the evolution of the eccentricities and inclination are independent, there exists terms mixing eccentricities and inclinations in the higher order expansion.

2.5 Mean motion resonances

When one solves the homologic equation (2.55), it can happen that for some $\mathbf{k} \in \mathbb{Z}^N$, $\mathbf{k} \cdot \mathbf{n} < \varepsilon$. In this case the transformation is not defined. Such a combination of mean motions is called a mean motion resonance (MMR). Resonances and MMR in particular are the main source of chaos and instability in planets dynamics.

When a system is close to a MMR, the transformation W is no longer close to the identity and therefore, the expansion in power of ε is no longer accurate. As a result, it is not possible to average over every mean longitudes. Indeed, if $\mathbf{k} \cdot \mathbf{n} = 0$, the mean longitudes are no longer independent. Nevertheless, it is possible to average over the non-resonant angles and obtain a normal form that still depends on the resonant combination of angles. The effect of the MMR on dynamical stability is developed in chapter 4.

The sum $k = \sum_{i=1}^n k_i$ is called the order of the resonance. From the d'Alembert rule (2.45) we deduce that the terms associated with a particular resonance \mathbf{k} also verifies

$$k = - \sum_{i=1}^N (l_i - \bar{l}_i) + (l'_i - \bar{l}'_i). \quad (2.65)$$

In particular, the terms associated with a MMR of order k are at least of degree k in eccentricities and inclinations. In the case of first order MMR, the leading order only depends on eccentricities since the Hamiltonian is even in the inclination variables.

Chapter 3

AMD-stability and the classification of planetary systems

The content of this chapter was initially published in (Laskar and Petit, 2017).

3.1 Introduction

The increasing number of known planetary systems has made necessary the search for a possible classification of these planetary systems. Ideally, such classification should not require heavy numerical analysis as it needs to be applied to large sets of systems. Some possible approach can rely on the stability analysis of these systems, as this stability analysis is also part of the process used to consolidate planetary systems discovery. The stability analysis can also be considered as a key part of the understanding of the wider question of the architecture of planetary systems. In fact, the distances between planets and other orbital characteristic distributions is one of the oldest question in celestial mechanics, the most famous attempts to set laws for this distribution of planetary orbits being the so-called Titius-Bode power laws (for a review, see Nieto, 1972; Graner and Dubrulle, 1994, see also table 1.1).

The recent research has focused on statistical analysis of observed architecture (Fabrycky *et al.*, 2014; Lissauer *et al.*, 2011; Mayor *et al.*, 2011), eccentricity distribution (Moorhead *et al.*, 2011; Shabram *et al.*, 2016; Xie *et al.*, 2016) or inclination distribution (Fang and Margot, 2012; Figueira *et al.*, 2012), see Winn and Fabrycky (2015) for a review.

These observations analysis have been compared with models of systems architecture (Fang and Margot, 2013; Pu and Wu, 2015; Tremaine, 2015). These theoretical works usually used empirical criteria based on Hill separation proposed by Gladman (1993) and refined by Chambers *et al.* (1996) and Smith and Lissauer (2009) and Pu and Wu (2015). Those stability criteria usually multiply the Hill radius by a numerical factor Δ_{sep} empirically evaluated to a value around 10. They are extensions of the analytical results on Hill spheres for the 3-body problem

(Marchal and Bozis, 1982; Petit *et al.*, 2018, see also chapter 5).

Works on chaotic motion caused by overlap of mean motion resonances (MMR, Wisdom, 1980; Deck *et al.*, 2013; Ramos *et al.*, 2015; Petit *et al.*, 2017; Hadden and Lithwick, 2018) could justify the Hill-type criteria, but the results on the overlap of MMR island are valid only for close orbits and for short term stability.

Another approach to stability analysis is to consider the secular approximation of a planetary system. In this framework, the conservation of semi-major axis leads to the conservation of another quantity, the Angular Momentum Deficit (AMD, Laskar, 1997; Laskar, 2000). An architecture model can be developed from this consideration (Laskar, 2000). The AMD can be interpreted as a measure of the orbits' excitation (Laskar, 1997) that limit the planets close encounters and ensure the longterm stability.

Therefore a stability criterion can be derived from the semi-major axis, the masses and the AMD of a system. Besides, it can be demonstrated that the AMD decreases during inelastic collisions (see chapter 7), accounting for the gain of stability of a lower multiplicity system. Here we extend the previous analysis of (Laskar, 2000), and derive more precisely the AMD-stability criterion that can be used to establish a classification of the multi-planetary systems.

The main goal of the article (Laskar and Petit, 2017) was to present the AMD-stability and the classification that results from it. However, in (Laskar, 2000), which was published as a letter, the detailed computations were refereed as a preprint to be published. Although this preprint was in nearly final form for more than a decade, and had even been provided to some researchers (Hernández-Mena and Benet, 2011), it was still unpublished. As a result, the fundamental concepts of AMD, the full description and all proofs for the model that was described in (Laskar, 2000), and the associated appendices were published altogether in (Laskar and Petit, 2017). The article material is thus close to the unpublished preprint.

In this thesis, I chose to separate in two chapters, the definition of the AMD-stability and the classification of the planetary systems (this chapter), from the matter related to the planet formation toy-model described in (Laskar, 2000, developed in chapter 7). Moreover, I also added to chapter 7 some unpublished improvements made during my thesis. As such, I believe that the two chapters gain in coherence and readability.

Sections 3.2 and 3.3 are dedicated to the introduction of the AMD and the development of the AMD-stability. In section (section 3.4), we show how the AMD-stability criterion can be used to develop a classification of planetary systems. This AMD-stability classification is then applied to a selection of 131 multi-planet systems from the `exoplanet.eu` database with known eccentricities.

3.2 Angular Momentum Deficit (AMD)

We consider the N -planetary system introduced in section 2.2 and we use the heliocentric variables (eq. 2.33) as well as the Delaunay coordinates defined in equation (2.37).

Let \mathbf{G} be the total angular momentum. When expressed in heliocentric variables,

the angular momentum is thus the sum of the angular momentum of the Keplerian problems of the unperturbed Hamiltonian \mathcal{H}_0 (eq. 2.34). In particular, if the angular momentum direction is assumed to be the axis z , the norm of the angular momentum is

$$G = \sum_{k=1}^N \Lambda_k - C_k - D_k = \sum_{k=1}^N \Lambda_k \sqrt{1 - e_k^2} \cos i_k \quad (3.1)$$

where $\Lambda_k = m_k \sqrt{\mu a_k}$. For such a system, the angular momentum deficit (AMD) is defined as the difference between the norm of the angular momentum of a coplanar and circular system with the same semi-major axis values, and the norm of the angular momentum G , i.e. (Laskar, 1997; Laskar, 2000)

$$C = \left(\sum_{k=1}^N \Lambda_k \right) - G = \sum_{k=1}^N C_k + D_k = \sum_{k=1}^N \Lambda_k \left(1 - \sqrt{1 - e_k^2} \cos i_k \right). \quad (3.2)$$

In the secular approximation, the Λ_k are conserved so the total AMD C is conserved due to the conservation of angular momentum. We show that this quantity is conserved in the secular system at all orders of averaging (see Appendix B.2). For small eccentricities and inclinations, we can write

$$C = \sum_{k=1}^N \frac{\Lambda_k}{2} (e_k^2 + i_k^2) + O(|e, i|^4). \quad (3.3)$$

We see that the AMD acts as a weighted sum of the eccentricities and inclinations of a system. In other words C measures the degree of non linearity of the orbital dynamics and can be considered as a dynamical temperature. Since its definition (Laskar, 1997), the AMD has been used extensively in planet formation in order to measure the excitation of systems created by numerical simulations *e.g.* (Chambers, 2001). Indeed, it simplifies the analysis of planetary systems by replacing the many degree of freedom of eccentricities and inclinations by a single parameter.

In this chapter, we present a classification of exoplanetary systems based on their AMD. Another application of the conservation of AMD is developed in chapter 7 where I present a simplified model of planetary formation as well as consideration on the planetary systems architecture.

3.3 AMD-stability

We will say that a planetary system is AMD-stable if the AMD amount in the system is not sufficient to allow for planetary collisions. Since the AMD is conserved in the secular system, we conjecture that in absence of short period resonances, the AMD-stability ensures the practical¹ long time stability of the system. Thus for an AMD-stable system, short-time stability will imply long time stability.

The condition of AMD-stability is obtained when the orbits of two planets of semi-major axis a, a' cannot intersect under the assumption that the total AMD

¹ practical stability means here stability over a very long time compared to the expectation life of the central star.

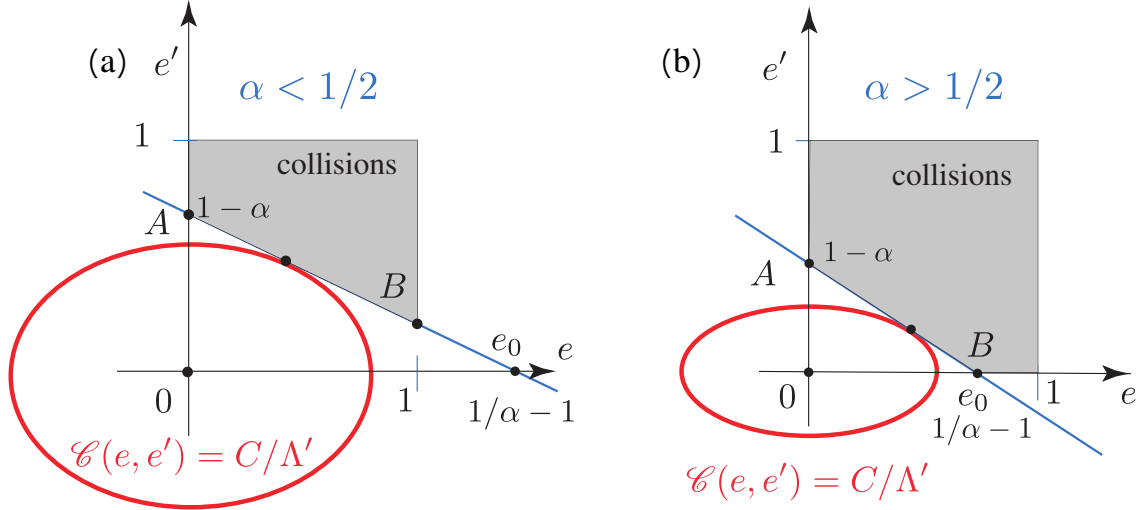


Figure 3.1 – Collision conditions. $e_0 = 1/\alpha - 1$. Case (a) : $\alpha < 1/2 \iff e_0 > 1$. Case (b) $\alpha > 1/2 \iff e_0 < 1$. Collisions can occur only in the shaded region.

C has been absorbed by these two planets. It can be seen easily that the limit condition of collision is obtained in the planar case and can thus be written as

$$a(1+e) = a'(1-e') \quad (3.4)$$

$$m\sqrt{\mu a}(1 - \sqrt{1 - e^2}) + m'\sqrt{\mu a'}(1 - \sqrt{1 - e'^2}) = C \quad (3.5)$$

where (m, a, e) are the parameters of the inner orbit, and (m', a', e') those of the outer one ($a \leq a'$).

3.3.1 Collisional condition

We assume that a, a', m, m' , are non zero. Denoting $\alpha = a/a'$, $\gamma = m/m'$, The system (3.5) becomes

$$\mathcal{D}(e, e') = \alpha e + e' - 1 + \alpha = 0, \quad (3.6)$$

$$\mathcal{C}(e, e') = \gamma\sqrt{\alpha}(1 - \sqrt{1 - e^2}) + (1 - \sqrt{1 - e'^2}) = C/\Lambda', \quad (3.7)$$

with $\Lambda' = m'\sqrt{\mu a'}$, and where $\mathcal{C}(e, e') = C/\Lambda'$ will be called the relative AMD. As e and e' are planetary eccentricities, we have also

$$0 \leq e \leq 1 ; \quad 0 \leq e' \leq 1. \quad (3.8)$$

The set of collisional conditions given in equations (3.6) to (3.8), can be solved using Lagrange multipliers. We are looking for the minimum value of the relative AMD \mathcal{C} (eq. 3.7), for which the collision condition (3.6) is satisfied. These conditions are visualized in the (e, e') plane in figure 3.1. The collision condition (3.6) corresponds to the segment AB of figure 3.1. The domain of collisions is limited by the conditions (3.8). For $e = 0$, we have $e'_0 = 1 - \alpha < 1$, and the intersection of the collision line with the axis $e' = 0$ is obtained for $e_0 = 1/\alpha - 1$. This value can

be greater or smaller than 1 depending of the value of α . We have thus the cases displayed on figure 3.1,

$$\begin{aligned} (a) : \quad \alpha < \frac{1}{2} &\iff e_0 > 1 \quad \text{and} \quad e \leq 1, \\ (b) : \quad \alpha > \frac{1}{2} &\iff e_0 < 1 \quad \text{and} \quad e \leq e_0 \end{aligned} \quad (3.9)$$

and the limit case $\alpha = 1/2$, for which $e_0 = 1$. In all cases, the Lagrange multipliers condition is written

$$\lambda \nabla \mathcal{D}(e, e') = \nabla \mathcal{C}(e, e'), \quad (3.10)$$

which gives

$$\frac{\sqrt{1 - e'^2}}{e'} = \frac{\sqrt{\alpha}}{\gamma} \frac{\sqrt{1 - e^2}}{e} \quad (3.11)$$

This relation allows to eliminate e' in the collision condition (3.6), which becomes an equation in the single variable e , and parameters (α, γ) .

$$F(e, \alpha, \gamma) = \alpha e + \frac{\gamma e}{\sqrt{\alpha(1 - e^2) + \gamma^2 e^2}} - 1 + \alpha = 0. \quad (3.12)$$

$F(e, \alpha, \gamma)$ is properly defined for (e, α, γ) in the domain $D_{e, \alpha, \gamma}$ defined by $e \in [0, 1]$, $\alpha \in]0, 1]$ and $\gamma \in]0, +\infty[$, as in this domain, $1 - e^2 + \gamma^2 e^2/\alpha > 0$. We have also

$$\frac{\partial F}{\partial e}(e, \alpha, \gamma) = \alpha + \frac{\alpha \gamma}{(\alpha(1 - e^2) + \gamma^2 e^2)^{3/2}}. \quad (3.13)$$

Thus $\frac{\partial F}{\partial e} > 0$ on the domain $D_{e, \alpha, \gamma}$ and $F(e, \alpha, \gamma)$ is strictly increasing with respect to e for $e \in [0, 1]$. Moreover, as $0 < \alpha < 1$,

$$F(0, \alpha, \gamma) = -1 + \alpha < 0; \quad F(1, \alpha, \gamma) = 2\alpha > 0; \quad (3.14)$$

and

$$F(e_0, \alpha, \gamma) = \frac{\gamma e_0}{\sqrt{\alpha(1 - e_0^2) + \gamma^2 e_0^2}} > 0. \quad (3.15)$$

The equation of collision (3.12) has thus always a single solution e_c in the interval $]0, \min(1, e_0)[$. This ensures that this critical value of e will fulfill the condition (3.8). The corresponding value of the relative AMD $C_c(\alpha, \gamma) = \mathcal{C}(e_c, e'_c)$ is then obtained through (3.7). When $\alpha \rightarrow 0$, we see from equation (3.6) that the limit of e' is 1. We conclude that $\lim_{\alpha \rightarrow 0} C_c = 1$.

3.3.2 Critical AMD $C_c(\alpha, \gamma)$

We have thus demonstrated that for a given pair of ratios of semi-major axes α and masses γ , there is always a unique critical value $C_c(\alpha, \gamma)$ of the relative AMD $\mathcal{C} = C/\Lambda'$ which defines the AMD-stability. The system of two planets is AMD-stable if and only if

$$\mathcal{C} = \frac{C}{\Lambda'} < C_c(\alpha, \gamma). \quad (3.16)$$

Table 3.1 – Special values of $C_c(\alpha, \gamma)$. The detail of the computations is provided in Annex C.

γ	α	$e_c(\alpha, \gamma)$	$e'_c(\alpha, \gamma)$	$C_c(\alpha, \gamma)$
$\gamma \rightarrow 0$	$\alpha < 1/2$	$1 - 2\frac{1-\alpha}{(1-2\alpha)^2}\gamma^2$	$1 - 2\alpha + 2\frac{\alpha(1-\alpha)}{(1-2\alpha)^2}\gamma^2$	$1 - 2\sqrt{\alpha(1-\alpha)} + \sqrt{\alpha}\gamma$
$\gamma \rightarrow 0$	$\alpha = 1/2$	$1 - (4\gamma)^{2/3}$	$2^{1/3}\gamma^{2/3}$	$\frac{\gamma}{\sqrt{2}}$
$\gamma \rightarrow 0$	$\alpha > 1/2$	$e_0 - \frac{e_0}{\sqrt{\alpha(2\alpha-1)}}\gamma$	$\frac{\sqrt{\alpha}e_0\gamma}{\sqrt{2\alpha-1}}$	$(\sqrt{\alpha} - \sqrt{2 - \frac{1}{\alpha}})\gamma$
$\gamma \rightarrow +\infty$	$0 < \alpha < 1$	$\frac{1}{\gamma}\frac{1-\alpha}{\sqrt{2-\alpha}}$	$1 - \alpha - \frac{1}{\gamma}\frac{\alpha(1-\alpha)}{\sqrt{2-\alpha}}$	$1 - \sqrt{\alpha(2-\alpha)} - \frac{\sqrt{\alpha}(1-\alpha)^2}{2-\alpha}\frac{1}{\gamma}$
1	$0 \leq \alpha \leq 1$	$\frac{1-\sqrt{1-\alpha+\alpha^2}}{\alpha}$	$\sqrt{1-\alpha+\alpha^2} - \alpha$	$1 + \sqrt{\alpha} - \frac{\sqrt{\alpha-2+2\sqrt{1-\alpha+\alpha^2}}}{\sqrt{\alpha}}$ $-\sqrt{\alpha}\sqrt{1-2\alpha+2\sqrt{1-\alpha+\alpha^2}}$
$\sqrt{\alpha}$	$0 \leq \alpha \leq 1$	$\frac{1-\alpha}{1+\alpha}$	$\frac{1-\alpha}{1+\alpha}$	$(1 - \sqrt{\alpha})^2$

The value of the critical AMD $C_c(\alpha, \gamma)$ is obtained by computing first the critical eccentricity $e_c(\alpha, \gamma)$ which is the unique solution of the collisional equation (3.12) in the interval $[0, 1]$. The critical AMD is then $C_c(\alpha, \gamma) = \mathcal{C}(e_c, e'_c)$ (eq. 3.7) where the critical value e'_c is obtained from e_c through equation (3.6). It is important to note that the critical AMD, and thus the AMD-stability condition depends only on (α, γ) .

3.3.3 Behaviour of the critical AMD

We will now analyse the general properties of the critical AMD function $C_c(\alpha, \gamma)$. As $\frac{\partial F}{\partial e}(e, \alpha, \gamma) > 0$, on the domain $D_{e, \alpha, \gamma}$, we can apply the implicit function theorem, which then ensures that the solution of the collision equation (3.12), $e_c(\alpha, \gamma)$, is a continuous function of γ (and even analytic for $\gamma \in]0, +\infty[$). Moreover, on $D_{e, \alpha, \gamma}$,

$$\frac{\partial F}{\partial \gamma}(e, \alpha, \gamma) = \frac{\alpha e (1 - e^2)}{(\alpha (1 - e^2) + \gamma^2 e^2)^{3/2}} \geq 0. \quad (3.17)$$

We have also

$$\frac{\partial e_c}{\partial \gamma}(\alpha, \gamma) = -\frac{e_c (1 - e_c^2)}{(\alpha (1 - e_c^2) + \gamma^2 e_c^2)^{3/2} + \gamma} \leq 0 \quad (3.18)$$

and $e_c(\alpha, \gamma)$ is a decreasing function of γ . For any given values of the semi-major axes ratio α , and masses, γ , we can thus find the critical value $C_c(\alpha, \gamma)$ which allows for a collision (3.16). For the critical value $C_c(\alpha, \gamma)$, a single solution corresponds to the tangency condition (fig. 3.1), and this solution is obtained at the critical value $e_c(\alpha, \gamma)$ for the eccentricity of the orbit \mathcal{O} . The values of the critical relative AMD $C_c(\alpha, \gamma)$ are plotted in figure 3.2 versus α , for different values of γ . Derivating equation (3.7) with respect to γ , one obtains

$$\frac{\partial \mathcal{C}}{\partial \gamma} = \sqrt{\alpha} \left(1 - \sqrt{1 - e^2} \right) + \gamma \sqrt{\alpha} \frac{e}{\sqrt{1 - e^2}} \frac{\partial e}{\partial \gamma} + \frac{e'}{\sqrt{1 - e'^2}} \frac{\partial e'}{\partial \gamma}. \quad (3.19)$$

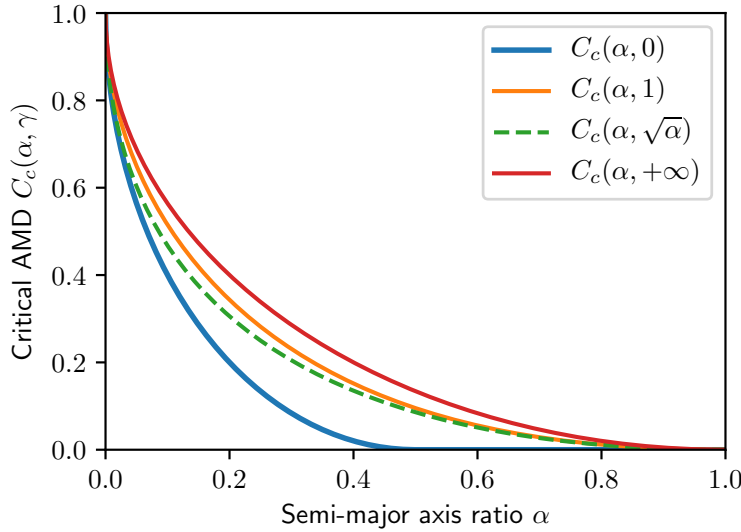


Figure 3.2 – Values of the critical AMD $C_c(\alpha, \gamma)$ versus α for the different γ values for which an explicit expression of $C_c(\alpha, \gamma)$ is obtained.

Using the two relations (3.6, 3.11), this reduces to

$$\frac{\partial C_c(\alpha, \gamma)}{\partial \gamma} = \sqrt{\alpha} \left(1 - \sqrt{1 - e_c^2} \right) > 0 \quad (3.20)$$

Thus $C_c(\alpha, \gamma)$ is strictly increasing with γ . In the same way

$$\frac{\partial C_c(\alpha, \gamma)}{\partial \alpha} = \frac{\gamma}{2\sqrt{\alpha}} \left(1 - \frac{(1 + e_c^2)}{\sqrt{1 - e_c^2}} \right) < 0 \quad (3.21)$$

and $C_c(\alpha, \gamma)$ is decreasing with α .

Now that the general behaviour of the critical AMD $C_c(\alpha, \gamma)$ is known, we can specify its explicit expression in a few special cases that are displayed in Table 3.1. The computations as well as higher order developments can be found in appendix B.3.

A development of $C_c(\alpha, \gamma)$ for $\alpha \rightarrow 1$ can also be obtained (see appendix B.3). With $\eta = 1 - \alpha$ we have,

$$C_c(\alpha, \gamma) \sim \frac{\gamma}{\gamma + 1} \frac{\eta^2}{2} + O(\eta^3) . \quad (3.22)$$

3.4 AMD-classification of planetary systems

Now let show how the AMD-stability can be used as a criterion to derive a classification of planetary systems. In section 3.3.2, we saw that in the secular approximation, the stability of a pair of planets is determined by the computation of

$$\beta = \frac{\mathcal{C}}{C_c} = \frac{C}{\Lambda' C_c} . \quad (3.23)$$

We will call β the AMD-stability coefficient. For pairs of planets, $\beta < 1$ means that collisions are not possible. The pair of planets will then be called AMD-stable. We extend naturally this definition to multiple planets systems. A system is AMD-stable if every adjacent pair is AMD-stable². We can also define an AMD-stability coefficient regarding to the collision with the star. We define β_S , the AMD-stability coefficient of the pair formed by the star and the innermost planet. For this pair, we have $\alpha = 0$ and thus $C_c = 1$. With this simplification $\beta_S = C/\Lambda$, where Λ is the circular momentum of the innermost planet.

3.4.1 Sample studied and methods of computation

We have studied the AMD-stability of some systems referenced in the catalogue The Extrasolar Planets Encyclopædia³ (Schneider *et al.*, 2011). From the catalogue, we selected the 131 systems⁴ that have measured masses, semi-major axis and eccentricities for all their planets. Since the number of systems with known mutual inclinations is too small, we assumed the systems to be almost coplanar. This claim is supported by previous statistical studies that constrain the observed mutual inclinations distribution (Fang and Margot, 2012; Lissauer *et al.*, 2011; Fabrycky *et al.*, 2014 and Figueira *et al.*, 2012). For some systems where the uncertainties were not provided, we consulted the original papers or the Exoplanet Orbit Database⁵ (Wright *et al.*, 2011).

On figure 3.3, we compare the cumulative distribution of adjacent planets period ratios of our sample and the one of all the multiplanetary systems of the database `exoplanet.eu`. The sample is biased toward higher period ratios. Indeed, most of the multiplanetary systems of the database come from the Kepler data. Since these systems are mostly tightly packed ones, their period ratios are rather small. However, the majority of them do not have measured eccentricities and are consequently, excluded from this study. Our sample contains thus mostly systems detected by radial velocities (RV) methods that have on average, higher period ratios.

Since all the AMD computations are done with the relative quantities α and γ , we can use equivalent quantities that are measured more precisely in observations than the masses and semi-major axis. We used the period ratios elevated to the power 3/2 instead of the semi-major axis ratios, and the minimum mass $m \sin(i)$ for RV systems. This is not a problem for the computation of γ because if we assume that the systems are close to coplanarity, then

$$\gamma = \frac{m}{m'} = \frac{m \sin(i)}{m' \sin(i)} \simeq \frac{m \sin(i)}{m' \sin(i')} . \quad (3.24)$$

Even though we assume the systems to be coplanar, we want to take into account the contribution of mutual inclinations to the AMD. Since we have only access to the eccentricities, we define the coplanar AMD of a system C_p , as the AMD of the

²This is equivalent to require that all pairs are AMD-stable.

³<http://exoplanet.eu/>

⁴The systems were selected in November 2016.

⁵<http://exoplanets.org/>

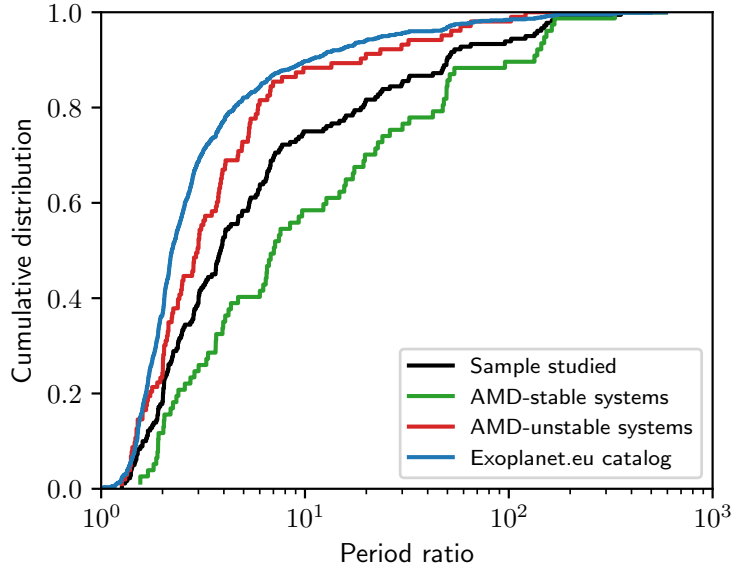


Figure 3.3 – Cumulative distributions of adjacent planets period ratios of the sample studied here, of the AMD-stable (both weak and strong) systems, AMD-unstable systems, and for all the systems referenced in the `exoplanet.eu` database.

same system if it was coplanar. We can also define

$$\beta_p = C_p / (\Lambda' C_c) , \quad (3.25)$$

the coplanar AMD-stability coefficient. Motivated by both theoretical arguments on chaotic diffusion in the secular dynamics (Laskar, 1994; Laskar, 2008) and observed correlations in statistical distributions (Xie *et al.*, 2016), we assume that the AMD contribution of mutual inclinations is equal to the one of eccentricities. This hypothesis is equivalent to assume the on average equipartition of the AMD between the secular degrees of freedom for a chaotic system. The total AMD is thus twice the measured AMD and we use in this study

$$\beta = 2\beta_p . \quad (3.26)$$

We can also define a coplanar AMD-stability coefficient associated with the star and similarly we set $\beta_S = 2\beta_{Sp}$. We then compute the coefficients β_S and β for each pair and the associated uncertainty distributions. We report in Table 3.2 the results of the analysis. In the considered dataset, 70 systems are AMD-stable. The highest multiplicity systems are in majority AMD-unstable. In Figure 3.4 we plot the probability distribution of β for the considered systems. The AMD-stability is a sufficient condition for the stability of a system. It means that AMD-unstable systems are not necessarily dynamically unstable, but rather that a more refined analysis need to be performed in order to determine whether they are long lived or not.¹

Table 3.2 – Result of the analysis split in function of the multiplicity of the system. The column labels are defined in sections 3.4.3 and 3.4.4.

Multiplicity	Strong stable	Weak stable	Unstable	Total
2	42	21	34	97
3	4	1	17	22
4+	2	0	10	12
Total	48	22	61	131

3.4.2 Propagation of uncertainties

The uncertainties are propagated using Monte Carlo simulations of the distributions. After determining the distributions from the input quantities (m, a, e), we generate 10,000 values for each of these parameters. We then compute the derived quantities ($\alpha, \gamma, C_c, \beta \dots$) in these 10,000 cases and the associated distributions.

For masses (or $m \sin(i)$ if no masses were provided) and periods, we assume a Gaussian uncertainty centered on the value referenced in the database and with standard deviation, the half width of the confidence interval. The distributions are truncated to 0.

For eccentricity distributions, the previous method does not provide satisfying results. Most of the Gaussian distributions constructed with the mean value and confidence interval given in the catalogue make probable negative eccentricities (in the case of almost circular planets with large upper bound on the eccentricity). A solution is to assume that the rectangular eccentricity coordinates ($e \cos \omega, e \sin \omega$) are Gaussian. Since the average value of ω has no importance in the computation of the eccentricity distribution, we assume it to be 0. Therefore, $e \sin \omega$ has 0 mean. We define the distribution of $\tilde{e} = e \cos \omega$ as a Gaussian distribution with mean value, the value referenced in the catalogue and standard deviation, the half-width of the confidence interval. If we assume $e \sin \omega$ has the same standard deviation as $e \cos \omega$, we have $e \sin \omega = \tilde{e} - \langle \tilde{e} \rangle$. The distribution of e is then deduced from the \tilde{e} one using

$$e = \sqrt{\tilde{e}^2 + (\tilde{e} - \langle \tilde{e} \rangle)^2} . \quad (3.27)$$

Due to the Gaussian assumption, some masses or periods can take values close to 0 with a small probability (less than a few percent). This causes the distributions of α or γ to diverge if it happens that a' or m' can take values close to 0. To address this issue, a linear expansion around the mean value is used for the quotients, for example for α ,

$$\alpha = \frac{a}{a'} = \frac{a}{\langle a' \rangle} \left(1 - \frac{\Delta a'}{\langle a' \rangle} \right) , \quad (3.28)$$

with $\Delta a' = a' - \langle a' \rangle$. To consider AMD-stable a pair, we require $\beta < 1$ in at least 86 % of the system realizations. This value corresponds to a 1σ uncertainty.

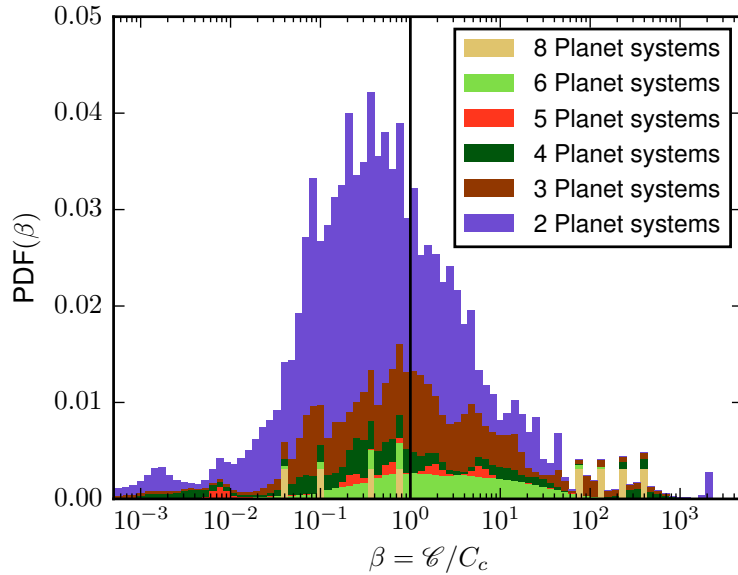


Figure 3.4 – Probability distribution function of β for the sample studied. The systems are grouped by multiplicity. The vertical line $\beta = 1$ marks the separation between AMD-stable and AMD-unstable pairs.

3.4.3 AMD-stable systems

As said above, we call AMD-stable a system where collisions between planets are impossible for dynamics ruled by AMD ($\max \beta < 1$). Besides, if the AMD-stability coefficient of the star $\beta_S < 1$ (resp. $\beta_S > 1$), the system is defined as strong AMD-stable (resp. weak AMD-stable).

Strong AMD-stable systems

The strong AMD-stable systems can be considered longterm dynamically stable. In Figure 3.5, we plot the architecture of the strong AMD-stable systems. If the system is out of the mean motion resonances (MMR) islands, the AMD will not raise and therefore, no collision between planets nor with the star can occur. We can see on Figure 3.3 that the AMD-stable systems have period ratios on average larger than the ones from the considered sample.

Weak AMD-stable systems

As defined above, in a weak AMD-stable system, no planets collisions can occur but the innermost planet can increase its eccentricity up to 1 and collide with the star. We separate these systems from the strong AMD-stable ones because the system can still lose a planet only by AMD exchange. However, the remaining system will not be affected by the destruction of the inner planet. On Figure 3.6, we plot their architecture. In these systems, the inner planet is much closer to the star than the others.

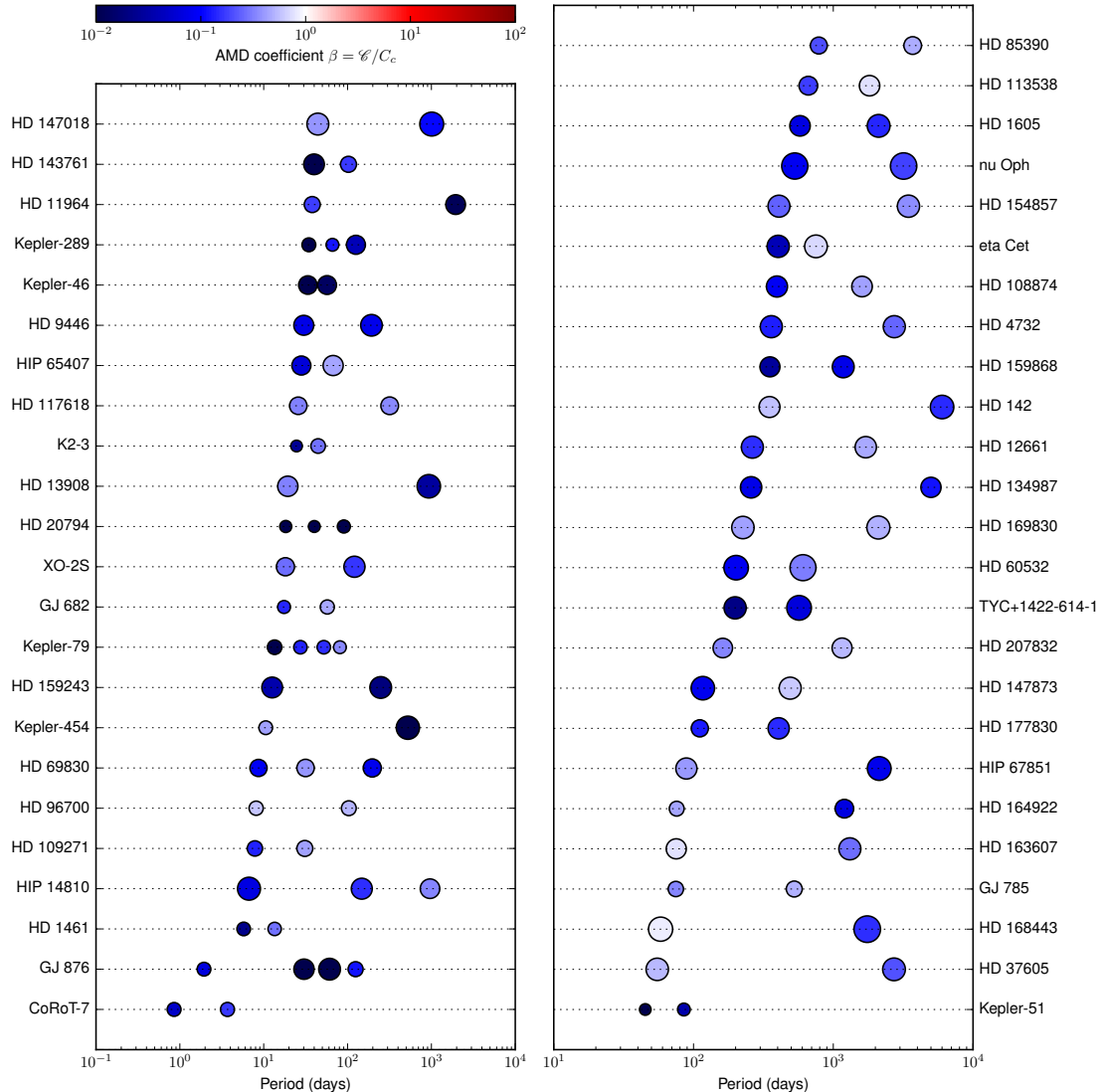


Figure 3.5 – Architecture of the strong AMD-stable systems, each planet is represented by a circle of size proportional $\log_{10}(m)$ where m is the mass of the planet. The color represents the AMD-stability coefficient of the *inner* pair associated to the planet (in particular the first planet is represented with the AMD-stability coefficient associated to the star β_S). This means that a 'red' planet can collide with its inner neighbour.

3.4.4 AMD-unstable systems

The AMD-unstable systems have at least one unstable planet pair. But as we can see in Figure 3.7 where we plot the architecture of these systems, this category is not homogeneous. It gathers high multiplicity systems where planets are too close to each other for the criterion to be valid; multi-scale systems like the Solar System where the inner system is AMD-unstable due to its small mass in comparison to the outer part; systems experiencing mean motion resonances... In all these cases, an

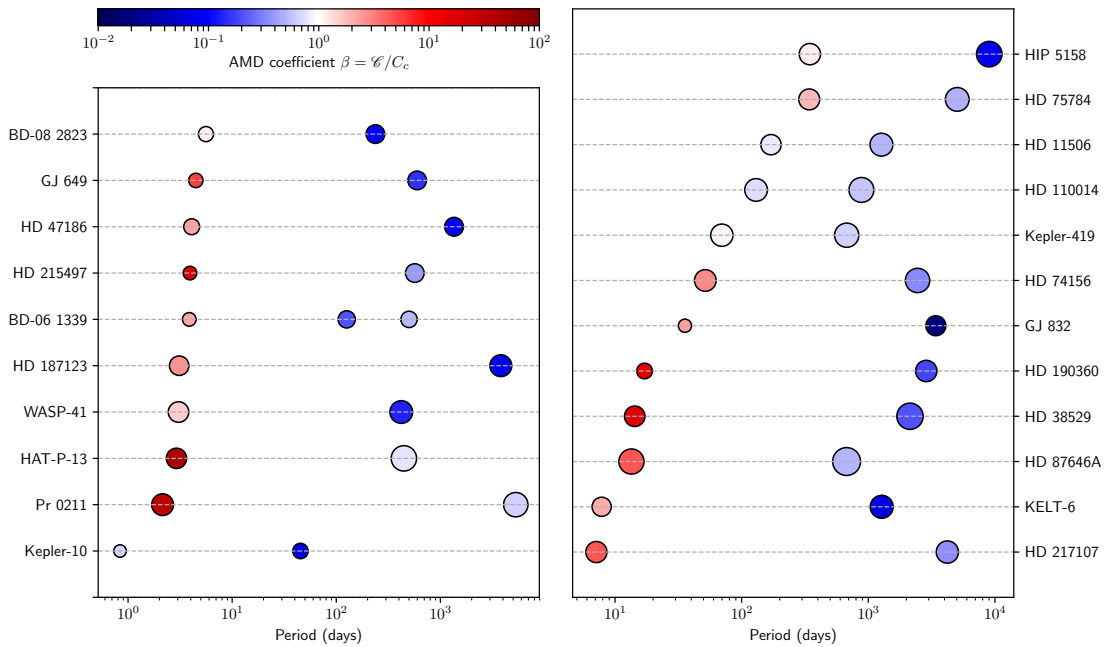


Figure 3.6 – Architecture of the weak AMD-stable systems, each planet is represented by a circle of size proportional $\log_{10}(m)$ where m is the mass of the planet. The color represents the AMD-stability coefficient of the *inner* pair associated to the planet (in particular the first planet is represented with the AMD-stability coefficient associated to the star β_S). Certains systems such (*e.g.* Kepler-10) seems to be strong stable, the color represents the median value of the AMD-stability coefficient whereas we choose to consider AMD-unstable, the pairs with $\beta > 1$ in more than 14% of the realizations.

in-depth dynamical study is necessary to conclude on the short or long term stability of these systems. In the next subsections, we will detail how the AMD-stability and AMD driven dynamics can help to understand these systems.

Hierarchically AMD-stable systems (Solar system like)

Let us first consider the Solar System. Due to the large amount of AMD created by the giants planets, the inner system is not AMD-stable (Laskar, 1997). However, long term secular and direct integrations have shown that the inner system has only a probability of about 1% to become unstable over 5 Gyr (Laskar, 2008; Laskar and Gastineau, 2009; Batygin *et al.*, 2015). Indeed the chaotic dynamics is mainly restricted to the inner system while the outer system is mostly quasi-periodic. However, when AMD exchanges occur between the outer and inner systems, the inner system becomes highly unstable and can lose one or several planets.

We plot on Figure 3.8, the AMD as well as the circular momenta of the Solar System planets. We see that the inner system planets (resp. the outer planets) have comparable AMD which is an indication that they belong to the same AMD reservoir. Indeed, Laskar (2008) showed that over 5 Gyr, there is almost no AMD

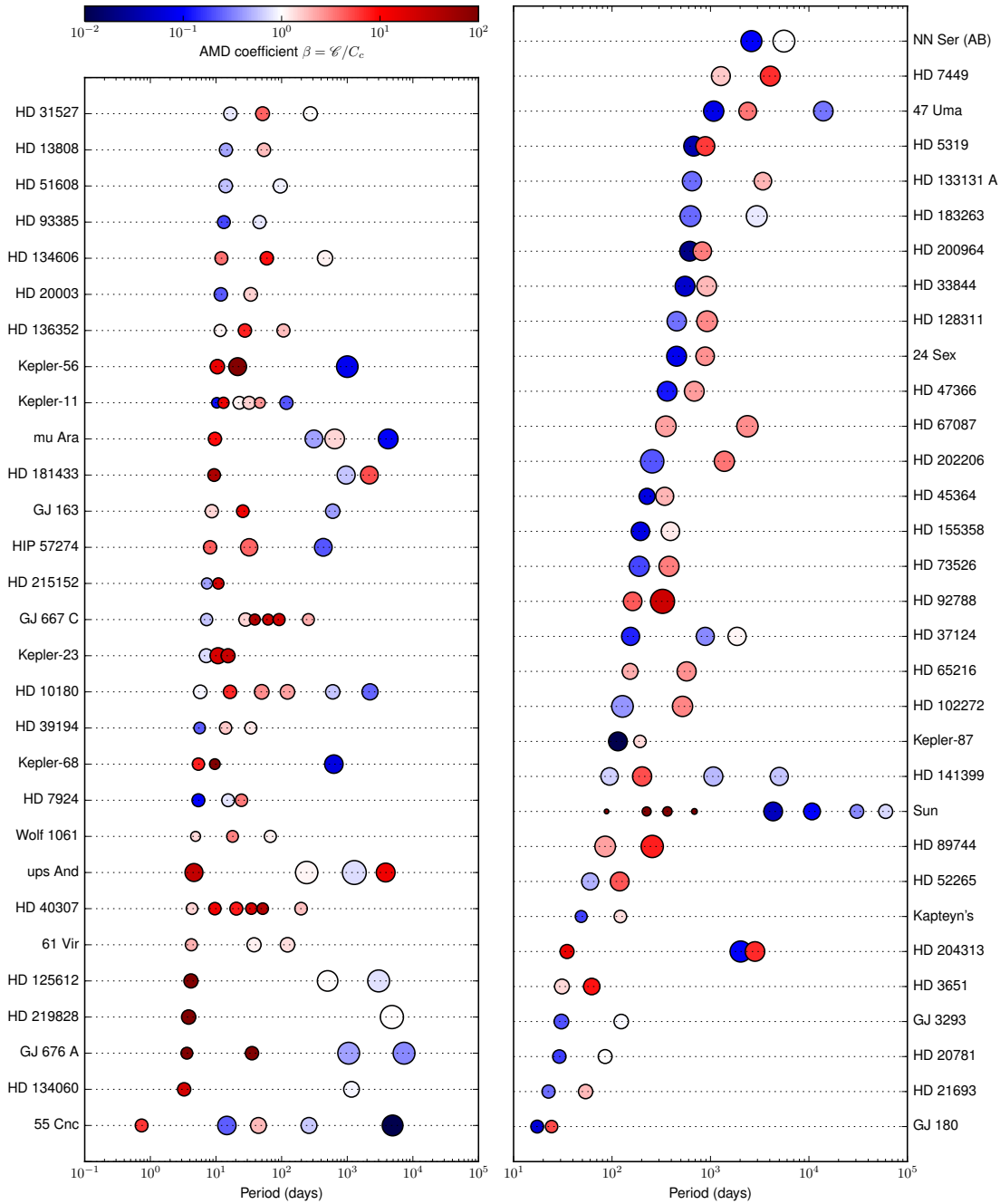


Figure 3.7 – Architecture of the AMD-unstable systems, each planet is represented by a circle of size proportional $\log_{10}(m)$ where m is the mass of the planet. The color represents the AMD-stability coefficient of the *inner* pair associated to the planet (in particular the first planet is represented with the AMD-stability coefficient associated to the star β_S).

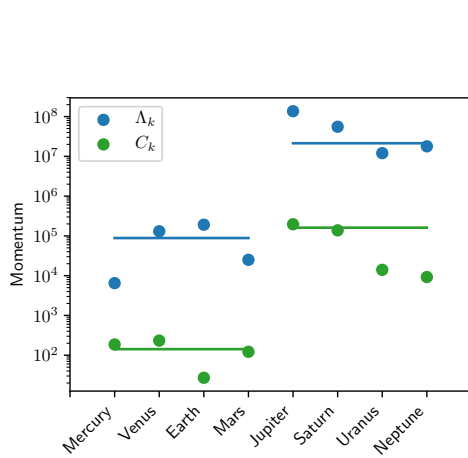


Figure 3.8 – Circular momenta and AMD of the Solar system planets. The horizontal lines corresponds to the respective mean Λ and C for the inner and outer system.

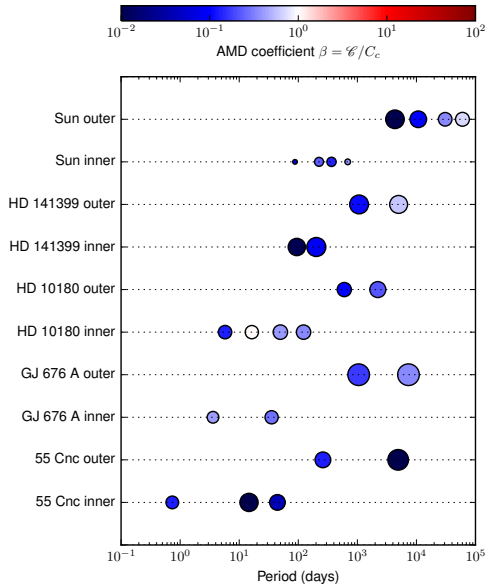


Figure 3.9 – Examples of systems where the outer part is AMD-stable and the inner part becomes AMD-stable if considered alone.

exchanges between the two parts of the system (but in the 1% cases where an exchange occurs, it leads to the destruction of the inner system). Moreover, the spacing of the planets follows surprisingly well the distribution laws mentioned in section 7.3 if we consider the two parts of the system separately (Laskar, 2000).

We see that given an analysis of the secular dynamics, the tools developed above can still help to understand how an *a priori* unstable system can still exist in its current state. The case of AMD-unstable systems with an AMD-stable part is not restricted to the Solar system. If we look for systems where the outer part is AMD-stable while the whole system is AMD-unstable, we find 4 similar systems in our sample as shown in Figure 3.9. We will call these systems hierachic AMD-stable systems.

Resonant systems

As shown on the cumulative distributions plotted on the Figure 3.3, the AMD-unstable systems have period ratios smaller than the AMD-stable ones. For example, in our sample, 66% of the adjacent pairs of the AMD-unstable systems have a period ratio below 4 whereas this proportion is of only 33% for the AMD-stable systems. For period ratios close to small integer ratios, the MMR can rule a great part of the dynamics. Particularly, if pairs of planets are trapped into a large resonance island, the system could be dynamically stable even if it is not AMD-stable.

As an example, we can consider a multiplanetary system with a pair of planet trapped in a MMR while the rest of the system experiences a secular chaotic motion. We can also assume that all planet pairs but the resonant one are AMD-stable while the resonant pair is AMD-unstable. Since the exchange of AMD between

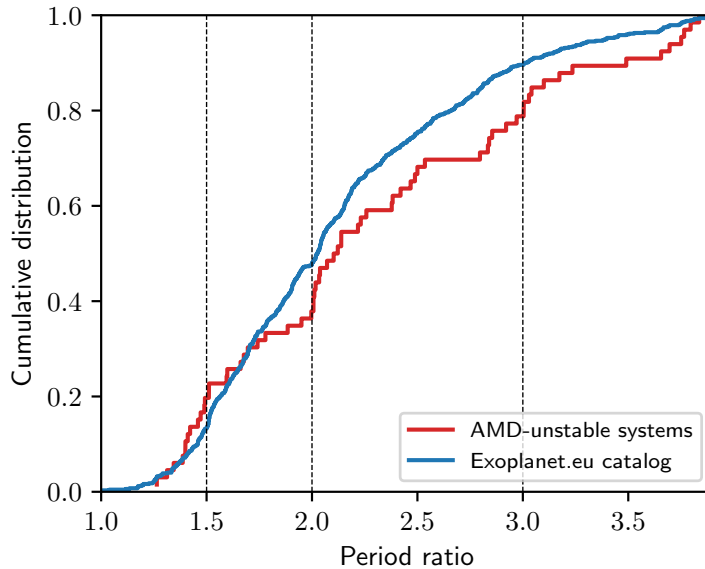


Figure 3.10 – Normalized cumulative period ratios distribution of the AMD-unstable systems and of all systems in the catalogue for small period ratios. The vertical line represents low order MMR.

the two resonant planets is ruled by the resonant mechanics and not the chaotic secular motion, we can imagine that the resonance protects this particular pair from collision, leading to a system globally stable.

Individual dynamical studies are necessary in order to claim that a system is stable due to a MMR. We can however remark that the AMD-unstable systems considered here are statistically constituted of more resonant pairs than a typical sample of the catalogue.

Concentration around MMR

In this part, we want to test if the unstable systems have been drawn randomly from the `exoplanet.eu` catalogue or if the period ratios of the pairs of adjacent planets are statistically closer to small integer ratios. Let us note \mathcal{H}_0 , the hypothesis that the period ratios of the unstable systems have been drawn randomly from the catalogue distribution. We consider only the period ratios smaller than 4 because the higher ones are not significant for a study of the MMR. We plot on figure 3.10 the cumulative distribution of the period ratios of the AMD-unstable systems as well as the cumulative distribution of the period ratios of all the systems of `exoplanet.eu`. Let us call R_u the set of period ratios of the AMD-unstable planets.

We first test \mathcal{H}_0 thanks to a Kolmogorov-Smirnov test (Lehmann and Romano, 2006) between the sample R_u and the period ratios of the catalogue. The test fails to reject \mathcal{H}_0 with a p-value of about 9%. Therefore, we cannot reject \mathcal{H}_0 on the global shape of the distribution of the AMD-unstable period ratios.

However, we want to determine if the AMD-unstable pairs are close to small

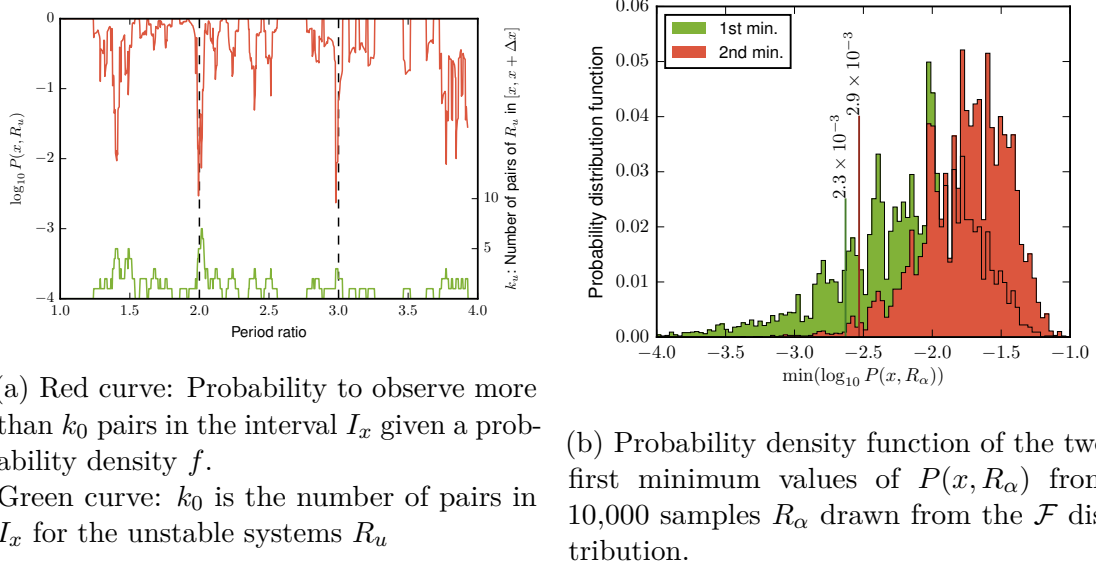


Figure 3.11 – Estimates on the clustering of period ratios in the AMD-unstable subsample.

integer ratios, which means study the fine structure of the distribution. We propose here another method to demonstrate this.

Let us note the probability density of the catalogue period ratios f and the associated cumulative distribution \mathcal{F} . Let us consider an interval $I_x = (x, x + \Delta x)$, if we assume \mathcal{H}_0 , the probability for a ratio r to be in I_x is

$$\Pr(r \in I_x | \mathcal{H}_0) = \int_x^{x+\Delta x} f(r') dr' = \mathcal{F}(x + \Delta x) - \mathcal{F}(x) = \Delta \mathcal{F}(x) . \quad (3.29)$$

Therefore, the probability that more than k_0 pairs out of N pairs drawn randomly from the distribution \mathcal{F} are in I_x is

$$\Pr(x, k_0 | \mathcal{H}_0) = \sum_{k=k_0}^N \binom{N}{k} (1 - \Delta \mathcal{F})^{N-k} \Delta \mathcal{F}^k . \quad (3.30)$$

This is the probability of a binomial trial. From now on, N designates the number of period ratios in R_u . For a given Δx , we can compute the probability $P(x, R_u) = \Pr(x, k_u(x))$ where $k_u(x)$ is the number of pairs from R_u in I_x . This probability measures the likelihood of a concentration of elements of R_u around x , assuming they were drawn from \mathcal{F} . We choose $\Delta x = 0.05$ and plot the function $P(x, R_u)$ as well as k_u in Figure 3.11a. We observe that the concentrations around 3 and 2 are very unlikely with a probability of 2.3×10^{-3} and 2.9×10^{-3} respectively. Other peaks appear for $x = 1.4$ and around 3.8. However $P(x, R_u)$ is the probability to see a concentration around x precisely. It is not the probability to observe a concentration somewhere between 1 and 4.

To demonstrate that the concentrations around 2 and 3 are meaningful, we compare this result to samples drawn randomly from the distribution \mathcal{F} . We create 10,000 datasets R_α by drawing N points from \mathcal{F} and compute $P(x, R_\alpha)$ for these

datasets. Then, we record the two minimum values (at least distant by more than Δx) and plot the distribution of these minima on Figure 3.11b. From these simulations, we see that on average, 17.2% of the samples have a minimum as small as R_u . However, the presence of a secondary peak as significant as the second one of R_u has a probability of 1.3%. Moreover, the R_u concentrations are clearly situated around small integer ratios which would not be the case in general for a randomly generated sample.

We thus demonstrated here that the AMD-unstable systems period ratios are significantly more concentrated around small integer ratios than a random sample of the `exoplanet.eu` database. While we do not prove that the pairs of planets close to these ratios are actually in MMR, this result motivates further investigations toward the behaviour of these pairs in a context of secular chaotic dynamics.

3.5 Conclusion

The Angular Momentum Deficit (AMD Laskar, 1997; Laskar, 2000) is a key parameter for the understanding of the outcome of the formation processes of planetary systems (e.g. Chambers, 2001; Morbidelli *et al.*, 2012; Tremaine, 2015). We have shown here how AMD can be used to derive a well defined stability criterion : the AMD-stability. The AMD-stability of a system can be checked by the computation of the critical AMD C_c (eq. 3.12) and AMD-stability coefficients β_i that depend only on the eccentricities and ratios of semi major axis and masses (eqs. 3.7, 3.12, 3.16, 3.23). This criterion thus does not depend on the degeneracy of the masses coming from radial velocity measures. Moreover, the uncertainty on the mutual inclinations can be compensated by assuming equipartition of the AMD between eccentricities and inclinations. AMD-stability will ensure that in absence of mean motion resonances, the system is long term stable. A rapid estimate of the stability of a system can thus be obtain by a short term integration and the simple computation of the AMD-stability coefficients.

We have also proposed here a classification of the planetary systems based on AMD-stability (Section 3.4). The strong AMD-stable systems are the systems where no planetary collisions are possible, and no collisions of the inner planet with its central star, while the weak AMD-stable systems allow for the collision of the inner planet with the central star. The AMD-unstable systems are the systems for which the AMD-coefficient does not prevent the possibility of collisions. The Solar System is AMD-unstable, but it belongs to the sub category of hierarchical AMD-stable systems that are the systems which are AMD-unstable but which becomes AMD-stable when they are split in two parts (giant planets and terrestrial planets for the Solar System) (Laskar, 2000). Out of the 131 studied systems from `exoplanet.eu`, we find 48 strong AMD-stable, 22 weak AMD-stable, and 61 AMD-unstable systems, including 5 hierarchical AMD-stable systems.

As for the Solar System, the AMD-unstable systems are not necessarily unstable, but to decide for their stability requires some further dynamical analysis. Several

mechanisms can stabilize AMD-unstable systems. The absence of secular chaotic interactions between parts of the systems like in the Solar System case, or the presence of mean motion resonances protecting pairs of planets from collision. In this case, the AMD-stability classification is still useful in order to select the systems that require this more in-depth dynamical analysis. It should also be noticed that the discovery of additional planets in a system will require to revise the computation of the AMD-stability of the system. An additional planet will always increase the total AMD, and thus the maximum AMD-coefficient of the system, decreasing its AMD-stability unless it is split into two subsystems.

In the present work, we have not taken into account mean motion resonances (MMR) and the chaotic behaviour resulting from their overlap. This is the subject of the next chapter whose results have been published in (Petit *et al.*, 2017). Indeed, criteria on MMR developed by Wisdom (1980) or more recently Deck *et al.* (2013) help to improve our stability criterion by considering the MMR chaotic zone as a limit for stability instead of the limit considered here that is given by the collisions of the orbits (eqs. 3.12). The drawback is to renounce to the rigorous results that we have established here in section 3.3, and to allow for some more empirical studies. The present work will in any case remain the backbone of the future developments.

Chapter 4

AMD-stability in presence of first order MMR overlap

The content of this chapter was initially published in (Petit et al., 2017).

4.1 Introduction

The AMD-stability criterion (see chapter 3 and also; Laskar, 2000; Laskar and Petit, 2017) allows to discriminate between a-priori stable planetary systems and systems needing an in-depth dynamical analysis to ensure their stability. The AMD-stability is based on the conservation of the angular momentum deficit (AMD, Laskar, 1997) in the secular system at all orders of averaging (see appendix B.2). Indeed, the conservation of the AMD fixes an upper bound to the eccentricities. Since the semi-major axes are constant in the secular approximation, a low enough AMD forbids collisions between planets. The AMD-stability criterion can be used to classify planetary systems based on the stability of their secular dynamics (section 3.4).

However, while the analytical criterion developed in the previous chapter does not depend on series expansions for small masses or spacing between the orbits, the secular hypothesis does not hold for systems experiencing mean motion resonances (MMR). Although a system with planets in MMR can be dynamically stable, chaotic behavior may result from the overlap of adjacent MMR, leading to a possible increase of the AMD and eventually to close encounters, collisions or ejections.

For systems with small orbital separations, averaging over the mean anomalies is thus impossible due to the contribution of the first-order MMR terms. For example, two planets in circular orbits very close to each other are AMD-stable, however the dynamics of this system cannot be approximated by the secular dynamics. We thus need to modify the notion of AMD-stability in order to take into account those configurations.

In studies of planetary systems architecture, a minimal distance based on the

Hill radius (Marchal and Bozis, 1982, see chapter 5) is often used as a criterion of stability (Gladman, 1993; Chambers *et al.*, 1996; Smith and Lissauer, 2009; Pu and Wu, 2015). However, Deck *et al.* (2013) suggested that stability criteria based on the MMR overlap are more accurate in characterizing the instability of the three-body planetary problem.

Based on the considerations of Chirikov (1979) for the overlap of resonant islands, Wisdom (1980) proposed a criterion of stability for the first-order MMR overlap in the context of the restricted circular three-body problem. This stability criterion defines a minimal distance between the orbits such that the first-order MMRs overlap with one another. For orbits closer than this minimal distance, the MMR overlapping induces chaotic behavior eventually leading to the instability of the system.

Wisdom showed that the width of the chaotic region in the circular restricted problem is proportional to the ratio of the planet mass to the star mass to the power 2/7. Duncan *et al.* (1989) confirmed numerically that orbits closer than the Wisdom's MMR overlap condition were indeed unstable. More recently, another stability criterion was proposed by Mustill and Wyatt (2012) to take into account the planet's eccentricity. Deck *et al.* (2013) improved the two previous criteria by developing the resonant Hamiltonian for two massive, coplanar, low-eccentricity planets and Ramos *et al.* (2015) proposed a criterion of stability taking into account the second-order MMR in the restricted three-body problem. Since the publication of this work, Hadden and Lithwick (2018) have proposed an overlap criterion taking into account MMR of all order. While this criterion is in better agreement with the chaotic limit for eccentric orbits, it remains inaccurate for circular orbits due to some assumptions.

Deck's criteria are in good agreement with numerical simulations (Deck *et al.*, 2013) and can be applied to the three-body planetary problem. However, the case of circular orbits is still treated separately from the case of eccentric orbits. Indeed, the minimal distance imposed by the eccentric MMR overlap stability criterion vanishes with eccentricities and therefore cannot be applied to systems with small eccentricities. In this case, Mustill and Wyatt (2012), Deck *et al.* (2013) use the criterion developed for circular orbits. A unified stability criterion for first-order MMR overlap had yet to be proposed.

In this chapter, we propose in section 4.2 a new derivation of the MMR overlap criterion based on the development of the three-body Hamiltonian by Delisle *et al.* (2012). We show in section 4.3 how to obtain a unified criterion of stability working for both initially circular and eccentric orbits. In section 4.4, we then use the defined stability criterion to limit the region where the dynamics can be considered to be secular and adapt the notion of AMD-stability thanks to the new limit of the secular dynamics. Finally we study in section 4.5 how the modification of the AMD-stability definition affects the classification proposed in section 3.4.

4.2 Resonant Hamiltonian

The problem of two planets close to a first-order MMR on nearly circular and coplanar orbits can be reduced to a one-degree-of-freedom system through a sequence of

canonical transformations (Wisdom, 1986; Henrard *et al.*, 1986; Delisle *et al.*, 2012; Delisle *et al.*, 2014). We follow here the reduction of the Hamiltonian used in (Delisle *et al.*, 2012; Delisle *et al.*, 2014).

4.2.1 Averaged Hamiltonian in the vicinity of a resonance

Let us consider two planets of masses m_1 and m_2 orbiting a star of mass m_0 in the plane. The motivation to the planar restriction will be justified hereafter. We use the heliocentric coordinates $(\tilde{\mathbf{r}}_i, \mathbf{r}_i)$ defined in the introduction in equation (2.33). For two planets, the Hamiltonian is (2.34)

$$\mathcal{H} = \frac{1}{2} \sum_{i=1}^2 \left(\frac{\|\tilde{\mathbf{r}}_i\|^2}{m_i} - \mathcal{G} \frac{m_0 m_i}{r_i} \right) + \frac{1}{2} \frac{\|\tilde{\mathbf{r}}_1 + \tilde{\mathbf{r}}_2\|^2}{m_0} - \mathcal{G} \frac{m_1 m_2}{\Delta_{12}}, \quad (4.1)$$

where $\Delta_{12} = \|\mathbf{r}_1 - \mathbf{r}_2\|$, and \mathcal{G} is the constant of gravitation. We denote \mathcal{K} the sum of the Keplerian Hamiltonians (2.35) of the planets and $\varepsilon \hat{\mathcal{H}}_1$ the perturbation, where the small parameter ε (2.31) is defined as the ratio of the planet masses over the star mass $\varepsilon = (m_1 + m_2)/m_0$. I also recall the definition of the angular momentum (2.44)

$$\mathbf{G} = \sum_{i=1}^2 \mathbf{r}_i \wedge \tilde{\mathbf{r}}_i \quad (4.2)$$

which is simply the sum of the two planets Keplerian angular momentum. \mathbf{G} is a first integral of the system. The Hamiltonian can be expressed in complex Poincaré coordinates (2.29), where the inclination related coordinates are ignored as we only consider the planar case

$$\mathcal{H} = \mathcal{K} + \varepsilon \mathcal{H}_1(\Lambda_i, x_i, -\iota \bar{x}_i) = - \sum_{i=1}^2 \frac{\mu^2 m_i^3}{2 \Lambda_i^2} + \varepsilon \sum_{\substack{l, \bar{l} \in \mathbb{N}^2 \\ k \in \mathbb{Z}^2}} \mathcal{C}_{l, \bar{l}, k}(\Lambda) \prod_{i=1}^2 x_i^{l_i} \bar{x}_i^{\bar{l}_i} e^{\iota k_i \lambda_i}, \quad (4.3)$$

where $\mu = \mathcal{G} m_0$ and we recall that

$$\Lambda_i = m_i \sqrt{\mu a_i}, \quad \lambda_i = M_i + \varpi_i. \quad (4.4)$$

$$x_i = \sqrt{C_i} e^{\iota \varpi_i}, \quad C_i = \Lambda_i (1 - \sqrt{1 - e_i^2}). \quad (4.5)$$

The coefficients $\mathcal{C}_{l, \bar{l}, k}$ depend on Λ and the masses of the bodies. They are linear combinations of Laplace coefficients (Laskar and Robutel, 1995). In this problem, the d'Alembert rule (2.45) gives a relation on the indices of the non-zero $C_{l, \bar{l}, k}$ coefficients

$$\sum_{i=1}^2 k_i + l_i - \bar{l}_i = 0. \quad (4.6)$$

We study here a system with periods close to the first-order MMR $p : p + 1$ with $p \in \mathbb{N}^*$. For periods close to this configuration, we have $-pn_1 + (p+1)n_2 \simeq 0$, where $n_i = \mu^2 m_i^3 / \Lambda_i^3$ is the Keplerian mean motion of the planet i .

4.2.1.1 Averaging over non-resonant mean-motions

Due to the $p : p + 1$ resonance, we cannot average on both mean anomalies independently. Therefore, there is no conservation of Λ_i as in the secular problem. However, the partial averaging over one of the mean anomaly gives another first integral. Following (Delisle *et al.*, 2012), we make the partial change of angles

$$\begin{pmatrix} \sigma \\ \lambda_2 \end{pmatrix} = \begin{pmatrix} -p & p+1 \\ 0 & 1 \end{pmatrix} \begin{pmatrix} \lambda_1 \\ \lambda_2 \end{pmatrix}. \quad (4.7)$$

The actions associated to these angles are

$$\begin{pmatrix} \Gamma_1 \\ \Gamma \end{pmatrix} = \begin{pmatrix} \frac{-1}{p} & 0 \\ \frac{p+1}{p} & 1 \end{pmatrix} \begin{pmatrix} \Lambda_1 \\ \Lambda_2 \end{pmatrix} = \begin{pmatrix} \frac{-1}{p}\Lambda_1 \\ \frac{p+1}{p}\Lambda_1 + \Lambda_2 \end{pmatrix}. \quad (4.8)$$

We can now average the Hamiltonian over M_2 using a change of variables close to the identity given by the Lie series method (see section 2.4.1). Up to terms of orders ε^2 , we can remove all the terms with indices not of the form $\mathcal{C}_{l,\bar{l},-jp,j(p+1)}$. In order to keep the notations light, we do not change the name of the variables after the averaging. We also designate the remaining coefficients $\mathcal{C}_{l,\bar{l},-jp,j(p+1)}$ by the lighter expression $C_{l,\bar{l},j}$. Since M_2 does not appear explicitly in the remaining terms,

$$\Gamma = \frac{p+1}{p}\Lambda_1 + \Lambda_2 \quad (4.9)$$

is a first integral of the averaged Hamiltonian. The parameter $p\Gamma$ is often designed as the spacing parameter (Michtchenko *et al.*, 2008) and has been used extensively in the study of the first-order MMR dynamics. Expressed with the variables $(\Lambda, \lambda, x, \bar{x})$, the Hamiltonian can be written

$$\hat{\mathcal{H}}_{\text{av}} = -\sum_{i=1}^2 \frac{\mu^2 m_i^3}{2\Lambda_i^2} + \varepsilon \sum_{\substack{l, \bar{l} \in \mathbb{N}^2 \\ j \in \mathbb{Z}}} \mathcal{C}_{l,\bar{l},j}(\Lambda) x_1^{l_1} \bar{x}_1^{\bar{l}_1} x_2^{l_2} \bar{x}_2^{\bar{l}_2} e^{\imath j((p+1)\lambda_2 - p\lambda_1)}, \quad (4.10)$$

where we dropped the terms of order ε^2 .

4.2.1.2 Poincare-like complex coordinates

Delisle *et al.* (2012) used a change of the angular coordinates in order to remove the exponential in the second term of eq. (4.10) and use \mathbf{G} and Γ as actions. The new set of angles $(\theta_\Gamma, \theta_G, \sigma_1, \sigma_2)$ is defined as

$$\begin{pmatrix} \theta_\Gamma \\ \theta_G \\ \sigma_1 \\ \sigma_2 \end{pmatrix} = \begin{pmatrix} p & -p & 0 & 0 \\ -p & p+1 & 0 & 0 \\ -p & p+1 & 1 & 0 \\ -p & p+1 & 0 & 1 \end{pmatrix} \cdot \begin{pmatrix} \lambda_1 \\ \lambda_2 \\ -\varpi_1 \\ -\varpi_2 \end{pmatrix}. \quad (4.11)$$

The conjugated actions are

$$\begin{pmatrix} \Gamma \\ G \\ C_1 \\ C_2 \end{pmatrix} = \begin{pmatrix} \frac{p+1}{p} & 1 & 0 & 0 \\ 1 & 1 & -1 & -1 \\ 0 & 0 & 1 & 0 \\ 0 & 0 & 0 & 1 \end{pmatrix} \cdot \begin{pmatrix} \Lambda_1 \\ \Lambda_2 \\ C_1 \\ C_2 \end{pmatrix}. \quad (4.12)$$

We define $\mathfrak{x}_i = \sqrt{C_i} e^{-\iota\sigma_i}$, the complex coordinates associated to (C_i, σ_i) . Since we have $\mathfrak{x}_i = x_i e^{-\iota\theta_G}$, the terms of the perturbation in (4.10) can be written

$$\prod_{i=1}^2 x_i^{l_i} \bar{x}_i^{\bar{l}_i} e^{\iota j \theta_G} = \prod_{i=1}^2 \mathfrak{x}_i^{l_i} \bar{\mathfrak{x}}_i^{\bar{l}_i} e^{\iota(-l_i + \bar{l}_i + j)\theta_G} = \prod_{i=1}^2 \mathfrak{x}_i^{l_i} \hat{\mathfrak{x}}_i^{\bar{l}_i}; \quad (4.13)$$

the last equality resulting from the d'Alembert rule (4.6). Γ and G are conserved and the averaged Hamiltonian no longer depends on the angles θ_Γ and θ_G

$$\mathcal{H}_{\text{av}} = - \sum_{i=1}^2 \frac{\mu^2 m_i^3}{2\Lambda_i^2} + \varepsilon \sum_{\substack{l, \bar{l} \in \mathbb{N}^2 \\ j \in \mathbb{Z}}} \mathcal{C}_{l, \bar{l}, j}(\Lambda) \prod_{i=1}^2 \mathfrak{x}_i^{l_i} \bar{\mathfrak{x}}_i^{\bar{l}_i}. \quad (4.14)$$

Λ_1 and Λ_2 can be expressed as functions of the new variables and we have

$$\Lambda_1 = -p(C + G - \Gamma) \quad (4.15)$$

$$\Lambda_2 = (p + 1)(C + G) - p\Gamma, \quad (4.16)$$

where $C = C_1 + C_2$ is the total AMD (3.2) of the system. Up to the value of the first integrals Γ and G , the system now has two effective degrees of freedom.

4.2.2 Computation of the perturbation coefficients

We now truncate the perturbation, keeping only the leading-order terms. Since we consider the first-order MMR, the Hamiltonian contains some linear terms in \mathfrak{x}_i . Therefore the secular terms are neglected since they are at least quadratic. Moreover, the restriction to the planar problem is justified since the inclination terms are at least of order two.

We follow the method described in (Laskar, 1991) and (Laskar and Robutel, 1995) to determine the expression of the perturbation $\varepsilon\mathcal{H}_1$. The details of the computation are given in Appendix C.1. Since we compute an expression at first order in eccentricities and ε , the semi major axes and in particular their ratio, $\alpha = a_1/a_2$, are evaluated at the resonance. At the first order, the perturbation term $\varepsilon\mathcal{H}_1$ has for expression

$$\varepsilon\mathcal{H}_1 = R_1(\mathfrak{x}_1 + \bar{\mathfrak{x}}_1) + R_2(\mathfrak{x}_2 + \bar{\mathfrak{x}}_2), \quad (4.17)$$

where

$$R_1 = -\varepsilon \frac{\gamma}{1 + \gamma} \frac{\mu^2 m_2^3}{\Lambda_2^2} \frac{1}{2} \sqrt{\frac{2}{\Lambda_1}} \mathcal{R}_1(\alpha) \quad \text{and} \quad R_2 = -\varepsilon \frac{\gamma}{1 + \gamma} \frac{\mu^2 m_2^3}{\Lambda_2^2} \frac{1}{2} \sqrt{\frac{2}{\Lambda_2}} \mathcal{R}_2(\alpha) \quad (4.18)$$

with $\gamma = m_1/m_2$,

$$\mathcal{R}_1(\alpha) = -\frac{\alpha}{4} \left(3b_{3/2}^{(p)}(\alpha) - 2\alpha b_{3/2}^{(p+1)}(\alpha) - b_{3/2}^{(p+2)}(\alpha) \right), \quad (4.19)$$

$$\mathcal{R}_2(\alpha) = \frac{\alpha}{4} \left(3b_{3/2}^{(p-1)}(\alpha) - 2\alpha b_{3/2}^{(p)}(\alpha) - b_{3/2}^{(p+1)}(\alpha) \right) + \frac{1}{2} b_{1/2}^{(p)}(\alpha). \quad (4.20)$$

In the two previous expressions, $b_s^{(k)}(\alpha)$ are the Laplace coefficients that can be expressed as

$$b_s^{(k)}(\alpha) = \frac{1}{\pi} \int_{-\pi}^{\pi} \frac{\cos(k\phi)}{(1 - 2\alpha \cos \phi + \alpha^2)^s} d\phi \quad (4.21)$$

for $k > 0$. For $k = 0$, a $1/2$ factor has to be added in the second-hand member of (4.21).

For $p = 1$, it should be noted that a contribution from the kinetic part should be added (Appendix C.1 and Delisle *et al.*, 2012)

$$\varepsilon \mathcal{H}_{1,i} = \frac{\mu^2 m_1^2 m_2^2}{2m_0 \Lambda_1 \Lambda_2} \sqrt{\frac{2}{\Lambda_2}} (\mathfrak{x}_2 + \bar{\mathfrak{x}}_2). \quad (4.22)$$

Using the expression of α at the resonance $p : p+1$, $\alpha_0 = \left(\frac{p}{p+1}\right)^{2/3}$, we can give the asymptotic development of the coefficients \mathcal{R}_1 and \mathcal{R}_2 for $p \rightarrow +\infty$ (see Appendix C.1.1). The equivalent is

$$-\mathcal{R}_1 \sim \mathcal{R}_2 \sim \frac{K_1(2/3) + 2K_0(2/3)}{\pi} (p+1). \quad (4.23)$$

where $K_\nu(x)$ is the modified Bessel function of the second kind. We note \mathcal{R} the numerical factor of the equivalent (4.23), we have

$$\mathcal{R} = \frac{K_1(2/3) + 2K_0(2/3)}{\pi} = 0.80199. \quad (4.24)$$

For the resonant coefficients \mathcal{R}_1 and \mathcal{R}_2 , Deck *et al.* (2013) used the expressions $f_{p+1,27}(\alpha)$ and $f_{p+1,31}(\alpha)$ given in (Murray and Dermott, 1999, pp. 539-556). The expressions (4.19) and (4.20) are similar to $f_{p+1,27}(\alpha)$ and $f_{p+1,31}(\alpha)$ up to algebraic transformations using the relations between Laplace coefficients (Laskar and Robutel, 1995). In their computations, Deck et al. used a numerical fit of the coefficients for $p = 2$ to 150 and obtained

$$-f_{p+1,27} \sim f_{p+1,31} \sim 0.802p. \quad (4.25)$$

Note that we obtain the same numerical factor \mathcal{R} through the analytical development of the functions \mathcal{R}_1 and \mathcal{R}_2 .

4.2.3 Renormalization

So far, the Hamiltonian has two degrees of freedom $(\mathfrak{x}_1, -\iota\bar{\mathfrak{x}}_1, \mathfrak{x}_2, -\iota\bar{\mathfrak{x}}_2)$ and depends on two parameters G and Γ . As shown in (Delisle *et al.*, 2012), the constant Γ can be used to scale the actions, the Hamiltonian and the time without modifying the dynamics. We define

$$\begin{aligned} \hat{\Lambda}_i &= \frac{\Lambda_i}{\Gamma}, & \hat{G} &= \frac{G}{\Gamma}, \\ \hat{C}_i &= \frac{C_i}{\Gamma}, & \hat{\mathfrak{x}}_i &= \frac{\mathfrak{x}_i}{\sqrt{\Gamma}}, \\ \hat{\mathcal{H}} &= \Gamma^2 \mathcal{H}, & \hat{t} &= \frac{t}{\Gamma^3}. \end{aligned} \quad (4.26)$$

With this change of variables, the new Hamiltonian $\hat{\mathcal{H}}$ no longer depends on Γ .

The shape of the phase space is now only dependent on the first integral \hat{G} . However, \hat{G} does not vanish for the configuration around which the Hamiltonian is developed: the case of two resonant planets on circular orbits. To be able to develop the Keplerian part in power of the system's parameter, we define $\Delta\hat{G} = \hat{G}_0 - \hat{G}$, the difference in angular momentum between the circular resonant system and the actual configuration. We have

$$\hat{G}_0 = \hat{\Lambda}_{1,0} + \hat{\Lambda}_{2,0}, \quad (4.27)$$

where $\hat{\Lambda}_{1,0}$ and $\hat{\Lambda}_{2,0}$ are the value of $\hat{\Lambda}_1$ and $\hat{\Lambda}_2$ at resonance the unperturbed resonance. By definition, we have

$$\frac{\hat{\Lambda}_{1,0}}{\hat{\Lambda}_{2,0}} = \gamma\sqrt{\alpha_0} = \gamma \left(\frac{p}{p+1} \right)^{1/3}. \quad (4.28)$$

Moreover, we can express $\hat{\Lambda}_{1,0}$ as a function of the ratios α_0 and γ ,

$$\hat{\Lambda}_{1,0} = \frac{\Lambda_{1,0}}{\Gamma_0} = \frac{1}{\left(\frac{p+1}{p}\right) + \frac{\hat{\Lambda}_{2,0}}{\hat{\Lambda}_{1,0}}} = \left(\frac{p}{p+1} \right) \frac{\gamma}{\gamma + \alpha_0}. \quad (4.29)$$

Similarly, $\hat{\Lambda}_{2,0}$ can be expressed as

$$\hat{\Lambda}_{2,0} = \frac{\alpha_0}{\alpha_0 + \gamma}. \quad (4.30)$$

Since \hat{G}_0 is constant, $\Delta\hat{G}$ is also a first integral of $\hat{\mathcal{H}}$. From now on, we consider $\Delta\hat{G}$ as a parameter of the two-degrees-of-freedom (\hat{x}_1, \hat{x}_2) Hamiltonian $\hat{\mathcal{H}}$. The Keplerian part depends on the coordinates \hat{x}_i through the dependence of $\hat{\Lambda}_i$ in \hat{C} .

$\hat{\Lambda}_1$ and $\hat{\Lambda}_2$ can be expressed as functions of the Hamiltonian coordinates and their value at the resonance,

$$\begin{aligned} \hat{\Lambda}_1 &= \hat{\Lambda}_{1,0} - p(\hat{C} - \Delta\hat{G}) \\ \hat{\Lambda}_2 &= \hat{\Lambda}_{2,0} + (p+1)(\hat{C} - \Delta\hat{G}). \end{aligned} \quad (4.31)$$

4.2.4 Integrable Hamiltonian

The system can be made integrable by a rotation of the coordinates \hat{x}_i (Sessin and Ferraz-Mello, 1984; Henrard *et al.*, 1986; Delisle *et al.*, 2014). We introduce R and ϕ such that

$$\hat{R}_1 = \hat{R} \cos(\phi) \quad \text{and} \quad \hat{R}_2 = \hat{R} \sin(\phi), \quad (4.32)$$

where $\hat{R}_i = \Gamma^{-5/2} R_i$ are the renormalized coefficients R_i . We have $\hat{R}^2 = \hat{R}_1^2 + \hat{R}_2^2$ and $\tan(\phi) = R_2/R_1$. If we note \mathbf{R}_ϕ the rotation of angle ϕ we define y such that $\hat{x} = \mathbf{R}_\phi y$. We still have $\hat{C} = \sum y_i \bar{y}_i$ so the only change in the Hamiltonian is the perturbation term

$$\hat{\mathcal{H}} = \hat{\mathcal{K}}(\hat{C}, \Delta\hat{G}) + \hat{R}(y_1 + \bar{y}_1) = \hat{\mathcal{K}}(\hat{C}, \Delta\hat{G}) + 2\hat{R}\sqrt{I_1} \cos(\theta_1), \quad (4.33)$$

where (I, θ) are the action-angle coordinates associated to y . With these coordinates, I_2 is a first integral. \hat{R} has for expression

$$\hat{R} = \left(\frac{\varepsilon\gamma}{1+\gamma} \frac{\mu^2 m_2^3}{\hat{\Lambda}_{2,0}^2} \right) \sqrt{\left(\frac{\mathcal{R}_1(\alpha_0)^2}{2\hat{\Lambda}_{1,0}} + \frac{\mathcal{R}_2(\alpha_0)^2}{2\hat{\Lambda}_{2,0}} \right)}. \quad (4.34)$$

We now develop the Keplerian part around the circular resonant configuration in series of $(\hat{C} - \Delta\hat{G})$ thanks to the relations (4.31). We develop the Keplerian part to the second order in $(\hat{C} - \Delta\hat{G})$ since the first order vanishes (see Appendix C.2). The computation of the second-order coefficient gives

$$\frac{1}{2}\mathcal{K}_2 = -\frac{3}{2}\mu^2 m_2^3 \frac{(\gamma + \alpha_0)^5}{\gamma\alpha_0^4} (p+1)^2. \quad (4.35)$$

We drop the constant part of the Hamiltonian and obtain the following expression

$$\mathcal{H} = \frac{\mathcal{K}_2}{2}(I_1 + I_2 - \Delta\hat{G})^2 + 2\hat{R}\sqrt{I_1} \cos(\theta_1). \quad (4.36)$$

We again change the time scale by dividing the Hamiltonian by $-\mathcal{K}_2$ and multiplying the time by this factor. We define

$$\chi = -\frac{\sqrt{2}\hat{R}}{\mathcal{K}_2} \quad (4.37)$$

and after simplification,

$$\chi = \frac{1}{3} \frac{\varepsilon(\gamma\alpha_0)^{3/2}}{(1+\gamma)(\alpha_0+\gamma)^2} \frac{\mathcal{R}_2(\alpha_0)}{(p+1)^2} f(p) = \frac{\mathcal{R}}{3} \frac{\varepsilon\gamma^{3/2}}{(1+\gamma)^3} \frac{1}{p+1} + \mathcal{O}((p+1)^{-2}), \quad (4.38)$$

where \mathcal{R} was defined in (4.24) and $f(p) = 1 + \mathcal{O}(p^{-1})$ is a function of p and γ

$$f(p) = \sqrt{1 - \frac{\alpha_0}{\alpha_0 + \gamma} \left(1 - \frac{p+1}{p} \left(\frac{\mathcal{R}_1}{\mathcal{R}_2} \right)^2 \right)}. \quad (4.39)$$

At this point the Hamiltonian can be written

$$\mathcal{H} = -\frac{1}{2}(I_1 + I_2 - \Delta\hat{G})^2 + \chi\sqrt{2I_1} \cos(\theta_1) \quad (4.40)$$

and has almost its final form. We divide the actions and the time by $\chi^{2/3}$ and the Hamiltonian by $\chi^{4/3}$ and we obtain

$$\mathcal{H}_A = -\frac{1}{2}(\mathcal{I} - \mathcal{I}_0)^2 + \sqrt{2\mathcal{I}} \cos(\theta_1), \quad (4.41)$$

where

$$\mathcal{I} = \chi^{-2/3} I_1 \quad \text{and} \quad \mathcal{I}_0 = \chi^{-2/3} (\Delta\hat{G} - I_2). \quad (4.42)$$

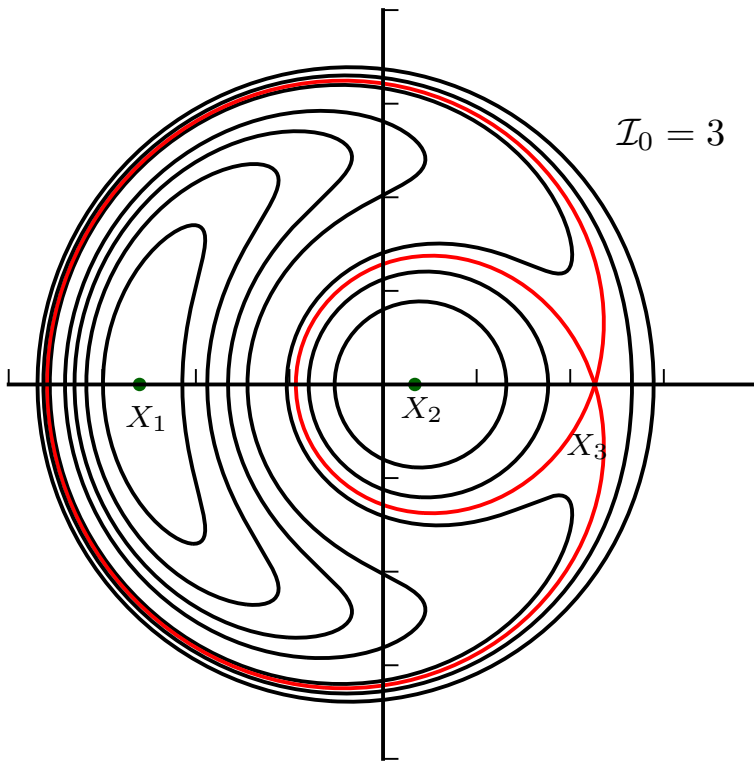


Figure 4.1 – Hamiltonian \mathcal{H}_A (4.44) represented with the saddle point and the separatrices in red.

4.2.5 Andoyer Hamiltonian

We now perform a polar to Cartesian change of coordinates with

$$X = -\sqrt{2\mathcal{I}} \cos(\theta_1), \quad \text{and} \quad Y = \sqrt{2\mathcal{I}} \sin(\theta_1). \quad (4.43)$$

We change the sign of X in order to have the same orientation as (Deck *et al.*, 2013). Doing so, the Hamiltonian becomes

$$\mathcal{H}_A = -\frac{1}{2} \left(\frac{1}{2}(X^2 + Y^2) - \mathcal{I}_0 \right)^2 - X. \quad (4.44)$$

We recognize the second fundamental model of resonance (Henrard and Lemaître, 1983). This Hamiltonian is also called an Andoyer Hamiltonian (Ferraz-Mello, 2007). We show in Figure 4.1 the level curves of the Hamiltonian \mathcal{H}_A for $\mathcal{I}_0 = 3$.

The fixed points of the Hamiltonian satisfy the equations

$$\dot{X} = Y \left(\frac{1}{2}(X^2 + Y^2) - \mathcal{I}_0 \right) = 0 \quad (4.45)$$

$$\dot{Y} = -X \left(\frac{1}{2}(X^2 + Y^2) - \mathcal{I}_0 \right) - 1 = 0, \quad (4.46)$$

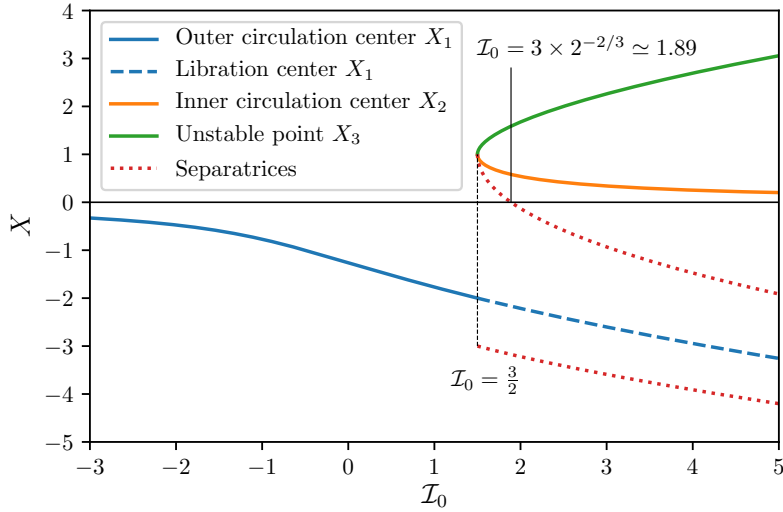


Figure 4.2 – Position of the fixed points of the Hamiltonian \mathcal{H}_A as a function of \mathcal{I}_0 . For $\mathcal{I}_0 > \frac{3}{2}$, the resonance opens and we also plot the intersections of the separatrices with the $Y = 0$ axis.

which have for solutions $Y = 0$ and the real roots of the cubic equation in X

$$X^3 - 2\mathcal{I}_0 X + 2 = 0. \quad (4.47)$$

Equation (4.47) has three solutions (Deck *et al.*, 2013) if $\Delta = 32(\mathcal{I}_0^3 - 27/8) > 0$, *i.e.* $\mathcal{I}_0 > 3/2$. In this case, we note these roots $X_1 < X_2 < X_3$. X_1 and X_2 are elliptic fixed points while X_3 is a hyperbolic one. We plot in figure 4.2, the position of the fixed points as a function of \mathcal{I}_0 . We also plot the intersections of the separatrices with the $Y = 0$ axis. X_1 is the only fixed point for $\mathcal{I}_0 < \frac{3}{2}$ and is a center of circulation. For $\mathcal{I}_0 > \frac{3}{2}$, the resonance opens and X_1 becomes the center of the resonance while X_2 is the center of the inner circulation region. It should be noted that the inner separatrix crosses the origin before the disappearance of the resonance.

4.3 Overlap criterion

As seen in the previous section, the motion of two planets near a first-order MMR can be reduced to an integrable system for small eccentricities and planet masses. However, if two independent combinations of frequencies are close to zero at the same time, the previous reduction is not valid anymore. Indeed, we must then keep, in the averaging, the terms corresponding to both resonances. While for a single resonant term the system is integrable, overlapping resonant islands will lead to chaotic motion (Chirikov, 1979).

Wisdom (1980) first applied the resonance overlap criterion to the first-order MMR and found, in the case of the restricted three-body problem with a circular planet, that the overlap occurs for

$$1 - \alpha < 1.3\epsilon^{2/7}. \quad (4.48)$$

Through numerical simulations, (Duncan *et al.*, 1989) confirmed Wisdom's expression up to the numerical coefficient ($1 - \alpha < 1.5 \varepsilon^{2/7}$). A similar criterion was then developed by Mustill and Wyatt (2012) for an eccentric planet. They found that for an eccentricity above $0.2 \varepsilon^{3/7}$, the overlap region satisfies the criterion $1 - \alpha < 1.8(\varepsilon e)^{1/5}$. Deck *et al.* (2013) adapted those two criteria to the case of two massive planets, finding little difference up to the numerical coefficients. However, Deck *et al.* (2013) treat two different situations; the case of orbits initially circular and the case of two eccentric orbits. As in (Mustill and Wyatt, 2012), the eccentric criterion proposed in Deck *et al.* (2013) can be used for eccentricities verifying $e_1 + e_2 \gtrsim 1.33 \varepsilon^{3/7}$. We show here that the two Deck's criteria can be obtained as the limit cases of a general expression.

4.3.1 Width of the libration island

Using the same approach as (Wisdom, 1980; Deck *et al.*, 2013), we express the width of the resonant island as a function of the orbital parameters and compare it with the distance between the two adjacent centers of MMR.

In the (X, Y) plane, the center of the resonance is located at the point of coordinates $(X_1, 0)$. The width of the libration area is defined as the distance between the two separatrices on the $Y = 0$ axis. It is indeed the direction where the resonant island is the widest.

We note X_1^*, X_2^* the abscissas of the intersections between the separatrices and the $Y = 0$ axis. Relations between X_1^*, X_2^* , and X_3 can be derived (see Appendix C.3.1) and we obtain the expressions of X_1^* and X_2^* as functions of X_3 (Ferraz-Mello, 2007; Deck *et al.*, 2013). We have

$$X_1^* = -X_3 - \frac{2}{\sqrt{X_3}}, \quad \text{and} \quad X_2^* = -X_3 + \frac{2}{\sqrt{X_3}}. \quad (4.49)$$

The width of the libration zone δX depends solely on the value of X_3 ,

$$\delta X = \frac{4}{\sqrt{X_3}}. \quad (4.50)$$

In order to study the overlap of resonance islands, we need the width of the resonance in terms of α , the semi-major axis ratio. Let us invert the previous change of variables in order to express the variation of α in terms of the variation of X . In this subsection, for any function $Q(X)$, we note

$$\delta Q = |Q(X_1^*) - Q(X_2^*)|. \quad (4.51)$$

The computation of $\delta \mathcal{I}$ (4.43) is straightforward from the computation of δX

$$\begin{aligned} \delta \mathcal{I} &= \left| \frac{X_1^{*2}}{2} - \frac{X_2^{*2}}{2} \right| = \frac{1}{2} |X_2^* + X_1^*| |X_2^* - X_1^*| = X_3 \delta X \\ &= 4\sqrt{X_3}. \end{aligned} \quad (4.52)$$

We then directly deduce $\delta I_1 = \chi^{2/3} \delta \mathcal{I}$ from (4.42). Since I_2 and $\Delta \hat{G}$ are first integrals, the variation of $\hat{\Lambda}_i$ only depends on δI_1 . And finally, since we have

$$\alpha = \left(\gamma^{-1} \frac{\Lambda_1}{\Lambda_2} \right)^2, \quad (4.53)$$

α can be developed to the first order in $(\hat{C} - \Delta \hat{G})$ thanks to (4.31). This development gives

$$\alpha = \alpha_0 \left(1 - \frac{2(\alpha_0 + \gamma)^2}{\gamma \alpha_0} (p+1)(I_1 - \chi^{2/3} \mathcal{I}_0) \right). \quad (4.54)$$

Using 4.38, the width of the resonance in terms of α is directly related to X_3 through

$$\delta \alpha = \alpha_0 \frac{8\mathcal{R}^{2/3}}{3^{2/3}} \varepsilon^{2/3} (p+1)^{1/3} \sqrt{X_3} + o(\varepsilon^{2/3} (p+1)^{1/3}). \quad (4.55)$$

The computation of the width of resonance is thus reduced to the computation of the root X_3 as a function of the parameters. The resonance only exists if X_3 is defined so the expression (4.55) is well defined in all cases. It should also be remarked that at the leading order in p and thus in $1 - \alpha$, the width of resonance does not depend on the mass ratio γ .

4.3.2 Minimal AMD of a resonance

We are now interested in the overlap of adjacent resonant islands. Planets trapped in the chaotic zone created by the overlap will experience variations of their actions eventually leading to collisions.

For a configuration close to a given resonance $p : p+1$, the AMD can evolve toward higher values if the original value places the system in a configuration above the inner separatrix, eventually leading the planets to collision or chaotic motion in case of MMR overlap. On the other hand, if the initial AMD of the planets forces them to remain in the inner circulation region of the overlapped MMR islands, the system will remain stable in regards to this criterion. Since $C = I_1 + I_2$, and I_2 is a first integral, we define the minimal AMD of a resonance¹ $C_{\min}(p)$ as the minimal value of I_1 to enter the resonant island given $\Delta \hat{G} - I_2$. Two cases must be discussed:

- The point $I_1 = 0$ is already in the libration zone and then $C_{\min} = 0$,
- The point $I_1 = 0$ is in the inner circulation zone and then we have

$$C_{\min} = I_1(X_2^*) = \frac{\chi^{2/3}}{2} \left(X_3 - \frac{2}{\sqrt{X_3}} \right)^2. \quad (4.56)$$

In the second case, we have an implicit expression of X_3 depending on C_{\min}

$$\chi^{-1/3} \sqrt{2C_{\min}} = X_3 - \frac{2}{\sqrt{X_3}}, \quad (4.57)$$

¹We summarize the notations of the various AMD expressions used in this paper in Table 4.1.

where χ was defined in (4.37). In other words, there is a one-to-one correspondence between C_{\min} (4.56) and the Hamiltonian parameter \mathcal{I}_0 for $C_{\min} > 0$. The shape of the resonance island is completely described by C_{\min} .

We can also use the definition of C_{\min} to give an expression depending on the system parameters

$$\begin{aligned} C_{\min} &= I_1 = u_1 \bar{u}_1 \\ &= \left| \frac{\hat{R}_1}{\hat{R}} \sqrt{\frac{\hat{\Lambda}_{1,0}}{2}} \mathfrak{X}_1 + \frac{\hat{R}_2}{\hat{R}} \sqrt{\frac{\hat{\Lambda}_{2,0}}{2}} \mathfrak{X}_2 \right|^2 \\ &= \left(\frac{\hat{R}_1}{\hat{R}} \right)^2 \frac{\hat{\Lambda}_{1,0}}{2} \left| \mathfrak{X}_1 - \left| \frac{\hat{R}_2}{\hat{R}_1} \right| \sqrt{\frac{\hat{\Lambda}_{2,0}}{\hat{\Lambda}_{1,0}}} \mathfrak{X}_2 \right|^2 \\ &\simeq \frac{\alpha_0 \gamma}{2(\alpha_0 + \gamma)^2} (c_1^2 + c_2^2 - 2c_1 c_2 \cos \Delta\varpi), \end{aligned} \quad (4.58)$$

where $c_i = \sqrt{2} \sqrt{1 - \sqrt{1 - e_i^2}} = |\mathfrak{X}_i|$. We note

$$c_m = c_1^2 + c_2^2 - 2c_1 c_2 \cos \Delta\varpi, \quad (4.59)$$

the reduced minimal AMD. We can use the expression (4.58) to compute the quantity $\chi^{-1/3} \sqrt{2C_{\min}}$ appearing in equation (4.57)

$$\chi^{-1/3} \sqrt{2C_{\min}} \simeq \frac{3^{1/3}}{\mathcal{R}^{1/3}} \frac{(p+1)^{1/3}}{\varepsilon^{1/3}} \sqrt{c_m} + \mathcal{O}(p^{1/3}). \quad (4.60)$$

As an example, we represent in figure 4.3 the resonance 4:3 in a plane $(\alpha, \sqrt{c_m})$, for $\varepsilon = 10^{-5}$. We plot the position of the center of the resonance as well as the separatrices. We also draw in green the locus of the points that corresponds to a certain \mathcal{I}_0 (or equivalently X_3). The width of the resonance $\delta\alpha$ is computed between the two intersections of this curve with the separatrices. The minimum AMD of the resonance corresponds to the AMD at the intersection of the inner separatrix (on the right in figure 4.3) with the curve of constant \mathcal{I}_0 .

The function $C_{\min}(X_3)$ defined in (4.56) is plotted in Figure 4.4 with the two approximations used by Deck *et al.* (2013) to obtain the width of the resonance. For $C_{\min} \gg \chi^{2/3}$ or C_{\min} close to zero, the relation can be simplified and we obtain

$$X_3 \sim \chi^{-1/3} \sqrt{2C_{\min}} \quad (4.61)$$

$$X_3 = 2^{2/3} + \frac{2}{3} \chi^{-1/3} \sqrt{2C_{\min}} + \mathcal{O}(\chi^{-2/3} C_{\min}). \quad (4.62)$$

We can use the developments (4.61) and (4.62) in order to compute the width of the resonance in these two cases (see Appendix C.3). It should be noted as well that for $C_{\min} = 0$, we have $X_3 = 2^{2/3}$. As a result the resonance always reaches circular orbits before disappearing since $X_3 = 2^{2/3}$ corresponds to a value of $\mathcal{I}_0 = 3 \times 2^{-2/3} \simeq 1.89$.

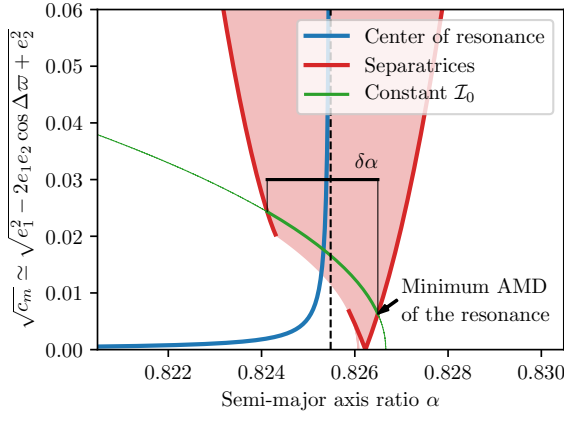


Figure 4.3 – Resonance 4:3 for $\varepsilon = 10^{-5}$ in the space $(\alpha, \sqrt{c_m})$. We plot the locus of the center of the resonance as well as the separatrices. We also plot a curve with constant I_0 in order to show what corresponds to the width of the resonance and the minimum AMD of the resonance.

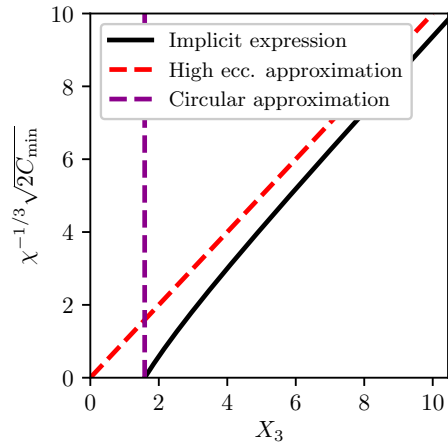


Figure 4.4 – Relation (4.57) between X_3 and C_{\min} (4.56) and two different approximations. In red, the approximation used by Deck *et al.* (2013) for eccentric orbits and in purple the constant evaluation used for circular orbits.

Table 4.1 – Summary of the diverse notations of AMD used in this paper.

Notation	Description	Definition
C	Total AMD of the system	
C_{\min}	Minimal AMD to enter a resonance island	(4.56)
c_m	Normalized minimal AMD	(4.59)
\mathcal{C}	Relative AMD	(4.92)
C_c	Critical AMD deduced from the collision condition	sec. 3.3.2
C_c^{MMR}	Critical AMD deduced from the MMR overlap	(4.96)

4.3.3 Implicit overlap criterion

The overlap of MMR can be determined by finding the first integer p such that the sum of the half-width of the resonances $p : p+1$ and $p+1 : p+2$ is larger than the distance between the respective centers of these two resonances (Wisdom, 1980; Deck *et al.*, 2013)

$$\frac{\Delta\alpha}{\alpha_{0,p}} \lesssim \frac{1}{2} \left(\frac{\delta\alpha_p}{\alpha_{0,p}} + \frac{\delta\alpha_{p+1}}{\alpha_{0,p+1}} \right), \quad (4.63)$$

where $\Delta\alpha$ is the distance between the two centers and $\delta\alpha_k$ corresponds to the width of the resonance $k : k+1$.

Up to terms of order $\varepsilon^{2/3}$, the center of the resonance island $p : p+1$ is located at the center of the resonance of the unperturbed Keplerian problem,

$\alpha_{0,p} = (p/(p+1))^{2/3}$. We develop $\alpha_{0,p}$ for $p \gg 1$

$$\alpha_{0,p} = \left(\frac{p}{p+1} \right)^{2/3} = 1 - \frac{2}{3(p+1)} - \frac{1}{9(p+1)^2} + O((p+1)^{-3}). \quad (4.64)$$

Therefore, we have at second order in p

$$\frac{\Delta\alpha}{\alpha_{0,p}} = \frac{2}{3} \frac{1}{(p+1)^2}. \quad (4.65)$$

We can use the implicit expression (4.57) of X_3 as a function of $\sqrt{c_m}$ (Eq. 4.59) in order to derive an overlap criterion independent of approximations on the value of C_{\min} . Equating the general width of resonance (4.55) with the distance between two adjacent centers (4.65) and isolating X_3 gives

$$X_3 = \frac{3^{4/3}}{144\mathcal{R}^{4/3}} \varepsilon^{-4/3} (p+1)^{-14/3}. \quad (4.66)$$

We can inject this expression of X_3 into (4.57), and using equation (4.60),

$$\sqrt{c_m} = \frac{1}{48\mathcal{R}\varepsilon(p+1)^5} - 8\mathcal{R}\varepsilon(p+1)^2. \quad (4.67)$$

Using the first order expression of $(p+1)$ as a function of α ,

$$\frac{1}{p+1} = \frac{3}{2}(1-\alpha) \quad (4.68)$$

we obtain an implicit expression of the overlap criterion

$$\sqrt{c_m} = \frac{3^4(1-\alpha)^5}{2^9\mathcal{R}\varepsilon} - \frac{32\mathcal{R}\varepsilon}{9(1-\alpha)^2}. \quad (4.69)$$

4.3.4 Overlap criterion for circular orbits

The implicit expression (4.69) can be used to find the criteria proposed by Deck *et al.* (2013) for circular and eccentric orbits. Let us first obtain the circular criterion by imposing $c_m = 0$ in equation (4.69)

$$3^6(1-\alpha)^7 = 2^{14}\mathcal{R}^2\varepsilon^2. \quad (4.70)$$

We can express $1-\alpha$ as a function of ε and we obtain

$$1 - \alpha_{\text{overlap}} = \frac{4\mathcal{R}^{2/7}}{3^{6/7}} \varepsilon^{2/7} = 1.46\varepsilon^{2/7}. \quad (4.71)$$

The exponent 2/7 was first proposed by Wisdom (1980) and the numerical factor 1.46 is similar to the one found by Deck *et al.* (2013).

4.3.5 Overlap criterion for high-eccentricity orbits

For large eccentricity, Deck *et al.* (2013) proposes a criterion based on the development (4.61) of equation (4.57). This criterion is obtained from (4.69) by ignoring the second term of the right-hand side which leads to

$$2^9 \mathcal{R} \varepsilon \sqrt{c_m} = 3^4 (1 - \alpha)^5. \quad (4.72)$$

Isolating $1 - \alpha$ gives

$$1 - \alpha = \frac{2^{9/5}}{3^{4/5}} \mathcal{R}^{1/5} \varepsilon^{1/5} c_m^{1/10} = 1.38 \varepsilon^{1/5} c_m^{1/10}. \quad (4.73)$$

This result is also similar to Deck's one. For small c_m , the criterion (4.73) is less restrictive than the criterion (4.71) obtained for circular orbits. The comparison of these two overlap criteria provides a minimal value of c_m for the validity of the eccentric criterion

$$\sqrt{c_m} = 1.33 \varepsilon^{3/7}. \quad (4.74)$$

4.3.6 Overlap criterion for low-eccentricity orbits

For smaller eccentricities, we can develop the equation (4.69) for small $\sqrt{c_m}$ and α close to $\alpha_{\text{cir}} = 1 - 1.46 \varepsilon^{2/7}$, the critical semi major axis ratio for the circular overlap criterion (4.71). We have

$$3^2 2^9 \mathcal{R} \varepsilon (1 - \alpha)^2 \sqrt{c_m} = 3^6 (1 - \alpha)^7 - 2^{14} \mathcal{R}^2 \varepsilon^2. \quad (4.75)$$

We develop the right-hand side at the first order in $(\alpha_{\text{cir}} - \alpha)$ and evaluate the left-hand side for $\alpha = \alpha_{\text{cir}}$ and after some simplifications obtain

$$\alpha_{\text{cir}} - \alpha = \frac{2^9 \mathcal{R} \varepsilon}{7 \times 3^4} \frac{\sqrt{c_m}}{(1 - \alpha_{\text{cir}})^4}. \quad (4.76)$$

We inject the expression of α_{cir} into this equation and obtain the following development of the overlap criterion for low eccentricity:

$$\alpha_{\text{cir}} - \alpha = \frac{2 \sqrt{c_m}}{7 \times 3^{4/7} r^{1/7} \varepsilon^{1/7}} = 0.157 \frac{\sqrt{c_m}}{\varepsilon^{1/7}}. \quad (4.77)$$

This development remains valid for small enough $\sqrt{c_m}$ if $\alpha_{\text{cir}} - \alpha \ll 1 - \alpha_{\text{cir}}$, which can be rewritten

$$0.157 \varepsilon^{-1/7} \sqrt{c_m} \ll 1.46 \varepsilon^{2/7}, \quad (4.78)$$

which leads to

$$\sqrt{c_m} \ll 9.30 \varepsilon^{3/7}. \quad (4.79)$$

It is worth noting that the low-eccentricity approximation allows to cover the range of eccentricities where the criterion (4.73) is not applicable, since both boundaries depend on the same power of ε .

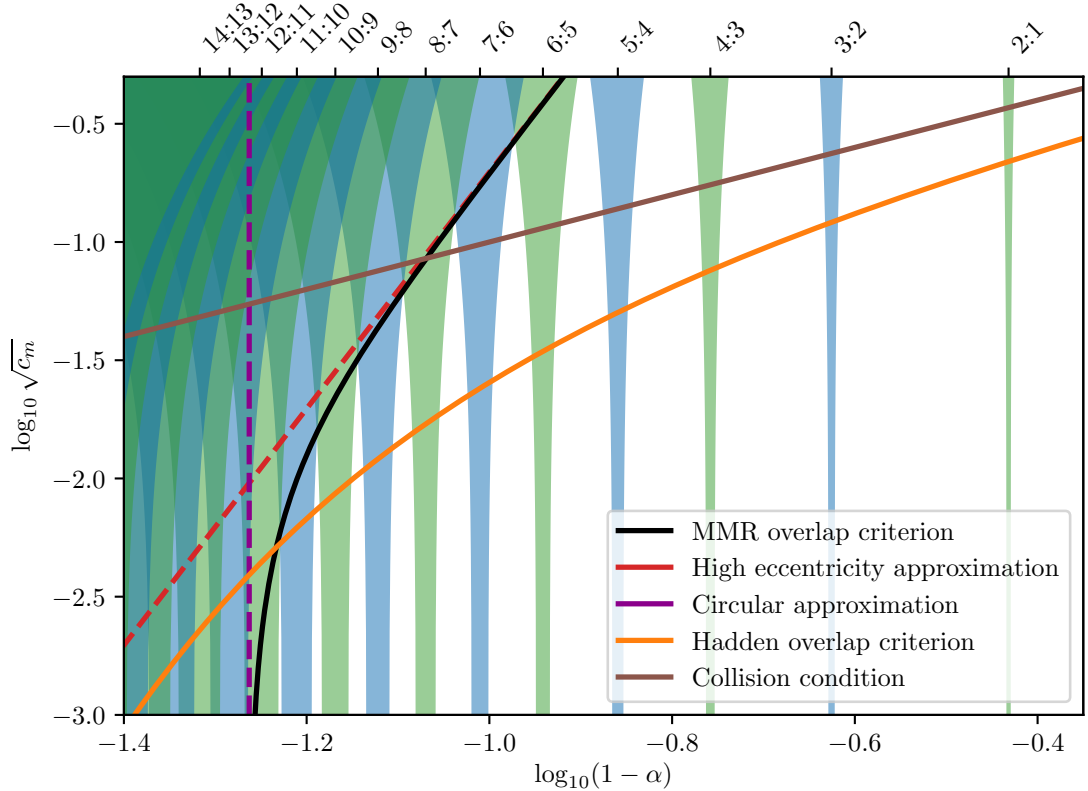


Figure 4.5 – Representation of the MMR overlap criteria. The dotted lines correspond to the criteria proposed by (Deck *et al.*, 2013), and the collision curve is the approximation of the collision curve for $\alpha \rightarrow 1$. In orange we added the recently proposed general order MMR overlap criterion of (Hadden and Lithwick, 2018, see section 4.3.7). We represent in transparent green (p odd) and blue (p even) the first $p : p + 1$ MMR islands to show the agreement between the proposed overlap criterion and the actual intersections. In this figure, $\varepsilon = 10^{-5}$.

We plot in Figure 4.5 the overlap criteria (4.69) for $\varepsilon = 10^{-5}$, the two approximations (4.71) and (4.73) from (Deck *et al.*, 2013), as well as the collision condition used in chapter 3 (eq. 3.6) and (Laskar and Petit, 2017)

$$1 - \alpha \simeq e_1 + e_2 \simeq \sqrt{c_m}, \quad (4.80)$$

where we made the approximation $\alpha \rightarrow 1$. We also plot the first MMR islands in order to show the agreement between the proposed criterion and the actual intersections. We see that for high eccentricities, and large $1 - \alpha$, the system can verify the MMR overlap stability criterion while allowing for collision between the planets. For widely separated planets, the MMR overlap criterion alone cannot account for the stability of the system.

4.3.7 General order MMR overlap criterion

Since the publication of (Petit *et al.*, 2017), another MMR overlap criterion has been proposed by Hadden and Lithwick (2018). The criterion they proposed takes into account MMR of all orders. There, we present this result and compare it with the first order MMR overlap criterion detailed above. Moreover, I will explain how the criterion of Hadden and Lithwick can be adapted to the AMD framework.

The authors first consider the restricted circular problem. They remark that at first order in $1 - \alpha$, the width in terms of α of all resonances of order k can be expressed as (Hadden and Lithwick, 2018, eq. 5 and 7)

$$\delta\alpha = \alpha_0 \sqrt{\frac{16\alpha_0 \varepsilon s_k(e/e_{\text{cross}})}{3}} \quad (4.81)$$

where we adapted the authors' notations to be consistent to the ones used in this thesis. In (4.81), α is the semi-major axis ratio at the consider resonance $p + k:p$, *i.e.* $\alpha_0 = (p/(p+k))^{2/3}$; $\varepsilon = m/m_0$ is the planet to star mass ratio; e is the test particle eccentricity, $e_{\text{cross}} = 1 - \alpha$ is the crossing eccentricity developed at first order in $1 - \alpha$. s_k is a function defined as an integral

$$s_k\left(\frac{e}{e_{\text{cross}}}\right) = \frac{1}{\pi^2} \int_0^{2\pi} K_0\left[\frac{2k}{3}\left(1 + \frac{e}{e_{\text{cross}}} \cos M\right)\right] \cos\left[k\left(M + \frac{4}{3}\frac{e}{e_{\text{cross}}} \sin M\right)\right] dM \\ \underset{k \rightarrow +\infty}{\sim} \frac{\sqrt{3} \exp(k/3)}{\pi k} \left(\frac{e}{e_{\text{cross}}}\right)^k \quad (4.82)$$

where K_0 is a modified Bessel function of the first kind. In particular, for first order MMR ($k = 1$), they assume the width of the resonance (4.81) to be proportional to \sqrt{e} and shrink to zero for vanishing eccentricity instead of stopping at a finite value.

They then point out that the resonant structure between two first order mean motion resonances $J:J-1$ and $J+1:J$ is always the same up to a rescaling. Therefore, they only need to compute the overlap criterion between two adjacent first order MMR to be able to give an expression up to the 2:1 resonance *i.e.* $\alpha = 0.63$. The overlap criterion is estimated by considering the "optical depth" of the resonances (Quillen, 2011) between two first order MMR. The "optical depth" τ_{res} is defined by the sum of the width resonances comprised between two first order MMR divided by the distance between those two MMR (equation 4.65). Using the close orbit approximation (first order in $1 - \alpha$) they obtain

$$\tau_{\text{res}} = \frac{1}{\Delta\alpha} \sum_{k=1}^{\infty} \phi(k) \delta\alpha = \frac{8}{3\sqrt{3}} \frac{\sqrt{\alpha\varepsilon}}{(1-\alpha)^2} \sum_{k=1}^{\infty} \phi(k) \left|s_k\left(\frac{e}{e_{\text{cross}}}\right)\right|^{1/2}, \quad (4.83)$$

where $\delta\alpha$ is defined in (4.81), $\Delta\alpha$ in (4.65) and $\phi(k)$, the Euler totient function, counts the number of resonances of order k in the considered interval. The authors assume that the overlap occurs whenever $\tau_{\text{res}} = 1$, which is confirmed by numerical simulations. From there, the sum in (4.83) can be computed numerically using the exact expression for s_k (4.82). It is also possible to approximate s_k and ϕ for $k \rightarrow +\infty$ to obtain a functional form for the criterion. Isolating e leads to the

overlap criterion (Hadden and Lithwick, 2018, eq. 14)

$$e \simeq 0.72 e_{\text{cross}} \exp \left(-1.4 \frac{\varepsilon^{1/3}}{(1-\alpha)^{4/3}} \right). \quad (4.84)$$

However, this approximate expression is not satisfying for $\varepsilon \rightarrow 0$. In particular, for two massless planets ($\varepsilon = 0$), e should be equal to e_{cross} . The authors choose to keep the functional form but fit a new numerical coefficient in the exponential

$$e \simeq e_{\text{cross}} \exp \left(-2.2 \frac{\varepsilon^{1/3}}{(1-\alpha)^{4/3}} \right). \quad (4.85)$$

The authors then generalize their criterion to the two massive planets case by replacing the mass of the single planet by $\varepsilon = (m_1 + m_2)/m_0$ and the test particle eccentricity by the $\sqrt{2}$ times the norm of the difference of planets' complex eccentricity

$$\mathcal{Z} = \frac{1}{\sqrt{2}} (e_1 e^{\iota \varpi_1} - e_2 e^{\iota \varpi_2}). \quad (4.86)$$

The justification for this change is motivated by the analysis of the dynamics near resonances and the complete justification will be published in a future paper by Hadden. Although this general work has not been published yet, the dependency in \mathcal{Z} rather than another combination of the eccentricities or inclinations has already been observed in the study of low order MMRs such as (Deck *et al.*, 2013) or this work for first order MMR and (Delisle *et al.*, 2014) for second order MMR. It should be remarked that at first order in eccentricity, $|\mathcal{Z}|$ corresponds to the eccentricity dependency $\sqrt{c_m}$ (4.59) of the overlap criterion derived in this chapter (4.69). As a result, the conversion to the framework used here is straightforward and Hadden and Lithwick's criterion can be rewritten as

$$\sqrt{c_m} = \frac{1-\alpha}{\sqrt{2}} \exp \left(-2.2 \frac{\varepsilon^{1/3}}{(1-\alpha)^{4/3}} \right) \quad (4.87)$$

We add the criterion (4.87) to figure 4.5. We see that their general overlap criterion is always below the collision line. However, for α close to 1, Hadden and Lithwick's critical $\sqrt{c_m}$ does not go to zero at finite $1-\alpha$ as the overlap criterion for first order MMR (4.69). Indeed, they use the same resonance model for first order resonances than for higher order ones. As a result, the width of resonance they compute goes to zero with the eccentricity instead of reaching a finite value as demonstrated in section 4.3.1.

4.4 Critical AMD and MMR

4.4.1 Critical AMD in a context of resonance overlap

In chapter 3, we present the AMD-stability criterion based on the conservation of AMD. We assume the system dynamics to be secular chaotic. As a consequence the averaged semi-major axis and the total averaged AMD are conserved. Moreover,

in this approximation the dynamics is limited to AMD exchanges between planets with conservation of the total AMD. Based on these assumptions, collisions between planets are possible only if the AMD of the system can be distributed such that the eccentricities of the planets allow for collisions. Particularly, for each pair of adjacent planets, there exists a critical AMD, noted $C_c(\alpha, \gamma)$ (see section 3.3.2), such that for smaller AMD, collisions are forbidden.

The critical AMD was determined thanks to the limit collision condition

$$\alpha(1 + e_1) = 1 - e_2. \quad (4.88)$$

However, in practice, the system may become unstable long before orbit intersections; in particular the secular assumption does not hold if the system experiences chaos induced by MMR overlap. We can, though, consider that if the islands do not overlap, the AMD is, on average, conserved on timescales of order $\varepsilon^{-2/3}$ (*i.e.*, of the order of the libration timescales). Therefore, the conservation, on average, of the AMD is ensured as long as the system adheres to the above criteria for any distribution of the AMD between planets. Based on the model of (Laskar and Petit, 2017), we compute a critical AMD associated to the criterion (4.69).

We consider a pair as AMD-stable if no distribution of AMD between the two planets allows the overlap of MMR. A first remark is that no pair can be considered as AMD-stable if $\alpha > \alpha_{\text{cir}}$, because in this case, even the circular orbits lead to MMR overlap. Let us write the criterion (4.69) as a function of α and ε ;

$$\sqrt{c_m} = \varrho(\alpha, \varepsilon), \quad (4.89)$$

where

$$\begin{aligned} \varrho(\alpha, \varepsilon) &= \frac{3^4(1-\alpha)^5}{2^9\mathcal{R}\varepsilon} - \frac{32\mathcal{R}\varepsilon}{9(1-\alpha)^2}, & \text{if } \alpha < \alpha_{\text{cir}}, \\ &= 0 & \text{if } \alpha > \alpha_{\text{cir}}. \end{aligned} \quad (4.90)$$

$\sqrt{c_m}$ depends on $\Delta\varpi$ and has a maximum for $\Delta\varpi = \pi$. Since the variation of $\Delta\varpi$ does not affect the AMD of the system, we fix $\Delta\varpi = \pi$ since it is the least-favorable configuration. Therefore we have

$$\sqrt{c_m} = c_1 + c_2. \quad (4.91)$$

Let express the relative AMD \mathcal{C} (eq. 3.7) as a function of the variables c_i ,

$$\mathcal{C} = \frac{C}{\Lambda_2} = \frac{1}{2} \left(\gamma\sqrt{\alpha}c_1^2 + c_2^2 \right). \quad (4.92)$$

The critical AMD C_c^{MMR} associated to the overlap criterion (4.69) can be defined as the smallest value of relative AMD such that the conditions

$$\begin{aligned} \mathcal{E}(c_1, c_2) &= c_1 + c_2 = g(\alpha, \varepsilon) \\ \mathcal{C}(c_1, c_2) &= \frac{1}{2} \left(\gamma\sqrt{\alpha}c_1^2 + c_2^2 \right) = C_c^{\text{MMR}} \end{aligned} \quad (4.93)$$

are verified by any couple (c_1, c_2) . As in section 3.3, the critical AMD is obtained through Lagrange multipliers $\nabla \mathcal{C} \propto \nabla \mathcal{E}$. The tangency condition gives a relation between c_1 and c_2 ,

$$\gamma\sqrt{\alpha}c_1 = c_2. \quad (4.94)$$

Replacing c_2 in relation (4.93) gives the critical expression of c_1 and we immediately obtain the expression of c_2

$$c_{c,1} = \frac{g(\alpha, \varepsilon)}{1 + \gamma\sqrt{\alpha}} \quad c_{c,2} = \frac{\gamma\sqrt{\alpha}g(\alpha, \varepsilon)}{1 + \gamma\sqrt{\alpha}}. \quad (4.95)$$

The value of C_c^{MMR} is obtained by injecting the critical values $c_{c,1}$ and $c_{c,2}$ into the expression of \mathcal{C}

$$C_c^{\text{MMR}}(\alpha, \gamma, \varepsilon) = \frac{\varrho(\alpha, \varepsilon)^2}{2} \frac{\gamma\sqrt{\alpha}}{1 + \gamma\sqrt{\alpha}}. \quad (4.96)$$

4.4.2 Comparison with the collision criterion

It is then natural to compare the critical AMD C_c^{MMR} to the critical AMD C_c (denoted C_c^{col} in this section to avoid ambiguity) derived from the collision condition in section 3.3. If $\alpha > \alpha_{\text{cir}}$, the circular overlap criterion implies that $C_c^{\text{MMR}} = 0$ and therefore C_c^{MMR} should be preferred to the previous criterion C_c .

However, C_c^{MMR} was obtained thanks to the assumption that α was close to 1. Particularly, it makes no sense to talk about first-order MMR overlap for $\alpha < 0.63$ which corresponds to the center of the MMR 2:1. Therefore, the collision criterion should be used for α away from 1 *i.e.* larger orbital separations. We need then to find α_{MMR} such that for $\alpha < \alpha_{\text{MMR}}$, we should use the critical AMD C_c^{col} . Since we are close to 1, we use a development of C_c^{col} presented in equation (3.22), and similarly, only keep the leading terms in $1 - \alpha$ in C_c^{MMR} . The two expressions are

$$C_c^{\text{col}} = \frac{\gamma}{1 + \gamma} \frac{(1 - \alpha)^2}{2}, \quad C_c^{\text{MMR}} = \frac{\gamma}{1 + \gamma} \frac{\varrho(\alpha, \varepsilon)^2}{2}. \quad (4.97)$$

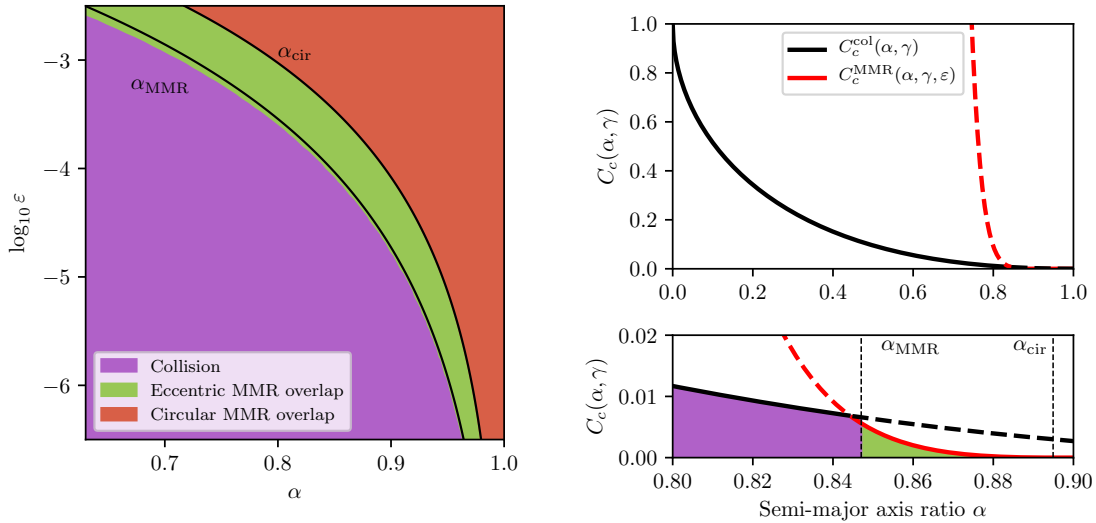
We observe that for α close to 1, the two terms have the same dependence on γ , therefore, α_{MMR} depends solely on ε . Simplifying $C_c^{\text{col}} = C_c^{\text{MMR}}$ gives α_{MMR} as a solution of the polynomial equation in $(1 - \alpha)$;

$$3^6(1 - \alpha)^7 - 3^2 2^9 \mathcal{R}\varepsilon(1 - \alpha)^3 - 2^{14}(\mathcal{R}\varepsilon)^2 = 0. \quad (4.98)$$

While an exact analytical solution cannot be provided, a development in powers of ε gives the following expression

$$\begin{aligned} 1 - \alpha_{\text{MMR}} &= \frac{4}{3}(2\mathcal{R}\varepsilon)^{1/4} + \frac{1}{4}\sqrt{2\mathcal{R}\varepsilon} + O(\varepsilon^{3/4}) \\ &= 1.50\varepsilon^{1/4} + 0.316\sqrt{\varepsilon} + O(\varepsilon^{3/4}). \end{aligned} \quad (4.99)$$

It should be remarked that the first term can be directly obtained using Deck's high-eccentricity approximation.



(a) Region of validity of the criteria. In the purple region, C_c^{col} is the smallest, in the green zone, it is C_c^{MMR} and the circular overlap criterion is verified in the red zone. We see that the curve α_{MMR} computed through a development of C_c^{col} and C_c^{MMR} presents a good agreement with the real limit between the green and the purple area. Here $\gamma = 1$.

(b) Critical AMD C_c^{col} and C_c^{MMR} for $\varepsilon = 10^{-4}$ and $\gamma = 1$. C_c^{col} (in black) is the collisional criterion (section 3.3), C_c^{MMR} (in red) is the critical AMD derived from the MMR overlap criterion (4.96). The colors are here to represent the region described in figure 4.6a

Figure 4.6 – Representation and comparison of the two critical AMD presented in the previous and the present chapter.

In Figure 4.6a we plot α_{MMR} and α_{cir} and indicate which criterion is used in the areas delimited by the curves. We specifically represented the region $\alpha > \alpha_{\text{cir}}$ because we cannot treat this region in a similar manner as the remaining region since comparing the relative AMD \mathcal{C} to C_c^{MMR} does not provide any information. We see that the curve α_{MMR} is not exactly at the limit where $C_c^{\text{col}} = C_c^{\text{MMR}}$ for higher ε due to the development of the critical AMDs for $\alpha \rightarrow 1$. We study the influence of γ on the difference between α_{MMR} and the actual limit in Appendix C.4

For stability analysis, we need to choose the smallest of the two critical AMD. For $\alpha < \alpha_{\text{MMR}}$, the collisional criterion is better and the MMR overlap criterion is used for $\alpha > \alpha_{\text{MMR}}$. We thus define a piece-wise global critical AMD represented in Figure 4.6b

$$C_c(\alpha, \gamma, \varepsilon) = \min(C_c^{\text{col}}(\alpha, \gamma), C_c^{\text{MMR}}(\alpha, \gamma, \varepsilon)) \quad (4.100)$$

4.5 Effects of the MMR overlap on the AMD-classification of planetary systems

In section 3.4, we proposed a classification of the planetary systems based on their AMD-stability. We recall that a system is considered as AMD-stable if every adjacent pair of planets is AMD-stable, and a pair is considered as AMD-stable if

its AMD-stability coefficient

$$\beta = \frac{C}{\Lambda' C_c^{\text{col}}} < 1, \quad (4.101)$$

where C is the total AMD of the system, Λ' is the circular momentum of the outer planet and C_c^{col} is the pair critical AMD derived from the collision condition. A similar AMD-coefficient can be defined using the global critical AMD defined in (4.100) instead of the collisional critical AMD C_c^{col} . Let us note $\beta^{(\text{MMR})}$, the AMD-stability coefficient associated to the critical AMD (4.96).

We can first observe that $\beta^{(\text{MMR})}$ is not defined for $\alpha > \alpha_{\text{cir}}$. Indeed, the conservation of the AMD cannot be guaranteed for orbits experiencing short-term chaos. By comparing $\beta^{(\text{MMR})}$ to the collisional AMD-stability coefficient, we test how including the MMR overlap effects the AMD-classification proposed in chapter 3.

4.5.1 Sample and methodology

Let me first briefly recall the methodology used in section 3.4; to which I refer the reader for full details. We compute the AMD-stability coefficients for the systems taken from the database `exoplanet.eu` with known periods, planet masses, eccentricities, and stellar mass. For each pair of adjacent planets, ε is computed using the expression

$$\varepsilon = \frac{m_1 + m_2}{m_0}, \quad (4.102)$$

where m_1 and m_2 are the two planet masses and m_0 , the star mass. The semi-major axis ratio was derived from the period ratio and Kepler third law in order to reduce the uncertainty.

The systems are assumed coplanar, however in order to take into account the contribution of the real inclinations to the AMD, we define C_p , the coplanar AMD of the system, defined as the AMD of the same system if it was coplanar. We can compute coplanar AMD-stability coefficients $\beta_p^{(\text{MMR})}$ and β_p using C_p instead of C , and we define the total AMD-stability coefficients as $\beta = 2\beta_p^{(\text{MMR})}$. Doing so, we assume the equipartition of the AMD between the different degree of freedom of the system.

We assume the uncertainties of the database quantities to be Gaussian. For the eccentricities, we use the same method as in section 3.4. The quantity $e \cos \varpi$ is assumed to be Gaussian with the mean, the value of the database and standard deviation, the database uncertainty. The quantity $e \sin \varpi$ is assumed to have a Gaussian distribution with zero mean and the same standard deviation. The distribution of eccentricity is then derived from these two distributions.

We then propagate the uncertainties through the computations thanks to Monte-Carlo simulations of the original distributions. For each of the systems, we draw 10,000 values of masses, periods and eccentricities from the computed distributions. We then compute $\beta^{(\text{MMR})}$ for each of these configurations and compute the $1-\sigma$ confidence interval.

In chapter 3, we studied 131 systems but we did not find the stellar mass for 4 of these systems. They were, as a consequence, excluded from this study. Moreover,

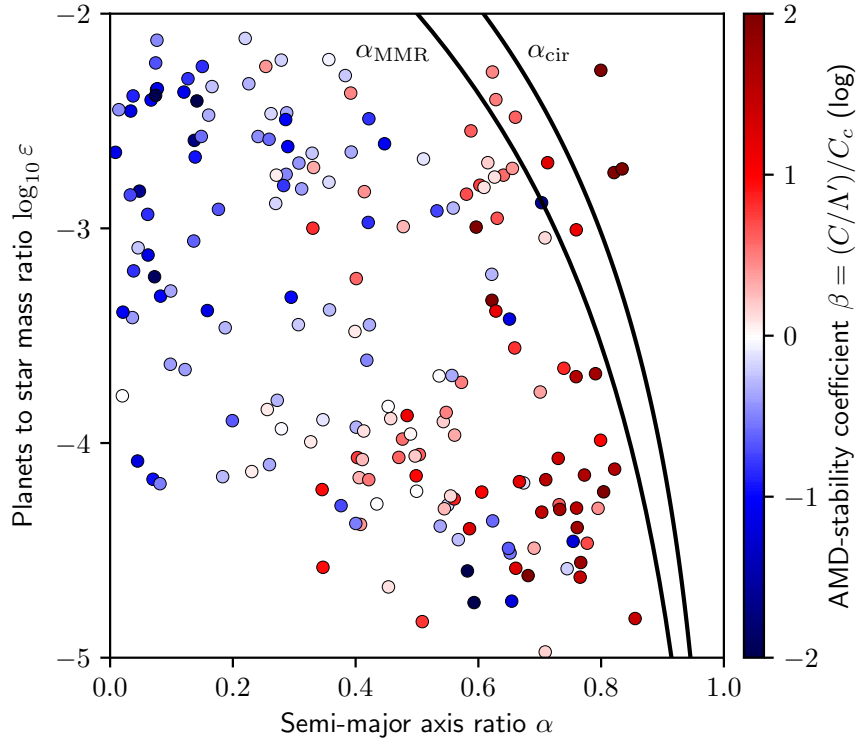


Figure 4.7 – Pairs of adjacent planets represented in the (α, ε) plane. The color corresponds to the AMD-stability coefficient. We plot the two limits α_{MMR} corresponding to the limit between the collision and the MMR-overlap-based criterion and α_{cir} corresponding to the MMR overlap for circular orbits.

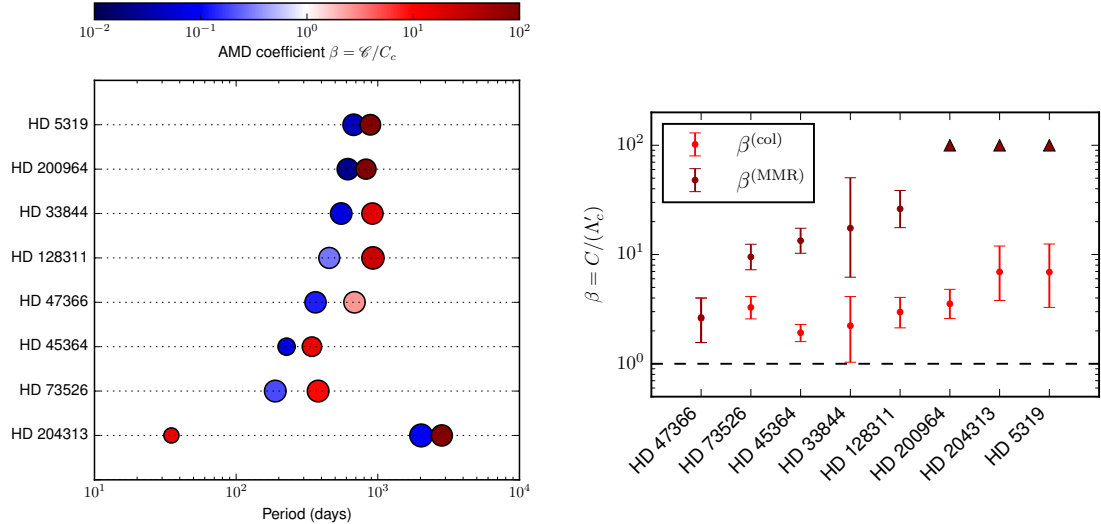
the computation of ε for the pairs of planets of the 127 remaining systems of the sample led in some cases to high planet-to-star mass ratios. We decide to exclude the systems such that α_{cir} was smaller than the center of the resonance 2:1. We thus discard systems such that a pair of planets has

$$\varepsilon > \varepsilon_{\text{lim}} = 8.20 \times 10^{-3}. \quad (4.103)$$

As a result, we only consider in this study 111 systems that meet the above requirements. A pair is considered stable if the $1-\sigma$ confidence interval (84% of the simulated systems) of both of the AMD-stability coefficients $\beta^{(\text{MMR})}$ and β is below 1. A system is stable if all adjacent pairs are stable.

4.5.2 Results

Figure 4.7 shows the planet pairs of the considered systems in a plane (α, ε) . The color associated to each point is the AMD-stability coefficient of the pair. The values chosen for the plot correspond, for all quantities, to the median. We remark that very few systems are concerned by the change of the critical AMD, indeed, only



(a) Architecture of the systems where the MMR overlap criterion changes the AMD-stability. The color corresponds to the value of the AMD-stability coefficient associated with the innermost planet. For the innermost planet, it corresponds to the star AMD-stability criterion (see chapter 3). The diameter of the circle is proportional to the log of the mass of the planet.

(b) AMD-stability coefficient of the pairs affected by the change of criterion. $\beta^{(\text{col})}$ corresponds to the coefficient computed with the collisional critical AMD, and $\beta^{(\text{MMR})}$ refers to the one computed with the MMR overlap critical AMD. The triangles represent the pairs where $\beta^{(\text{MMR})}$ goes to infinity.

Figure 4.8 – Architecture and AMD-stability coefficients of the system affected by the MMR overlap criterion

eight systems² have a pair of planets such that $C_c^{\text{MMR}} < C_c^{\text{col}}$. The 111 considered systems contain 162 planet pairs plotted in figure 4.7. This means that less than 5% of the pairs are in a configuration leading to MMR overlap.

We plot in Figure 4.8a, the architecture of these eight systems and give in Table C.1 the values of the AMD-stability coefficients. For each of these systems, the pair verifying the MMR overlap criterion was already considered AMD-unstable by the criterion based on the collision.

In order to show this, we plot in Figure 4.8b the AMD-stability coefficients computed with both critical AMD. We see that the pairs affected by the change of criterion were already considered AMD-unstable in the purely secular dynamics. However, while those pairs have a collisional AMD-coefficient β between 1 and 10, their AMD-stability coefficient $\beta^{(\text{MMR})}$ is greater by roughly an order of magnitude for the four pairs with α between α_{MMR} and α_{cir} . The AMD-coefficient is not defined for the three pairs verifying the circular MMR overlap criterion. The pair HD 47366 b/c does not see a significant change of its AMD-stability coefficient because it is very close to the limit $C_c^{\text{col}} = C_c^{\text{MMR}}$.

² It should be noted that for one of the systems, the MMR overlap criterion was preferred in 16% of the Monte Carlo simulations.

We identify three systems, HD 200964, HD 204313 and HD 5319, that satisfy the circular overlapping criterion. As already explained in (Laskar and Petit, 2017), AMD-unstable planetary systems may not be dynamically unstable. However, it should be noted that the period ratios of the AMD-unstable planet pairs are very close to particular MMR. Indeed, we have

$$\begin{aligned}\frac{T_c^{\text{HD 200964}}}{T_b^{\text{HD 200964}}} &= 1.344 \simeq 4/3, \\ \frac{T_d^{\text{HD 204313}}}{T_c^{\text{HD 204313}}} &= 1.399 \simeq 7/5, \\ \frac{T_c^{\text{HD 5319}}}{T_b^{\text{HD 5319}}} &= 1.313 \simeq 4/3.\end{aligned}$$

The AMD-instability of those systems strongly suggests that they are indeed into a resonance which stabilizes their dynamics.

4.6 Conclusions

As shown in chapter 3, the notion of AMD-stability is a powerful tool to characterize the stability of planetary systems. In this framework, the dynamics of a system is reduced to the AMD transfers allowed by the secular evolution.

However, we need to ensure that the system dynamics can be averaged over its mean motions. While a system can remain stable and the AMD or semi-major axis can be averaged over timescales longer than the libration period in presence of MMR, the system stability and particularly the conservation of the AMD is no longer guaranteed if the system experiences MMR overlap. In this work, we use the MMR overlap criterion as a condition to delimit the zone of the phase space where the dynamics can be considered as secular.

We refine the criteria proposed by (Wisdom, 1980; Mustill and Wyatt, 2012; Deck *et al.*, 2013) and demonstrate that it is possible to obtain a global expression (4.69), valid for all cases. The previous circular (4.71) and eccentric (4.73) criteria can then be derived from (4.69) as particular approximations. Moreover, we show that expression (4.69) can be used to directly take into account the first-order MMR in the notion of AMD-stability.

With this work on first-order MMR, we improve the AMD-stability definition by addressing the problem of the minimal distance between close orbits. For semi-major axis ratios α above a given threshold α_{cir} (4.71), that is, $\alpha_{\text{cir}} < \alpha < 1$, the system is considered unstable whichever value the AMD may take given that even two circular orbits satisfy the MMR overlap criterion. At wider separations, circular orbits are stable but as eccentricities increase two outcomes may happen: either the system enters a region of MMR overlap or the collision condition is reached. The system is said to be AMD-unstable as soon as any of these conditions is reached. Above a second threshold, $\alpha_{\text{MMR}} < \alpha < \alpha_{\text{cir}}$ (eq. 4.99) the AMD-stability is governed by MMR overlap while for wider separations ($\alpha < \alpha_{\text{MMR}}$) we retrieve the critical AMD defined in (Laskar and Petit, 2017) which only depends on the collision condition.

We show in Section 4.5 that very few systems satisfy the circular MMR overlap criterion. Moreover, the presence of systems satisfying this criterion strongly suggests that they are protected by a particular MMR. In this case, the AMD-instability is a simple tool suggesting unobvious dynamical properties.

In order to improve the AMD-stability definition for the collision region, we could even take into account the non-secular dynamics induced by higher-order MMR (Hadden and Lithwick, 2018) and close-encounter consequences on the AMD.

For two planet systems, or if the dynamics can be safely simplify by only considering the mutual interactions between only two planets, there exists a strong stability criterion induced by a topological boundary of the three body problem (Marchal and Bozis, 1982). This criterion, called Hill stability is the subject of the next chapter.

Chapter 5

Hill stability in the AMD framework

The content of this chapter was initially published in (Petit et al., 2018).

5.1 Introduction

The chaotic nature of planetary dynamics has made the development of stability criteria necessary because the complete study of individual systems for the lifetime of the central star would require very large computational power. Moreover, in the context of exoplanet dynamics, the orbital parameters are often not known with great precision, making it impossible to conduct a precise dynamical study. For multiplanetary systems, the best solutions yet are empirical stability criteria based on minimum spacing between planets obtained from numerical simulations (Chambers *et al.*, 1996; Pu and Wu, 2015). For tightly packed systems, Tamayo *et al.* (2016) have suggested a solution based on short integrations and a machine-learning algorithm.

Another approach consists in the study of the angular momentum deficit (AMD; see chapter 3). The AMD is a weighted sum of the eccentricities and mutual inclinations of planets and can be interpreted as a dynamical temperature of the planetary system. The AMD is conserved at all orders of averaging over the mean motions. In chapter 3, it was shown that if the AMD is small enough, collisions are impossible. We can define a sufficient stability condition from the secular conservation of the AMD, i.e., the AMD stability. Systems that are AMD stable are long-lived, whereas a more in-depth dynamical study is necessary for AMD-unstable systems.

The initial AMD-stability definition is based on the secular approximation. In chapter 4, the criterion was slightly modified to exclude systems experiencing short term chaos due to first order mean motion resonances (MMR) overlap. The MMR overlap is the main source of chaos and instability in planetary dynamics. Based on Chirikov (1979) resonance overlap criterion, Wisdom (1980) has derived an analytical stability criterion for the two-planet systems that has since been widely

used. Wisdom's criterion is obtained for circular and coplanar planets. It was improved to take into account moderate eccentricities (Mustill and Wyatt, 2012; Deck *et al.*, 2013; Hadden and Lithwick, 2018). We have shown in (Petit *et al.*, 2017) that this MMR overlap criterion can be expressed solely as a function of the AMD, semi-major axes, and masses for almost coplanar and low eccentricity systems.

The MMR overlap criterion gives a clear limit between regular and chaotic orbits for small eccentricities. However, this criterion is based on first order expansions in the planet-to-star mass ratio, that is the spacing between planets, eccentricities, and inclinations. As a result, for wider orbit separations, the secular collision criterion from chapter 3 remains a better limit. Moreover, the MMR overlap criterion only takes into account the interaction between a couple of planets, making it really accurate only for two-planet systems.

In the case of two-planet systems, the topology of the phase space gives a far simpler criterion of stability, that is the Hill stability. Based on a work by Sundman (1912) on the moment of inertia in the three-body problem, Marchal and Saari (1975) noted the existence of forbidden zones in the configuration space. Marchal and Bozis (1982) extended the notion of Hill stability to the general three-body problem and showed that some systems can forbid close encounters between the outer body and any of the inner bodies. In particular, the Hill stability ensures that collisions between the outer body and the close binary (in a two-planet system, between the outer planet and the inner planet or the star) are impossible for infinite time.

The results of (Marchal and Saari, 1975; Marchal and Bozis, 1982) have many applications outside of the Hill stability. It is possible to cite a sufficient condition for the ejection of a body from the system (Marchal *et al.*, 1984a; Marchal *et al.*, 1984b) or the determination of the limit of a triple close approach for bounded orbits (Laskar and Marchal, 1984).

Marchal and Bozis (1982) presented the planetary problem (one body with a much larger mass) as a particular case, but the result was mainly popularized by Gladman (1993) who introduced a minimal spacing for initially circular and coplanar systems. Gladman also proposed some criteria for eccentric orbits in some particular configurations of masses. The result by Gladman was refined to cover other situations as, for example, the case of inclined orbits (Veras and Armitage, 2004). Georgakarakos (2008) provided a review of stability criteria for hierarchical three-body problems.

The Hill stability is consistent with numerical integrations, where a sharp transition between Hill stable and Hill unstable systems is often observed (Gladman, 1993; Barnes and Greenberg, 2006; Deck *et al.*, 2013). Moreover, Deck *et al.* (2013) analyzed the differences between the MMR overlap and Hill stability criteria. They remarked that there exists an area where orbits are chaotic because of the overlap of MMR but long-lived owing to Hill stability.

In this chapter, we show that the Hill stability criterion from (Marchal and Bozis, 1982) fits extremely well in the AMD-stability framework. In section 5.2, we derive a criterion for Hill stability solely expressed as a function of the total AMD, semi-major axes, and masses. Our criterion does not need any expansion in the spacing, eccentricities, or inclinations of the orbits and admits all previous Hill criteria as particular approximations.

In order to do so we follow the reasoning proposed by Marchal and Bozis (1982). We then compare the Hill stability criterion with the AMD-stability criteria proposed in chapter 3 and 4. In the last section, we carry numerical integrations of two-planet systems over a large part of the phase space. We show that the only parameters of importance are the initial AMD and semi-major axis ratio.

5.2 Hill stability in the three-body problem

5.2.1 Generalized Hill curves

Let us use the formalism proposed in (Marchal and Saari, 1975; Marchal and Bozis, 1982) for the definition of the Hill regions for the general three-body problem. We mainly consider the planetary case and therefore slightly adapt their notations to this particular problem. Let us consider two planets of masses m_1, m_2 orbiting a star of mass m_0 . Let \mathcal{G} be the constant of gravitation, $\mu = \mathcal{G}m_0$,

$$\varepsilon = \frac{m_1 + m_2}{m_0}, \quad (5.1)$$

the planet mass to star mass ratio and

$$\gamma = \frac{m_1}{m_2}. \quad (5.2)$$

As in the previous chapters, we use the heliocentric canonical coordinates $(\tilde{\mathbf{r}}_j, \mathbf{r}_j)_{j=1,2}$. In those coordinates, the Hamiltonian is

$$\mathcal{H} = \sum_{j=1}^2 \left(\frac{1}{2} \frac{\|\tilde{\mathbf{r}}_j\|^2}{m_j} - \frac{\mu m_j}{r_j} \right) + \frac{1}{2} \frac{\|\tilde{\mathbf{r}}_1 + \tilde{\mathbf{r}}_2\|^2}{m_0} - \frac{\mathcal{G}m_1 m_2}{r_{12}}, \quad (5.3)$$

where $r_{12} = \|\mathbf{r}_1 - \mathbf{r}_2\|$. We denote \mathbf{G} the total angular momentum of the system assumed aligned with the vertical axis and G its norm. We also use the modified Delaunay coordinates (2.37) and in particular $\Lambda_j = m_j \sqrt{\mu a_j}$, where a_j is the semi-major axis of the j th planet. We also note e_j , the eccentricity and i_j , the inclination of the orbital plane with the horizontal plane. The AMD, C (Laskar, 1997; Laskar, 2000) is expressed

$$C = \sum_{j=1}^2 \Lambda_j \left(1 - \sqrt{1 - e_j^2} \cos(i_j) \right). \quad (5.4)$$

Following (Marchal and Bozis, 1982), we define a generalized semi-major axis

$$a = -\frac{\mathcal{G}M^*}{2\mathcal{H}}, \quad (5.5)$$

and a generalized semilatus rectum

$$p = \frac{m_0(1 + \varepsilon)}{\mathcal{G}M^{*2}} G^2, \quad (5.6)$$

where

$$M^* = m_0m_1 + m_0m_2 + m_1m_2 = m_0^2\varepsilon \left(1 + \varepsilon \frac{\gamma}{(1+\gamma)^2}\right). \quad (5.7)$$

The values a and p are the two length units that can be built from the first integrals \mathcal{H} and G . We finally define two variable lengths. First, ρ the mean quadratic distance

$$M^*\rho^2 = m_0m_1r_1^2 + m_0m_2r_2^2 + m_1m_2r_{12}^2, \quad (5.8)$$

that is proportional to the moment of inertia I computed in the center of mass frame (Marchal and Bozis, 1982)

$$I = \frac{1}{2} \frac{M^*\rho^2}{m_0 + m_1 + m_2}. \quad (5.9)$$

We introduce ν , the mean harmonic distance

$$\frac{M^*}{\nu} = \frac{m_0m_1}{r_1} + \frac{m_0m_2}{r_2} + \frac{m_1m_2}{r_{12}}, \quad (5.10)$$

which is proportional to the potential energy

$$U = -\frac{\mathcal{G}M^*}{\nu}. \quad (5.11)$$

For a system with given \mathcal{H} and G , some configurations of the planets are forbidden. Indeed, the value of the ratio ρ/ν is constrained by the inequality (Marchal and Saari, 1975)

$$\frac{\rho}{\nu} \geq \frac{\rho}{2a} + \frac{p}{2\rho}, \quad (5.12)$$

derived from Sundman's inequality (Sundman, 1912). Moreover, if the system has a negative energy, the right-hand side of (eq. 5.12) has a minimum value obtained for $\rho = \sqrt{ap}$. We therefore have the inequality (Marchal and Bozis, 1982)

$$\frac{\rho^2}{\nu^2} \geq \frac{p}{a} = -\frac{2m_0(1+\varepsilon)}{\mathcal{G}^2 M^{*3}} \mathcal{H} G^2. \quad (5.13)$$

If p/a is high enough, the inequality (5.13) makes some regions of the phase space inaccessible. In this case, we can ensure that certain initial conditions forbid collisions between the two planets for all times.

Let us study the values of the function $(\rho/\nu)^2$. Since this ratio only depends on the ratios of mutual distances, we can always place ourselves in the plane generated by the three bodies. We can also choose to place the first planet on the x -axis and normalize the lengths by r_1 . Let us call this plane \mathcal{P} and note (x, y) the coordinates of the second planet. In the plane \mathcal{P} (see Figure 5.1), the star S is at the origin, the first planet P_1 is situated at the point $(1, 0)$. For the planar circular restricted three-body problem, this reduction is equivalent to study the dynamics in the corotating frame. We note

$$R(x, y) = \left(\frac{\rho}{\nu}\right)^2. \quad (5.14)$$

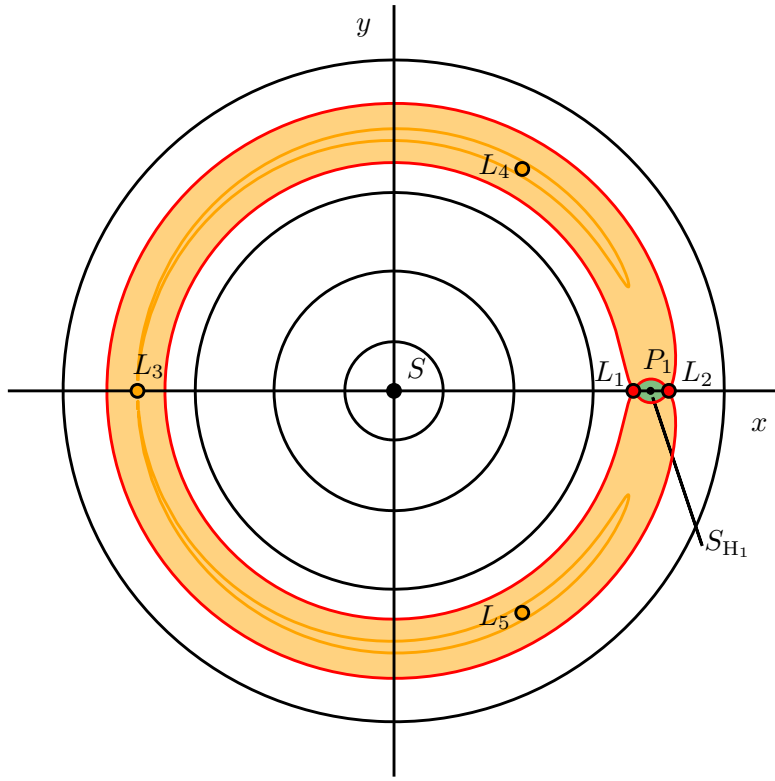


Figure 5.1 – Some levels of the function R defined in (5.14) for $\varepsilon = 10^{-3}$ and $\gamma = 1$ in the \mathcal{P} plane. The two red points correspond to the Lagrange points L_1 and L_2 and the three orange points to L_3 , L_4 , and L_5 . The orange-filled area corresponds to the region where $R(x, y) < R(L_1)$. The star S is at the origin, the planet P_1 at $(1,0)$ and (x,y) are the coordinates of the second planet. The green region S_{H_1} represents the Hill sphere of the first planet.

The shape of the function R in \mathcal{P} only depends on the relative mass distribution, *i.e.*, the two ratios ε and γ . In Figure 5.1, we can see level curves of the function R plotted in \mathcal{P} for $\varepsilon = 10^{-3}$ and $\gamma = 1$. The value R is minimal and equal to 1 at the two Lagrange points L_4 and L_5 and goes to $+\infty$ for $\|\mathbf{r}_2\| \rightarrow 0$, $\|\mathbf{r}_2 - \mathbf{r}_1\| \rightarrow 0$ or $\|\mathbf{r}_2\| \rightarrow +\infty$. The function has three saddle nodes at the Lagrange points L_1 , L_2 , and L_3 . We give the method to compute the position of the Lagrange points in appendix D.1. Let us denote x_1 , x_2 , and x_3 their abscissa, respectively. At the lowest order in ε we have

$$\begin{aligned} x_1 &= 1 - \left(\frac{\varepsilon}{3}\right)^{1/3} + O(\varepsilon^{2/3}), \\ x_2 &= 1 + \left(\frac{\varepsilon}{3}\right)^{1/3} + O(\varepsilon^{2/3}), \\ x_3 &= -1 + \frac{7}{12} \frac{\gamma - 1}{\gamma + 1} \varepsilon + O(\varepsilon^2). \end{aligned} \tag{5.15}$$

We deduce that at the lowest order in ε , the values of R at the Lagrange points

are

$$\begin{aligned} R(L_1) &= 1 + 3^{4/3}\varepsilon^{2/3}\frac{\gamma}{(\gamma+1)^2} + O(\varepsilon) \\ R(L_2) &= 1 + 3^{4/3}\varepsilon^{2/3}\frac{\gamma}{(\gamma+1)^2} + O(\varepsilon), \\ R(L_3) &= 1 + 2\varepsilon\frac{\gamma}{(\gamma+1)^2} + O(\varepsilon^2). \end{aligned} \quad (5.16)$$

The values $R(L_1)$ and $R(L_2)$ have the same first order term but differ in the expansion of higher order. Indeed, if $m_0 \geq m_1 \geq m_2$, we have $R(L_1) \geq R(L_2)$ (Marchal and Bozis, 1982). From now on, let us assume $R(L_1) \geq R(L_2)$ (if not, we can just substitute $R(L_2)$ to $R(L_1)$ in further equations).

For $p/a \geq R(L_1)$, the accessible domain is split into three parts: the Hill sphere of the star S , which is around the origin; the first planet Hill sphere¹ S_{H_1} (in green in Figure 5.1); and the outer region. In this case, if the second planet is not initially inside S_{H_1} , it will never be able to enter this region. However, if P_2 is in the outer region, the Hill stability cannot constrain the possibility of ejection. Similarly, if P_2 is closer to the star (in the inner region), a collision with the star is still possible.

The study of the function R and the inequality (5.13) gives a noncollision criterion for an infinite time. Marchal and Bozis called it the Hill stability.

Proposition 1 (Marchal and Bozis, 1982). *Let us consider a negative energy three-body problem with a body S of mass m_0 and two others P_1 and P_2 of mass m_1 and m_2 such that $m_0 \geq m_1 \geq m_2$. We place ourselves in the \mathcal{P} plane defined by S , P_1 , and P_2 (Figure 5.1). If P_2 is not initially inside the Hill sphere S_{H_1} of P_1 , the system is Hill stable if*

$$\frac{p}{a} > R(L_1), \quad (5.17)$$

where a is defined in (5.5), p in (5.6) and R in (5.14).

From this inequality, Gladman (1993) obtained criteria for initially circular orbits and for two particular cases of eccentric orbits: the case of equal masses and small eccentricities and the case of equal masses and large, but equal eccentricities.

While Gladman's Hill stability criterion for initially circular orbits is useful, the eccentric criteria are too particular to be used in the context of a generic system. It is however possible to obtain a very general Hill stability criterion using the AMD to take into account the eccentricities and inclinations of the orbits.

5.2.2 AMD condition for Hill stability

The total energy of the system can be written

$$\mathcal{H} = -\frac{m_2^3\mu^2}{2\Lambda_2^2} \left(\frac{\gamma}{\alpha} + 1 + h_1 \right), \quad (5.18)$$

where $\alpha = a_1/a_2$ and

$$h_1 = -\frac{2\Lambda_2^2}{m_2^3\mu^2} \left(\frac{1}{2} \frac{\|\tilde{\mathbf{r}}_1 + \tilde{\mathbf{r}}_2\|^2}{m_0} - \frac{Gm_1m_2}{r_{12}} \right). \quad (5.19)$$

¹The Hill region is usually called the Hill sphere although it is not technically a sphere.

From now on, we assume that initially $\alpha \leq 1$ (if not we can just renumber the two planets). Similarly the angular momentum can be rewritten

$$G = \Lambda_2 (\gamma\sqrt{\alpha} + 1 - \mathcal{C}), \quad (5.20)$$

where

$$\mathcal{C} = \frac{C}{\Lambda_2} = \gamma\sqrt{\alpha} \left(1 - \sqrt{1 - e_1^2} \cos i_1 \right) + 1 - \sqrt{1 - e_2^2} \cos i_2 \quad (5.21)$$

is the relative AMD already defined in (3.7). Combining (5.13), (5.18) and (5.20), we obtain

$$\frac{p}{a} = \frac{(1 + \varepsilon)}{(\gamma + 1)^3 (1 + \varepsilon\gamma/(\gamma + 1)^2)^3} \left(\frac{\gamma}{\alpha} + 1 + h_1 \right) (\gamma\sqrt{\alpha} + 1 - \mathcal{C})^2. \quad (5.22)$$

The Hill stability criterion (5.17) can be rewritten without any approximation as a condition on \mathcal{C} and we have the following formulation of the Hill stability.

Proposition 2 (Hill stability). *With the hypotheses of the proposition 1, assuming the elliptical elements can be defined (i.e., both Keplerian energies are negative), a system is Hill stable if*

$$\mathcal{C} < C_c^{\text{Ex}} = \gamma\sqrt{\alpha} + 1 - (\gamma + 1)^{3/2} \sqrt{\frac{R(L_1)(1 + \varepsilon\gamma/(\gamma + 1)^2)^3}{(1 + \varepsilon)(\gamma/\alpha + 1 + h_1)}}, \quad (5.23)$$

where \mathcal{C} is the relative AMD (5.21) and h_1 the normalized perturbation part (5.19).

The inequality (5.23) is equivalent to proposition 1 but we isolated the contribution from the AMD on the left-hand side. Up to the perturbation term h_1 , the right-hand side of (5.23) only depends on the masses and the semi-major axis ratio α . If we only keep the terms of leading order in ε in the square root of the right-hand side of (eq. 5.23), we obtain an expression that depends only on α , ε , and γ .

Proposition 3 (Hill stability, planetary case). *For small enough ε , a two-planet system is Hill stable if the relative AMD \mathcal{C} verifies the inequality*

$$\mathcal{C} < \gamma\sqrt{\alpha} + 1 - (1 + \gamma)^{3/2} \sqrt{\frac{\alpha}{\gamma + \alpha} \left(1 + \frac{3^{4/3}\varepsilon^{2/3}\gamma}{(1 + \gamma)^2} \right)} + O(\varepsilon). \quad (5.24)$$

As explained in appendix D.2, h_1 is of smaller order in ε and can be neglected if the criterion is verified. We want to stress that the expression (5.24) is obtained with only an expansion in ε and only depends on α , \mathcal{C} , and the masses of the bodies. The term of order $\varepsilon^{2/3}$ in Eq. 5.24 also depends on $\gamma/(\gamma + 1)^2$, but we show in appendix D.2 that (5.24) is still valid for $\gamma \ll 1$ or $\gamma \gg 1$.

5.2.3 Close planets approximation

Assuming $1 - \alpha \ll 1$, and a small AMD value, further approximations can be made. At leading order in \mathcal{C} , $1 - \alpha$, and ε , the inequality (5.24) becomes

$$\mathcal{C} < \frac{3\gamma}{8(\gamma + 1)} (1 - \alpha)^2 - \frac{3^{4/3}\gamma}{2(\gamma + 1)} \varepsilon^{2/3}. \quad (5.25)$$

We can isolate $1 - \alpha$ in this expression to obtain an approximate minimum spacing for Hill stable systems.

Proposition 4 (Hill stability, close planets case). *For a close planets system, the minimum spacing criterion for Hill stability is*

$$\frac{a_2 - a_1}{a_2} = 1 - \alpha > \sqrt{4 \times 3^{1/3} \varepsilon^{2/3} + \frac{8\gamma+1}{3\gamma} \mathcal{C}}. \quad (5.26)$$

Gladman's eccentric criteria can be recovered from (5.26) if the AMD is developed under the assumptions (same planet masses, small or large, and equal eccentricities) made in Gladman (1993). However (5.26) is more general as it takes into account mutual inclinations or uneven mass distribution.

In the case of circular orbits, we also get the well-known formula (Gladman, 1993)

$$1 - \alpha > 2\sqrt{3} \left(\frac{\varepsilon}{3}\right)^{1/3} = 2.40\varepsilon^{1/3}. \quad (5.27)$$

5.2.4 Comparison of the Hill criteria

We can compare the right-hand side of (5.23), (5.24), (5.25) and Gladman's circular approximation (5.27) to test how relevant are the approximations made here. In Figure 5.2, we plot the exact expression C_c^{Ex} (eq. 5.23, in green), the expansion in ε (eq. 5.24, in orange), the approximation for close planets (5.25, in red), and the minimum spacing for circular orbits (5.27, in blue). We see that the expansion in ε (5.24) cannot be distinguished from the exact curve (5.23). In order to better quantify this, we plot in Figure 5.3 the maximum difference between the two curves as a function of ε for various values of the mass ratio γ .

We see in figure 5.3 that for the range of ε used in planetary dynamics (typically from 10^{-6} to 10^{-3}), the expression (5.24) developed in ε is accurate even for very uneven planet mass distribution. From now, we use (5.24) to define the Hill stability.

5.3 Comparison with the AMD-stability

We can use (5.24) to define a critical AMD C_c^{H} for the Hill stability

$$C_c^{\text{H}} = \gamma\sqrt{\alpha} + 1 - (1 + \gamma)^{3/2} \sqrt{\frac{\alpha}{\gamma + \alpha} \left(1 + \frac{3^{4/3}\varepsilon^{2/3}\gamma}{(1 + \gamma)^2}\right)}. \quad (5.28)$$

A system is Hill stable if its initial relative AMD is smaller than the initial critical AMD C_c^{H} . We see that for two planets, the Hill stability definition fits extremely well in the AMD-stability framework. We can also compare C_c^{H} to the previously proposed critical AMD, C_c (chapter 3) and C_c^{MMR} (chapter 4).

The collision critical AMD C_c is plotted in Figure 5.2 with two values of C_c^{H} for $\varepsilon = 10^{-5}$ (resp. 10^{-3}). We can see that the Hill stability criterion is stricter ($C_c^{\text{H}} < C_c$) than the collision condition for secular dynamics. It can be easily understood since the Hill stability forbids the planets to approach each other.

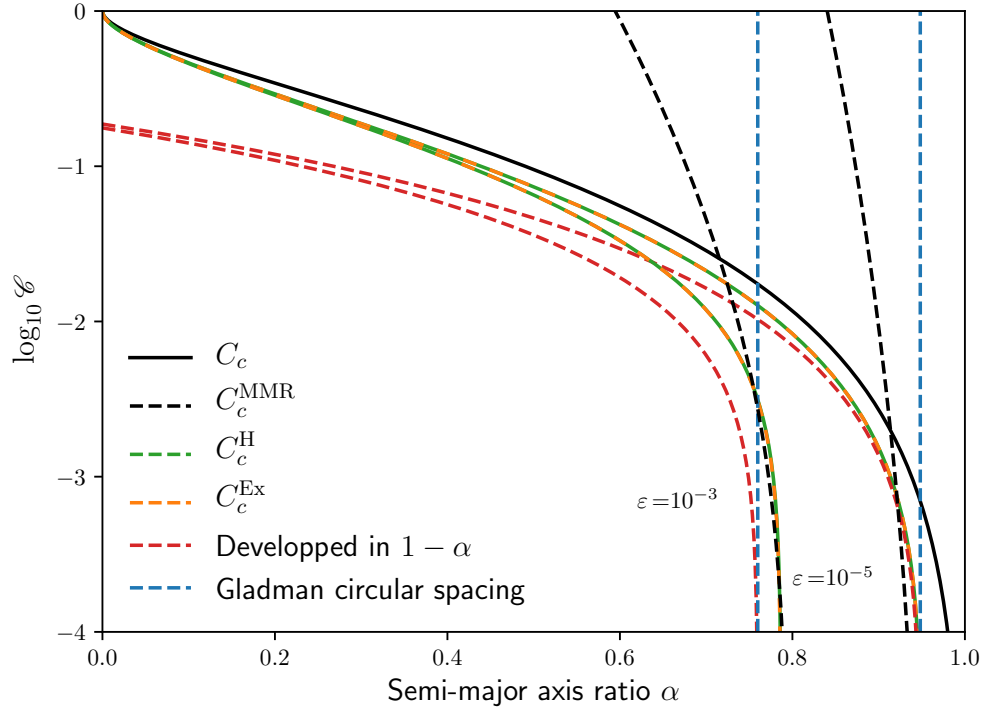


Figure 5.2 – Comparison of the right-hand sides of the inequalities (5.23, orange), (5.24, green), and (5.25, red) as a function of α for $\gamma = 1$ and $\varepsilon = 10^{-5}$ (upper three curves) or $\varepsilon = 10^{-3}$ (lower three curves). The black curve is the critical AMD for the collision condition. The green and orange curves are on top of each other (see Figure 5.3). The critical AMD from MMR overlap C_c^{MMR} and Gladman's (1993) circular criterion are also plotted for comparison.

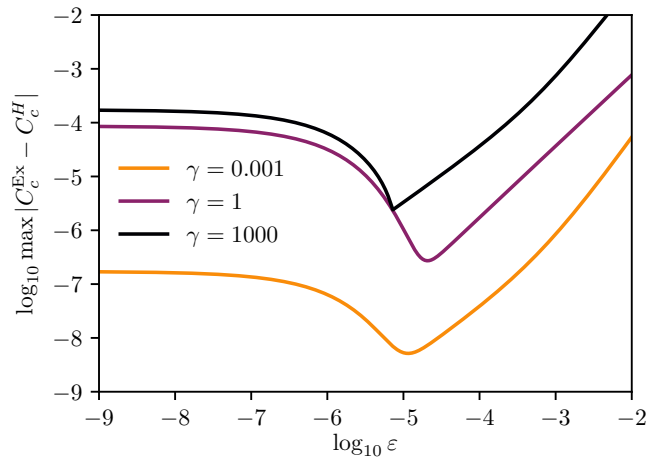


Figure 5.3 – Maximum difference between C_c^{Ex} (5.23) and C_c^{H} (5.28) as a function of ε for various values of $\gamma = m_1/m_2$. In (5.23), the term h_1 is evaluated using the approximation of the kinetic term given in appendix D.2

Indeed, let us consider a Hill stable system, *i.e.*, such that $\mathcal{C} < C_c^H$. As a result the two planets cannot approach each other by less than their mutual Hill radius for any variation of semi-major axes and thus also in the secular system. In particular, a configuration such that the two orbits intersect is impossible. Therefore, the system is AMD stable and $\mathcal{C} < C_c$. Since we are not making any additional hypothesis regarding \mathcal{C} , we have $C_c^H < C_c$. The strict inequality comes from the positive minimal distance between the two planets.

As a comparison, we also plot in Figure 5.2 the MMR critical AMD C_c^{MMR} . For small relative AMD \mathcal{C} , C_c^{MMR} , and C_c^H are almost identical. However, the proximity of two criteria is coincidental. Indeed, they emerge from two different mechanism and it is actually possible to exhibit regimes to highlight the difference as shown in the next section.

5.4 Numerical simulations

The Hill criterion proposed by Marchal and Bozis (1982) has already been tested numerically in particular cases (Gladman, 1993; Veras and Armitage, 2004; Barnes and Greenberg, 2006). In their comparison between the Hill and the overlap of MMR criteria, Deck *et al.* (2013) noted a sharp transition in the proportion of chaotic orbits at the Hill limit $(p/a) = (p/a)|_c$. It also appears that for small ε and α close to 1, the overlap of MMR criterion provides a better limit for the chaotic region.

We want to test whether the Hill criterion gives a good limit to the chaotic region for wider separations. Moreover, we want our initial conditions to sample homogeneously the phase space. Indeed, the Hill stability criterion studied in this paper only depends on few quantities, the relative AMD \mathcal{C} , and the ratio of semi-major axis and not the angles or the actual distribution of the AMD between the degrees of freedom of eccentricities or inclinations. Choosing an homogeneous sampling of the initial conditions also avoids giving too much importance to regions protected by MMR owing to particular combinations of angles while another choice of angles would have given an unstable orbit.

5.4.1 Numerical setup

We ran numerical simulations using the symplectic scheme $\mathcal{ABAH}(10, 6, 4)$ from (Farrés *et al.*, 2013). We chose our initial conditions such that

- the outer planet semi-major axis a_2 is fixed at 1 au;
- the AMD and inner planet semi-major axis a_1 are chosen such that we have a regular grid in the plane $(\alpha, \sqrt{\mathcal{C}})$. Such a scaling in \mathcal{C} is chosen to have an approximately uniform distribution in terms of eccentricities and inclination;
- the AMD is on average equipartitioned between the eccentricity and inclination degrees of freedom;
- the inclinations are chosen such that the angular momentum is on the z -axis;

- the angles are chosen randomly;
- the star mass is taken as $1M_{\odot}$ and the planets masses do not vary for each grid of initial conditions.

We then integrate each initial condition for 500 kyr using a time-step of 10^{-3} yr. The numerical integration is stopped if the planets approach each other by less than a quarter of their mutual Hill radius, if a planet reaches 0.01 AU or 20 AU or if the relative variation of energy is higher than 10^{-8} .

In order to measure the chaoticity of a system, we use frequency map analysis (Laskar, 1990b; Laskar, 1993). Our criterion is based on the relative variation of the main frequencies in the quasiperiodic best fit. More precisely, let $n_k^{(i)}$ (respectively $n_k^{(f)}$) be the frequency obtained by frequency analysis for the planet k for the first (resp. last) 100 kyr of integration. We consider an orbit to be chaotic if

$$\delta n = \max_k \left| \frac{n_k^{(f)} - n_k^{(i)}}{n_k^{(i)}} \right| \quad (5.29)$$

is greater than 10^{-4} . The chosen threshold is such that the semi-major axis changes by about 1% in a few Gyr if we assume a constant diffusion process as it would happen for a random walk. Indeed, δn measures the variation of frequency over 500 kyr. If the diffusion rate remains constant, a variation on the order of 1% on average needs a time 10,000 times larger, *i.e.*, 5 Gyr.

If the integration time is shorter due to a collision or ejection, we set δn to 1. Since we randomly draw most of the initial parameters, we bin the results into a two-dimensional grid in $(\alpha, \sqrt{\mathcal{C}})$ and average the frequency variation in each bin.

5.4.2 Results

We first integrate 100,000 initial conditions on a uniform grid with α taking values from 0.5 to 1 and \mathcal{C} from 0 to 0.1. The masses of the two planets are equal to $0.5 \times 10^{-5} M_{\odot}$, such that $\varepsilon = 10^{-5}$ and $\gamma = 1$. In this simulation, 78.4% of the orbits survive up to 500 kyr, 21.1% end up in a collision between the two planets, and 0.5% of the integrations are stopped because of the nonconservation of energy due to an unresolved close encounter.

The results of the frequency analysis are shown in Figure 5.4. We see that the chaotic region is well constrained by the Hill curve C_c^H . Indeed, very few orbits with $\mathcal{C} < C_c^H$ appear to be chaotic. The region where Hill stable orbits ($\mathcal{C} < C_c^H$) are chaotic seems restricted to the region where $C_c^{\text{MMR}} < \mathcal{C} < C_c^H$ around $\alpha \simeq 0.94$ and low \mathcal{C} , *i.e.*, for orbits experiencing MMR overlap (a zoomed view of Fig. 5.4 is given in Fig. 5.5). The behavior of planets initially in this region was already discussed in (Deck *et al.*, 2013). Orbits that are Hill unstable ($\mathcal{C} > C_c^H$) appear to be largely chaotic up to some resonant islands situated at $\alpha \simeq 1$ (co-orbital resonance) and near the 3:2 and 4:3 resonances ($\alpha \simeq 0.76$ and 0.82). We also see that for larger separations ($\alpha \lesssim 0.6$), orbits are less chaotic. However it is probable that for longer integration times, these orbits would end up unstable.

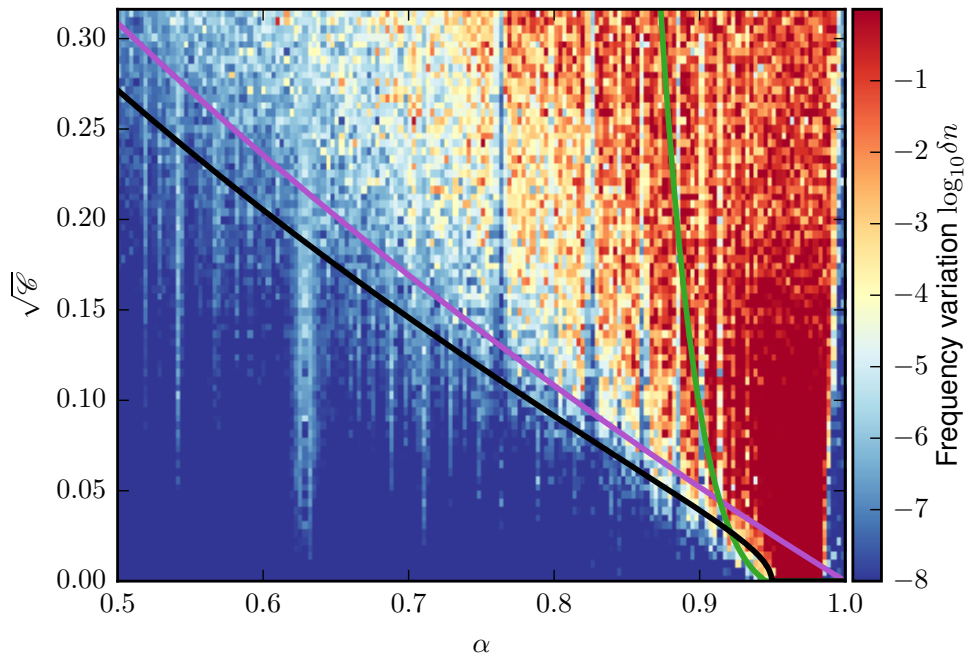


Figure 5.4 – Frequency variation δn (5.29) for 100,000 initial conditions binned in a 160×75 grid with $\varepsilon = 10^{-5}$ and $\gamma = 1$. The black curve is the Hill critical AMD C_c^H (5.28), the purple curve is the collisional critical AMD C_c (Laskar and Petit, 2017) and the green curve is the critical AMD obtained from the overlap of first order MMR C_c^{MMR} (Petit *et al.*, 2017). Each bin is average over about 8 initial conditions.

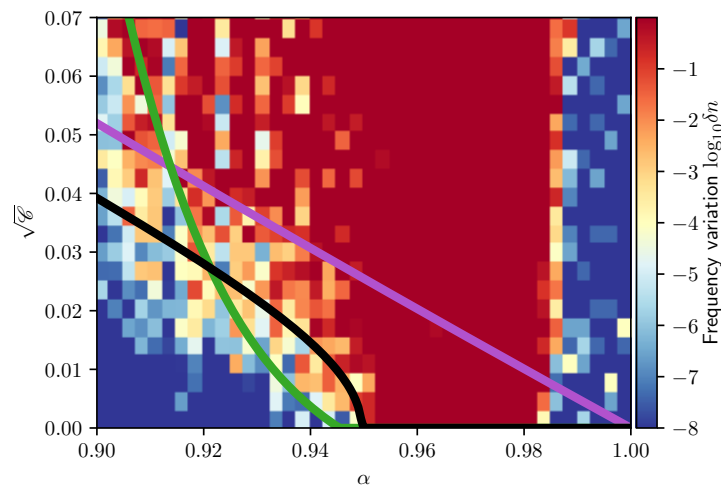


Figure 5.5 – Zoomed view of Figure 5.4 for $0.9 < \alpha < 1$ and $\sqrt{\mathcal{C}} < 0.07$. In the region where $C_c^{\text{MMR}} < \mathcal{C} < C_c^H$, we see that orbits are chaotic but Hill stable.

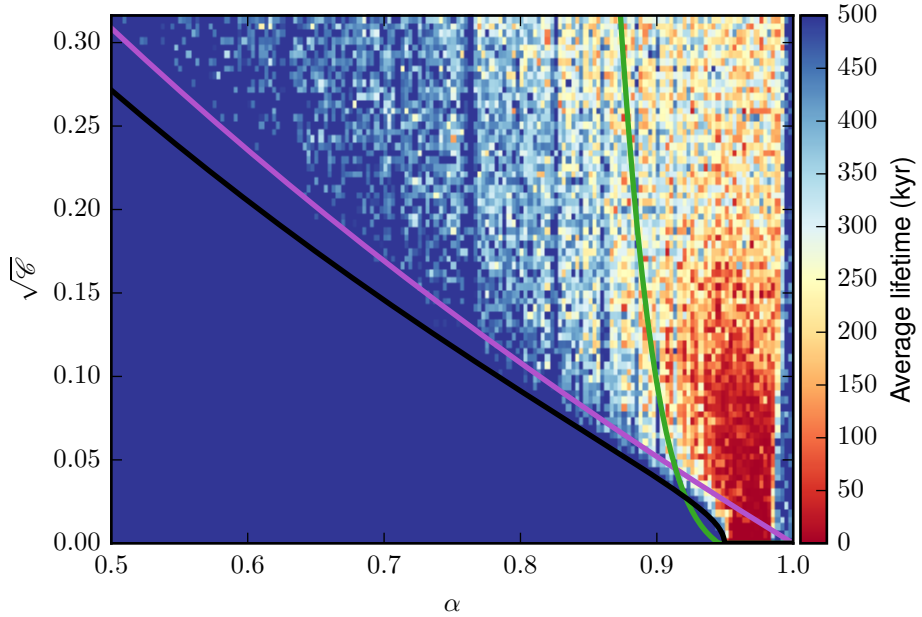


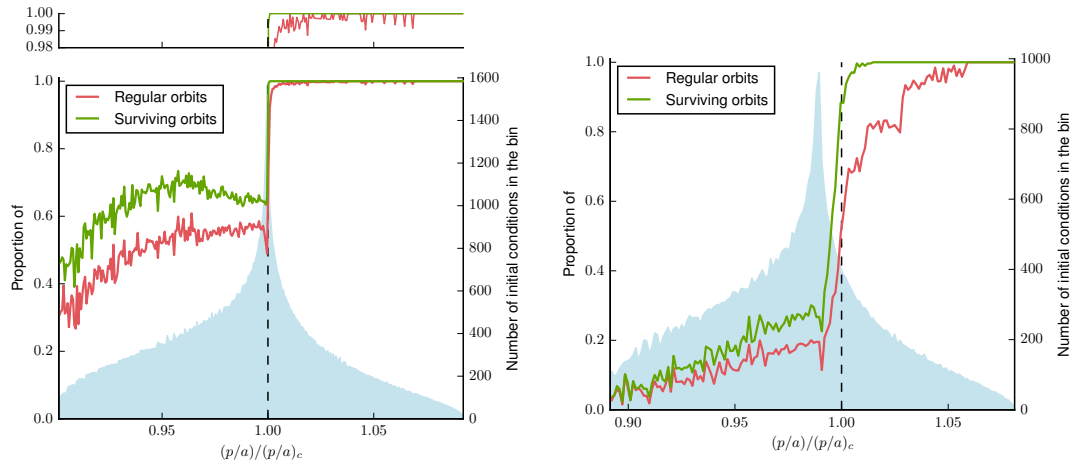
Figure 5.6 – Average lifetime of the system as a function of α and \mathcal{C} . The parameters are similar to figure 5.4. Each bin represents an average over 8 initial conditions. Dark blue implies that all integration ended at 500 kyr.

In order to highlight how the Hill criterion separates the chaotic orbits from the stable orbits, we can plot the fraction of regular orbits as a function of $(p/a)/(p/a)_c$ as suggested in Barnes and Greenberg (2006). We see in Figure 5.7a that there is a sharp limit at $p/a = (p/a)_c$. All Hill stable integrations go to 500 kyr and very few are chaotic. For Hill unstable orbits ($\mathcal{C} > C_c^H$), we see a slight increase of regular and surviving orbits with p/a but the decrease is not as significant as the change at the Hill limit. On average 64.9% of the Hill unstable orbits survive and 52.3% are regular.

We plot in Figure 5.6 the average time of the integrations as a function of initial α and \mathcal{C} . The initial conditions are binned in a 160×75 grid. We see in this figure that the average lifetime of a system is almost always smaller than 500 kyr in the Hill unstable region. We also remark that the average lifetime is less than 50 kyr for a system with $\alpha \gtrsim 0.9$ and not too large \mathcal{C} but increases for wider separations or greater AMD. Indeed for higher \mathcal{C} , the planets are on average initially further away from crossing orbits because the initial choice of eccentricities and inclinations is random.

5.4.3 Influence of the masses

To highlight the role of the mass of the planets, we ran another simulation with the same method but with $\varepsilon = 10^{-3}$ and $\gamma = 1$. We integrate 40,000 initial conditions and carry out a similar analysis. After 500 kyr, 54.6% of the systems lead to a



(a) Histogram for the initial conditions where $\varepsilon = 10^{-5}$. Above the main figure, we added a zoomed view of the upper part of the plot. The histogram has 300 bins.

(b) Histogram for the initial conditions where $\varepsilon = 10^{-3}$. The histogram has 150 bins.

Figure 5.7 – Proportion of orbits that survived for 500 kyr (green curve) and non-chaotic orbits ($\delta n < 10^{-4}$, red curve) as a function of $(p/a)/(p/a)_c$. $(p/a)/(p/a)_c > 1$ means that the initial condition verifies the Hill criterion. The light blue histogram represents the number of initial conditions in each of the bins used to compute the fractions plotted.

collision² between the two planets, 2% to an ejection, and 0.5% are stopped due to non-conservation of energy. If we consider only the Hill unstable systems ($\mathcal{C} > C_c^H$), only 24.0% have survived and 15.7% are regular. As expected, larger masses lead to much more unstable systems.

The results of the frequency analysis are plotted in Figure 5.8. We observe that the 3:2 MMR situated around $\alpha = 0.76$ is still very stable in comparison to the surrounding regions. The 2:1 MMR (around $\alpha = 0.63$) appears to create an area of moderate chaos in the Hill stable region but is not as marked in the Hill unstable part. The co-orbital resonance also appears more unstable.

We see in Figure 5.9 that some of the Hill stable systems do not survive for 500 kyr. These systems have led to an ejection of the outer planet. As a result, the Hill stability line appears to be more porous in comparison to the case $\varepsilon = 10^{-5}$.

We also see that a larger percentage of Hill stable orbits appear to be chaotic. This can be quantified thanks to the Figure 5.7b. We see that the proportion of regular orbits drops before it reaches the Hill stability limit. However, the more important change of behavior is still at the Hill stability limit.

²We consider the planet enter in collision if they approach by less than 0.25 of their mutual Hill radius.

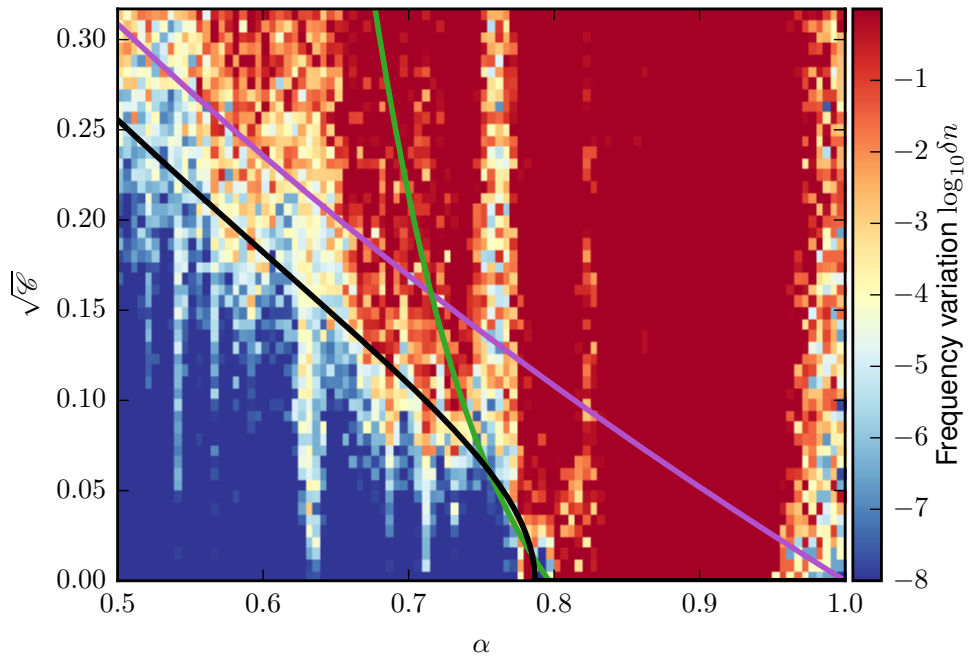


Figure 5.8 – Frequency variation δn (5.29) for 40,000 initial conditions binned in a 100×50 grid with $\varepsilon = 10^{-3}$ and $\gamma = 1$. The three curves are similar to figure 5.4.

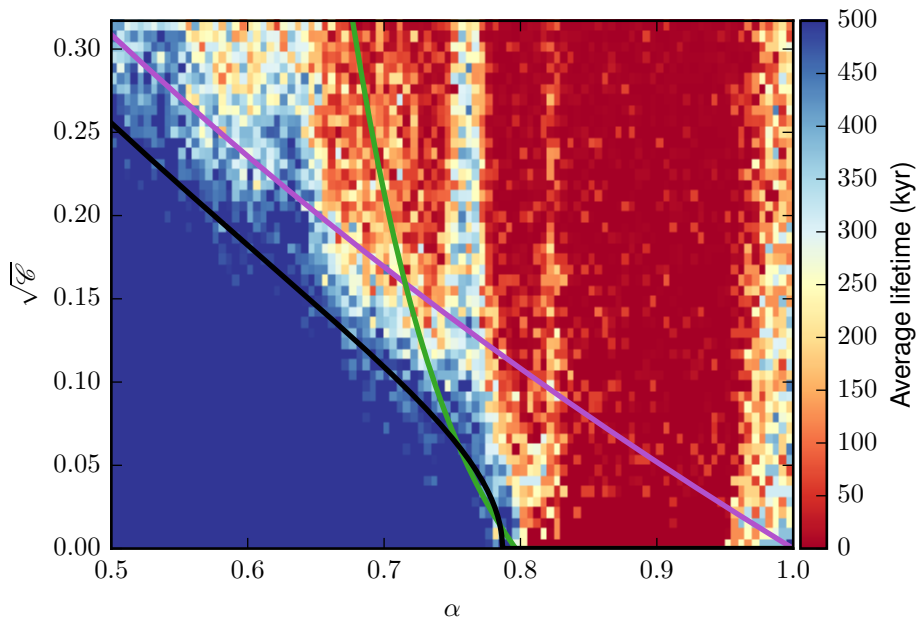


Figure 5.9 – Average lifetime of the system as a function of α and \mathcal{C} . The parameters are similar to figure 5.8. We see that some Hill stable initial conditions stopped before 500 kyr owing to ejections.

5.5 Conclusions

In a two-planet system, Hill stability is a topological limit that forbids close encounters between the outer planet and the inner planet or the star. If verified, the system remains stable if the outer planet does not escape or if the inner planet does not collide with the star. Moreover, since a minimal distance between planets is imposed, the planet perturbation remains moderate and the system is most likely regular.

We have generalized Gladman's Hill stability criterion and have shown that it is natural to express the Hill criterion in the AMD framework. Indeed, we obtained a simple expression for this criterion (proposition 3) with only an expansion in ε (eq. 5.1). Moreover, it is easy to recover all former published criteria as particular cases of this expression. Because of its formulation as a function of the AMD, the expression (5.24) is valid in the general spatial case for any value of eccentricities and inclinations. Moreover, our Hill criterion is accurate even for very different planet masses. We also highlight that the AMD and the semi-major axis ratio α are the main parameters to consider in a stability study.

We show that the Hill stability allows us to give an accurate stability limit up to large orbital separations. The sharp change of behavior at the Hill stability limit has already been studied in Barnes and Greenberg (2006) or in Deck *et al.* (2013). Nevertheless, our numerical integrations confirm it for a much larger range of α and AMD with randomized initial conditions for the parameters not taken into account.

Our simulations for large planet masses also show that the expansion in ε is valid even for larger planets and that the Hill stability accurately segregates between regular and short-lived initial conditions. However, it appears that for large mass values, ejections cannot be neglected and a model should be developed to understand this further behavior.

As shown in several works (Chambers *et al.*, 1996; Pu and Wu, 2015), Gladman's Hill criterion is no longer adapted in the cases of tightly packed systems. Such a sharp limit between almost eternal and short-lived systems no longer exists. Instead, it appears that there exists a scaling between the initial orbital separation and the time of instability, wider separated orbits becoming unstable after a longer time. In the cited works, the empirical stability criteria give stability spacing as a function of the mutual radius

$$a_{n+1} - a_n > KR_H, \quad (5.30)$$

where $R_H = a_{n+1}(\varepsilon/3)^{1/3}$ is the Hill radius. In the context of multiplanetary systems, an analytical work on long-term stability is still necessary.

Chapter 6

High order regularized symplectic integrator for collisional planetary systems

The content of this chapter is submitted to Astronomy and Astrophysics.

During this thesis, it appeared necessary to study in detail the dynamics of planetary systems that end up highly unstable. In particular, such studies are necessary to understand how the AMD evolves due to non secular perturbations. Numerical simulations have the advantage over analytical works that they help to get an intuition on the evolution of particular systems. As a result the numerical and analytical approaches are complementary and simulations can help elaborate an analytical model. The following work is motivated by the research of a high precision symplectic integrator able to integrate systems experiencing close encounters.

6.1 Introduction

Precise, long-term integration of planetary systems is still a challenge today. Indeed, the numerical simulations must resolve the motion of the planets along their orbits, however the lifetime of a system is typically of billions of years resulting in computationally expensive simulations. Besides, due to the chaotic nature of planetary dynamics, statistical studies are often necessary, which require to run multiple simulations with close initial conditions (Laskar and Gastineau, 2009). This remark is particularly true for unstable systems that can experience strong planet scattering due to close encounters.

There is therefore considerable interest in developing fast and accurate numerical integrators and numerous integrators have been developed over the years to fulfill this task. For long-term integrations, the most commonly used are symplectic integrators. Symplectic schemes incorporate the symmetries of Hamiltonian systems

and as a result, usually conserve the energy and angular momentum better than non-symplectic integrators. In particular, the angular momentum is usually conserved up to roundoff error in symplectic integrators.

Independently, Kinoshita *et al.* (1991) and Wisdom and Holman (1991) developed a class of integrators often called in the literature Mixed Variables Symplectic (MVS) integrators. This method takes advantage in the hierarchy between the Keplerian motion of the planets around the central star and the perturbations induced by planets interactions. It is thus possible to make accurate integrations using relatively large time-steps. The initial implementation of Wisdom and Holman (1991) is a low order integration scheme, that still necessitates small time-steps to reach machine precision. Improvements to the method has since been implemented.

The first category is symplectic correctors (Wisdom *et al.*, 1996; Wisdom, 2006), they consist in a modification of the initial conditions to improve the scheme accuracy. Since it is only necessary to apply them when an output is desired, they do not affect the performance of the integrator. This approach is for example used in WHFAST (Rein and Tamayo, 2015). The other approach is to consider higher order schemes (McLachlan, 1995b; Laskar and Robutel, 2001; Blanes *et al.*, 2013). High order schemes permit a very good control of the numerical error by fully taking advantage of the hierarchical structure of the problem. It has been used with success to carry high precision long-term integrations of the Solar System (Farrés *et al.*, 2013). The principal limitation of symplectic integrators is that they require the use of a fixed time-step (Gladman *et al.*, 1991). If the time-step is modified between each step, the integrator remains symplectic since each step is symplectic. However, the change of time-step introduces a possible secular energy drift that may reduce the interest of the method. As a consequence, classical symplectic integrators are not very adapted to treat the case of systems experiencing occasional close encounters where very small time-step is needed.

To resolve close encounters, Duncan *et al.* (1998) and Chambers (1999) provide solutions in the form of hybrid symplectic integrators. Duncan *et al.* (1998) developed a multiple time-step symplectic integrator, SYMBA, where the smallest time-steps are only used whenever a close encounter occurs. The method is however limited to an order two scheme. The hybrid integrator MERCURY (Chambers, 1999) moves terms from the perturbation step to the Keplerian step whenever an interaction between planets becomes too large. The Keplerian step is no longer integrable but can be solved at numerical precision using a non symplectic scheme such as Burlisch-Stoer or Gauss-Radau. However, the switch of numerical method leads to a linear energy drift (Rein and Tamayo, 2015).

Another way to build a symplectic integrator that correctly regularises close encounters is time renormalization. Indeed, up to an extension of the phase space and a modification of the Hamiltonian, it is always possible to modify the time that appears in the equations of motion. As a result, the real time becomes a variable to integrate. Providing some constraints on the renormalization function, it is possible to integrate the motion with a fixed fictitious time-step using an arbitrary splitting scheme. Here we show that with adapted time renormalization, it is possible to resolve accurately close encounters. While time renormalization has not been applied in the context of planet close encounter, it has been successful in the case of

perturbed highly eccentric problems (Mikkola, 1997; Mikkola and Tanikawa, 1999; Preto and Tremaine, 1999; Blanes and Iserles, 2012), see (Mikkola, 2008) for a general review. In the present work, we adapt a time renormalization proposed independently by Mikkola and Tanikawa (1999) and Preto and Tremaine (1999). We show that it is possible to use the perturbation energy to monitor close encounters in the context of systems of few planets with comparable masses. We are able to define a MVS splitting that can be integrated with any high order scheme.

We start in section 6.2 to briefly recall the basics of the symplectic integrator formalism. In section 6.3, we present the time renormalization that regularises close encounters and then discuss the consequence of the renormalization on the hierarchical structure of the equations (section 6.4). In section 6.5 we numerically demonstrate over short term integrations the behaviour of the integrator at close encounter. We then explain (section 6.6) how our time regularization can be combined with the perihelion regularization proposed by (Mikkola, 1997). Finally we show the results of long-term integration of six planet systems in a context of strong planet scattering (section 6.7) and compare our method to the modern implementation of **MERCURY** (Rein *et al.*, 2019) and to the non symplectic high order integrator **IAS15** (section 6.8).

6.2 Splitting symplectic integrators

We consider a Hamiltonian $H(\mathbf{p}, \mathbf{q})$ that can be written as a sum of two integrable Hamiltonians

$$H(\mathbf{p}, \mathbf{q}) = H_0(\mathbf{p}, \mathbf{q}) + H_1(\mathbf{p}, \mathbf{q}). \quad (6.1)$$

A classical example is given by $H_0 = T(\mathbf{p})$ and $H_1 = U(\mathbf{q})$ where $T(\mathbf{p})$ is the kinetic energy and $U(\mathbf{q})$ the potential energy. In planetary dynamics, we can split the system as $H_0 = K(\mathbf{p}, \mathbf{q})$ where K is the sum of the Kepler problems in Jacobi coordinates (*e.g.* Laskar, 1990a) and $H_1 = H_{\text{inter}}(\mathbf{q})$ is the interaction between the planets.

Using the Lie formalism (*e.g.* Koseleff, 1993; Laskar and Robutel, 2001), the equation of motion can be written

$$\frac{dz}{dt} = \{H, z\} = L_H z, \quad (6.2)$$

where $z = (\mathbf{p}, \mathbf{q})$, $\{\cdot, \cdot\}$ is the Poisson bracket¹ and we note $L_f = \{f, \cdot\}$, the Lie differential operator. The formal solution of (6.2) at time $t = \tau + t_0$ from the initial condition $z(t_0)$ is

$$z(\tau + t_0) = \exp(\tau L_H) z(t_0) = \sum_{k=0}^{+\infty} \frac{\tau^k}{k!} L_H^k z(t_0). \quad (6.3)$$

In general the operators L_{H_0} and L_{H_1} do not commute so

$$\exp(\tau L_H) \neq \exp(\tau L_{H_0}) \exp(\tau L_{H_1}). \quad (6.4)$$

¹ We use the convention $\{f, g\} = \sum_i \frac{\partial f}{\partial p_i} \frac{\partial g}{\partial q_i} - \frac{\partial f}{\partial q_i} \frac{\partial g}{\partial p_i}$.

However, using Baker-Campbell-Hausdorff(BCH) formula, we can find coefficients a_i and b_i such that

$$\exp(\tau(L_H + L_{H_{\text{err}}})) = \mathcal{S}(\tau) = \prod_{i=1}^N \exp(a_i \tau L_{H_0}) \exp(b_i \tau L_{H_1}), \quad (6.5)$$

where $H_{\text{err}} = O(\tau^r)$ is an error Hamiltonian depending on H_0 , H_1 , τ and the coefficients a_i and b_i .

Since H_0 and H_1 are integrable, we can explicitly compute the evolution of the coordinates z under the action of the maps $\exp(\tau L_{H_0})$ and $\exp(\tau L_{H_1})$. The map $\mathcal{S}(\tau)$ is symplectic because it is a composition of symplectic maps. Moreover, $\mathcal{S}(\tau)$ integrates exactly the Hamiltonian $H + H_{\text{err}}$.

If there is a hierarchy in the Hamiltonian H in the sense that $|H_1/H_0| \simeq \varepsilon \ll 1$, one can choose the coefficients such that the error Hamiltonian is of order

$$\sum_{i=1}^n O(\tau^{r_i} \varepsilon^i), \quad (6.6)$$

(see McLachlan, 1995b; Laskar and Robutel, 2001; Blanes *et al.*, 2013; Farrés *et al.*, 2013). For small ε and τ , the solution of $H + H_{\text{err}}$ is very close to the solution of H . In particular, it is thought that the energy error of a symplectic scheme is bounded. Since H_{err} depends on τ , a composition of steps $\mathcal{S}(\tau)$ also has this property if the time-step is kept constant. Otherwise, the exact integrated dynamics changes at each step, leading to secular drift of the energy error.

In planetary dynamics, we can split the Hamiltonian such that H_0 is the sum of the Keplerian motions in Jacobi coordinates and H_1 is the interaction Hamiltonian between planets that only depends on positions and thus is integrable (*e.g.* Laskar, 1990a). This splitting naturally introduces a scale separation ε given by

$$\varepsilon = \frac{\sum_{k=1}^N m_k}{m_0} \quad (6.7)$$

where N is the number of planets, m_k the mass of the k -th planet and m_0 the mass of the star. If the planets remain far from each other, H_1 is always ε small with respect to H_0 .

The perturbation term is of order ε/Δ where Δ is the typical distance between the planets in unit of a typical length of the system. During close encounters, Δ can become very small, and the step size needs to be adapted to $\varepsilon/\Delta_{\min}$. Here Δ_{\min} is the smallest expected separation between planets normalized by a typical length of the system.

6.3 The regularised Hamiltonian

In order to construct an adaptive symplectic scheme which regularises the collisions, we extend the phase space and integrate the system with a fictitious time. Let s be such that

$$dt = g(\mathbf{p}, p_t, \mathbf{q}) ds. \quad (6.8)$$

where g is a function to be determined and p_t is the conjugated momentum to the real time t in the extended phase space. In order to have an invertible function $t(s)$, we require g to be positive. We consider the new Hamiltonian Γ defined as

$$\Gamma(\mathbf{p}, p_t, \mathbf{q}, t) = g(\mathbf{p}, p_t, \mathbf{q}) (H(\mathbf{p}, \mathbf{q}) + p_t). \quad (6.9)$$

Γ does not depend on t therefore p_t is a constant of motion. The equation of motion of this Hamiltonian are

$$\frac{dt}{ds} = \{\Gamma, t\} = g(\mathbf{p}, p_t, \mathbf{q}) + \frac{\partial g}{\partial p_t}(\mathbf{p}, p_t, \mathbf{q}) (H(\mathbf{p}, \mathbf{q}) + p_t) \quad (6.10)$$

and for all function $f(z)$

$$\frac{df(z)}{ds} = \{\Gamma, f(z)\} = g(\mathbf{p}, p_t, \mathbf{q}) \{H, f\} + (H + p_t) \{g, f(z)\}. \quad (6.11)$$

In general H is not a constant of motion of Γ . We have

$$\frac{dH}{ds} = \{\Gamma, H\} = (H + p_t) \{g, H\}. \quad (6.12)$$

If we choose initial conditions z_0 such that $p_t = -H(z_0)$ we have $\Gamma|_{t=0} = 0$. Since Γ is constant and g is positive, we deduce from equation (6.3) that we have at all times

$$H + p_t = 0. \quad (6.13)$$

Since p_t is also a constant of motion, H is constant for all times. We can simplify the equations of motion (6.10) and (6.11) into

$$\begin{aligned} \frac{dt}{ds} &= g(\mathbf{p}, p_t, \mathbf{q}) \\ \frac{df}{ds}(z) &= g(\mathbf{p}, p_t, \mathbf{q}) \{H, f(z)\}. \end{aligned} \quad (6.14)$$

On the manifold $p_t = -H(t_0)$, the equations (6.14) describe the same motion as equation (6.2). We will call them the regularised equations.

We want now to write Γ as a sum of two integrable Hamiltonians such as in section 6.2. Based on previous works (Preto and Tremaine, 1999; Mikkola and Tanikawa, 1999; Blanes and Iserles, 2012), we write

$$H + p_t = (H_0 + p_t) - (-H_1), \quad (6.15)$$

for $H = H_0 + H_1$ and we define g as

$$g(\mathbf{p}, p_t, \mathbf{q}) = \frac{f(H_0 + p_t) - f(-H_1)}{H_0 + p_t + H_1}, \quad (6.16)$$

where f is a smooth function to be determined. g is the difference quotient of f and is well defined when $H_0 + p_t + H_1 \rightarrow 0$. We have

$$g(\mathbf{p}, p_t, \mathbf{q})|_{H+p_t=0} = f'(H_0 + p_t) = f'(-H_1). \quad (6.17)$$

With this choice of g , the Hamiltonian Γ becomes

$$\Gamma = f(H_0 + p_t) - f(-H_1) = \Gamma_0 + \Gamma_1, \quad (6.18)$$

where we note $\Gamma_0 = f(H_0 + p_t)$ and $\Gamma_1 = -f(-H_1)$. We remark that Γ_0 (resp. Γ_1) is integrable because it is a function of $H_0 + p_t$ (resp. H_1) which is integrable. Moreover, we have

$$\begin{aligned} L_{\Gamma_0} &= f'(H_0 + p_t)L_{H_0+p_t}, \\ L_{\Gamma_1} &= f'(-H_1)L_{H_1}. \end{aligned} \quad (6.19)$$

Since $H_0 + p_t$ (resp. H_1) is a first integral of Γ_0 (resp. Γ_1), we have

$$\begin{aligned} \exp(\sigma L_{\Gamma_0}) &= \exp(\sigma f'(H_0 + p_t)L_{H_0+p_t}) = \exp(\tau_0 L_{H_0+p_t}), \\ \exp(\sigma L_{\Gamma_1}) &= \exp(\sigma f'(-H_1)L_{H_1}) = \exp(\tau_1 L_{H_1}), \end{aligned} \quad (6.20)$$

where

$$\tau_0 = \sigma f'(H_0 + p_t) \text{ and } \tau_1 = \sigma f'(-H_1). \quad (6.21)$$

The operator $\exp(\sigma L_{\Gamma_0})$ (resp. $\exp(\sigma L_{\Gamma_1})$) is equivalent to the regular operator $\exp(\tau_0 L_{H_0+p_t})$ (resp. $\exp(\tau_1 L_{H_1})$) with a modified time-step. One can approximate the operator $\exp(\sigma L_{\Gamma})$ by a composition of operators $\exp(\sigma L_{\Gamma_k})$

$$\mathcal{S}_{\Gamma}(\sigma) = \prod_{i=1}^N \exp(a_i \sigma L_{\Gamma_0}) \exp(b_i \sigma L_{\Gamma_1}). \quad (6.22)$$

Using BCH formula $\mathcal{S}_{\Gamma}(\sigma) = \exp(\sigma(L_{\Gamma} + L_{\Gamma_{\text{err}}}))$ where Γ_{err} is an error Hamiltonian that depends on σ . The symplectic map $\mathcal{S}_{\Gamma}(\sigma)$ integrates exactly the modified Hamiltonian $\Gamma + \Gamma_{\text{err}}$. The iteration of $\mathcal{S}_{\Gamma}(\sigma)$ with fixed σ is a symplectic integrator algorithm for Γ .

If the time scale σ is small enough, H_0 and H_1 do not change significantly between each step of the composition. We have $\mathcal{S}_{\Gamma}(\sigma) \simeq \mathcal{S}(\tau)$ with $\tau \simeq \sigma f'(-H_1)$. In other words, \mathcal{S}_{Γ} behaves as \mathcal{S} with an adaptive time-step while keeping the bounded energy properties of a fixed time-step integrator.

6.3.1 Choice of the regularization function

We want the step sizes (6.21) to become smaller when planets experience close encounters. These time-steps are determined by the derivative of f . For nearly Keplerian systems, Mikkola and Tanikawa (1999) and Preto and Tremaine (1999) studied renormalization functions such that $f'(x) \propto x^{-\gamma}$, where $\gamma > 0$ (it corresponds to power law functions and the important case of $f = \ln$).

However, these authors consider splitting of the type $H_0 = T(\mathbf{p})$ and $H_1 = U(\mathbf{q})$. As pointed out in (Blanes and Iserles, 2012), when splitting the Hamiltonian as the Keplerian part plus an integrable perturbation, it appears that both terms $K(\mathbf{p}, \mathbf{q}) + p_t$ and $-H_1$ can change signs, resulting in large errors in the integration.

We remark that the use of $f = \ln$ is giving the best result when two planets are experiencing a close encounter, but it leads to large energy errors far away for collision when H_1 is nearly 0. Based on these considerations, we will require f to verify several properties to successfully regularise the perturbed Keplerian problem in presence of close encounters:

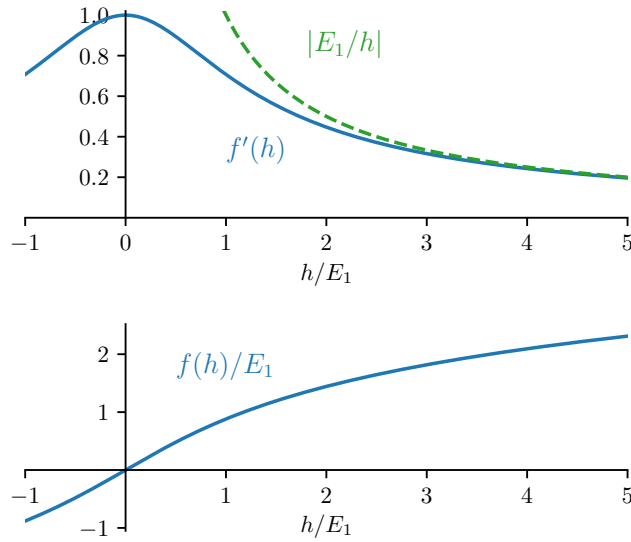


Figure 6.1 – Upper panel: f' , eq. (6.23) as a function of h/E_1 . The asymptotic value for $h/E_1 \rightarrow +\infty$ is given in green. Lower panel: f/E_1 , eq. (6.24) as a function of h/E_1 .

- f' should only depend on the magnitude of the perturbation H_1 , so we require f' even (and f odd).
- As already pointed out, t must be an increasing function of s therefore $f' > 0$.
- f' should be smooth, so we exclude piece wise renormalization functions.
- We want the regularization to vanish in absence of perturbation *i.e.* $f'(0) = 1$. It results that for vanishing perturbation, $\sigma = \tau$.
- Let E_1 be a typical value of H_1 far from close encounters that we will determine an expression further. f' should only depend on H_1/E_1 in order to only track relative changes in the magnitude of the perturbation.
- For large values of the perturbation (*e.g.* during close encounters), we require $f'(H_1) \sim |E_1/H_1|$ such that we preserve the good properties pointed out by previous studies (Preto and Tremaine, 1999; Mikkola and Tanikawa, 1999).
- To reduce the computational cost of the integrator, f' has to be numerically inexpensive to evaluate.

These properties lead to a very natural choice for f' (see in figure 6.1). We choose

$$f'(h) = \frac{1}{\sqrt{1 + \left(\frac{h}{E_1}\right)^2}}. \quad (6.23)$$

Taking the odd primitive of (6.23) we end up with

$$f(h) = E_1 \operatorname{arcsinh} \left(\frac{h}{E_1} \right). \quad (6.24)$$

For now on, f will always refer to the definition (6.24). With this choice of function f , the Hamiltonian Γ takes the form

$$\Gamma = E_1 \operatorname{arcsinh} \left(\frac{H_0 + p_t}{E_1} \right) + E_1 \operatorname{arcsinh} \left(\frac{H_1}{E_1} \right), \quad (6.25)$$

where we used the oddity of f .

We need to define more explicitly E_1 . When planets are far from each other, their mutual distance are of the same order as the typical distance between the planets and the star. Using the same idea as in (Marchal and Bozis, 1982; Petit *et al.*, 2018), we define a typical length unit of the system based on the initial system energy E_0 . We have

$$a_{\text{typical}} = -\frac{\mathcal{G}M^*}{2E_0}, \quad (6.26)$$

where $M^* = \sum_{0 \leq i < j} m_i m_j$. The typical value for the perturbation Hamiltonian far away from collision can be defined as

$$E_1 = \frac{\mathcal{G}m^*}{a_{\text{typical}}} = \frac{2|E_0|m^*}{M^*}, \quad (6.27)$$

where $m^* = \sum_{1 \leq i < j} m_i m_j$. We note that we have $E_1/E_0 = O(\varepsilon)$.

The behaviour of higher order derivative of f is useful for the error analysis and in particular their dependence in ε . The k -th derivative of f has for expression

$$f^{(k)}(h) = E_1^{1-k} \operatorname{arcsinh}^{(k)} \left(\frac{h}{E_1} \right) = O(\varepsilon^{1-k}). \quad (6.28)$$

6.4 Order of the scheme

As explained in section 6.2, most of the planet dynamics simulations are made with a simple a second order scheme such as the Wisdom-Holman leapfrog integrator (Wisdom and Holman, 1991). Indeed it is possible to take advantage of the hierarchy between H_0 and H_1 . This can be done by the addition of symplectic correctors (Wisdom *et al.*, 1996; Rein and Tamayo, 2015) or by canceling term of the form $\varepsilon \tau^k$ up to a certain order (Laskar and Robutel, 2001). Hierarchical order schemes such as $\mathcal{SABA}(10, 6, 4)$ (Blanes *et al.*, 2013; Farrés *et al.*, 2013) behaves effectively as a tenth order integrator if ε is small enough. Canceling only selected terms reduces the number of necessary steps of the scheme which reduce the numerical error and improve the performances.

Unfortunately, this property cannot be used for the regularised Hamiltonian since Γ_0 and Γ_1 are almost equal in magnitude. Nevertheless, it should be noted that the equations of motion (6.14) and the Lie derivatives (6.19) keep their hierarchical structure. The Poisson bracket of Γ_0 and Γ_1 gives

$$\{\Gamma_0, \Gamma_1\} = f'(H_0 + p_t) f'(H_1) \{H_0, H_1\}. \quad (6.29)$$

Since f' does not depend directly on ε (by choice, f' only tracks relative variations of H_1), $\{\Gamma_0, \Gamma_1\}$ is of order ε . However, for higher order terms in σ in H_{err} , it is

not possible to exploit the hierarchical structure in ε . Indeed, let us consider the terms of order σ^2 in the error Hamiltonian for the integration of Γ using the leapfrog scheme. We have (*e.g.* Laskar and Robutel, 2001)

$$\Gamma_{\text{err}} = \frac{\sigma^2}{12} \{ \{ \Gamma_0, \Gamma_1 \}, \Gamma_0 \} + \frac{\sigma^2}{24} \{ \{ \Gamma_0, \Gamma_1 \}, \Gamma_1 \} + O(\sigma^4). \quad (6.30)$$

In order to see the dependence in ε , we develop the Poisson brackets in (6.30)

$$\begin{aligned} \Gamma_{\text{err}} = & \frac{\sigma^2}{12} f'(H_0 + p_t)^2 f'(H_1) \{ \{ H_0, H_1 \}, H_0 \} \\ & - \frac{\sigma^2}{12} f'(H_0 + p_t)^2 f''(H_1) (\{ H_0, H_1 \})^2 \\ & + \frac{\sigma^2}{24} f'(H_1)^2 f'(H_0 + p_t) \{ \{ H_0, H_1 \}, H_1 \} \\ & + \frac{\sigma^2}{24} f'(H_1)^2 f''(H_0 + p_t) (\{ H_0, H_1 \})^2 + O(\sigma^4). \end{aligned} \quad (6.31)$$

The first and third terms only depend on f' and nested Poisson brackets of H_0 and H_1 . Their dependency on ε is thus determined by the Poisson brackets as in the fixed time-step case (McLachlan, 1995a). The first term is of order $\varepsilon\sigma^2$ and the third of order $\varepsilon^2\sigma^2$. On the other hand, the second and last terms introduce the second derivative of f as well as a product of Poisson bracket of H_0 and H_1 . From (6.28), it results that they are of order $\varepsilon\sigma^2$. In order to cancel every terms of order $\varepsilon\sigma^2$, it is necessary to cancel both terms in σ^2 in (6.30). Thus, the strategy used in (Blanes *et al.*, 2013) does not provide a scheme with a hierarchical order since every Poisson bracket contributes with terms of order ε to the error Hamiltonian.

It is easy to extend the previous result to all orders in σ . Indeed, let us consider a generic error term of the form

$$\Gamma_{\text{gen}} = \sigma^{n-1} \{ \{ \Gamma_{k_0}, \Gamma_{k_1} \}, \dots, \Gamma_{k_n} \}, \quad (6.32)$$

where k_j is either 0 or 1 and $k_0 = 0$ and $k_1 = 1$. The development of Γ_{gen} into Poisson brackets of H_0 and H_1 contains a term that has for expression

$$\sigma^{n-1} f^{(n_0)}(H_0 + p_t) f^{(n_1)}(H_0 + p_t) f_1'^{n_0} f_0'^{n_1} (\{ H_0, H_1 \})^{n-1}, \quad (6.33)$$

where n_j is the number of Γ_j in Γ_{gen} , and $f_1' = f'(H_1)$. Since $n = n_0 + n_1$, we deduce from (6.28) that the term (6.33) is of order $\varepsilon\sigma^{n-1}$. Thus, the effective order of the Hamiltonian will always be $\varepsilon\sigma^{r_{\min}}$ where r_{\min} is the smallest exponent r_k in (6.6). Note that the error is still linear in ε . Hence, it is still worth using the Keplerian splitting.

We use schemes that are not dependent on the hierarchy between H_0 and H_1 . McLachlan (1995a) provides an exhaustive list of the optimal methods for 4-th, 6-th and 8-th order integrators. Among the schemes he presents, we select a 6-th order method consisting of a composition of $n = 7$ leapfrog steps introduced by Yoshida (1990) and an 8-th order method that is a combination of $n = 15$ leapfrog steps. The coefficients of the schemes are given in Appendix E.2.

In order to solve the Kepler step, we adopt the same approach as (Mikkola, 1997; Rein and Tamayo, 2015). The details on this particular solution as well as other technical details are given in appendix E.1.

6.4.1 Non integrable perturbation Hamiltonian

When using the classical splitting of the Hamiltonian written in canonical heliocentric coordinates, H_1 depends on both positions and momenta. We can write H_1 as a sum of two integrable Hamiltonian $H_1 = T_1 + U_1$, where T_1 is the indirect part only depending on the momenta and U_1 is the planet interaction potential, only depending on positions (Farrés *et al.*, 2013). We thus approximate the evolution operator (6.20) by

$$\exp(\sigma L_{\Gamma_1}) = \exp\left(\frac{\tau_1}{2} L_{T_1}\right) \exp(\tau_1 L_{U_1}) \exp\left(\frac{\tau_1}{2} L_{T_1}\right) + O(\varepsilon^3 \tau_1^3), \quad (6.34)$$

The numerical results suggests that heliocentric coordinates give slightly more accurate results at constant cost. It is possible to define a variant of the heliocentric coordinates often called democratic heliocentric coordinates (Laskar, 1990a; Duncan *et al.*, 1998). In this set of coordinates, the kinetic and the potential part of the perturbation Hamiltonian commutes. Therefore, the step $\exp(\sigma L_{\Gamma_1})$ is directly integrable using the effective step size τ_1 (6.21). In the following numerical tests, when we refer to heliocentric coordinates, we always use the classical definition.

6.5 Error analysis near the close encounter

6.5.1 Time step and scheme comparison

In this section, we test how a single close encounter affects the energy conservation. To do so, we compare different integration schemes for a two-planet system, initially on circular orbits, during an initial synodic period

$$T_{\text{syn}} = \frac{2\pi}{n_1 - n_2} = \frac{2\pi}{n_2(\alpha^{-3/2} - 1)} \quad (6.35)$$

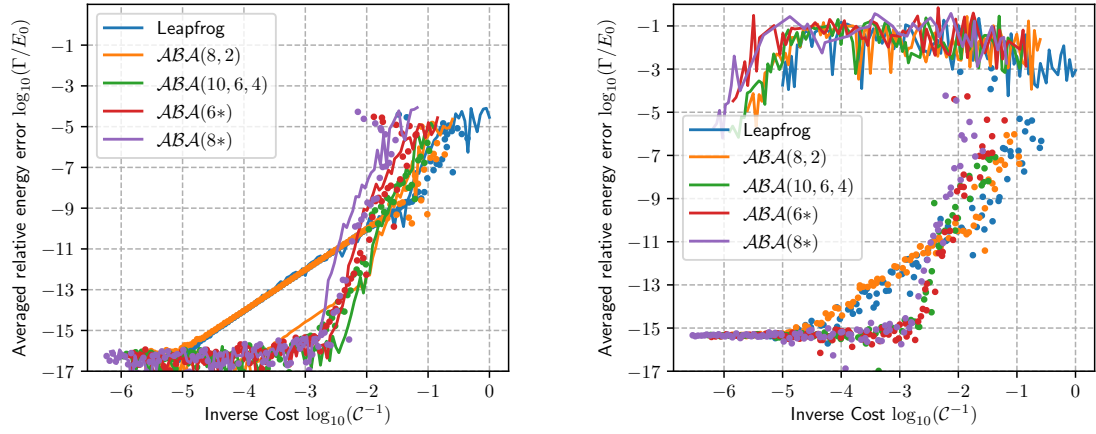
where n_i is the mean motion of planet i and α is the ratio of semi-major axis.

Since the time-step is renormalized, we need to introduce a cost function that depends on the fictitious time s as well as the number of stages involved in the scheme of the integrator. We define the cost of an integrator as the number of evaluations of $\exp(a\sigma L_{\Gamma_0}) \exp(b\sigma L_{\Gamma_1})$ that are required to integrate for a given real time period T_{syn}

$$\mathcal{C} = \frac{s_{\text{syn}} n}{T_{\text{syn}} \sigma} \quad (6.36)$$

where s_{syn} is the fictitious time after T_{syn} , σ the fixed fictitious time-step and n the number of stages of the integrator. We also compare the renormalized integrators to the same scheme with fixed time-step. For fixed time-step, the cost function is simply given by $\mathcal{C}_{\text{fixed}} = n/\tau$, where τ is the time-step (Farrés *et al.*, 2013). We present different configurations on figures 6.2a, 6.2b and 6.3.

In the two first sets, we integrate the motion of two equal masses planets on circular orbits, starting in opposition with respect to the star. In both simulations, we have $\varepsilon = (m_1 + m_2)/m_0 = 10^{-5}$, the stellar mass is $1 M_\odot$ and the outer planet



(a) System with initial semi-major axis ratio of $\alpha = 0.8$. The closest planet approach is 0.19992 AU.

(b) System with initial semi-major axis ratio of $\alpha = 0.97$. The closest planet approach is 3.68×10^{-5} AU.

Figure 6.2 – Comparison between various schemes detailed in the body of the text for the integration of a single synodic period for a system of equal mass planets initially on planar circular orbits with $\varepsilon = 2m/m_0 = 10^{-5}$. The solid lines represent the integrations using fixed real time-step and the dots the adaptive time-steps.

semi-major axis is 1 AU. In both figures, we represent the averaged relative energy variation

$$\frac{\Gamma}{E_0} \simeq f'(H_1) \frac{\Delta E}{E_0} \quad (6.37)$$

as a function of the inverse cost C^{-1} of the integration for various schemes:

- the classical order 2 leapfrog $\mathcal{ABA}(2, 2)$,
- the scheme $\mathcal{ABA}(8, 2)$ from (Laskar and Robutel, 2001),
- the scheme $\mathcal{ABA}(10, 6, 4)$ from (Blanes *et al.*, 2013)
- the 6-th and 8-th order schemes from (McLachlan, 1995a) already introduced in the previous section.

For each, scheme, we plot with a solid line the result of the fixed time-step algorithm and with dots, the results of the adaptive time-step integrator. In the results presented in figure 6.2a and 6.2b, the system are integrated in Jacobi coordinates. In figure 6.3 we integrate in heliocentric coordinates. For the three cases, the integrations were also carried out with the other set of coordinates with almost no differences.

In Figure 6.2a, the initial semi-major axis ratio α is 0.8 and the two planets minimal approach is 0.19992 AU. In this case, a fixed time-step algorithm provide accurate results and when using a generalized order scheme such as $\mathcal{ABA}(8, 2)$ or $\mathcal{ABA}(10, 6, 4)$, the performances are better with a fixed time-step than with an adaptive one. However, we see no sensitive differences in accuracy between the fixed

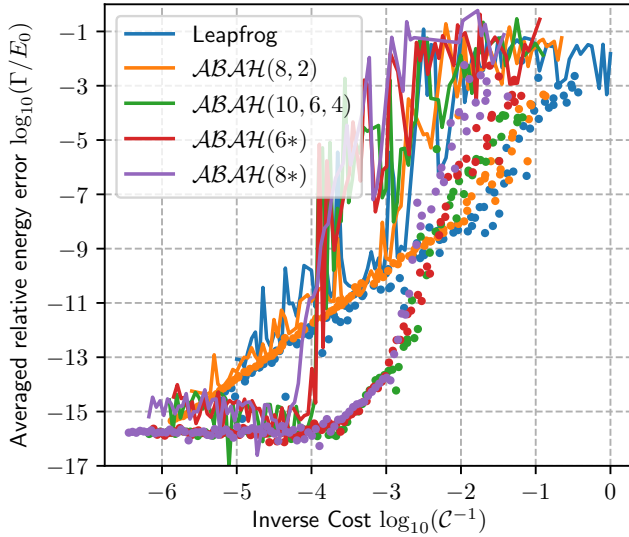


Figure 6.3 – Same as figure 6.2 for a system of two equal masses planet initially on planar circular orbits with $\varepsilon = 2m/m_0 = 10^{-3}$ and $\alpha = 0.9$. The closest planet approach is 1.7×10^{-2} AU. This system is integrated in heliocentric coordinates to demonstrates that we obtain similar results to the case of Jacobi coordinates.

and adaptive versions of the $\mathcal{ABA}(6*)$ and $\mathcal{ABA}(8*)$ schemes. For the most efficient schemes, machine precision is reached for an inverse cost of a few 10^{-3} . This case illustrates the point made on section 6.4 that there is no advantage at using the hierarchical structure of the original equation in the choice of the scheme.

In Figure 6.2b, the initial semi-major axis ratio α is 0.97 and the two planets minimal approach is 3.68×10^{-5} AU. It should be noted that the radius of a planet of mass $5 \times 10^{-6} M_\odot$ with a density of 5 g.cm^{-3} – denser than the Earth – is 5.21×10^{-4} AU, so ten times greater. We can compute the density that corresponds to a body of mass $5 \times 10^{-6} M_\odot$ and radius half the closest approach distance. We obtain a density of $1.1 \times 10^5 \text{ g.cm}^{-3}$ which is close to the white dwarf density. In this case, the fixed time-step algorithm is widely inaccurate while the performance of the adaptive time-step algorithm remains largely unchanged. We believe that this demonstrates how powerful this new approach is for the integration of few planet systems.

We also give an example with larger mass planets in figure 6.3. We plot the relative energy error as a function of the inverse cost for a system of two planets of mass $5 \times 10^{-4} M_\odot$ that correspond to the case of $\varepsilon = 10^{-3}$. The initial semi-major axis ratio is 0.9 to ensure a minimal approach distance of 1.7×10^{-2} AU.

We see that for this particular close encounter, it is still possible to reach machine precision with a fixed time-step at the price of a very small time-step. On the other hand, the close encounter is perfectly resolved for the adaptive time-step, even if ε is larger by two order of magnitude. Because of the larger masses, it is necessary to take smaller time-step to ensure that the relative energy error remains at machine precision.

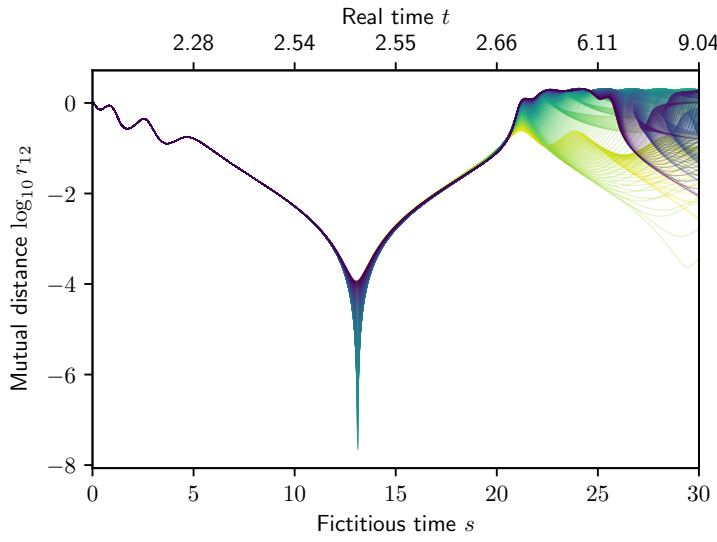


Figure 6.4 – Planet mutual distance as a function of the fictitious time for 1000 initial conditions chosen as described in the body of the text. On the upper axis, we give the real time for the initial condition that reached the closest approach.

6.5.2 Behaviour at exact collision

To demonstrate the power of our algorithm to resolve close encounters, we consider the case of two planets experiencing an almost exact collision (as if the bodies were material points). We take two planets of mass $m = 10^{-5} M_{\odot}$, the first one on an orbit of eccentricity 0.1 and semi-major axis 0.95 AU and the second one on a circular orbit of semi-major axis 1 AU. We then fine tune the mean longitudes of the two planets to ensure we approach the exact collision. We integrate 1000 initial conditions for which we vary linearly λ_1 between -0.589 and -0.587 and we take $\lambda_2 = -1.582$.

In figure 6.4, we represent for each initial condition the planets mutual distance as a function of the fictitious time s . In the upper axis, we give the real time of the particular initial condition that gave the closest approach. In this simulation, all initial conditions reached a mutual distance smaller than 1.1×10^{-4} AU and the closest approach is 5.5×10^{-9} AU. For the chosen masses, we can compute the physical radius of such bodies assuming a particular bulk density. We have

$$R_p = 5.21 \times 10^{-2} \left(\frac{\rho}{1 \text{g.cm}^{-3}} \right)^{-1/3} \left(\frac{m_p}{1 M_{\odot}} \right)^{1/3}, \quad (6.38)$$

where ρ is the bulk density of the planet. The radius is only a weak function of the density over the range of planet bulk densities. If we assume a very conservative value of $\rho = 6 \text{ g.cm}^{-3}$, we obtain a planet radius of 6.17×10^{-4} AU, *i.e* well above the close encounters considered here.

We plot the energy error as a function of the minimal approach distance on figure 6.5. Besides, we also consider a more practical case where 4 other planets are added to the system. The additional planets are located on circular orbits, have the

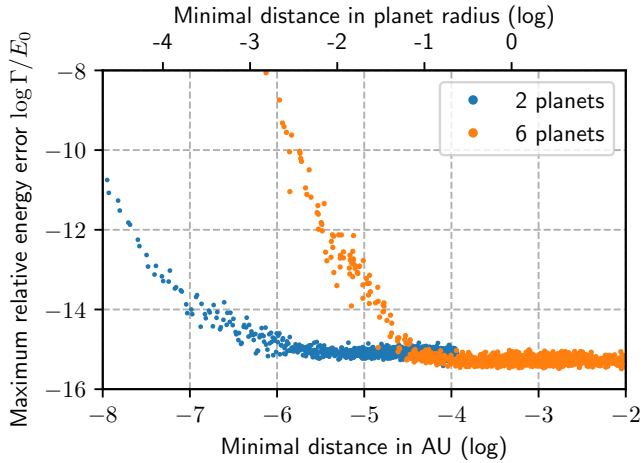


Figure 6.5 – Relative energy error as a function of the minimal mutual approach reached during a close encounter of Super Earths in a two-planet system and a six-planet system. The particular initial conditions are described in the text body. In the upper part, we give the mutual distance in unit of planet radius for a planet of density $\rho = 6 \text{ g.cm}^{-3}$.

same masses of $10^{-5} M_{\odot}$ and are situated outside of the second planet orbit with an equal spacing of 0.15 AU. Their initial angles are randomly drawn but are similar in every run.

In both set up, we use the heliocentric $\mathcal{ABA}(8*)$ scheme and the fictitious time-step is $\sigma = 10^{-2}$. In the case of the two-planet system, machine precision is reached even for an approach of approximately 10^{-6} AU that corresponds to about 10^{-3} planet radius. When planets are added, it is more difficult to reach very close encounters due to the perturbation of the other planets. Nonetheless, approaches up to 6×10^{-7} AU are reached and the close encounter is resolved at machine precision up to a minimal distance of 3×10^{-5} AU or 5×10^{-2} planet radius.

6.6 Pericenter regularization

When studying planet-planet scattering, the minimal distance between the planet and the star may be reduced. As a result, the fixed time-step becomes too large and the passage at pericenter is insufficiently resolved. In order to address this issue, we can combine the close-encounter regularization of section 6.3 with a regularization method introduced by (Mikkola, 1997).

Let first detail Mikkola's idea. When integrating a few-body problem Hamiltonian, one can introduce a time renormalization $dt = g(\mathbf{q})du$, where

$$g(\mathbf{q}) = \left(\sum_{i=1}^N \frac{A_i}{q_i} \right)^{-1}. \quad (6.39)$$

Here A_i are coefficients that can be chosen arbitrarily. In this article, we will define

them as

$$A_i = \frac{m_i a_{\text{typical}}}{\sum_{j=1}^N m_j}, \quad (6.40)$$

where a_{typical} , defined in (6.26), is the typical length-scale of the system. The new Hamiltonian Υ , on the extended phase space $(\mathbf{q}, t, \mathbf{p}, p_t)$ is

$$\Upsilon = \Upsilon_0 + \Upsilon_1 = g(\mathbf{q})(H_0 + p_t) + g(\mathbf{q})H_1. \quad (6.41)$$

As in section 6.3, on the sub-manifold $\{p_t = H(0)\}$, Υ and H have the same equations of motion up to the time transformation. If H_1 only depend on \mathbf{q} (using Jacobi coordinates for instance), Υ_1 is trivially integrable.

6.6.1 Kepler step

It is also possible to integrate Υ_0 as a modified Kepler motion due to the expression of g (Mikkola, 1997). Indeed, let us denote $v_0 = \Upsilon_0(0)$ and $\tilde{H}_0 = g^{-1}(\mathbf{q})(\Upsilon_0 - v_0)$. \tilde{H}_0 has the same equations of motion as Υ_0 up to a time transformation $d\tilde{t} = g^{-1}(\mathbf{q})du$. We have

$$\begin{aligned} \tilde{H}_0 &= H_0 + p_t - v_0 \sum_{i=1}^N \frac{A_i}{q_i} \\ &= p_t + \sum_{i=1}^N \frac{\|\mathbf{p}_i\|^2}{2m_i} - \frac{\mu_i m_i + v_0 A_i}{q_i} = p_t + \sum_{i=1}^N \tilde{K}_i, \end{aligned} \quad (6.42)$$

where \tilde{K}_i is the Hamiltonian of a Keplerian motion of the planet i with a modified central mass

$$\tilde{\mu}_i = \mu_i \left(1 + \frac{v_0 A_i}{\mu_i m_i} \right) = \mu_i \left(1 + \frac{v_0 a_{\text{typical}}}{\mu_i \sum_{j=1}^N m_j} \right). \quad (6.43)$$

However, the time equation must be solved as well. Indeed, we integrate with a fixed fictitious time-step Δu . The time $\Delta\tilde{t}(u)$ is related to u thanks to the relation

$$\Delta u = \int_0^{\Delta\tilde{t}} g^{-1}(\mathbf{q}(\tilde{t})) d\tilde{t} = \sum_{i=1}^N A_i \int_0^{\Delta\tilde{t}} \frac{1}{r_i(\tilde{t})} d\tilde{t} \quad (6.44)$$

where $r_i(\tilde{t})$ follow a Keplerian motion. We can rewrite equation (6.44) thanks to the Stumpff's formulation of the Kepler equation (Mikkola, 1997; Rein and Tamayo, 2015, see appendix E.1.1). Since $\int_0^{\Delta\tilde{t}} \frac{1}{r_i(\tilde{t})} d\tilde{t} = X_i$, we have

$$\Delta u = \sum_{i=1}^N A_i X_i. \quad (6.45)$$

As a consequence, the N Stumpff-Kepler equations

$$\Delta\tilde{t} = r_{0i} X_i + \eta_{0i} G_2(\beta_{0i}, X_i) + \zeta_{0i} G_3(\beta_{0i}, X_i) = \kappa_i(X_i) \quad (6.46)$$

must be solved simultaneously with equation (6.45). To do so, we use a multidimensional Newton-Raphson method on the system of $N+1$ equations consisting of the

N Kepler equations (6.46) and equation (6.45) of unknowns $Y = (X_1, \dots, X_N, \Delta\tilde{t})$. The algorithm is almost as efficient as the fixed time Kepler evolution since it does not add up computation of Stumpff's series. Indeed, at step k , we can obtain $Y^{(k+1)}$ thanks to the equation

$$Y^{(k+1)} = Y^{(k)} - dF^{-1}(Y^{(k)})(F(Y^{(k)})) \quad (6.47)$$

where

$$F = \begin{pmatrix} \kappa_1(X_1) - \Delta\tilde{t} \\ \vdots \\ \kappa_N(X_N) - \Delta\tilde{t} \\ \sum_{i=1}^N A_i X_i - \Delta u \end{pmatrix} \quad (6.48)$$

and

$$dF = \begin{pmatrix} \kappa'_1(X_1) & 0 & \cdots & -1 \\ 0 & \ddots & 0 & -1 \\ \cdots & 0 & \kappa'_N(X_N) & -1 \\ A_1 & \cdots & A_N & 0 \end{pmatrix} \quad (6.49)$$

with κ'_i being the derivative with respect to X_i of κ_i (eq. 6.46).

Equation (6.47) can be rewritten as a two-step process where a new estimate for the time $\Delta\tilde{t}^{(k+1)}$ is computed and then used to estimate $X_i^{(k+1)}$. We have

$$\Delta\tilde{t}^{(k+1)} = \left(\Delta u + \sum_{i=1}^N \frac{A_i (\kappa_i(X_i^{(k)}) - \kappa'_i(X_i^{(k)}) X_i^{(k)})}{\kappa'_i(X_i^{(k)})} \right) \Bigg/ \left(\sum_{i=1}^N \frac{A_i}{\kappa'_i} \right), \quad (6.50)$$

and

$$X_i^{(k+1)} = \frac{\Delta\tilde{t}^{(k+1)} + \kappa'_i(X_i^{(k)}) X_i^{(k)} - \kappa_i(X_i^{(k)})}{\kappa'_i(X_i^{(k)})}. \quad (6.51)$$

6.6.2 The case of heliocentric coordinates

In heliocentric coordinates, H_1^H depends on \mathbf{p} as well. As a result, gH_1^H is not easily integrable and it is not even possible write it as a sum of integrable Hamiltonians. To circumvent this problem, we can split gH_1^H into gU_1^H and gT_1^H . The potential part gU_1^H is integrable, but a priori gT_1^H is not integrable.

One can approximate the integration of gT_1^H using a logarithmic method as proposed in (Blanes and Iserles, 2012). Indeed, the evolution of gT_1^H during a step Δt is the same as the evolution of $\log gT_1^H = \log g + \log T_1^H$, which is separable, for a step $T_1 \Delta t$ where $T_1 = gT_1^H|_{t=0}$. Therefore, we can approximate $\log gT_1^H$ using a leapfrog scheme and the error is of order $\Delta u^2 \varepsilon^3$ as well.

Then, we can approximate the heliocentric step by using the same method as in 6.4.1. It should be noted that in this case, it is necessary to approximate the step even when using democratic heliocentric coordinates since $g(\mathbf{q})$ does not commute with T_1^H .

6.6.3 Combining both regularizations

We have seen that the Hamiltonian Υ is separable into two parts that are integrable (or nearly integrable for heliocentric coordinates). Therefore we can simply regularise the close encounters by integrating the Hamiltonian

$$\tilde{\Gamma} = f(\Upsilon_0 + p_u) + f(\Upsilon_1) = f(g(\mathbf{q})(H_0 + p_t) + p_u) + f(g(\mathbf{q})H_1), \quad (6.52)$$

where p_u is the momentum associated to the intermediate time u used to integrate Υ alone. The time equation is

$$\frac{dt}{ds} = \frac{\partial \tilde{\Gamma}}{\partial p_t} = f'(\Upsilon_0)g(\mathbf{q}). \quad (6.53)$$

Note that we need to place ourselves on the sub-manifold such that $\Upsilon_0 + p_u + \Upsilon_1 = 0$ and $H_0 + p_t + H_1 = 0$, in order to have the same equations of motion for $\tilde{\Gamma}$, Υ and H . Both of these conditions are fulfilled by choosing $p_t = -E_0$ and $p_u = 0$.

6.7 Long-term integration performance

So far, we only presented the performance of the algorithm for very short integrations. In this section, we present the long-term behaviour of the integrator for systems with a very chaotic nature. We consider two different configurations, a system composed of equal planet masses on initially circular, coplanar and equally spaced orbits, used as a test model for stability analysis since the work of Chambers *et al.*, 1996. The second is a similar system but with initial moderate eccentricities and inclinations.

6.7.1 Initially circular and coplanar systems

We integrate 100 systems of six initially coplanar and circular planets. The planet masses are taken equal to $10^{-5} M_{\oplus}$, the outermost planet semi-major axis is fixed to 1 AU and the adjacent planet semi-major axis ratios are all equal to 0.88. Such a value is chosen to ensure that the system lifetime is of order 300 kyr before the first collision. The fixed fictitious time-step is $\sigma = 10^{-2}$ yr. Due to the renormalization, it corresponds approximately to a fixed time-step of 6.3×10^{-3} yr in term of computational cost. It should be noted that the initial period of the inner planet is of the order of 0.38 yr, *i.e* we have an order of 50 steps per orbit.

The simulations are stopped whenever two planet centers approach by less than half the planet radii assuming a density of 6 g.cm^{-3} . This stopping criterion is voluntarily nonphysical as it allows for a longer chaotic phase leading to more close encounters. We also keep track of any encounter with an approach closer than 2 Hill radii at 1 AU (0.054 AU) and record its time, the planets involved and the minimal distance between the two planets. For the majority of the integration, we observe moderate semi-major axis diffusion without close encounters. About 1 kyr before the final collision, the system enters a true scattering phase with numerous close encounters. The integrations last on average 353 kyr, the shortest is 129 kyr long and the longest 824 kyr. On average, we recorded 557 close encounters and 68% happen

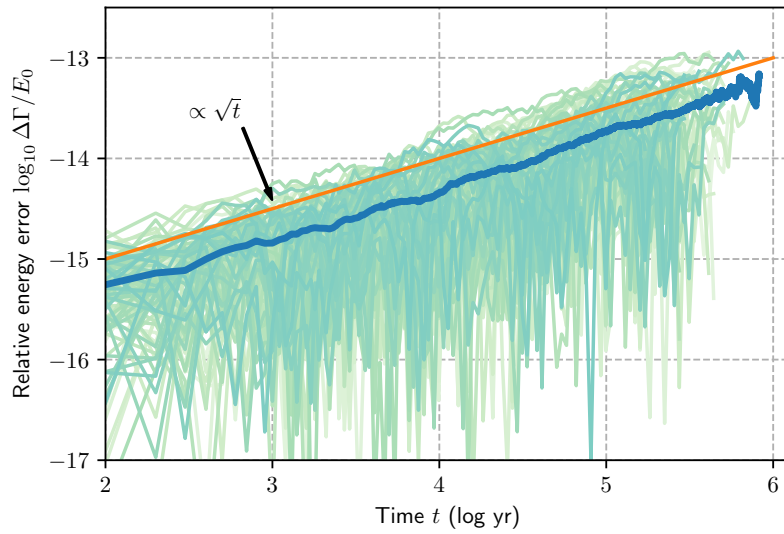


Figure 6.6 – Evolution of the relative energy error for 100 systems composed of six planets on initially circular orbits. The light curves represent individual system and the thicker blue the average over the 100 systems. The orange straight line is proportional to \sqrt{t} in order to show that the integrator follows Brouwer’s law. The orange line is the same in all energy error figures to allow for comparison.

during the last 10000 years. Among the close encounters, we record on average 6.4 approaches below 0.01 AU per system. 95% of these very close encounters happen during the last 1000 years.

The relative energy error evolution is shown on figure 6.6. We observe that the the integrator follows the Brouwer (1937) law since the energy error behave as a random walk (the error grows as \sqrt{t}). We see that the scattering phase do not harm the energy conservation as we do not see spikes of higher error values toward the end of the integrations.

6.7.2 Planet scattering on inclined and eccentric orbits

Our second long-term test problem is a set of planetary systems with moderate eccentricities and inclinations. The goal is here to test the integrator in a regime where strong scattering occurs on long timescales with a much higher frequency in very close encounters (less than 0.01 AU). Besides, this case helps to demonstrate the interest of the pericenter regularization. The initial conditions are chosen as follow.

- Similarly to the previous case, we consider systems of six planets with an equal mass of $10^{-5} M_{\odot}$.
- The semi-major axis ratio among adjacent pairs is 0.85.
- The Cartesian components of the eccentricities ($e \cos(\varpi), e \sin(\varpi)$) and inclinations ($i \cos(\Omega), i \sin(\Omega)$) are drawn from centered Gaussian distribution of

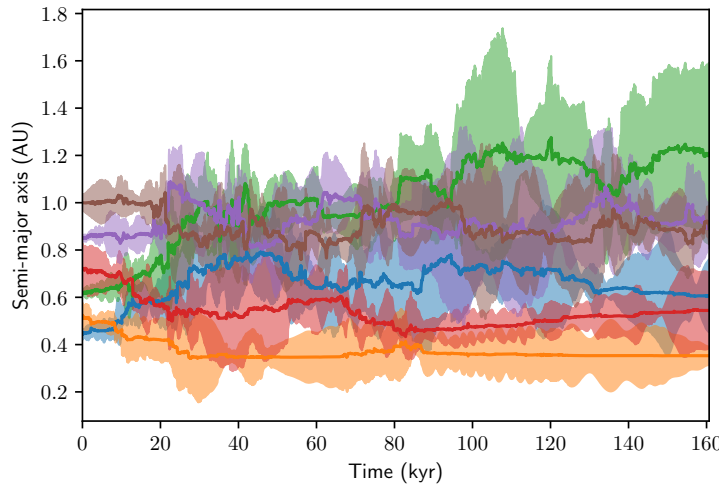


Figure 6.7 – Evolution of the semi-major axis, periapsis and apoapsis for a typical initial condition. The bold curve is the semi-major axis while the filled region represents the extent of the orbit. The mutual inclinations are not represented.

Table 6.1 – Summary of the main stats and specifications of the spatial and eccentric runs

Run	J1	J2	H1	H2
Coordinates	Jacobi	Jacobi	Heliocentric	Heliocentric
Pericenter	No	Yes	No	Yes
Equivalent fixed time-step (yr^{-1})	2.6×10^{-3}	2.6×10^{-3}	2.9×10^{-3}	2.9×10^{-3}
Time-step per shortest orbit	112	112	102	102
Average lifetime	53.3 kyr	53.0 kyr	52.6 kyr	46.3 kyr
Av. number of close encounters	1.26×10^4	1.17×10^4	1.20×10^4	1.07×10^4
Av. number of very close encounters	458	415	426	384

standard deviation 0.08. The average eccentricities and inclinations are about 0.11.

- The mean longitudes are chosen randomly.

We also keep the same stopping criterion and also record the close encounters (under 2 Hill radii).

The integrations are performed with the two sets of coordinates, Jacobi and heliocentric; with and without pericenter regularization. The main statistics from the runs are summarized in table 6.1. For all integrations, we use the 8-th order scheme and a fictitious time-step $\sigma = 4 \times 10^{-3}$. We see that the systems experience on average a close encounter every 5 yr. A typical evolution is presented in figure 6.7. In this particular run, we see numerous planet exchanges, almost 35000 close encounters occur and the system experiences more than 1200 very close encounters. Nevertheless, the final relative energy error is 6.8×10^{-15} .

We plot respectively on figure 6.8a, 6.8b, 6.8c and 6.8d the relative energy errors

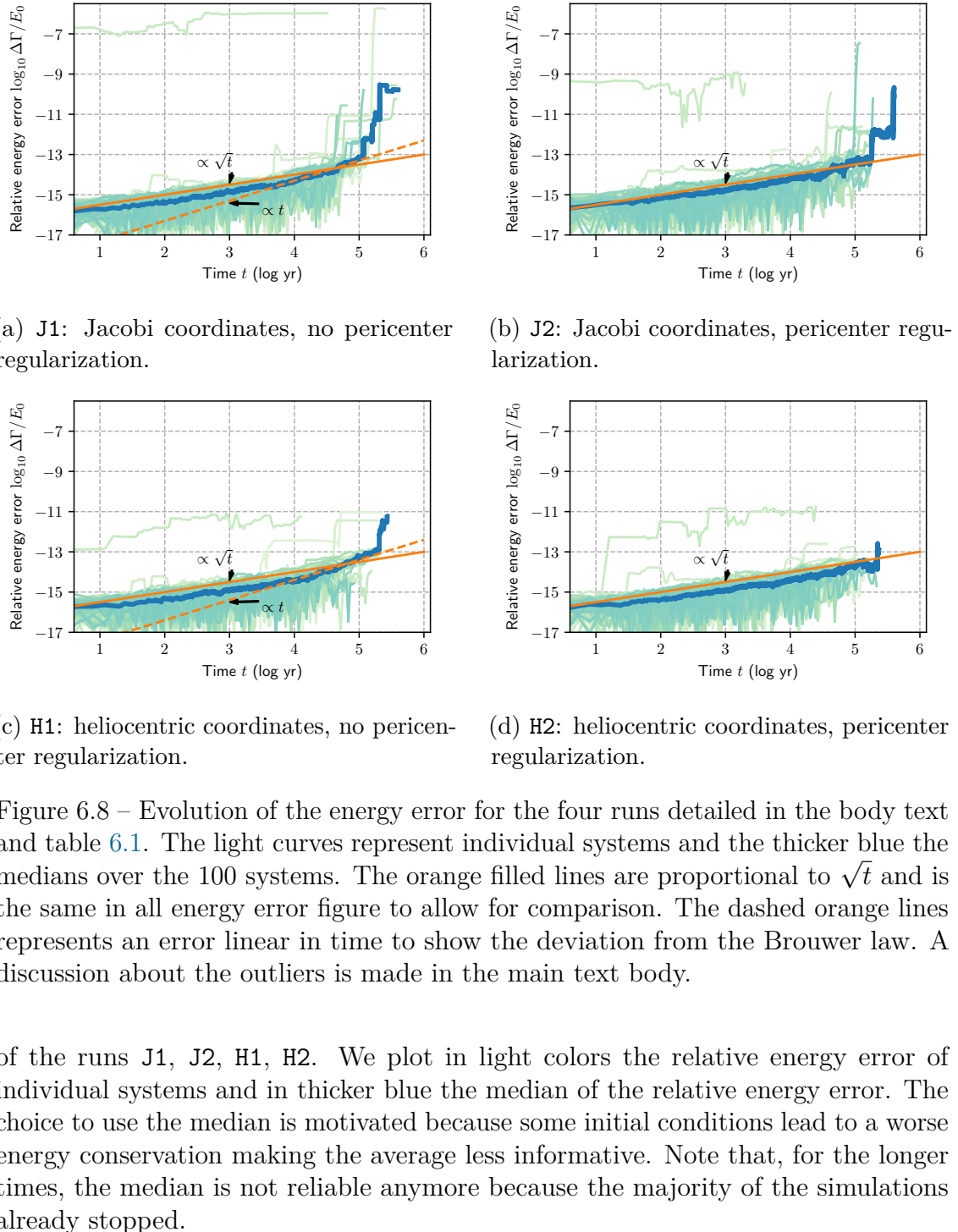


Figure 6.8 – Evolution of the energy error for the four runs detailed in the body text and table 6.1. The light curves represent individual systems and the thicker blue the medians over the 100 systems. The orange filled lines are proportional to \sqrt{t} and is the same in all energy error figure to allow for comparison. The dashed orange lines represents an error linear in time to show the deviation from the Brouwer law. A discussion about the outliers is made in the main text body.

of the runs J1, J2, H1, H2. We plot in light colors the relative energy error of individual systems and in thicker blue the median of the relative energy error. The choice to use the median is motivated because some initial conditions lead to a worse energy conservation making the average less informative. Note that, for the longer times, the median is not reliable anymore because the majority of the simulations already stopped.

We see that despite the extreme scattering that occurs, the energy is conserved in most systems within the numerical round-off error prescription. We also remark that the heliocentric coordinates seems to provide a more stable integrator even though the interaction step is approximated. In both cases where we do not use the pericenter regularization, J1 and H1, it seems that the energy error is no longer proportional to \sqrt{t} but linear in t .

As already explained, because of the large eccentricities, the innermost pericenter passage is not very well resolved and therefore, the step to step energy variation is

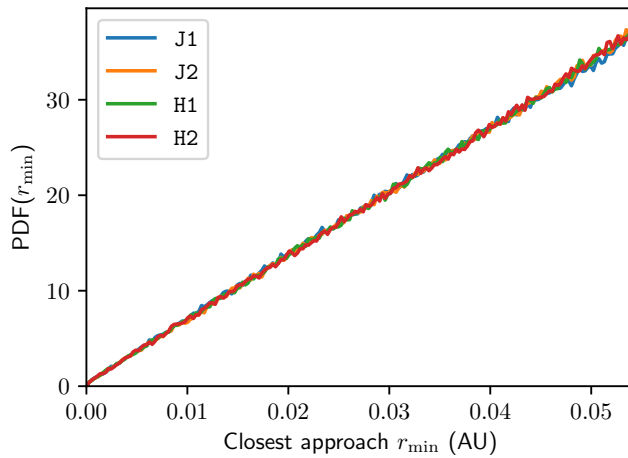


Figure 6.9 – PDF of the closest approach during close encounters. The four runs PDFs are almost identical.

no longer close to machine precision. This effect has been confirmed by the detailed analysis of the time-series close to energy spikes thanks to restarts of the integration from a binary file. We observed that the energy is not changing during the close encounter, but shortly after, when the inner planet passes closer to the star due to the scattering.

We also observe an initial condition well above the machine precision level in all four runs. In this particular system, we have $e_5(t = 0) = 0.81$ which gives an initial pericenter at 0.15 AU. In this extreme case, the pericenter regularization leads to an improvement by two order of magnitude of the error in Jacobi coordinates. The heliocentric coordinates remain however more efficient and we do not see an improvement in this particular case.

In all runs, the time distribution of the close encounters appears to be rather uniform. Moreover, the probability distribution function (PDF) of the closest approach during a close encounter is linear in the distance as shown in figure 6.9. It proves that the systems are in a scattering regime where the impact parameters for the close encounters are largely random (see also Laskar *et al.*, 2011, figure 5).

6.8 Comparison with existing integrators

We ran the same eccentric and inclined initial conditions using the REBOUND (Rein and Liu, 2012) package’s integrators IAS15 (Rein and Spiegel, 2015) and MERCURIUS (Rein *et al.*, 2019). IAS15 is an adaptive high order Gauss–Radau integrator and MERCURIUS is an hybrid symplectic integrator comparable to MERCURY (Chambers, 1999). This choice is motivated because the REBOUND team made recent and precise comparisons with other available integrators (Rein and Spiegel, 2015; Rein and Tamayo, 2015). Moreover, we use a very similar implementation of the Kepler step. We also run the same tests with the multi-time-step symplectic integrator SYMBA

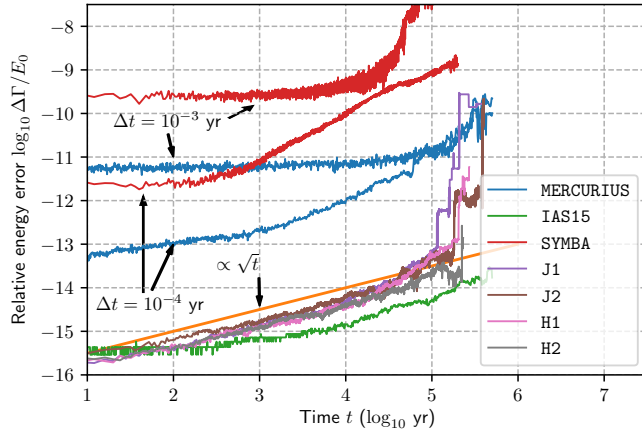


Figure 6.10 – Comparison of the different adaptive integrator runs presented in table 6.1 to other used codes **IAS15**, **MERCURIUS** and **SYMBA** integrating the same initial conditions. We plot the median of the energy error.

(Duncan *et al.*, 1998).

We plot the energy error median that result from the integration. We see that our integrator perform similarly to the non-symplectic integrator **IAS15** and better than **MERCURIUS** and **SYMBA**. Our integrator runs at the same speed as **MERCURIUS** and **SYMBA** with a time-step of $\Delta t = 10^{-4}$. However **IAS15** is much faster on this particular problem (by a factor 10 on average). It should be noted that **MERCURIUS** and **SYMBA** are not designed to work efficiency at such low energy errors. However, our motivation for this work was to find a precise symplectic integrator for close encounters. We thus try to obtain the best precision from **MERCURIUS** and **SYMBA** to make the comparison relevant.

6.9 Discussion

We showed that time renormalization can lead to very good results for the integration of highly unstable planetary systems using a symplectic integrator (section 6.3). The algorithm can use a scheme of arbitrary order, however, we have not been able to take advantage of the hierarchical structure beyond the first order in ε . This is due to the non linearity of the time renormalization as explained in section 6.4. It is however possible to cancel every term up to arbitrary order in the time-step using non hierarchical schemes (McLachlan, 1995a).

Our time renormalization uses the perturbation energy to monitor whenever two planets encounter. The algorithm is thus efficient if the two planet interaction contributes to a significant part of the perturbation energy. As a result this integrator is particularly well adapted for systems of few planets (up to a few tens), with comparable masses (within an order of magnitude). Moreover, it behaves extremely well in the two planet problem even if one planet mass is significantly smaller than the other.

However, the algorithm is not yet able to spot close encounters between terrestrials planets in a system containing giant planets such as the Solar System. Indeed, in the case of the Solar System, the perturbation energy is dominated by the interaction between Jupiter and Saturn. We plan to address this particular problem in the future.

Chapter 7

Architecture of planetary systems

Some of the content of this chapter was published in (Laskar and Petit, 2017). However, certain remarks and the simulations are original.

7.1 Introduction

As said in the introduction chapter, explaining the architecture of planetary systems is one of the oldest questions in astronomy. Historical attempts such as the Titius-Bode law (see Nieto, 1972) were based on empirical laws inspired by the particular architecture of the Solar System. The discovery of exoplanet systems has increased the interest in this question and I refer to the introduction for a more complete description of the architecture of the currently known systems.

In this section, I intend to give a brief overview on the recent theoretical attempts to explain the planetary systems architecture. Due to the large number of super-Earth systems discovered by *Kepler*, most of the recent studies have focused on a model often called the "tightly packed systems" (Laskar, 1996; Barnes and Raymond, 2004; Fang and Margot, 2013). In this model, the planetary systems are assumed dynamically full (a notion introduced in Laskar, 1996), in the sense that the addition of another planet between the existing one results in a destabilization. This hypothesis leads to the determination of minimal spacing stability criteria of the form

$$\log_{10} T_{\text{ins}}/T_{\text{orb}} = b\Delta + c, \quad (7.1)$$

inspired by the numerical simulations of (Chambers *et al.*, 1996). Various empirical studies have since been carried out and one can cite (Smith and Lissauer, 2009; Lissauer *et al.*, 2011; Pu and Wu, 2015) and (Obertas *et al.*, 2017) as notable examples. Quillen (2011) has proposed a theoretical mechanism based on the overlap of three planet resonances.

Using the tools of statistical mechanics and an empirical minimal spacing criterion, Tremaine (2015) proposed a statistical distribution of the orbital elements of planetary systems. Such approach has also been used by (Mogavero, 2017) to

describe the probability distribution functions of the eccentricities and inclinations in the Solar System based on the numerical simulations of (Laskar, 2008).

Planetary system population synthesis has also been used to fit the observed distributions. Indeed, it is easier to make statistical analysis on synthesized populations since the planet characteristics are then perfectly known. We refer to the introduction chapter and the recent reviews (Morbidelli *et al.*, 2012; Raymond *et al.*, 2014; Morbidelli and Raymond, 2016; Johansen and Lambrechts, 2017) for more details.

In (Laskar, 2000), Laskar introduced an analytical model of planetary formation. The model is based on a modelization of the dynamics by random AMD exchanges between planets under the secular assumption. He showed that under those assumptions, the AMD decreases during perfect merger collisions. This model also allows to obtain analytical expressions for the averaged systems architecture and orbital parameter distribution, depending on the initial mass distribution. Because of its simple formalism, the model can be implemented and is able to synthesize planetary systems at almost no computational cost.

Since (Laskar, 2000) was a letter, the proofs of the model were announced to be published in a future paper. Although this preprint was in nearly final form for more than a decade, and had even been provided to some researchers (Hernández-Mena and Benet, 2011), it was only published in (Laskar and Petit, 2017) along with the classification that is presented in chapter 3. In this manuscript, I decided to split the model of planetary accretion from the definition of AMD-stability.

I thus reproduce the proofs from Laskar's preprint in section 7.2.1 and 7.3. I also prove that the collision assumptions are more general than they seem to be in section 7.2.2. In 7.4, I revisit the numerical implementation of the model and show that it can be adapted to the new paradigms in planet formation. This model is still a good tool to quickly simulate the outcome of giant impacts driven planet formation.

7.2 AMD and planet collisions

7.2.1 Collision in the secular case

The instabilities of a planetary system often result in a modification of its architecture. A planet can be ejected from the system or can fall into the star, which in both cases results in a loss of AMD for the system.

The outcome of the AMD after a planetary collision is less trivial and needs to be computed. We reproduce here the proof of the decrease of the AMD during collision announced in (Laskar, 2000) that was published in (Laskar and Petit, 2017).

Let assume that among N planets, the totally inelastic collision of two bodies of masses m_1 and m_2 , and orbits $\mathcal{O}_1, \mathcal{O}_2$ occurs, forming a new body (m, \mathcal{O}) . During this collision, we consider that the other bodies are not affected.

Moreover, Laskar assumes that the orbital elements at collision have not been affected by the planet interaction. In other words, the two planets are on intersecting Keplerian orbits and follow an unperturbed motion along them. In particular, the total AMD is constant along the trajectory leading to the collision. While such an

assumption appears unrealistic, we will see in section 7.2.2 how the conclusions from this section are still valid in the general case.

Since the collision results in a perfect merging the total mass and momentum are conserved

$$m = m_1 + m_2, \quad (7.2)$$

$$\tilde{\mathbf{r}} = \tilde{\mathbf{r}}_1 + \tilde{\mathbf{r}}_2; \quad (7.3)$$

On the other hand, at the time of the collision, $\mathbf{r} = \mathbf{r}_1 = \mathbf{r}_2$, so the angular momentum is also conserved

$$\mathbf{r} \wedge \tilde{\mathbf{r}} = \mathbf{r}_1 \wedge \tilde{\mathbf{r}}_1 + \mathbf{r}_2 \wedge \tilde{\mathbf{r}}_2 \quad (7.4)$$

Note that the orbit transformation $(m_1, \mathcal{O}_1) + (m_2, \mathcal{O}_2) \rightarrow (m, \mathcal{O})$ that results from the collision is perfectly defined by equations (7.2, 7.3). The problem which remains is to compute the evolution of the elliptical elements during the collision.

Energy evolution during collision

Just before the collision, the orbits (m_1, \mathcal{O}_1) and (m_2, \mathcal{O}_2) are elliptical heliocentric orbits. At the time of the collision, only these two bodies are involved, and the other bodies are not affected. The evolution of the orbits are thus given by the conservation laws (7.2, 7.3). The Keplerian energy of each particle is

$$h_i = \frac{1}{2} \frac{\|\tilde{\mathbf{r}}_i\|^2}{m_i} - \frac{\mu m_i}{r_i} = -\mu \frac{\mu m_i}{2a_i}, \quad (7.5)$$

where $\mu = Gm_0$. We use here the orbital elements associated with the democratic heliocentric coordinates (2.37) such that μ is the same for all planets. At collision, we have $\mathbf{r}_1 = \mathbf{r}_2 = \mathbf{r}$, the potential energy is thus conserved

$$-\mu \frac{m}{r} = -\mu \frac{m_1 + m_2}{r} = -\mu \frac{m_1}{r_1} - \mu \frac{m_2}{r_2}. \quad (7.6)$$

The change of Keplerian energy is given by the change of kinetic energy

$$\delta h = h - h_1 - h_2 = \frac{\|\tilde{\mathbf{r}}\|^2}{2m} - \frac{\|\tilde{\mathbf{r}}_1\|^2}{2m_1} - \frac{\|\tilde{\mathbf{r}}_2\|^2}{2m_2} \quad (7.7)$$

that is, with (7.2, 7.3),

$$\begin{aligned} \delta h &= \frac{\|\tilde{\mathbf{r}}_1 + \tilde{\mathbf{r}}_2\|^2}{2(m_1 + m_2)} - \frac{\|\tilde{\mathbf{r}}_1\|^2}{2m_1} - \frac{\|\tilde{\mathbf{r}}_2\|^2}{2m_2} = -\frac{m_1 m_2}{2(m_1 + m_2)} \left\| \frac{\tilde{\mathbf{r}}_1}{m_1} - \frac{\tilde{\mathbf{r}}_2}{m_2} \right\|^2 \\ &= -\frac{m_1 m_2}{2(m_1 + m_2)} \|\dot{\mathbf{u}}_1 - \dot{\mathbf{u}}_2\|^2 \leq 0, \end{aligned} \quad (7.8)$$

where we recall that $\dot{\mathbf{u}}_k$ is the barycentric speed of body k (see eq. 2.33). Part of the kinetic energy is dispelled during the collision. Hence, the Keplerian energy of the system decreases during collision. As expected, there is no loss of energy when $\dot{\mathbf{u}}_1 = \dot{\mathbf{u}}_2$. As an immediate consequence of the decrease of energy during the collision, we have

$$\frac{1}{a} \geq \frac{\eta}{a_1} + \frac{1 - \eta}{a_2}, \quad (7.9)$$

where $\eta = m_1/m$.

AMD evolution during collision

Let $f(x) = 1/\sqrt{x}$. Since $f'(x) < 0$ and $f''(x) > 0$, we note that f is decreasing and convex. Thus applying f to (7.9) yields

$$f\left(\frac{1}{a}\right) \leq f\left(\frac{\eta}{a_1} + \frac{1-\eta}{a_2}\right) \leq \eta f\left(\frac{1}{a_1}\right) + (1-\eta)f\left(\frac{1}{a_2}\right) \quad (7.10)$$

thus

$$m\sqrt{\mu a} \leq m_1\sqrt{\mu a_1} + m_2\sqrt{\mu a_2} \quad (7.11)$$

During the collision, the angular momentum is conserved (7.4), and so is the conservation of its normal component, that is

$$m\sqrt{\mu a}\sqrt{1-e^2}\cos i = m_1\sqrt{\mu a_1}\sqrt{1-e_1^2}\cos i_1 + m_2\sqrt{\mu a_2}\sqrt{1-e_2^2}\cos i_2. \quad (7.12)$$

Laskar deduces that in all circumstances, there is a decrease of the angular momentum deficit during the collision, that is

$$C \leq C_1 + C_2, \quad (7.13)$$

where C_k is the AMD of planet k (eq. 2.37). The equality can hold in (7.13) only if $m_1 = 0$, $m_2 = 0$, or $a_1 = a_2$ and $\dot{\mathbf{u}}_1 = \dot{\mathbf{u}}_2$, that is when one of the bodies is massless, or when the two bodies are on the same orbit, at the same position (at the time of the collision, we have also $\mathbf{r}_1 = \mathbf{r}_2$).

The diminution of AMD during collisions acts as a stabilisation of the system. A parallel can be made with thermodynamics, the AMD behaving for the orbits like the kinetic energy for the molecules of a perfect gas. The loss of AMD during collisions can thus be interpreted as a cooling of the system.

7.2.2 General collision case

The secular case treated above and in (Laskar, 2000) is actually a very good approximation. Indeed, while the orbital elements of the planets experiencing a close encounter or a collision vary significantly, we can show that the orbital elements of the resulting planet are not affected by the last close encounter. It is thus correct to compute the outcome of a collision from an unperturbed trajectory. What we call the unperturbed trajectory is the motion of the two planet along their initial Keplerian orbits up to the collision that occurs at the intersection of the two orbits.

Here, we compare the unperturbed motion to the dynamics of two interacting planets on trajectories leading to a collision on their next approach. As in the previous section, we assume the collision to result in a perfect merging. In order to keep the equations light we neglect the other planets interactions but this assumption will also be discussed toward the end of the section.

We recall the Hamiltonian of the two planet problem (2.34) expressed in heliocentric coordinates (2.33)

$$\mathcal{H}_{\text{helio}} = \underbrace{\sum_{k=1}^2 \frac{\|\tilde{\mathbf{r}}_k\|^2}{2m_k} - \frac{\mu m_k}{r_k}}_{\mathcal{H}_0} - \underbrace{\frac{\mathcal{G}m_1m_2}{\Delta_{12}} + \frac{\|\tilde{\mathbf{r}}_1 + \tilde{\mathbf{r}}_2\|^2}{2m_0}}_{\varepsilon\mathcal{H}_1}, \quad (7.14)$$

where $\Delta_{12} = \|\mathbf{r}_1 - \mathbf{r}_2\|$, $\mu = \mathcal{G}m_0$ and m_0 is the star mass.

As explained in the previous section, the orbit that results from the collision can be computed from the conservation of the mass (7.2) and the linear momentum (7.3). Moreover the loss of energy only depends on the relative barycentric velocity (7.8). Based on those considerations, let make the symplectic change of variables $(\mathbf{r}_1, \mathbf{r}_2, \tilde{\mathbf{r}}_1, \tilde{\mathbf{r}}_2) \rightarrow (\mathbf{r}, \boldsymbol{\rho}, \tilde{\mathbf{r}}, \tilde{\boldsymbol{\rho}})$

$$\begin{aligned}\mathbf{r} &= \frac{m_1}{m}\mathbf{r}_1 + \frac{m_2}{m}\mathbf{r}_2, & \tilde{\mathbf{r}} &= \tilde{\mathbf{r}}_1 + \tilde{\mathbf{r}}_2, \\ \boldsymbol{\rho} &= \mathbf{r}_2 - \mathbf{r}_1, & \tilde{\boldsymbol{\rho}} &= \beta \left(\frac{\tilde{\mathbf{r}}_2}{m_2} - \frac{\tilde{\mathbf{r}}_1}{m_1} \right),\end{aligned}\quad (7.15)$$

where m is the total planet mass (7.2) and $\beta = m_1 m_2 / m$ is the reduced mass. The orbital elements of the new planet are completely determined by $\tilde{\mathbf{r}}$ and \mathbf{r} just before the collision. The change of variables (7.15) is a generalization of the Hill approximation used in (Hénon and Petit, 1986) for instance. Therefore, most of the approximations that can be done in the Hill regime remain valid. In the variables (7.15), the Hamiltonian (7.14) takes the form

$$\mathcal{H} = \frac{\|\tilde{\mathbf{r}}\|^2}{2m} + \frac{\|\tilde{\boldsymbol{\rho}}\|^2}{2\beta} - \underbrace{\frac{\mu m_1}{r_1} - \frac{\mu m_2}{r_2} - \frac{\varepsilon \mu \beta}{\rho}}_{U_K} + \varepsilon \frac{\|\tilde{\mathbf{r}}\|^2}{2m}, \quad (7.16)$$

where r_1 and r_2 are function of \mathbf{r} , $\boldsymbol{\rho}$ and the planet masses and $\varepsilon = (m_1 + m_2)/m_0$. There is no general convergent expansion of the Keplerian potential U_K in function of ρ/r . Indeed, when the two planets are far away from each other, \mathbf{r} and $\boldsymbol{\rho}$ can be of comparable size or $\boldsymbol{\rho}$ can even be larger than \mathbf{r} . In the unperturbed system (like in the previous section), the dynamics are reduced to the terms of the zeroth order in ε in the Hamiltonian (7.16).

We can distinguish two regimes depending on the ratio ρ/r . Far away from the collision *i.e.* when $\rho/r \gg \varepsilon^{1/3}$, where the factor $\varepsilon^{1/3}$ corresponds to the Hill scaling (Hénon and Petit, 1986), the unperturbed and the perturbed motion are similar since the planet-planet interactions are weak. The difference between the two trajectories will be of order ε and the variation of the elliptical variables occurs on a timescale much longer than the one considered here (that is of the order of the synodic period of the two planets).

On the other hand, when the two planets enter their Hill sphere *i.e.* when $\rho/r \lesssim \varepsilon^{1/3}$, the perturbation is important and cannot be neglected anymore. It is however, possible to develop the Keplerian potential U_K in order to study in more details the dynamics of $\tilde{\mathbf{r}}$ and \mathbf{r} as they will determine the orbit of the resulting planet.

To do so, we first rescale the variable $\boldsymbol{\rho}$ by $\varepsilon^{1/3}$ in order to develop U_K in power of ε rather than solely into power of the ratio ρ/r . This renormalization allows the comparison between the terms from U_K and the planet-planet interaction term. In order to keep symplectic variables, we define

$$\boldsymbol{\rho} = \varepsilon^{1/3} \boldsymbol{\rho}', \quad \tilde{\boldsymbol{\rho}} = \varepsilon^{-1/3} \tilde{\boldsymbol{\rho}}'. \quad (7.17)$$

Since we consider a case where $\rho/r \lesssim \varepsilon^{1/3}$, ρ'/r is at most of order unity. The Keplerian potential developed in power of $\varepsilon^{1/3}$ have for expression

$$U_K = -\frac{\mu m}{r} + \frac{\mu \varepsilon^{2/3} \beta}{2} \left(\frac{3(\boldsymbol{\rho}' \cdot \mathbf{r})^2}{r^5} - \frac{\rho'^2}{r^3} \right) + O\left(\varepsilon \left(\frac{\rho'}{r}\right)^3\right). \quad (7.18)$$

Note that the main term only depends on r and corresponds to the potential that the planets would have if they were merged into a single body in their center of mass. The remaining terms are at least of order $\varepsilon^{2/3}$ and are quadratic in ρ' . Because we only focus on the dynamics within the Hill sphere, we can safely drop the terms of order ε into U_K . The Hamiltonian has for expression

$$\mathcal{H}_{\text{Hill}} = \frac{\|\tilde{\mathbf{r}}\|^2}{2m} + \frac{\|\tilde{\boldsymbol{\rho}}'\|^2}{2\varepsilon^{2/3}\beta} - \frac{\mu m}{r} + \underbrace{\frac{\mu \varepsilon^{2/3} \beta}{2} \left(\frac{3(\boldsymbol{\rho}' \cdot \mathbf{r})^2}{r^5} - \frac{\rho'^2}{r^3} \right)}_{\text{Hill interaction term}} - \frac{\mu \varepsilon^{2/3} \beta}{\rho'} + \varepsilon \frac{\|\tilde{\mathbf{r}}\|^2}{2m}. \quad (7.19)$$

We remark that the variables $(\boldsymbol{\rho}', \tilde{\boldsymbol{\rho}}')$ are coupled to the variables $(\mathbf{r}, \tilde{\mathbf{r}})$ only through a term that results from the development of the Keplerian potential. We call this term the Hill interaction term.

From expression (7.19), it is clear that the dynamics of $\tilde{\mathbf{r}}$ and \mathbf{r} are weakly affected by the close encounter. Indeed, the Hill interaction term goes to zero at the collision and is of order $\varepsilon^{2/3}$ with respect to the main term in r . However, the Hill interaction term cannot be neglected in the dynamics of $\boldsymbol{\rho}'$ and $\tilde{\boldsymbol{\rho}}'$ as it is of dominant order in ε . The kinetic term $\varepsilon \frac{\|\tilde{\mathbf{r}}\|^2}{2m}$ is continuous at the collision and its effect is only significant on longer timescales. We also remark that as $\rho'/r \rightarrow 0$, the dynamics of $(\boldsymbol{\rho}', \tilde{\boldsymbol{\rho}}')$ is well approximated by the motion of a Keplerian problem of gravitational parameter μ and mass $\varepsilon^{2/3}\beta$.

Energy evolution during collision

We can refine the computation of the energy evolution at collision by considering every term instead of only the Keplerian energy. The energy after collision is given by

$$h = \frac{\|\tilde{\mathbf{r}}\|^2}{2m} - \frac{\mu m}{r} + \varepsilon \frac{\|\tilde{\mathbf{r}}\|^2}{2m} = -\frac{\mu m}{2a} + \varepsilon \frac{\|\tilde{\mathbf{r}}\|^2}{2m}, \quad (7.20)$$

where a is the semi-major axis of the newly formed planet. It should be noted that since we use the democratic heliocentric splitting of the Hamiltonian (2.34), there remain a kinetic perturbation term in the post-collision energy. Therefore the variation of energy at collision is given by the limit $\rho' \rightarrow 0$ in the difference of (7.19) and (7.20)

$$\delta h = -\lim_{\rho' \rightarrow 0} \frac{\|\tilde{\boldsymbol{\rho}}'\|^2}{2\varepsilon^{2/3}\beta} - \frac{\mu \varepsilon^{2/3} \beta}{\rho'} + \frac{\mu \varepsilon^{2/3} \beta}{2} \left(\frac{3(\boldsymbol{\rho}' \cdot \mathbf{r})^2}{r^5} - \frac{\rho'^2}{r^3} \right). \quad (7.21)$$

The last term is continuous at the collision and we can neglect it from now. We remark that the remaining terms corresponds to the energy of a Keplerian problem. We deduce that δh has a finite limit. Since the two planets are originally not

gravitationally bounded, $-\delta h > 0$. Therefore the system loses energy. If we neglect the interaction term, δh can be computed for $\rho' \rightarrow +\infty$. We obtain $\delta h = -\|\tilde{\rho}_0\|^2/(2\beta)$ where $\tilde{\rho}_0$ is the unperturbed relative linear momentum, *i.e.* δh is similar to the unperturbed case up to terms of order $\varepsilon^{2/3}$.

Far away from the collision (for $\rho/r \gg \varepsilon^{1/3}$), the total energy can be written as

$$h_0 = -\frac{\mu m_1}{2a_1} - \frac{\mu m_2}{2a_2} + O(\varepsilon). \quad (7.22)$$

We deduce from (7.22) and (7.20) and the discussion on δh that up to terms of order $\varepsilon^{2/3}$, the inequality (7.9) demonstrated in the case of an unperturbed motion remains valid.

In presence of other planets, we have to verify that the interaction terms are also continuous at collision. Before the collision, the term that depend on the planets 1 and 2 in the N -planet Hamiltonian (2.34) have for expression¹

$$-\sum_{k=3}^N \left(\frac{\mathcal{G}m_k m_1}{\Delta_{1k}} + \frac{\mathcal{G}m_k m_2}{\Delta_{2k}} \right) + \frac{\|\tilde{\mathbf{r}}_1 + \tilde{\mathbf{r}}_2 + \sum_{k=3}^N \tilde{\mathbf{r}}_k\|^2}{2m_0}. \quad (7.23)$$

After the collision, we shall replace those terms by the interaction of the newly formed planets with the other ones

$$-\sum_{k=3}^N \frac{\mathcal{G}m_k(m_1 + m_2)}{\Delta_k} + \frac{\|\tilde{\mathbf{r}} + \sum_{k=3}^N \tilde{\mathbf{r}}_k\|^2}{2m_0}, \quad (7.24)$$

where $\Delta_k = |\mathbf{r}_k - \mathbf{r}|$. At the collision, we have $\mathbf{r}_1, \mathbf{r}_2 \rightarrow \mathbf{r}$ so the potential term is continuous. Similarly, the total linear momentum $\tilde{\mathbf{r}} = \tilde{\mathbf{r}}_1 + \tilde{\mathbf{r}}_2$ is conserved at collision so is the kinetic term.

AMD evolution

In the variables (7.15), the angular momentum conservation at the collision can be written

$$\mathbf{G} = \mathbf{r}_1 \times \tilde{\mathbf{r}}_1 + \mathbf{r}_2 \times \tilde{\mathbf{r}}_2 = \mathbf{r} \times \tilde{\mathbf{r}}. \quad (7.25)$$

As in the unperturbed case, the evolution of the AMD comes from the evolution of the energy at the collision. We have also proved that up to term of order $\varepsilon^{2/3}$, one can compute the semi-major axis of the new planet from the orbital elements far away from the collision. Thus, the reasoning of the previous section is still valid and the results from the unperturbed case gives a very good approximation of the evolution of the energy and AMD in perfect merging collisions.

In figure 7.1, I plot the difference between the semi-major axis computed from the unperturbed case and the result of one of the numerical simulations of collision test from chapter 6. More precisely, we compute the semi-major axis of the new planet using (7.20) in the unperturbed case noted $a^{(0)}$ (*i.e.* we assume the planets evolve on their initial Keplerian orbits) and the same quantity using the result of the numerical integration noted a . We use the initial condition that led to the

¹If the collision occurs between other planets, the bodies are simply renumbered.

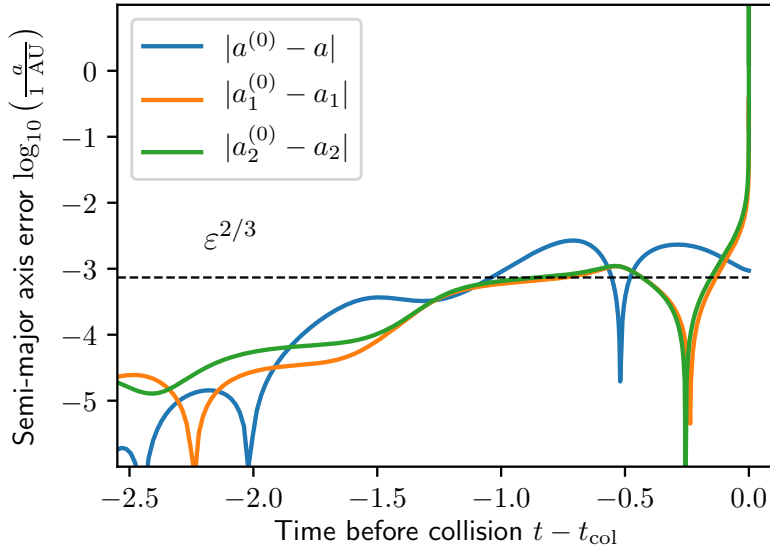


Figure 7.1 – Difference $|a^{(0)} - a|$ between the semi-major axis of the newly formed planet computed using the unperturbed solution and the result of a numerical integration. The initial conditions are described in chapter 6 in figure 6.4. We also plot the same difference for the semi-major axes of the two original planets.

closest approach displayed on figure 6.4. We compare the difference $|a^{(0)} - a|$ to the same difference on the original planet semi-major axes $|a_k^{(0)} - a_k|$ (using the same convention). We see that the error remains of order $\varepsilon^{2/3}$ for the semi-major axis of the newly formed planet while the error made on the former planets semi-major axes is large.

7.3 AMD model of planet formation

Once the disk has been depleted, the last phase of terrestrial planet formation begins with a disk composed of planetary embryos and planetesimals (Morbidelli *et al.*, 2012). In numerical simulations of this phase, the AMD has been used as a statistical measure for comparison with the inner Solar System (Chambers, 2001). In this part, we remind the very simple model of embryos accretion described in Laskar (2000) interpreting the N -body dynamics as AMD-exchange.

7.3.1 Dynamical assumption

Up to now, we did not make special simplifications, and the model simply preserves the mass and the momentum in the barycentric reference frame. As in (Laskar, 2000), we will make here an additional assumption: between collisions, the evolution of the orbits is similar to the evolution they would have in the averaged system in presence of chaotic behaviour. The orbital parameters will thus evolve in a limited manner, with a stochastic diffusion process, bounded by the conservation

of the total AMD. As shown in section 7.2, during a collision the AMD decreases (eq. 7.13). We assume the collisions to be perfect merging since Kokubo and Genda (2010) and Chambers (2013) have shown that the detailed mechanism of collisions such as possibilities of hit-and-run or fragmentation of embryos barely change the final architecture of simulated systems. The total AMD of the system will thus be constant between collisions, and will decrease during collisions. On the other hand, the AMD for a particle is of the order of $\frac{1}{2}m\sqrt{\mu a}e^2$. As the mass of the particle increases, its excursion in eccentricity will be more limited, and less collisions will be possible. The collisions will stop when the total AMD of the system will be too small to allow for planetary collisions.

In the accretion process, we consider a planetesimal of semi major axis a , and its immediate neighbour, defined as the planetesimal with semi major axis a' such that there are no other planetesimal with semi-major axis between a and a' . In this case, we can assume that α is close to 1, and, as explained in Appendix B.3, we will use as an approximation of the critical AMD value $C_c(\alpha, \gamma)$,

$$C_c(\alpha, \gamma) = k(\gamma) \left(\frac{\delta_a}{a} \right)^2 \quad (7.26)$$

where $\delta_a = a' - a$ and $k(\gamma) = \frac{\gamma}{2(\gamma+1)}$.

7.3.2 AMD-Stable Planetary distribution

In this section, I recall the demonstrations of (Laskar, 2000; Laskar and Petit, 2017) of the laws followed by the planetary distribution of a model formed following the above assumptions. Let start from an arbitrary distribution of mass of planetesimals $\rho(a)$, and let the system evolve under the previous rules. We search for the condition of AMD-stable planetary systems, obtained by random accretion of planetesimals. This condition requires that the final AMD value cannot allow for orbit crossing among the planets. Let note C the value of the AMD at the end of the accretion process. Using (7.26), the mass of the planetesimal of semi-major axis a will continue to increase by accretion with a body of semi major axis $a' > a$, as long as

$$\mathcal{C} = \frac{C}{\Lambda'} \geq C_c = k \left(\frac{\delta_a}{a} \right)^2 \quad (7.27)$$

The initial linear density of mass is $\rho(a)$. As a' is the closest neighbour to a , Laskar assumes that all the planetesimal initially between a and a' have been absorbed by the two bodies of mass $m(a)$ and $m(a')$. At first order with respect to δ_a/a , the masses are

$$m(a') \sim m(a) \sim \rho(a)\delta_a \quad (7.28)$$

and from (7.27), we have, at the limiting case,

$$\frac{C}{\delta_a \rho(a) \sqrt{\mu a}} = k \left(\frac{\delta_a}{a} \right)^2 \quad (7.29)$$

One can isolate δ_a

$$\delta_a = \left(\frac{C}{k\sqrt{\mu}} \right)^{1/3} a^{1/2} \rho^{-1/3} \quad (7.30)$$

and from (7.28), we obtain

$$m(a) = \left(\frac{C}{k\sqrt{\mu}} \right)^{1/3} a^{1/2} \rho^{2/3}. \quad (7.31)$$

7.3.3 Scaling laws with initial mass distribution $\rho(a) \propto a^p$.

Using the previous relations, Laskar computes the resulting systems for various initial mass distribution, in particular, for a linear mass density of embryos $\rho(a) = \rho_0(a/a_0)^p$ where a_0 is the inner edge of the distribution. From equation (7.31), one obtain for two consecutive planets

$$\frac{m}{m'} = \alpha^{1/2} \left(\frac{\rho(a)}{\rho(a')} \right)^{2/3} = \alpha^{\frac{1}{2} + \frac{2}{3}p} \quad (7.32)$$

and from eq (7.26), as $\lim_{\alpha \rightarrow 1} \gamma = 1$ we thus have $k(\gamma) = \frac{1}{4}$ in all cases. The relation (7.30) can be rewritten

$$\delta_a a^{\frac{p}{3} - \frac{1}{2}} = \left(\frac{4a_0^p C}{\sqrt{\mu} \rho_0} \right)^{1/3} \delta n, \quad (7.33)$$

where $\delta n = 1$ is the increment from planet a to a' . By integration, this difference relation becomes for $p \neq -\frac{3}{2}$,

$$a_n^{\frac{2p+3}{6}} = a_0^{\frac{2p+3}{6}} + \frac{2p+3}{6} \left(\frac{4a_0^p C}{\sqrt{\mu} \rho_0} \right)^{1/3} n. \quad (7.34)$$

For $p = -\frac{3}{2}$, one obtains,

$$\ln(a_n) = \ln(a_0) + \left(\frac{4C}{\sqrt{\mu} \rho_0 a_0^{3/2}} \right)^{1/3} n. \quad (7.35)$$

For $p = -3/2$, the planet position follows an exponential law similar to Titius-Bode's law for the planetary distribution². The different expressions deduced from this model of planetary accretion are summed up in Table 7.1.

To complete the results presented in Laskar's preprint and published in (Laskar and Petit, 2017), let compute the expected number of planets in the final system. Let now assume that the initial embryos distribution has an inner edge a_0 and an

² This exponent corresponds to a surface density proportional to $r^{-5/2}$, which is not the one of the Minimum Mass Solar Nebula (Weidenschilling, 1977, $p = -1/2$). For the Solar system, (Laskar, 2000) found $p = 0$ (a surface density proportional to r^{-1}) to be best fitting.

Table 7.1 – Planetary distribution corresponding to different initial mass distribution (adapted from Laskar, 2000).

p	$a(n)$	$m(a)$
$p \neq -3/2$	$a_n^{\frac{2p+3}{6}} = a_0^{\frac{2p+3}{6}} + \frac{2p+3}{6}n \left(\frac{4a_0^p C}{\sqrt{\mu} \rho_0} \right)^{1/3}$	$\left(\frac{4C\rho_0^2}{\sqrt{\mu} a_0^{2p}} \right)^{1/3} a^{\frac{4p+3}{6}}$
$-\frac{3}{2}$	$\ln(a_n) = \ln(a_0) + n \left(\frac{4C}{\sqrt{\mu} \rho_0 a_0^{3/2}} \right)^{1/3}$	$\left(\frac{4C\rho_0^2}{\sqrt{\mu}} \right)^{1/3} a_0 a^{-1/2}$
0	$\sqrt{a_n} = \sqrt{a_0} + n \left(\frac{C}{2\sqrt{\mu} \rho_0} \right)^{1/3}$	$\left(\frac{4C\rho_0^2}{\sqrt{\mu}} \right)^{1/3} \sqrt{a}$

outer edge a_∞ . We denote m_{tot} the total mass of the system. m_{tot} is related to ρ_0 through the relation

$$m_{\text{tot}} = \int_{a_0}^{a_\infty} \rho(a) da = \frac{\rho_0 a_0}{(p+1)} \left(\left(\frac{a_\infty}{a_0} \right)^{p+1} - 1 \right), \quad \text{if } p \neq -1, \quad (7.36)$$

$$= \rho_0 a_0 \ln \left(\frac{a_\infty}{a_0} \right), \quad \text{if } p = -1.$$

From equations (7.34) and (7.35), we can deduce the average number of planets N in a system in function of its final AMD, the extent of the initial system and the total mass of the planets. Indeed, for $p \neq -3/2$, we can write

$$N = \left(\left(\frac{a_\infty}{a_0} \right)^{\frac{2p+3}{6}} - 1 \right) \frac{6}{2p+3} \left(\frac{4C}{\sqrt{\mu} \rho_0 a_0^{3/2}} \right)^{-1/3}, \quad (7.37)$$

where ρ_0 should be computed thanks to equation (7.36). Similarly, in the case of $p = -3/2$, we obtain

$$N = \ln \left(\frac{a_\infty}{a_0} \right) \left(\frac{4C}{\sqrt{\mu} \rho_0 a_0^{3/2}} \right)^{-1/3}. \quad (7.38)$$

7.4 Planetary system population synthesis

While, it is possible to analytically derive the average distribution of the model described above, a numerical simulation has still a lot of interest. Indeed, it allows to compare the model to results from actual N -body population synthesis integrations. Moreover, it allows to build a planetary systems population based on the AMD mixing assumptions instead of just looking at the average outcome. Because we do not model precisely the dynamics but only the random evolution of the orbits, the simulations are computationally cheap.

The previous analytical results were tested on a numerical model of the accretion scheme (Laskar, 2000). The model was designed to fulfill the conditions (7.2, 7.3) of section 7.2. In (Laskar, 2000), 5000 simulations were started with a large number of

orbits and followed, looking for orbit intersections. When an intersection occurs, the two bodies merge in a new one, which orbital parameters are determined by the collisional equations (7.2,7.3) (see annex B.1). Between collisions, the orbits do not evolve, apart from a diffusion of their eccentricities, which fulfills the condition of conservation of the total AMD. This is roughly what would occur in a chaotic secular motion.

The main parameter of these simulations is the final AMD value, C . As the AMD decreases during collisions, and in order to obtain final systems with a given value C of the AMD, the eccentricities were increased by a small amount in order to raise the AMD to the desired final value. This is justified as close encounters can also increase the AMD value. Comparisons with N -body simulations (Chambers, 2001; Raymond *et al.*, 2006) show that after a phase of excitation at the beginning of the simulations, the AMD does decrease and converges to its final value. The orbital motion of the orbits is not integrated. Instead, Laskar looks for collisions of ellipses which fulfill the conservation of mass and of linear momentum. These simulations are thus started with a large number of initial bodies (10 000) and continued until their final evolution.

7.4.1 AMD-driven models in the context of modern planet formation

In this section we revisit Laskar's model. In their study of a similar planet formation toy model, Hernández-Mena and Benet (2011) who had access to Laskar's preprint; discuss several improvements to this simple modeling of planet formation. In particular, they point out that in Laskar's algorithm, the step where eccentricities are raised in order to simulate systems at a certain AMD does not conserve energy nor angular momentum. They therefore implemented the model without any increase of AMD, resulting in systems highly unrealistic with tens of planets on almost circular orbits.

While the goal here is not to accurately reproduce planets dynamics, it appears necessary to at least conserve the basic first integrals of the system during the dynamical evolution. However, we wish to keep the AMD increase step as it is motivated by the excitation induced by close encounters. Moreover, as pointed out in (Laskar, 2000), the fixed final AMD allow for a better statistical analysis as the final distribution can be compared to the analytic model. I decide to stick with the constraint on the final AMD but I changed its implementation in order to conserve the energy and angular momentum.

Since the last studies on this model, the paradigms of planet formation have dramatically changed. Indeed, the classical in-situ core accretion model is no longer thought realistic (Morbidielli and Raymond, 2016). As a result, the giant impact phase (Chambers, 2001; Kokubo *et al.*, 2006), where a swarm of planetesimals collides into each other until they eventually form Earth-like or super-Earth planets is no longer considered prevalent. In modern planet formation models, it is thought that a reduced number of embryos grow from pebble accretion (Lambrechts and Johansen, 2012) during the gaseous disk phase. Depending on the intensity of the pebble flux (Lambrechts *et al.*, 2019), the embryos may start a runaway growth and

migrates towards the star to form compact super-Earth chains. On the other hand, if the pebble flux is weaker, embryos will only reach Mars size without significant migration. As a result, when the gas disk dissipates, the system may still enter a giant impact phase.

Besides, the embryo distribution is modified by this new paradigm. Indeed, in (Laskar, 2000) or (Hernández-Mena and Benet, 2011), the embryos are assumed to contain the majority of the refractory material and the population synthesis is made assuming a radial distribution of the embryos following a power law of exponent 0 or -1/2. However, in recent model (Lambrechts *et al.*, 2019), the pebble accretion seems to result in a distribution following a much steeper slope with exponent -1.

While the toy-model cannot be used to explain every type of planet formation, we believe that in the right context and with the right initial conditions, its results can still be useful.

7.4.2 Numerical implementation

7.4.2.1 Initial conditions

We aim to simulate the formation of terrestrial planets that result from a giant impact phase after the gas dissipation. Our goal is to use as initial conditions, systems of Mars-like embryos similar to the ones that emerge from the gaseous disk phase after pebble accretion (Lambrechts *et al.*, 2019). We consider an initial system of total mass of about $6M_{\oplus}$ and composed of $N_0 = 30$ embryos. If the initial masses are taken equal, the small number of embryos leads to a final distribution of planet masses clustered around integer multiples of the initial mass. To smooth the distribution and consider a more realistic system population, the total mass M , is drawn from a normal distribution centered around $6M_{\oplus}$ of standard deviation $1M_{\oplus}$. Each embryos mass is then chosen from a normal distribution centered around the M/N_0 with a standard deviation of $0.1M/N_0$.

The exact number of embryos plays actually little role in the final distribution. Indeed, simulations started with a large number of particles (10,000) result in similar systems up to a smoothed distribution for the mass and semi-major axes. The semi-major axis are drawn randomly from a power law distribution of slope -1 with limits at $a_0 = 0.1$ AU and $a_{\infty} = 3$ AU to match the post gas dissipation distribution from (Lambrechts *et al.*, 2019). Simulations started with fixed spacing tends to give similar results.

Because we look for exact orbit intersections, we restrain ourselves to the planar case. The orbit's eccentricities are set to 0 initially and as in (Laskar, 2000), we fix a final AMD C_f such that when the total system AMD is smaller, we raise it by a process described below. The final AMD is chosen to be equal to 1% of the total angular momentum of the system. As result, the typical final eccentricity will be of order 0.1. The computation of such a final AMD is voluntarily out of the scope of this study but will be the subject of future work.

7.4.2.2 Dynamical evolution

Since we work on the plane, each orbit is fully determined by the set of parameters $m_k, \Lambda_k, C_k, \varpi_k$. At each step, we make the following modifications of the orbits:

- We choose a new set of perihelion longitude from a uniform distribution. This change will have an effect on the loss of AMD at collisions.
- We draw randomly $N/2$ pairs of planets from the systems (N being the current number of bodies) and make a transfer δC of AMD from one planet to the other. More precisely, let us denote with subscript 1 and 2 the two considered orbits. We denote $C_{\min} = -\min(C_2, \Lambda_1 - C_1)$ and $C_{\max} = \min(C_1, \Lambda_2 - C_2)$. The transfer of AMD is made from planet 1 to planet 2 *i.e.* we have $C'_1 = C_1 - \delta C$ and $C'_2 = C_2 + \delta C$ where the prime denote the new values and

$$\delta C = \frac{(C_{\max} + C_{\min}) + X(C_{\max} - C_{\min})}{2}, \quad (7.39)$$

where X is a random number between -1 and 1, drawn from a truncated normal distribution of standard deviation 0.4. The actual distribution for δC has little to no impact on the results. The boundaries C_{\min} and C_{\max} ensure that the new orbits are well defined. This step preserves the secular invariant quantities.

- If the total AMD $C < C_f$, we need to raise the AMD. As already pointed out, we want this step to preserve the total Keplerian energy³ and angular momentum of the system. Ideally, this step should mimic the effect of planet close encounters. To do so, we choose an adjacent pair of planet. In two-planet dynamics, an increase of the AMD translate in an increase in semi-major axis separation as shown by the conservation of p/a (5.22) in chapter 5. We define the AMD increase mechanism by a change on the ratio of semi-major axis α of the considered pair. We choose the new semi-major axis ratio to be $\alpha' = \alpha \left(1 - \left(\frac{\varepsilon}{3}\right)^{1/3}\right)$, where ε is the two planet to star mass ratio. In other words, the semi-major axis separation is increased by a Hill radius. The computation of the new orbital elements is straightforward from this single requirement. Indeed, the conservation of energy gives

$$h = -\frac{\mu m_1}{2a_1} - \frac{\mu m_2}{2a_2} = -\frac{\mu m_1}{2a'_1} - \frac{\mu m_2}{2a'_2} = -\frac{\mu m_2}{2a'_2} \left(\frac{\gamma}{\alpha'} + 1\right), \quad (7.40)$$

which gives

$$a'_2 = -\frac{\mu m_2}{2h} \left(\frac{\gamma}{\alpha'} + 1\right) \quad \text{and} \quad a'_1 = a'_2 \alpha'. \quad (7.41)$$

The new total AMD for the two planets is obtained through the conservation of angular momentum

$$C' = \Lambda'_1 + \Lambda'_2 - (G_1 + G_2). \quad (7.42)$$

³We neglect the perturbation energy.

Table 7.2 – Distribution of the final number of planet for 10,000 systems simulated. The average number is 4.67 while the theory predicts 6.35.

Number of planets	3	4	5	6	7
Number of systems	107	3712	5520	657	4

We then attribute the individual AMD proportionally to the initial one

$$C'_1 = \frac{C_1}{C_1 + C_2} C' \quad \text{and} \quad C'_2 = \frac{C_2}{C_1 + C_2} C'. \quad (7.43)$$

- We then look for eventual collisions. As in (Laskar, 2000), we look for orbit intersections using the method from (Albouy, 2002, see also appendix B.1) and resolve the collision immediately by assuming it to be a perfect merger. The new orbital elements are computed thanks to the collisional equations (7.2,7.3).

If the system experiences 10^4 steps without a collision, the system is considered stable and the algorithm stops. Such a value was found empirically and results were almost similar for 10^6 steps without any collision. The simulation are very fast, which allows for large number of computations.

7.4.3 Results

We compare the numerical results to the analytical predictions. Because of the exponent chosen for the linear mass density $\rho = \rho_0(a/a_0)^{-1}$, we expect that the average system will follow the distributions described in table 7.1 and equations (7.31), (7.34) and (7.37). In particular, we expect the systems to host on average

$$N = 6 \left(\left(\frac{a_\infty}{a_0} \right)^{1/6} - 1 \right) \left(\frac{4C \ln(a_\infty/a_0)}{m_{\text{tot}} \sqrt{\mu a_0}} \right)^{-1/3} \quad (7.44)$$

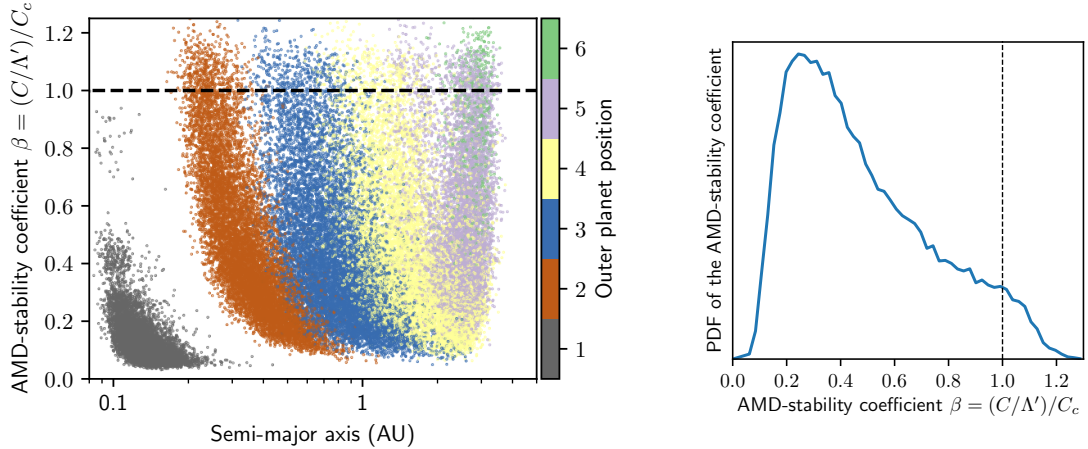
planets. On average, the semi-major axis of the n -th planet should be

$$a_n^{1/6} = a_0^{1/6} + \frac{1}{6} \left(\frac{4C \ln(a_\infty/a_0)}{\sqrt{\mu m_{\text{tot}}}} \right)^{1/3} n. \quad (7.45)$$

Finally, the average mass at a given semi-major axis a is a power law

$$m(a) = \left(\frac{4C m_{\text{tot}}^2}{\sqrt{\mu} \ln(a_\infty/a_0)^2} \right)^{1/3} a^{-1/6}. \quad (7.46)$$

We create 10,000 systems in total using the initial conditions described in 7.4.2.1. The distribution of the final number of planets is given in table 7.2. The number of planets in system span from 3 to 7 and the mean value is 4.67 planets. If we



(a) AMD-stability coefficient for each pair of planets in all systems as a function of the outer planet semi-major axis. The color encodes the position of the planet in its system. For the first planet, we represent the star's AMD-stability coefficient (see 3.3).

(b) Probability density of the AMD-stability coefficients for the pair of planets. The average value is 0.41

Figure 7.2 – Statistics on the AMD-stability coefficients of the created systems.

compute the theoretical number of planet with equation (7.44), we find that we should form 6.35 planets instead.

The discrepancy between the predicted average number of planet and the numerical result can actually be explained. The analytical results from section 7.3 are based on the assumption that each pair of planet is at the limit of AMD-stability (eq. 7.29). However, in the numerical results, we observe that this is not the case at all. We plot in figure 7.2a, the AMD-stability coefficient β (3.23) as a function of the semi-major axis of the outer planet. Each dot is colored by the position of the outer planet in its system. Like in chapter 3, the first planet AMD-stability coefficient gives the criterion for the first planet to fall into the star. We see that pairs are overwhelmingly AMD-stable. Indeed, only 4% of the pairs have an AMD-stability coefficient above 1. But as shown in figure 7.2b, the PDF of the AMD-stability coefficient peaks close to 0.3 and is widespread between 0 and 1. The average of β for the considered systems is 0.41 when we exclude the star's stability coefficient.

We can modify equation (7.29) to take this point into account. We note $\beta_{av} = 0.41$ the average of β . We have

$$\frac{C}{\delta_a \rho(a) \sqrt{\mu a}} = \beta_{av} k \left(\frac{\delta_a}{a} \right)^2. \quad (7.47)$$

From there it is easy to see that we can rescale all the theoretical predictions simply by using C/β_{av} instead of C in the formula (7.44), (7.46) and (7.45). By doing so, we predict that the system should host 4.68 planets, in very good agreement with the actual average.

The theory gives also a very good prediction for the mass and semi-major axis relation (7.46). We plot on figure 7.3 the mass as a function of the semi-major axis

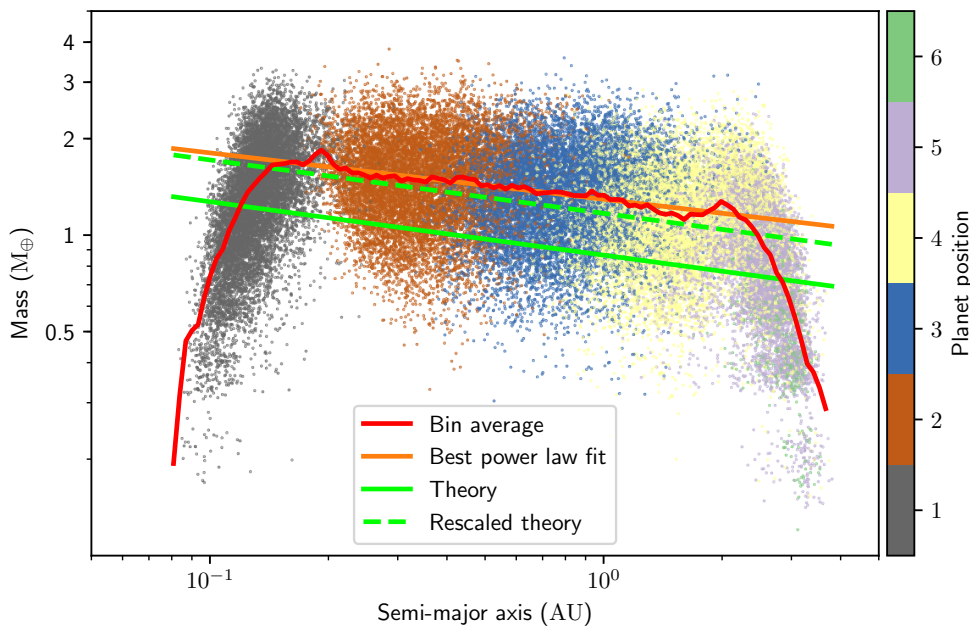


Figure 7.3 – Mass as function of the semi-major axis of the synthesized population, the color code gives the planet position. Additionally, we plot the binned average in red as well as the best-fit power law for the inner region. The green curves correspond to the theoretical prediction (7.46) with and without rescaling.

of each planet in the population. We also plot the bin average mass as well as the best power law fit (for semi-major axis within 0.2 AU to 2 AU), the theoretical curve (7.46) and the rescaled theoretical curve using C/β_{av} in place of C .

From the shape of the binned average, we can distinguish three different clusters on the figure. The inner one is composed of the first planet of each system where the mass increases rapidly with the semi-major axis. In the second cluster, the average follow closely a power law of exponent -0.145 ± 0.005 that is very close from the theoretical exponent $-1/6 = -0.167$. The third cluster is composed of the outer planet of each system where we see that the mass decreases rapidly with the semi-major axis. We conclude that the inner and outer planet are strongly affected by the effects due to the sharp edges of the distribution. The decrease of the planet mass on the edges is explained by the smaller feeding zone. This effect has been observed in outcomes of giant impact simulations where the initial distribution of embryos is confined on a narrow annulus (Hansen, 2009).

The scaling laws developed for a density following a power law (section 7.3.3) do not consider the boundaries conditions, it is therefore natural that the inner and outer planet masses differ from the prediction. However, the middle planets mass distribution is very well described by the rescaled theoretical curve.

The edge effects make the comparison between the theoretical and numerical spacing relations complicated. We consider together the systems with a similar number of planets. For each planet, we compute the semi-major axis average and plot on figure 7.4 the quantity $\Delta_n = \langle a_n \rangle^{1/6} - \langle a_1 \rangle^{1/6}$ as a function of n , the position

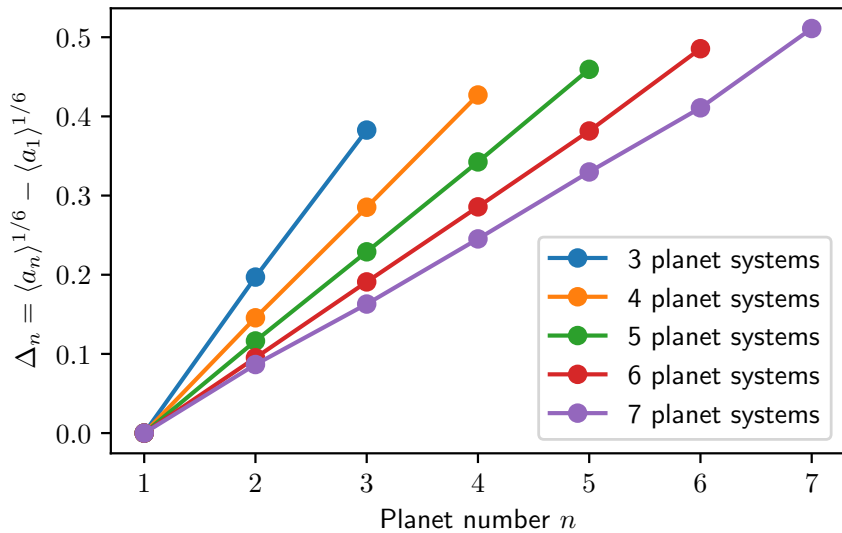


Figure 7.4 – Average of the n -th planet semi major axis among systems with the same number of planets.

of the planet in the system. From (7.45), we see that Δ_n should be proportional to $n - 1$ and does not depend anymore on a_0 . We see in figure 7.4 that it indeed the case, thus the spacing follows a power law of exponent 1/6 as expected from the analytical development.

7.4.4 Final remarks

The results of the AMD-driven planet formation models are very promising to understand planet formation scenarii where the architecture is heavily influenced by a growth phase by giant impacts. The simplicity of the model allows to expose the link between the initial conditions and the resulting systems. Moreover, the analytic solution provides observables to test the model consistency. Besides, the algorithm speed allows to generate easily large quantities of systems.

It is also tempting to compare the systems generated to results of complete formation simulations including n -body dynamics. To do so, I plot in figure 7.5 ten systems randomly drawn from the sample to give an idea of the individual realizations. This figure is completed by an example of initial conditions. When comparing to the figure 7 of (Lambrechts *et al.*, 2019), we observe that the systems look very similar. While this analysis is not quantitatively motivated, it look worthy to make a more in-depth comparison.

However, the model can still be improved. The first caveat comes from the prescription of the final AMD. Indeed, since the core of the dynamics is secular, it is impossible to find in this framework the final AMD of the system and we are forced to consider it as a parameter of the model. One of the main problem to solve is that in multiplanetary systems, non secular instabilities might appears or not depending on the timescales considered. However, the model is intrinsically time independent

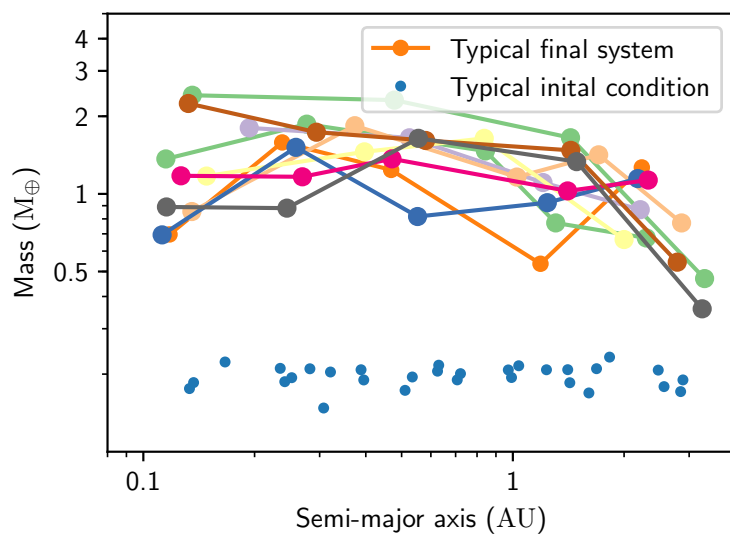


Figure 7.5 – Ten randomly drawn systems from the AMD-driven formation model. Each system is a different line and planets are represented by dots. The blue dots represent a randomly chosen initial condition.

and the only physical states are the final equilibrium states. Nevertheless, the toy model is flexible enough to expect that we could improve this point in the future.

Chapter 8

Conclusions

In this thesis I studied the link between planetary systems architecture and their stability, in particular in the context of exoplanet systems. Because of the large uncertainties on the orbital parameters of observed exoplanets and the chaotic nature of n -body dynamics, it is impossible to carry a complete numerical stability analysis for every discovered system. We developed a simplified dynamical framework to have an intuition on the possible outcome for planetary systems evolution. The work presented in chapter 3 (published in Laskar and Petit, 2017) is based on preliminary works (Laskar, 1997; Laskar, 2000) on the conservation of the Angular Momentum Deficit (AMD) in the secular system. The AMD is a weighted sum of the eccentricities and mutual inclinations. It acts as a dynamical temperature of the system *i.e.* a high AMD system is more likely to be unstable and the dynamics may lead to planet collisions. On the other hand, in a zero AMD system, the orbits are circular and coplanar and the system is more likely to be stable.

In the secular system, the AMD is conserved and bounds the eccentricities. As a result a system with low enough AMD cannot experience close encounters or collisions. We say that a system is the AMD-stable if its total AMD forbids all collisions in the secular system. A system that is AMD-unstable is not guaranteed to end up in a collision. However, a more detailed stability analysis has to be carried out. The AMD-stability of a pair of planets can be quantified thanks to the AMD-stability coefficient, that is the ratio of the total system's AMD with the minimum AMD such that orbit crossing is possible.

I studied the AMD-stability of selected exoplanet systems for which the orbital elements were sufficiently known. I showed that roughly half of them can be considered AMD-stable. While I did not make a detailed analysis of the AMD-unstable systems, I showed that these systems are more clustered around MMR than an average sample from the known exoplanet systems. Such clustering suggests that some AMD-unstable systems may be protected by MMR. Inspired by the Solar System example, we defined hierarchical AMD-stable systems as the systems becoming stable if we assume that there is no AMD exchanges between the inner and the outer part.

The AMD is only conserved if the dynamics can safely be averaged over the mean motions. If the mean motion resonances (MMR) play an important role in the dynamics, the secular hypothesis is no longer valid and the AMD-stability definition needs to be adapted. A pair of planets can be into a MMR and be stable. However, when MMRs start overlapping, a chaotic region appears and the semi-major axes are no longer constant. In chapter 4, I made an in depth analysis of the overlap of first order MMR. I showed that the previously used criteria developed by (Wisdom, 1986; Deck *et al.*, 2013) can be combined into a single expression. I also showed that this criterion fits the AMD framework. Indeed, the overlap of first order MMR allows to discriminate between systems where the secular hypothesis is valid and systems were it is not. I analyzed the effects of this modification of the AMD-stability definition onto the classification proposed in chapter 3. It results, that most systems do not experience MMR overlap.

In the three body problem, there exists a topological boundary that forbids planet close encounters (Marchal and Bozis, 1982). This limit gives an effective long term stability criterion for the two planet problem that has been popularized by Gladman (1993) in the case of circular and coplanar orbits. I demonstrate in chapter 5 that the Hill stability can be very naturally expressed in terms of the total system AMD, the planet masses and the semi-major axis ratio. This new Hill stability criterion generalizes previous expressions obtained in particular cases and have an explicit form.

Nevertheless, numerical simulations are still necessary to study chaotic and unstable systems. In particular, it is crucial to understand how the AMD evolves when the secular assumption cannot be applied. In order to study the behaviour of systems where close encounters occur, it is necessary to use numerical methods that stay accurate even if the planets interaction become dominant. However, the classical integrators for planet dynamics, the fixed time step mixed variable symplectic (MVS) integrators are not suitable for such integrations. In a first step towards the study of unstable systems, I developed in chapter 6, a new high order symplectic integrator that uses time regularization to be able to integrate systems experiencing close encounters. This integrator has a comparable speed to classical MVS integrators such as the one developed in (Blanes *et al.*, 2013) but conserves the energy at machine precision until planet collisions.

Finally, in his original paper on the AMD, Laskar (2000) introduces a toy-model for planet formation. Laskar showed that the AMD always decreases at collisions (assuming they result in a perfect merger). In his model, he assumed that planet dynamics can be modeled by stochastic AMD exchanges between orbits in a secular model. When two orbits intersect, a collision occurs that reduces the total system AMD. The final system is formed whenever the total AMD is too small to allow for anymore collisions. The final average distribution that results from this model can be computed analytically and gives the average number of planets, the planet spacing law as well as the average mass as a function of the semi-major axis. The final distribution only depends on the initial mass distribution function and the final AMD. It is also possible to numerically synthesize planetary system populations using this model (Laskar, 2000) that reproduce the analytical results. In chapter 7, I present again Laskar's model and justify some of the hypotheses. I also adapt the

numerical population synthesis algorithm to the new paradigms of planet formation theory. I show that this model is still useful to rapidly model the giant impact phase that happens during the formation of terrestrial planets after the protoplanetary disk dissipation.

I believe that this thesis shows how simple stability considerations can be used in the study of exoplanet architecture and formation. Moreover, the AMD framework developed here has proven to be a useful and powerful tool in the understanding of various aspect of planet dynamics.

Appendix A

Jacobi coordinates

In section 2.2, we introduced the N -planet Hamiltonian (2.32) and the heliocentric coordinates (2.34). The Jacobi coordinates are another set of coordinates that allow to remove the centre of mass dynamics and write the Hamiltonian as a sum of Keplerian Hamiltonians (2.7). Moreover, when expressed with these coordinates, the perturbation only depends on the positions and no longer on the momenta. It is thus integrable, which allow to separate the Hamiltonian into a sum of integrable Hamiltonians.

We recall equation (2.32) that is the Hamiltonian form of the $N+1$ body problem in an inertial frame. We have

$$\mathcal{H}_{\text{inert}} = \frac{1}{2} \sum_{k=0}^N \frac{\|\tilde{\mathbf{u}}_k\|^2}{m_k} - \mathcal{G} \sum_{0 \leq j < k \leq N} \frac{m_j m_k}{\Delta_{jk}}, \quad (\text{A.1})$$

where $\Delta_{jk} = \|\mathbf{u}_j - \mathbf{u}_k\|$, and \mathcal{G} is the constant of gravitation.

For $k = 0 \dots N$, we define

$$\begin{aligned} \mathbf{R}_k &= \frac{1}{M_k} \sum_{j=0}^k m_j \mathbf{u}_j, \\ \tilde{\mathbf{R}}_k &= \sum_{j=0}^k \tilde{\mathbf{u}}_j, \end{aligned} \quad (\text{A.2})$$

where $M_k = \sum_{j=0}^k m_j$. \mathbf{R}_k and $\tilde{\mathbf{R}}_k$ are respectively the barycenter position of the first $k+1$ body and their total linear momentum. The Jacobi coordinates are defined recursively for $k = 1 \dots N$ as

$$\begin{aligned} \mathbf{r}'_k &= \mathbf{u}_k - \mathbf{R}_{k-1} = \frac{M_{k-1}}{M_k} (\mathbf{u}_k - \mathbf{R}_k) \\ \tilde{\mathbf{r}}'_k &= \frac{M_{k-1}}{M_k} \tilde{\mathbf{u}}_k - \frac{m_k}{M_k} \tilde{\mathbf{R}}_{k-1} = \tilde{\mathbf{u}}_k - \frac{m_k}{M_k} \tilde{\mathbf{R}}_k \end{aligned} \quad (\text{A.3})$$

and

$$\mathbf{r}'_0 = \frac{1}{M_N} \sum_{j=0}^N m_j \mathbf{u}_j, \quad \tilde{\mathbf{r}}'_0 = \sum_{j=0}^N \tilde{\mathbf{u}}_j. \quad (\text{A.4})$$

In other words, r'_k is the position of the k th body with respect to the barycenter of the first $k - 1$. To compute the kinetic energy in function of $\tilde{\mathbf{r}}'_k$, we write

$$\begin{aligned} \tilde{\mathbf{u}}_0 &= \frac{m_0}{M_N} \tilde{\mathbf{r}}'_0 - \sum_{k=1}^N \frac{m_0}{M_{k-1}} \tilde{\mathbf{r}}'_k \\ \tilde{\mathbf{u}}_k &= \tilde{\mathbf{r}}'_k + \frac{m_k}{M_N} \tilde{\mathbf{r}}'_0 - \sum_{j>k} \frac{m_k}{M_{j-1}} \tilde{\mathbf{r}}'_j, \text{ for } k = 1 \dots N. \end{aligned} \quad (\text{A.5})$$

The kinetic energy has for expression

$$\begin{aligned} T &= \sum_{k=0}^N \frac{\|\tilde{\mathbf{u}}_k\|^2}{2m_k} \\ &= \frac{1}{2m_0} \left\| \frac{m_0}{M_N} \tilde{\mathbf{r}}'_0 - \sum_{k=1}^N \frac{m_0}{M_{k-1}} \tilde{\mathbf{r}}'_k \right\|^2 + \sum_{k=1}^N \frac{1}{2m_k} \left\| \tilde{\mathbf{r}}'_k + \frac{m_k}{M_N} \tilde{\mathbf{r}}'_0 - \sum_{j>k} \frac{m_k}{M_{j-1}} \tilde{\mathbf{r}}'_j \right\|^2 \\ &= \frac{\|\tilde{\mathbf{r}}'_0\|^2}{2M_N} + \sum_{k=1}^N \left(\frac{1}{m_k} + \frac{1}{M_{k-1}} \right) \frac{\|\tilde{\mathbf{r}}'_k\|^2}{2}. \end{aligned} \quad (\text{A.6})$$

Indeed, all cross product terms cancel out. The kinetic energy is decomposed into the barycenter kinetic energy and the kinetic energy of each body with respect to the barycenter of the previous bodies.

For the potential energy, we need the inverse transformation on the position coordinates. We have

$$\begin{aligned} \mathbf{u}_0 &= \mathbf{r}'_0 - \sum_{k=1}^N \frac{m_k}{M_k} \mathbf{r}'_k \\ \mathbf{u}_k &= \mathbf{r}'_0 + \frac{M_{k-1}}{M_k} \mathbf{r}'_k - \sum_{j>k} \frac{m_j}{M_j} \mathbf{r}'_j, \text{ for } k = 1 \dots N. \end{aligned} \quad (\text{A.7})$$

While this transformation leads to complicated expressions, it should be remark that the Hamiltonian dependence on positions is through terms of the form Δ_{jk} that no longer depends on \mathbf{r}'_0 . This is expected since the barycentre motion should be inertial. As in heliocentric coordinates, we can safely assume $\tilde{\mathbf{r}}'_0 = 0$ and place the origin at the barycenter *i.e.* $\mathbf{r}'_0 = 0$.

In order to write the Hamiltonian as a perturbed sum of Keplerian problems, we rewrite it as

$$\mathcal{H}_{\text{Jacobi}} = \underbrace{\sum_{k=1}^N \frac{M_k}{M_{k-1}} \frac{\|\tilde{\mathbf{r}}'_k\|^2}{2m_k} - \frac{\mathcal{G}M_{k-1}m_k}{r'_k}}_{\mathcal{H}_0^J} + \underbrace{\sum_{k=1}^N \frac{\mathcal{G}M_{k-1}m_k}{r'_k} - \sum_{0 \leq j < k \leq N} \frac{\mathcal{G}m_j m_k}{\Delta_{jk}}}_{\varepsilon \mathcal{H}_1^J}. \quad (\text{A.8})$$

\mathcal{H}_0^J is a sum of N Keplerian Hamiltonians (2.7) of planet mass $\frac{m_k M_{k-1}}{M_k}$ and gravitational coupling constant $\mathcal{G}M_{k-1}$. Let me demonstrate that $\varepsilon \mathcal{H}_1^J$ is linear in ε . \mathcal{H}_1^J

can be rewritten

$$\mathcal{H}_1^J = \sum_{k=1}^N \sum_{j=0}^{k-1} \mathcal{G} m_j m_k \left(\frac{1}{r'_k} - \frac{1}{\Delta_{jk}} \right). \quad (\text{A.9})$$

Among the terms of this sum, only the terms with $j = 0$ can have a size comparable to \mathcal{H}_0^J . We can write for $k = 1 \dots N$,

$$\mathbf{r}'_k = \mathbf{u}_k - \mathbf{u}_0 + \mathbf{u}_0 - \mathbf{R}_{k-1} = \Delta_{0k} - \frac{1}{M_{k-1}} \sum_{j=1}^{k-1} m_j \Delta_{0j} = \Delta_{0k}(1 + O(\varepsilon)). \quad (\text{A.10})$$

Therefore, we can develop the terms $\left(\frac{1}{r'_k} - \frac{1}{\Delta_{0k}} \right)$ for \mathbf{r}'_k close to Δ_{0k} and the leading term is of order ε .

Similarly to the heliocentric case, elliptical elements and Delaunay coordinates can be defined based on the Keplerian problems in \mathcal{H}_0^J . The perturbation can also be developed in these coordinates.

Appendix B

AMD-stability appendices

This appendix regroups the appendices from (Laskar and Petit, 2017) that were originally part of the preprint announce in (Laskar, 2000).

B.1 Intersection of planar orbits

In this section, we present an efficient algorithm for the computation of the intersection of two elliptical orbits in the plane, following (Albouy, 2002). Let us consider an elliptical orbit defined by $(\mu, \mathbf{r}, \dot{\mathbf{r}})$ and let $\mathbf{G} = \mathbf{r} \times \dot{\mathbf{r}}$ be the angular momentum. We recall the definition of the Runge-Laplace vector (2.13)

$$\mathbf{P} = \frac{\dot{\mathbf{r}} \times \mathbf{G}}{\mu m^2} - \frac{\mathbf{r}}{r} \quad (\text{B.1})$$

that is an integral of the motion with coordinates $(e \cos \omega, e \sin \omega)$. One has

$$\mathbf{P} \cdot \mathbf{r} = \frac{G^2}{\mu m^2} - r = p - r \quad (\text{B.2})$$

where $p = a(1 - e^2)$ is the parameter of the ellipse. Let $\mathbf{r} = (x, y)$ in the plane. We can consider the ellipse in the 3-dimensional space (x, y, r) (see figure B.1), as the intersection of the cone

$$r^2 = x^2 + y^2 \quad (\text{B.3})$$

with the plane defined by Eq. (B.2), that is

$$x(e \cos \omega) + y(e \sin \omega) + r = p \quad (\text{B.4})$$

If we consider now two orbits \mathcal{O}_1 and \mathcal{O}_2 . Their intersection is easily obtained as the intersection of the line of intersection of the two planes

$$\begin{aligned} x(e_1 \cos \omega_1) + y(e_1 \sin \omega_1) + r &= p_1 \\ x(e_2 \cos \omega_2) + y(e_2 \sin \omega_2) + r &= p_2 \end{aligned} \quad (\text{B.5})$$

with the cone of equation $r^2 = x^2 + y^2$. Depending of the initial conditions, if \mathcal{O}_1 and \mathcal{O}_2 are distinct, we will get either 0, 1, or 2 solutions.

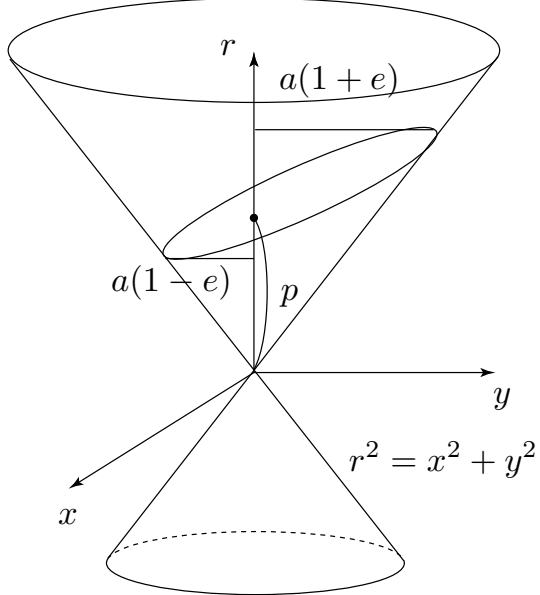


Figure B.1 – Elliptical orbit, as the intersection of the cone $r^2 = x^2 + y^2$ and the plane $\mathcal{P} \cdot \mathbf{r} + r = p$.

B.2 AMD in the averaged equations

In this section, we show that the AMD conserves the same form in the averaged planetary Hamiltonian at all order. More generally, this is true for any integral of H which does not depends on the longitudes λ_k . Let

$$H = H_0(\Lambda) + \varepsilon H_1(\Lambda, \lambda, J, \phi) \quad (\text{B.6})$$

be a perturbed Hamiltonian system, and let $K(\Lambda, J, \phi)$ be a first integral of $H(\Lambda, \lambda, J, \phi)$ (such that $\{K, H\} = 0$, where $\{\cdot, \cdot\}$ is the usual Poisson bracket), and independent of λ . And let

$$H' = e^{L_S} H \quad (\text{B.7})$$

be a formal averaging of H with respect to λ following the method detailed in 2.4.1. If $S(\Lambda, \lambda, J, \phi)$ is a generator defined as below (equations B.9, B.11, B.12), such that H' is independent of λ . Then, K is an integral of H' , *i.e.*

$$\{K, H'\} = 0 \quad (\text{B.8})$$

The generator $S = \varepsilon S_1 + \varepsilon^2 S_2 + \varepsilon^3 S_3 + \dots$ is obtained formally through the identification order by order

$$\begin{aligned} H'_0 &= H_0 \\ H'_1 &= H_1 + \{H_0, S_1\} \\ H'_2 &= \{H_0, S_2\} + \frac{1}{2}\{\{H_0, S_1\}, S_1\} + \{H_1, S_1\} \\ &\dots \end{aligned} \quad (\text{B.9})$$

For any function $G(\Lambda, \lambda, J, \phi)$, let

$$\langle G \rangle_\lambda = \frac{1}{(2\pi)^N} \int G d^N \boldsymbol{\lambda} \quad (\text{B.10})$$

be the average of G over all the angles λ_k . For each $n \geq 1$, the S_n are obtained through the resolution of an equation of the form

$$H'_n = \{H_0, S_n\} + \mathcal{R}_n \quad (\text{B.11})$$

where \mathcal{R}_n belongs to $\mathcal{L}(H_0, H_1, S_1, \dots, S_{n-1})$, the Lie algebra generated by $(H_0, H_1, S_1, \dots, S_{n-1})$. H'_n will be the averaged part of \mathcal{R}_n , $\langle \mathcal{R}_n \rangle_\lambda$ and S_n is obtained by solving the homological equation

$$\{H_0, S_n\} = \mathcal{R}_n - \langle \mathcal{R}_n \rangle_\lambda \quad (\text{B.12})$$

We will show by recurrence that $\{K, S_n\} = 0$ for all $n \geq 1$. First let us notice that as $\{K, H_0\} = 0$, we have also $\{K, H_1\} = 0$. As K is independent of λ_k , we have also for all G

$$\langle \{K, G\} \rangle_\lambda = \{K, \langle G \rangle_\lambda\} \quad (\text{B.13})$$

This can be seen by formal expansion of G in a Fourier series $G = \sum g_k e^{ik\lambda}$. We have thus $\langle G \rangle_\lambda = g_0$. Let us assume now that $\{K, S_k\} = 0$ for all $k \leq n$. As $\mathcal{R}_{n+1} \in \mathcal{L}(H_0, H_1, S_1, \dots, S_n)$, we have also $\{K, \mathcal{R}_{n+1}\} = 0$, and from (B.13) $\{K, \langle \mathcal{R}_{n+1} \rangle_\lambda\} = 0$ and thus,

$$\{K, \{H_0, S_{n+1}\}\} = 0 \quad (\text{B.14})$$

Using Jacobi identity, as $\{K, H_0\} = 0$, we have

$$\{H_0, \{K, S_{n+1}\}\} = 0 \quad (\text{B.15})$$

The solution of the homological equation (B.12) is unique up to a term independent of λ . But as $\langle \{K, S_{n+1}\} \rangle_\lambda = 0$, then the only possible solution for (B.15) is

$$\{K, S_{n+1}\} = 0. \quad (\text{B.16})$$

In the same way, as $H'_1 = \langle H_1 \rangle_\lambda$, we have $\{K, H'_1\} = \langle \{K, H_1\} \rangle_\lambda = 0$. Thus $\{K, \{H_0, S_1\}\} = 0$, by Jacobi identity, $\{H_0, \{K, S_1\}\} = 0$, and as previously, $\{K, S_1\} = 0$. Our recurrence is thus complete and it follows immediately that $\{K, H'\} = 0$.

B.3 Special values of $C_c(\alpha, \gamma)$

This annex provides the detailed computations and proofs of the results of section 3.3.2

We have shown that $e_c(\alpha, \gamma)$ is a differentiable function of γ , which is monotonic (3.18) and bounded ($e_c(a, \gamma) \in [0, 1]$). The limit $e_c(\alpha, 0) = \lim_{\gamma \rightarrow 0} e_c(\alpha, \gamma)$ exists for all $\alpha \in]0, 1]$. If $e_c(\alpha, \gamma)$ is a solution of equation (3.12), it will also be a solution of the following cubic equation (in e), which is directly obtained from (3.12) by squaring, multiplication, and simplification by $\alpha(1 + e)$

$$K(e, \alpha, \gamma) = \alpha(\gamma^2 - \alpha)e^3 - (2 - \alpha)(\gamma^2 - \alpha)e^2 - (1 - \alpha^2)e + (1 - \alpha)^2 = 0 \quad (\text{B.17})$$

B.3.1 Asymptotic value of $C_c(\alpha, \gamma)$ for $\gamma \rightarrow 0$

As $e_c(\alpha, \gamma)$, is a continuous function of γ , when $\gamma \rightarrow 0$, the limits $e_{0c}(\alpha)$ will satisfy the limit equation

$$K_0(e, \alpha) = (1 - \alpha - \alpha e)^2(1 - e) = 0 \quad (\text{B.18})$$

with solutions $e_0 = 1/\alpha - 1$ and $e_1 = 1$. Depending on α several cases are treated:

$\alpha < 1/2$: We have then $e_0 > 1$, and the only possibility for $e_c(\alpha, 0)$ is $e_1 = 1$ as it is the only root of (B.18) which belongs to $[0, 1]$ we have thus

$$\lim_{\gamma \rightarrow 0} e_c(\alpha, \gamma) = 1 \quad (\text{B.19})$$

We have then

$$\begin{aligned} \lim_{\gamma \rightarrow 0} e'_c(\alpha, \gamma) &= 1 - 2\alpha ; \\ \lim_{\gamma \rightarrow 0} C_c(\alpha, \gamma) &= 1 - 2\sqrt{\alpha(1 - \alpha)} ; \end{aligned} \quad (\text{B.20})$$

In order to study the behaviour of $e_c(\alpha, \gamma)$ in the vicinity of $\gamma = 0$, we can differentiate $K(e_c(\alpha, \gamma), \gamma) = 0$ twice, which gives

$$\frac{de_c}{d\gamma}(\alpha, 0) = 0 ; \quad \frac{d^2e_c}{d\gamma^2}(\alpha, 0) = \frac{4(\alpha - 1)}{(1 - 2\alpha)^2} < 0 . \quad (\text{B.21})$$

thus $e_c(\alpha, \gamma)$ is decreasing with respect to γ at $\gamma = 0$.

The second order development of C_c gives

$$C_c(\alpha, \gamma) = 1 - 2\sqrt{\alpha(1 - \alpha)} + \gamma\sqrt{\alpha} - \gamma^2\sqrt{\frac{1}{\alpha} - 1} + O(\gamma^3). \quad (\text{B.22})$$

$\alpha > 1/2$: In this case, $e_0 < 1$. As $e_c(\alpha, \gamma) \in]0, e_0[$, we have $e_c(\alpha, 0) \in [0, e_0]$, which gives as the unique possibility

$$\lim_{\gamma \rightarrow 0} e_c(\alpha, \gamma) = e_0 \quad (\text{B.23})$$

with 1

$$\lim_{\gamma \rightarrow 0} e'_c(\alpha, \gamma) = 0 ; \quad \lim_{\gamma \rightarrow 0} C_c(\alpha, \gamma) = 0 ; \quad (\text{B.24})$$

By setting $\gamma = 0$ in (3.18), we obtain also

$$\frac{de_c}{d\gamma}(\alpha, 0) = -\frac{e_0}{\alpha^{3/2}\sqrt{1 - e_0^2}} < 0 . \quad (\text{B.25})$$

The development of C_c gives

$$C_c(\alpha, \gamma) = \gamma \left(\sqrt{\alpha} - \sqrt{2 - \frac{1}{\alpha}} \right) - \frac{\gamma^2}{2\alpha - 1} \frac{(1 - \alpha)^2}{\alpha} + O(\gamma^3). \quad (\text{B.26})$$

$\alpha = 1/2$: In this case, $e_0 = 1$, and the only solution is

$$\lim_{\gamma \rightarrow 0} e_c(\alpha, \gamma) = 1 \quad (\text{B.27})$$

and

$$\lim_{\gamma \rightarrow 0} e'_c(\alpha, \gamma) = 0 ; \quad \lim_{\gamma \rightarrow 0} C_c(\alpha, \gamma) = 0 ; \quad (\text{B.28})$$

Moreover, equation (B.17) becomes $\gamma^2 2e^2(3 - e) = (1 - e)^3$. We obtain thus the asymptotic value for $e_c(1/2, \gamma)$ when $\gamma \rightarrow 0$ as

$$1 - e_c\left(\frac{1}{2}, \gamma\right) \sim (4\gamma)^{2/3}. \quad (\text{B.29})$$

For $\alpha = 1/2$, the development of C_c in γ contains non-polynomial terms in γ giving

$$C_c(1/2, \gamma) = \frac{\gamma}{\sqrt{2}} - 2^{-1/3}\gamma^{4/3} - 2^{-4/3}\gamma^2 + O(\gamma^{8/3}) \quad (\text{B.30})$$

B.3.2 Asymptotic value of $C_c(\alpha, \gamma)$ for $\gamma \rightarrow +\infty$

This case is more simple. If $e_c(\alpha, \gamma)$ is a solution of (3.12), then it will also be a solution of eq. (B.17), and thus of

$$\frac{K(e, \alpha, \gamma)}{\gamma^2} = 0 \quad (\text{B.31})$$

As $e_c(\alpha, \gamma)$ is monotonic and bounded, it has a limit when $\gamma \rightarrow +\infty$, which will verify the limit equation (B.31), when $\gamma \rightarrow +\infty$, that is

$$K_\infty(\alpha, e) = e^2(2 - \alpha - \alpha e) = 0 \quad (\text{B.32})$$

As $0 < \alpha < 1$, the only solution is $e = 0$, and thus

$$\lim_{\gamma \rightarrow +\infty} e_c(\alpha, \gamma) = 0 \quad (\text{B.33})$$

and

$$\lim_{\gamma \rightarrow +\infty} e'_c(\alpha, \gamma) = 1 - \alpha ; \quad \lim_{\gamma \rightarrow +\infty} C_c(\alpha, \gamma) = 1 - \sqrt{\alpha(2 - \alpha)} ; \quad (\text{B.34})$$

and more precisely,

$$C(\alpha, \gamma) = 1 - \sqrt{\alpha(2 - \alpha)} - \frac{1}{2\gamma} \frac{\sqrt{\alpha}(1 - \alpha)^2}{2 - \alpha} + O\left(\frac{1}{\gamma^2}\right) \quad (\text{B.35})$$

B.3.3 Study of $C_c(\alpha, \gamma)$ for $\gamma = 1$ and $\gamma = \sqrt{\alpha}$.

For $\gamma = 1$ or $\gamma = \sqrt{\alpha}$, we can also obtain simple expressions for $C_c(\alpha, \gamma)$. Indeed, If $\gamma = 1$, $K(e, \alpha, \gamma)$ factorises in $(1 - \alpha)(1 + e)(\alpha e^2 - 2e + 1 - \alpha)$ and we have a single solution for e_c in the interval $[0, 1]$,

$$e_c(\alpha, 1) = \frac{1 - \sqrt{1 - \alpha + \alpha^2}}{\alpha} ;$$

$$e'_c(\alpha, 1) = \sqrt{1 - \alpha + \alpha^2} - \alpha ; \quad (\text{B.36})$$

and

$$C_c(\alpha, 1) = \sqrt{\alpha} - \frac{\sqrt{\alpha - 2 + 2\sqrt{1 - \alpha + \alpha^2}}}{\sqrt{\alpha}} + 1 - \sqrt{\alpha}\sqrt{1 - 2\alpha + 2\sqrt{1 - \alpha + \alpha^2}} \quad (\text{B.37})$$

For $\gamma = \sqrt{\alpha}$, the cubic equation (B.17) reduces to

$$K(\alpha, \sqrt{\alpha}) = -(1 - \alpha^2)e + (1 - \alpha)^2 = 0 \quad (\text{B.38})$$

with the single solution

$$e_c(\alpha, \sqrt{\alpha}) = e'_c(\alpha, \sqrt{\alpha}) = \frac{1 - \alpha}{1 + \alpha} \quad (\text{B.39})$$

and

$$C_c(\alpha, \sqrt{\alpha}) = (1 - \sqrt{\alpha})^2 \quad (\text{B.40})$$

B.3.4 $C_c(\alpha, \gamma)$ for $\alpha \rightarrow 1$

Let us denote $\eta = 1 - \alpha$. The equation (B.17) can be developed in η ,

$$K(e, \alpha, \gamma) = (\gamma^2 - 1)e^2(e - 1) + \eta e \left((\gamma^2 - 1)(e - e^2) - 2 \right) + \eta^2(1 - e - e^2 - e^3) \quad (\text{B.41})$$

The zeroth and first orders of equation (B.41) implies that e_c must go to zero, moreover, it scales with η . We write $e_c(\eta, \gamma) = \kappa(\gamma)\eta + o(\eta)$. We inject this expression in (B.41) and keep the second order in η

$$(\gamma^2 - 1)\kappa^2 + 2\kappa - 1 = 0. \quad (\text{B.42})$$

We keep the solution that is positive and continuous in γ and we have

$$e_c(\eta, \gamma) = \frac{\eta}{\gamma + 1} + o(\eta). \quad (\text{B.43})$$

If we now compute C_c developed for $\alpha \rightarrow 1$ we have

$$C_c(1 - \eta, \gamma) = k(\gamma)\eta^2 + O(\eta^3) = \frac{1}{2} \frac{\gamma}{\gamma + 1} \eta^2 + O(\eta^3) \quad (\text{B.44})$$

Appendix C

Details on the computation of the MMR overlap criterion

C.1 Expression of the first-order resonant Hamiltonian

We use the method proposed in (Laskar, 1991) and (Laskar and Robutel, 1995) to determine the expression of the planetary perturbation \mathcal{H}_1 . \mathcal{H}_1 can be decomposed into a part from the gravitational potential between planets U_1 and a kinetic part T_1 as $\varepsilon\mathcal{H}_1 = U_1 + T_1$, with

$$U_1 = -G \frac{m_1 m_2}{\Delta_{12}} = -\frac{m_1}{m_0} \frac{\mu^2 m_2^3}{\Lambda_2^2} \frac{a_2}{\Delta_{12}} \quad (\text{C.1})$$

$$T_1 = \frac{\tilde{\mathbf{r}}_1 \cdot \tilde{\mathbf{r}}_2}{m_0} + \frac{1}{2m_0} (\|\tilde{\mathbf{r}}_1\|^2 + \|\tilde{\mathbf{r}}_2\|^2). \quad (\text{C.2})$$

The difficulty comes from the development of a_2/Δ_{12} and its expression in terms of Poincaré variables. We note S , the angle between \mathbf{r}_1 and \mathbf{r}_2 . We have

$$\Delta_{12}^2 = r_1^2 + r_2^2 - 2r_1 r_2 \cos S. \quad (\text{C.3})$$

Let us denote $\rho = u_1/u_2$, a_2/Δ_{12} can be rewritten

$$\frac{a_2}{\Delta_{12}} = \frac{a_2}{u_2} \left(1 + \rho^2 - 2\rho \cos S\right)^{-1/2} = \frac{a_2}{u_2} (A + V)^{-1/2}, \quad (\text{C.4})$$

where we denote

$$\begin{aligned} A &= 1 + \alpha^2 - 2\alpha \cos(\lambda_1 - \lambda_2), \\ V &= \alpha^2 V_2 + 2\alpha V_1, \\ V_1 &= \cos(\lambda_1 - \lambda_2) - \frac{\rho}{\alpha} \cos S, \\ V_2 &= \left(\frac{\rho}{\alpha}\right)^2 - 1. \end{aligned} \quad (\text{C.5})$$

V is at least of order one in eccentricity. We can therefore develop (C.4) for small V . We only keep the terms of first order in eccentricity,

$$\frac{a_2}{\Delta_{12}} = \frac{a_2}{r_2} A^{-1/2} - \frac{1}{2} \frac{a_2}{r_2} V A^{-3/2} + O(V^2). \quad (\text{C.6})$$

The well-known development of the circular coplanar motion A gives (*e.g.*, Poincaré, 1905)

$$A^{-s} = \frac{1}{2} \sum_{k \in \mathbb{Z}} b_s^{(k)}(\alpha) e^{\iota k(\lambda_1 - \lambda_2)}, \quad (\text{C.7})$$

where $b_s^{(k)}(\alpha)$ are the Laplace coefficients (4.21).

Because of the averaging over the non-resonant fast angles, the non-vanishing terms have a dependence on λ_i of the form $j((p+1)\lambda_2 - p\lambda_1)$. Since we only keep the terms of first order in eccentricity, the d'Alembert's rule (4.6) imposes $j = \pm 1$. Let us compute the first-order development of a_2/r_2 and V in terms of Poincaré variables and combine these expressions with $A^{-1/2}$ and $A^{-3/2}$ in order to select the non-vanishing terms.

Let us denote $z_i = e^{\iota \lambda_i}$ and $z = z_1 \bar{z}_2 = e^{\iota(\lambda_1 - \lambda_2)}$. The researched terms are of the form

$$e^{\iota((p+1)\lambda_2 - p\lambda_1)} = z_2 z^{-p} = z_1 z^{-(p+1)} \quad (\text{C.8})$$

$$e^{-\iota((p+1)\lambda_2 - p\lambda_1)} = \bar{z}_2 z^p = \bar{z}_1 z^{p+1}. \quad (\text{C.9})$$

Let us denote

$$X_i = x_i \sqrt{\frac{2}{\Lambda_i}} = \sqrt{\frac{2C_i}{\Lambda_i}} e^{\iota \varpi_i} = e_i e^{\iota \varpi_i} + O(e_i^2), \quad (\text{C.10})$$

the first term in the development (C.6) gives

$$\frac{a_2}{r_2} A^{-1/2} = \frac{1}{2} \left(1 + \frac{1}{2} \bar{X}_2 z_2 + \frac{1}{2} X_2 \bar{z}_2 \right) \sum_{k \in \mathbb{Z}} b_{1/2}^{(k)}(\alpha) z^k + O(e_2^2). \quad (\text{C.11})$$

The contributing term has for expression

$$\frac{1}{4} b_{1/2}^{(p)}(\alpha) (\mathfrak{X}_2 + \bar{\mathfrak{X}}_2), \quad (\text{C.12})$$

where $\mathfrak{X}_i = \mathfrak{x}_i \sqrt{2/\Lambda_i} = X_i e^{-\iota((p+1)\lambda_2 - p\lambda_1)}$.

For the computation of the second term of (C.6), the only contribution comes from V since $a_2/r_2 \sim 1$. We define

$$U = \bar{X}_1 z_1 - \bar{X}_2 z_2 = \sqrt{\frac{2C_1}{\Lambda_1}} e^{\iota(\lambda_1 - \varpi_1)} - \sqrt{\frac{2C_2}{\Lambda_2}} e^{\iota(\lambda_2 - \varpi_2)}.$$

V can be expressed as a function of z, \bar{z}, U and \bar{U} . Indeed we have

$$\frac{\rho}{\alpha} = 1 - \frac{1}{2}(U + \bar{U}) + O(e^2) \quad (\text{C.13})$$

and

$$\cos S = \frac{1}{2} (z + \bar{z} + U(z - \bar{z}) + \bar{U}(\bar{z} - z)) + O(e^2), \quad (\text{C.14})$$

where $O(e^2)$ corresponds to terms of total degree in eccentricities of at least 2. We deduce from these two last expressions that

$$V_1 = \frac{1}{4} (U(3\bar{z} - z) + \bar{U}(3z - \bar{z})) + O(e^2), \quad (\text{C.15})$$

$$V_2 = -(U + \bar{U}) + O(e^2). \quad (\text{C.16})$$

We can therefore write¹

$$V = \frac{1}{2}(UZ + \bar{U}\bar{Z}) + O(e^2), \quad (\text{C.17})$$

where $Z = \alpha(3\bar{z} - 2\alpha - z)$. With this expression of V , it is easy to gather the corresponding terms and the second term in the development (C.6) gives the contributing term

$$\begin{aligned} & -\frac{\alpha}{8} (3b_{3/2}^{(p)}(\alpha) - 2\alpha b_{3/2}^{(p+1)}(\alpha) - b_{3/2}^{(p+2)}(\alpha)) (\mathfrak{X}_1 + \bar{\mathfrak{X}}_1) + \\ & \frac{\alpha}{8} (3b_{3/2}^{(p-1)}(\alpha) - 2\alpha b_{3/2}^{(p)}(\alpha) - b_{3/2}^{(p+1)}(\alpha)) (\mathfrak{X}_2 + \bar{\mathfrak{X}}_2). \end{aligned} \quad (\text{C.18})$$

After gathering the terms (C.12, C.18), we can give the expression of the resonant Hamiltonian

$$\mathcal{H} = \mathcal{K} + R_1(\mathfrak{X}_1 + \bar{\mathfrak{X}}_1) + R_2(\mathfrak{X}_2 + \bar{\mathfrak{X}}_2), \quad (\text{C.19})$$

where

$$R_1 = -\varepsilon \frac{\gamma}{1+\gamma} \frac{\mu^2 m_2^3}{\Lambda_2^2} \frac{1}{2} \sqrt{\frac{2}{\Lambda_1}} \mathcal{R}_1(\alpha), \quad (\text{C.20})$$

$$R_2 = -\varepsilon \frac{\gamma}{1+\gamma} \frac{\mu^2 m_2^3}{\Lambda_2^2} \frac{1}{2} \sqrt{\frac{2}{\Lambda_2}} \mathcal{R}_2(\alpha) \quad (\text{C.21})$$

$$(C.22)$$

with $\gamma = m_1/m_2$, and

$$\mathcal{R}_1(\alpha) = -\frac{\alpha}{4} (3b_{3/2}^{(p)}(\alpha) - 2\alpha b_{3/2}^{(p+1)}(\alpha) - b_{3/2}^{(p+2)}(\alpha)), \quad (\text{C.23})$$

$$\mathcal{R}_2(\alpha) = \frac{\alpha}{4} (3b_{3/2}^{(p-1)}(\alpha) - 2\alpha b_{3/2}^{(p)}(\alpha) - b_{3/2}^{(p+1)}(\alpha)) + \frac{1}{2} b_{1/2}^{(p)}(\alpha). \quad (\text{C.24})$$

The kinetic part T_1 has no contribution to the averaged resonant Hamiltonian for $p > 1$. Indeed, as explained above, due to the d'Alembert rule, the first-order terms must have an angular dependence of the form $j(-p\lambda_1 + (p+1)\lambda_2)$. At the first order in ε , such a term can only be present in the development of the inner

¹ In Laskar and Robutel, 1995 the first-order expression of V is written $W_1 = (UZ + \bar{U}\bar{Z})$ instead of $W_1 = (UZ + \bar{U}\bar{Z})/2$. This misprint in equation (47) of (Laskar and Robutel, 1995) is transmitted as well in equation (51). It has no consequences in the results of the paper.

product $\tilde{\mathbf{r}}_1 \cdot \tilde{\mathbf{r}}_2$. At the first order in eccentricities, we have (Laskar and Robutel, 1995)

$$\tilde{\mathbf{r}}_1 \cdot \tilde{\mathbf{r}}_2 = \frac{\mu^2 m_1^2 m_2^2}{\Lambda_1 \Lambda_2} \Re((e^{\iota w_1} + X_1)(e^{-\iota w_2} + \bar{X}_2)) + O(e^2), \quad (\text{C.25})$$

where w_j is the true longitude of the planet j . The only term with the good angular dependence comes from $\Re e^{\iota(w_1-w_2)}$ since the other first-order terms only depend on one mean longitude. The development of $e^{\iota(w_1-w_2)}$ at the first order in eccentricities gives

$$e^{\iota(w_1-w_2)} = z + z_1 z \bar{X}_1 - \bar{z}_2 X_1 + z \bar{z}_2 X_2 - z_1 \bar{X}_2 + O(e^2). \quad (\text{C.26})$$

Thus for $p > 1$, \hat{T}_1 has no contribution to the averaged Hamiltonian, and for $p = 1$ we have

$$\mathcal{H}_{1,i} = \frac{1}{2m_0} \frac{\mu m_1^2}{\Lambda_1} \frac{\mu m_2^2}{\Lambda_2} (\mathfrak{X}_2 + \bar{\mathfrak{X}}_2). \quad (\text{C.27})$$

C.1.1 Asymptotic expression of the resonant coefficients

We present the method we used to obtain the analytic development of the coefficients r_1 and r_2 defined in equations (C.23) and (C.24). Using the expression of $b_s^{(k)}(\alpha)$, we have

$$\mathcal{R}_1(\alpha) = -\frac{\alpha}{4\pi} \int_{-\pi}^{\pi} \left[\frac{3 \cos(p\phi) - 2\alpha \cos((p+1)\phi) - \cos((p+2)\phi)}{(1 + \alpha^2 - 2\alpha \cos \phi)^{3/2}} \right] d\phi. \quad (\text{C.28})$$

We can rewrite this expression

$$\mathcal{R}_1(\alpha) = -\frac{\alpha}{2\pi} \int_{-\pi}^{\pi} \left[\frac{(\cos(\phi) - \alpha) \cos((p+1)\phi)}{(1 + \alpha^2 - 2\alpha \cos \phi)^{3/2}} + \frac{2 \sin \phi \sin((p+1)\phi)}{(1 + \alpha^2 - 2\alpha \cos \phi)^{3/2}} \right] d\phi. \quad (\text{C.29})$$

We make the change of variable $\phi = (1 - \alpha)u$ in the integrals. Factoring $(1 - \alpha)^3$, the denominators in the integrals can be developed for $\alpha \rightarrow 1$

$$(1 + \alpha^2 - 2\alpha \cos \phi)^{3/2} = \left(1 + 2\alpha \frac{1 - \cos((1 - \alpha)u)}{(1 - \alpha)^2} \right)^{3/2} \simeq (1 - \alpha)^3 (1 + u^2)^{3/2}. \quad (\text{C.30})$$

Using the relation $\alpha_0 = (p/(p+1))^{2/3}$, the numerators can be developed

$$\mathcal{N}_1 = (\cos((1 - \alpha)u) - \alpha) \cos((p+1)(1 - \alpha)u) \simeq (1 - \alpha) \cos\left(\frac{2u}{3}\right), \quad (\text{C.31})$$

$$\mathcal{N}_2 = 2 \sin((1 - \alpha)u) \sin((p+1)(1 - \alpha)u) \simeq 2(1 - \alpha)u \sin\left(\frac{2u}{3}\right). \quad (\text{C.32})$$

Therefore, we deduce the equivalent of \mathcal{R}_1 for $p \rightarrow +\infty$

$$\begin{aligned} \mathcal{R}_1(\alpha) &\sim -\frac{3(p+1)}{4\pi} \int_{-\infty}^{+\infty} \frac{\cos\left(\frac{2u}{3}\right) + 2u \sin\left(\frac{2u}{3}\right)}{(1 + u^2)^{3/2}} du \\ &\sim -\frac{K_1(2/3) + 2K_0(2/3)}{\pi} (p+1) \end{aligned} \quad (\text{C.33})$$

$$\sim 0.802(p+1), \quad (\text{C.34})$$

where $K_\nu(x)$ is the modified Bessel function of the second kind. Similarly, we have $\mathcal{R}_2 \sim -\mathcal{R}_1$ since the additional term is of lower order in p .

We can obtain the constant term of the development by using the second order expression of α_0 and developing the integrand to the next order in $(1 - \alpha)$. We give here the numerical expressions of the two developments

$$\mathcal{R}_1(\alpha_0) = -0.802(p + 1) - 0.199 + O(p^{-1}), \quad (\text{C.35})$$

$$\mathcal{R}_2(\alpha_0) = 0.802(p + 1) + 0.421 + O(p^{-1}). \quad (\text{C.36})$$

C.2 Development of the Keplerian part

We show here that the first order in $(\hat{C} - \Delta\hat{G})$ of the Keplerian part vanishes and give the details of the computation for the second order. The Keplerian part can be written

$$\hat{\mathcal{K}} = -\frac{\mu^2 m_1^3}{2(\hat{\Lambda}_{1,0} - p(\hat{C} - \Delta\hat{G}))^2} - \frac{\mu^2 m_2^3}{2(\hat{\Lambda}_{2,0} + (p + 1)(\hat{C} - \Delta\hat{G}))^2}. \quad (\text{C.37})$$

Therefore, the first order in $\hat{C} - \Delta\hat{G}$ has for expression

$$\mathcal{K}_1(\hat{C} - \Delta\hat{G}) = -\frac{\mu^2 m_2^3}{\hat{\Lambda}_{2,0}^3} \left(\frac{p\gamma^3 \hat{\Lambda}_{2,0}^3}{\hat{\Lambda}_{1,0}^3} - (p + 1) \right) (\hat{C} - \Delta\hat{G}) = 0, \quad (\text{C.38})$$

since we have

$$\left(\frac{\hat{\Lambda}_{1,0}}{\hat{\Lambda}_{2,0}} \right)^3 = \gamma^3 \frac{p}{p + 1}. \quad (\text{C.39})$$

The second-order term has for coefficient

$$\begin{aligned} \frac{1}{2}\mathcal{K}_2 &= -\frac{3}{2}\mu^2 m_2^3 \left(\frac{\gamma^3 p^2}{\hat{\Lambda}_{1,0}^4} + \frac{(p + 1)^2}{\hat{\Lambda}_{2,0}^4} \right) \\ &= -\frac{3}{2}\mu^2 m_2^3 (\gamma + \alpha_0)^4 \left(\frac{p^2}{\gamma \left(\frac{p}{p+1} \right)^4} + \frac{(p + 1)^2}{\alpha_0^4} \right) \\ &= -\frac{3}{2}\mu^2 m_2^3 (\gamma + \alpha_0)^4 (p + 1)^2 \frac{\alpha_0^4 \left(\frac{p+1}{p} \right)^2 + \gamma}{\gamma \alpha_0^4} \\ \frac{1}{2}\mathcal{K}_2 &= -\frac{3}{2}\mu^2 m_2^3 \frac{(\gamma + \alpha_0)^5}{\gamma \alpha_0^4} (p + 1)^2. \end{aligned} \quad (\text{C.40})$$

C.3 Width of the resonance island

We detail in this appendix the computation of the resonance island's width (see also Ferraz-Mello, 2007, Appendix C).

C.3.1 Coefficients-roots relations

We first explain how the width of the resonance can be related to the position of the saddle point on the X -axis. The resonant island has a maximal width on the X -axis. Therefore we need to compute the expression of the intersections of the separatrices with the X -axis.

Let us note \mathcal{H}_3 , the energy at the saddle point $(X_3, 0)$. Since the energy of the separatrices is \mathcal{H}_3 as well, the two intersections of the separatrices with the X -axis are the solution of the equation

$$\mathcal{H}_A(X, 0) = -\frac{X^4}{8} + \frac{\mathcal{I}_0 X^2}{2} - X = \mathcal{H}_3 + \frac{\mathcal{I}_0^2}{2} = \tilde{\mathcal{H}}_3. \quad (\text{C.41})$$

This equation has three solutions X_1^* , X_2^* , and X_3 which has a multiplicity of 2. We can therefore rewrite the equation as

$$(X - X_1^*)(X - X_2^*)(X - X_3)^2 = X^4 - 4\mathcal{I}_0 X^2 + 8X + 8\tilde{\mathcal{H}}_3. \quad (\text{C.42})$$

We detail here the relations between the coefficients and the roots of the polynomial equation (C.42). We have

$$X_1^* + X_2^* + 2X_3 = 0 \quad (\text{C.43})$$

$$X_1^* X_2^* + 2X_3(X_1^* + X_2^*) + X_3^2 = -2\mathcal{I}_0 \quad (\text{C.44})$$

$$X_1^* X_2^* X_3^2 = 8\tilde{\mathcal{H}}_3 = -X_3^4 + 2\mathcal{I}_0 X_3^2 - 8X_3. \quad (\text{C.45})$$

From relation (C.43), we have directly $X_1^* + X_2^* = -2X_3$, and since

$$4X_1^* X_2^* = (X_1^* + X_2^*)^2 - (X_1^* - X_2^*)^2, \quad (\text{C.46})$$

we can express $(X_1^* - X_2^*)^2$ as a function of X_3 thanks to eq. (C.44) and (C.45)

$$|X_1^* - X_2^*| = \frac{4}{\sqrt{X_3}}. \quad (\text{C.47})$$

We thus deduce the expressions of X_1^* and X_2^* as functions of X_3

$$X_1^* = -X_3 - \frac{2}{\sqrt{X_3}}, \quad X_2^* = -X_3 + \frac{2}{\sqrt{X_3}}. \quad (\text{C.48})$$

As explained in section 4.3.1, we obtain the width of the resonance in terms of variation of α as a function of X_3 (equation 4.55). We can use this expression to obtain the width of the resonance for particular cases detailed in the following subsections.

C.3.2 Width for initially circular orbits

In the case of initially circular orbits, the minimal AMD to enter the resonance is 0. For $C_{\min} = 0$, the equation (4.57) gives $X_3 = 2^{2/3}$ as a solution and we have

$$\frac{\delta\alpha}{\alpha_0} = \frac{8 \times 2^{1/3} \mathcal{R}^{2/3}}{3^{2/3}} \varepsilon^{2/3} (p+1)^{1/3} = 4.18 \varepsilon^{2/3} (p+1)^{1/3}. \quad (\text{C.49})$$

We find here the same width of resonance as (Deck *et al.*, 2013).

C.3.3 Width for highly eccentric orbits

If we consider a system with $C_{\min} \gg \chi^{2/3}$, our formalism gives us the result first proposed by Mustill and Wyatt, 2012 and improved by Deck *et al.*, 2013 for eccentric orbits. In this case, we can inject the approximation (4.61) of X_3 in the expression (4.55) of $\delta\alpha$ and obtain

$$\frac{\delta\alpha}{\alpha_0} = \frac{8\sqrt{\mathcal{R}}}{\sqrt{3}} \sqrt{\varepsilon(p+1)} c_m^{1/4} = 4.14 \sqrt{\varepsilon(p+1)} c_m^{1/4}. \quad (\text{C.50})$$

This result is also similar to Deck's one, using $\sqrt{c_m}$ instead of σ (Deck *et al.*, 2013, equation (25)).

C.3.4 Width for low eccentric orbits

For $C_{\min} \ll \chi^{2/3}$, we propose here a new expression of the width of resonance thanks to the expression (4.62). This expression is an extension of the circular result presented above (C.49). Let us develop $\sqrt{X_3}$ for $C_{\min} \ll \chi^{2/3}$

$$\sqrt{X_3} = \sqrt{2^{2/3} + \frac{2}{3^{2/3}\mathcal{R}^{1/3}} \frac{(p+1)^{1/3}}{\varepsilon^{1/3}} \sqrt{c_m}} \simeq 2^{1/3} \left(1 + \frac{1}{6^{2/3}\mathcal{R}^{1/3}} \frac{(p+1)^{1/3}}{\varepsilon^{1/3}} \sqrt{c_m} \right). \quad (\text{C.51})$$

Therefore for low-eccentricity systems, we have

$$\frac{\delta\alpha}{\alpha_0} \simeq \frac{\delta\alpha_c}{\alpha_0} \left(1 + \frac{1}{6^{2/3}\mathcal{R}^{1/3}} \frac{(p+1)^{1/3}}{\varepsilon^{1/3}} \sqrt{c_m} \right), \quad (\text{C.52})$$

where $\delta\alpha_c$ is the width of the resonance for initially circular orbits defined in (C.49).

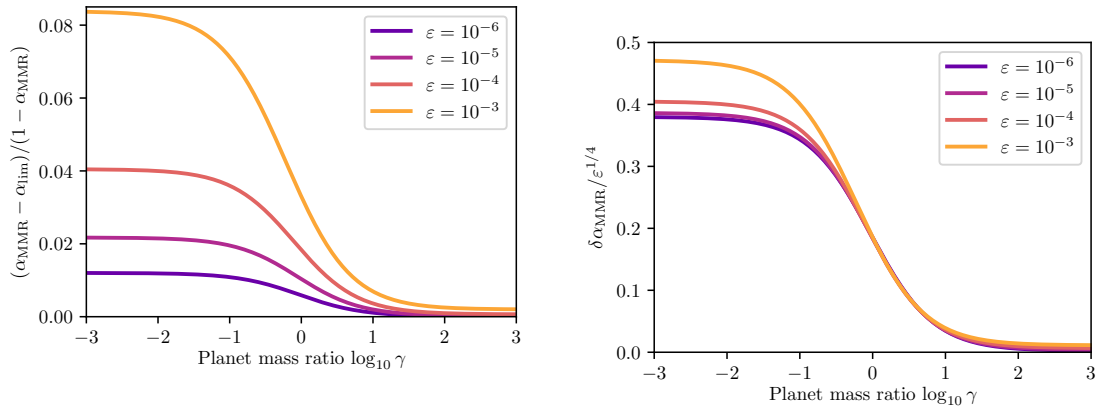
C.4 Influence of γ on the limit α_{MMR}

As can be seen in Figure 4.6a, the solution α_{MMR} of equation (4.98) is not the exact limit where the collision and the MMR criteria are equal. Indeed, equation (4.98) is obtained after the development of C_c^{col} and C_c^{MMR} for α close to 1. Since at first order, both expressions have the same dependence on γ , α_{MMR} does not depend on γ . In order to study the dependence on γ of the limit α_{\lim} where $C_c^{\text{col}} = C_c^{\text{MMR}}$, we plot in Figure (C.1a), for different values of ε , the quantity

$$\delta\alpha_{\text{MMR}}(\varepsilon, \gamma) = \frac{\alpha_{\text{MMR}}(\varepsilon) - \alpha_{\lim}(\varepsilon, \gamma)}{1 - \alpha_{\text{MMR}}(\varepsilon)}, \quad (\text{C.53})$$

which gives the error made when approximating α_{\lim} by α_{MMR} . We see that all the curves have the same shape with an amplitude increasing with ε . For high γ , α_{MMR} is very accurate even for the greatest values of ε . Moreover, the error is maximum for very small γ and always within a few percent.

The amplitude of the error scales with $1 - \alpha_{\text{MMR}} \propto \varepsilon^{1/4}$ as we can see in the Figure C.1b. We plot in this Figure C.1b the quantity $\delta\alpha_{\text{MMR}}/\varepsilon^{1/4}$; we see that the curves are almost similar, particularly for the smaller values of ε .



(a) Difference between the limit α_{lim} where C_c^{col} and C_c^{MMR} are equal and its approximation α_{MMR} scaled by $1 - \alpha_{\text{MMR}}$ versus γ for various values of ε .
(b) $\delta\alpha_{\text{MMR}}$ scaled by $\varepsilon^{1/4}$ versus γ for various values of ε .

Figure C.1 – Effect of the planet mass ratio on the limit where the collision criterion becomes better than the MMR overlap criterion.

C.5 AMD-stability coefficients of the system affected by the MMR overlap criterion

We report in Table C.1 the AMD-stability coefficients of the systems where more than 5% of the Monte Carlo realizations were affected by the change of critical AMD. Apart for the system HD 47366 where 16% of the simulations used the new criterion, the seven other systems used the critical AMD $C_c^{(1)}$ for almost all the realizations. For HD 204313, only the pair (b/d) is affected.

In Table C.1, $\sqrt{\langle e^2 \rangle}$ corresponds to the mean value of the squared eccentricity computed as explained in section (4.5.1).

Table C.1 – AMD-stability coefficients computed for the systems affected by the MMR overlap criterion

Planet	Period (d)	Mass ($(\mathcal{GM})_{\text{Ep}}^N$)	Eccentricity	$\sqrt{\langle e^2 \rangle}$	β	$\beta^{(\text{MMR})}$
HD 128311	Mass: 0.84 ($(\mathcal{GM})_{\odot}^N$)					
b	454.2	463.14	0.345	0.352	0.312	
c	923.8	1032.46	0.230	0.244	3.200	27.931
HD 200964	Mass: 1.44 ($(\mathcal{GM})_{\odot}^N$)					
b	613.8	587.98	0.040	0.067	0.024	
c	825	284.46	0.181	0.184	3.872	$+\infty$
HD 204313	Mass: 1.045 ($(\mathcal{GM})_{\odot}^N$)					
c	34.905	17.58	0.155	0.184	16.664	
b	2024.1	1360.31	0.095	0.095	0.110	0.110
d	2831.6	533.95	0.280	0.308	8.032	$+\infty$
HD 33844	Mass: 1.75 ($(\mathcal{GM})_{\odot}^N$)					
b	551.4	622.94	0.150	0.180	0.084	
c	916	556.20	0.130	0.189	2.939	22.676
HD 45364	Mass: 0.82 ($(\mathcal{GM})_{\odot}^N$)					
b	226.93	59.50	0.168	0.171	0.070	
c	342.85	209.10	0.097	0.099	1.975	13.700
HD 47366	Mass: 1.81 ($(\mathcal{GM})_{\odot}^N$)					
b	363.3	556.20	0.089	0.138	0.146	
c	684.7	591.16	0.278	0.292	2.896	2.896
HD 5319	Mass: 1.56 ($(\mathcal{GM})_{\odot}^N$)					
b	675	616.59	0.120	0.162	0.053	
c	886	365.50	0.150	0.171	8.659	$+\infty$
HD 73526	Mass: 1.08 ($(\mathcal{GM})_{\odot}^N$)					
b	188.9	715.11	0.290	0.293	0.200	
c	379.1	715.11	0.280	0.289	3.391	9.922

Note: Masses are given in terms of nominal terrestrial masses \mathcal{M}_{E}^N and stellar masses in terms of nominal solar masses \mathcal{M}_{\odot}^N as recommended by the IAU 2015 Resolution B3.

Appendix D

Complements on Hill stability

D.1 Computation of R at the Lagrange points

The function $R(x, y) = (\rho/\nu)^2$ defined in (5.14) admits three saddle points situated on the x axis, which are the Lagrange points L_1 , L_2 , and L_3 . If x_j is the abscissa of the point L_j on the plane \mathcal{P} , we have $0 < x_1 < 1$, $x_2 > 1$ and $x_3 < 0$. The x_j quantities only depends on the mass ratio ε and on

$$\zeta = \frac{\gamma}{\gamma + 1} = \frac{m_1}{m_1 + m_2}. \quad (\text{D.1})$$

They are the roots of the three different polynomial equations

$$\begin{aligned} & (1 + \zeta\varepsilon)x_1^5 - (2 + 3\zeta\varepsilon)x_1^4 + \\ & (1 + 2\varepsilon + \zeta\varepsilon)x_1^3 - (1 + 3\varepsilon(1 - \zeta))x_1^2 + \\ & (2 + 3\varepsilon(1 - \zeta))x_1 - (1 + \varepsilon(1 - \zeta)) = 0, \end{aligned} \quad (\text{D.2})$$

$$\begin{aligned} & (1 + \zeta\varepsilon)x_2^5 - (2 + 3\zeta\varepsilon)x_2^4 + \\ & (1 + 3\zeta\varepsilon)x_2^3 - (1 + 3\varepsilon - \zeta\varepsilon)x_2^2 + \\ & (2 + 3\varepsilon(1 - \zeta))x_2 - (1 + \varepsilon(1 - \zeta)) = 0, \end{aligned} \quad (\text{D.3})$$

$$\begin{aligned} & (1 + \zeta\varepsilon)x_3^5 - (2 + 3\zeta\varepsilon)x_3^4 + \\ & (1 + 3\zeta\varepsilon)x_3^3 + (1 + 3\varepsilon(1 - \zeta))x_3^2 - \\ & (2 + 3\varepsilon(1 - \zeta))x_3 + (1 + \varepsilon(1 - \zeta)) = 0, \end{aligned} \quad (\text{D.4})$$

At up to terms of order $\varepsilon^{4/3}$, we have

$$\begin{aligned} x_1 &= 1 - \left(\frac{\varepsilon}{3}\right)^{1/3} + \frac{\gamma + 2}{3(\gamma + 1)} \left(\frac{\varepsilon}{3}\right)^{2/3} + \frac{(\gamma - 2)\varepsilon}{27(\gamma + 1)} + O(\varepsilon^{4/3}), \\ x_2 &= 1 - \left(\frac{\varepsilon}{3}\right)^{1/3} + \frac{\gamma + 2}{3(\gamma + 1)} \left(\frac{\varepsilon}{3}\right)^{2/3} - \frac{(\gamma - 2)\varepsilon}{27(\gamma + 1)} + O(\varepsilon^{4/3}), \\ x_3 &= -1 + \frac{7}{12} \frac{\gamma - 1}{\gamma + 1} \varepsilon + O(\varepsilon^2). \end{aligned} \quad (\text{D.5})$$

We can then evaluate R (eq. 5.14) at those points and we have at order $\varepsilon^{4/3}$,

$$\begin{aligned} R(L_1) &= 1 + \frac{3^{4/3}\varepsilon^{2/3}\gamma}{(\gamma+1)^2} - \frac{(11+7\gamma)\gamma\varepsilon}{3(\gamma+1)^3} + O(\varepsilon^{4/3}), \\ R(L_2) &= 1 + \frac{3^{4/3}\varepsilon^{2/3}\gamma}{(\gamma+1)^2} - \frac{(11\gamma+7)\gamma\varepsilon}{3(\gamma+1)^3} + O(\varepsilon^{4/3}), \\ R(L_3) &= 1 + \frac{2\varepsilon\gamma}{(\gamma+1)^2} + O(\varepsilon^2). \end{aligned} \quad (\text{D.6})$$

D.2 Expansion of C_c^{Ex} and h_1

In section 5.2, the Hill stability criterion (5.24) is obtained by the expansion at the leading order in ε of

$$F = (\gamma+1)^{3/2} \sqrt{\frac{R(L_1)(1+\varepsilon\gamma/(\gamma+1)^2)^3}{(1+\varepsilon)(\gamma/\alpha+1+h_1)}}. \quad (\text{D.7})$$

In F , the main term depending on ε comes from the expansion of

$$R(L_1) = 1 + \frac{3^{4/3}\gamma\varepsilon^{2/3}}{(\gamma+1)^2} - \frac{(11+7\gamma)}{3(\gamma+1)} \frac{\gamma\varepsilon}{(\gamma+1)^2} + O(\varepsilon^{4/3}). \quad (\text{D.8})$$

However, we also need to make sure that h_1 remains small in comparison to this term. Thus, the expansion of F requires an estimate of h_1 with respect to ε and γ . As explained in section 5.2, h_1 is the renormalized perturbation part of the Hamiltonian (5.3)

$$h_1 = -\frac{2\Lambda_2^2}{m_2^3\mu^2} \left(\frac{1}{2} \frac{\|\tilde{\mathbf{r}}_1 + \tilde{\mathbf{r}}_2\|^2}{m_0} - \frac{\mathcal{G}m_1m_2}{r_{12}} \right). \quad (\text{D.9})$$

If we note $\dot{\mathbf{r}}_j = \tilde{\mathbf{r}}_j/m_j$ and simplify the expression (D.9), we obtain $h_1 = h_1^T + h_1^P$, where

$$h_1^T = -\frac{\varepsilon a_2}{\mu} \frac{\|\gamma\dot{\mathbf{r}}_1 + \dot{\mathbf{r}}_2\|^2}{\gamma+1}, \text{ and } h_1^P = \frac{2a_2}{r_{12}} \frac{\varepsilon\gamma}{\gamma+1}. \quad (\text{D.10})$$

As one can see on figure 5.2, the value of ε is only relevant for small values of the critical AMD C_c^{Ex} , *i.e.*, for close planets. Using the expansion in $1-\alpha$ (5.25), we can estimate that we need to compute h_1 for systems such that \mathcal{C} is of order $\varepsilon^{2/3}$. This corresponds to systems with eccentricities of order $\varepsilon^{1/3}$. We can therefore use the circular approximation in our estimation of h_1 . In particular we have $r_j = a_j(1+O(\varepsilon^{1/3}))$.

We first consider the term coming from the gravitational interaction between the two planets, h_1^P . If the system is Hill stable, the distance r_{12} is greater than the radius of the Hill sphere S_{H_1}

$$\begin{aligned} r_{12} > r_1 \max_{j=1,2} |1-x_j| &= r_1(\varepsilon/3)^{1/3} + O(\varepsilon^{2/3}) \\ &= a_1(\varepsilon/3)^{1/3} + O(\varepsilon^{2/3}), \end{aligned} \quad (\text{D.11})$$

where x_j is defined in (D.5). For all times, we therefore have

$$h_1^P = \frac{2a_2}{r_{12}} \frac{\varepsilon\gamma}{\gamma+1} \leq \frac{2 \times 3^{1/3}}{\alpha} \varepsilon^{2/3} \frac{\gamma}{\gamma+1} + O(\varepsilon). \quad (\text{D.12})$$

The gravitational potential term h_1^P is at most of the same order as the leading term in ε of $R(L_1)$. However, we can always choose to estimate the energy and actions values when the two planets are far from each other. In this case $a_2/r_{12} = O(1)$ and h_1^P is linear in ε . From now on, we assume that we have

$$h_1^P = \frac{\varepsilon\gamma}{\gamma+1} p_{12}, \quad (\text{D.13})$$

with $p_{12} = O(1)$.

Moreover, F is a decreasing function of h_1 , so C_c^{Ex} is an increasing function of h_1 . Since h_1^P is positive, neglecting it is equivalent to have a more conservative criterion.

Let us now consider the kinetic term h_1^T . We develop (D.10) for almost circular orbits. In this limit, we have $\|\dot{\mathbf{r}}_j\| = \sqrt{\mu/a_j} + O(\varepsilon^{1/3})$. We have

$$h_1^T = -\frac{\varepsilon}{\gamma+1} \left(\frac{\gamma^2}{\alpha} + 1 + \frac{2\gamma}{\sqrt{\alpha}} \cos(\lambda_1 - \lambda_2) \right) + O(\varepsilon^{4/3}). \quad (\text{D.14})$$

Therefore, h_1^T is always linear in ε . Combining the estimations (D.13) and (D.14), we see that $h_1 = O(\varepsilon)$.

We can now use the expansions of h_1 , (D.14) and (D.13) to obtain the expansion of F in function of ε and γ . Because of the term $3^{4/3}\varepsilon^{2/3}\gamma/(\gamma+1)^2$ from $R(L_1)$, we do not keep terms of order $O(\varepsilon\gamma/(\gamma+1)^2)$. We keep all other terms depending on ε up to the order $O(\varepsilon^{4/3})$. We obtain

$$F = \sqrt{\frac{\alpha(\gamma+1)^3}{\gamma+\alpha} \left(1 + \frac{3^{4/3}\varepsilon^{2/3}\gamma}{(\gamma+1)^2} \right) D} + O\left(\frac{\varepsilon\gamma}{(\gamma+1)^2}, \varepsilon^{4/3}\right), \quad (\text{D.15})$$

where $D = (1-\varepsilon) \left(1 - \frac{\alpha h_1}{\gamma+\alpha} \right)$ and $O\left(\frac{\varepsilon\gamma}{(\gamma+1)^2}, \varepsilon^{4/3}\right) = O\left(\frac{\varepsilon\gamma}{(\gamma+1)^2}\right) + O\left(\varepsilon^{4/3}\right)$. Let us develop D at the same order than F . We have

$$\begin{aligned} D &= 1 - \varepsilon - \frac{\alpha h_1^T}{\gamma+\alpha} + O\left(\frac{\varepsilon\gamma}{(\gamma+1)^2}, \varepsilon^{4/3}\right) \\ &= 1 + \varepsilon \left(\frac{\gamma^2 + \alpha}{(\gamma+1)(\gamma+\alpha)} - 1 \right) + O\left(\frac{\varepsilon\gamma}{(\gamma+1)^2}, \varepsilon^{4/3}\right) \\ &= 1 - \frac{\varepsilon\gamma}{(\gamma+1)^2} \frac{(\gamma+1)(\alpha+1)}{\gamma+\alpha} + O\left(\frac{\varepsilon\gamma}{(\gamma+1)^2}, \varepsilon^{4/3}\right) \\ &= 1 + O\left(\frac{\varepsilon\gamma}{(\gamma+1)^2}, \varepsilon^{4/3}\right). \end{aligned} \quad (\text{D.16})$$

We see that D has no contribution to F at the considered orders. Therefore, we can write

$$F = \sqrt{\frac{\alpha(\gamma+1)^3}{\gamma+\alpha} \left(1 + 3^{4/3} \frac{\varepsilon^{2/3}\gamma}{(\gamma+1)^2} \right)} + O\left(\frac{\varepsilon\gamma}{(\gamma+1)^2}, \varepsilon^{4/3}\right). \quad (\text{D.17})$$

As an immediate consequence of (D.17), the expression proposed in (5.24) remains valid in the case of a very uneven mass distribution between the two planets (*e.g.*, for $O(\varepsilon^{1/3}) < \gamma < O(\varepsilon^{-1/3})$).

Appendix E

Details on the adaptive integrator

E.1 Implementation

We give in this appendix technical details on our implementation choices.

E.1.1 Kepler equation

The key step in any Wisdom-Holman algorithm is the numerical resolution of the Kepler problem

$$H_{\text{Kepler}} = \frac{\mathbf{v}^2}{2} - \frac{\mu}{r}, \quad (\text{E.1})$$

where $\mu = GM$ and M is the central mass in the set of coordinates used in the integration. Since this is the most expensive step from a computational point of view, it is particularly important to optimize it. Here, we closely follow the works by (Mikkola, 1997; Mikkola and Innanen, 1999) and refer to them for more details. Rein and Tamayo (2015) present an unbiased numerical implementation that can be found in the package `REBOUND`¹.

Let us consider a planet with initial conditions \mathbf{r}_0 , and \mathbf{v}_0 , the goal is to determine the position of the planet \mathbf{r} and its velocity \mathbf{v} along the Keplerian orbit after a time t . In order to avoid conversions from Cartesian coordinates to elliptical elements, we use the Gauss f - and g -functions² formalism (*e.g.* Wisdom and Holman, 1991). We have

$$\begin{aligned} \mathbf{r} &= f\mathbf{r}_0 + g\mathbf{v}_0, \\ \mathbf{v} &= \dot{f}\mathbf{r}_0 + \dot{g}\mathbf{v}_0 \end{aligned} \quad (\text{E.2})$$

where the values of f , g , \dot{f} and \dot{g} depend on t , \mathbf{r}_0 , and \mathbf{v}_0 and are given in equations (E.7). Whenever two planets encounter, their orbits may become hyperbolic. To be

¹<https://rebound.readthedocs.io/en/latest/>

²Please note that those functions are different from the time renormalization functions used in this article.

able to resolve such events as well as ejections trajectories, we use a formulation of the Kepler problem allowing hyperbolic orbits. In order to do so, Stumpff (1962) developed a general formalism that comprehend the hyperbolic and the elliptical case in the same equations. Moreover, this approach avoids the singularity for an eccentricity close to 1. Stumpff introduces special functions

$$c_n(z) = \sum_{j=0}^{+\infty} \frac{(-z)^j}{(n+2j)!}. \quad (\text{E.3})$$

The c -functions allow to compute the so-called G -functions (Stiefel and Scheifele, 1971) defined as

$$G_n(\beta, X) = X^n c_n(\beta X^2). \quad (\text{E.4})$$

In this formalism, the Kepler equation takes the form (Stumpff, 1962)

$$t = r_0 X + \eta_0 G_2(\beta, X) + \zeta_0 G_3(\beta, X), \quad (\text{E.5})$$

of unknown $X = \int_0^t dt/r$ and where

$$\begin{aligned} \beta &= \frac{2\mu}{r_0} - \mathbf{v}_0^2, \\ \eta_0 &= \mathbf{r}_0 \cdot \mathbf{v}_0, \\ \zeta_0 &= \mu - \beta r_0. \end{aligned} \quad (\text{E.6})$$

In (E.5), X plays a similar role to the eccentric anomaly in the classical form. Equation (E.5) can be solved by the Newton method (Rein and Tamayo, 2015). The new position and velocity are then obtained with (E.2) and

$$\begin{aligned} f &= 1 - \mu \frac{G_2(\beta, X)}{r_0}, & \dot{f} &= -\frac{\mu G_1(\beta, X)}{r_0 r}, \\ g &= t - \mu G_3(\beta, X), & \dot{g} &= 1 - \mu \frac{G_2(\beta, X)}{r}, \end{aligned} \quad (\text{E.7})$$

where $r = r_0 + \eta_0 G_2 + \zeta_0 G_3$.

E.1.2 Computation of the effective time step

In both the Kepler and the perturbation step, it is important to compute precisely the effective time step (6.21). For the Kepler step in particular, τ_0 depends on the difference $H_0 - E_0$ with H_0 and E_0 being of comparable size. To avoid numerical errors, we compute the initial energy with compensated summation (Kahan, 1965). We save the value and the associated error. We then evaluate the Keplerian energy H_0 using compensated summation and then make the difference. Compensated summation is also used to update the positions, velocities and for the integration of the real time equation.

During the numerical tests, we remarked that in Jacobi coordinates, the perturbation energy H_1 is most of the time smaller by almost an order of magnitude than the typical planet energy interaction E_1 . On the other hand, H_1 and E_1 are roughly

of the same order for heliocentric coordinates. It results that the algorithm is less efficient in the detection of an increase of the interaction energy (that monitors the close encounters). To circumvent this problem, we slightly modify the expression (6.21) for Jacobi coordinates. The effective step sizes are computed with

$$\tau_0 = \sigma f'(H_0 - E_0 + E_1) \text{ and } \tau_1 = \sigma f'(-(H_1 - E_1)). \quad (\text{E.8})$$

It should be noted that the total energy sum is still zero

$$(H_0 - E_0 + E_1) + (H_1 - E_1) = 0 \quad (\text{E.9})$$

which preserves the equation of motion according to (6.14). With this modification, the results are comparable between Jacobi and heliocentric coordinates.

E.2 MacLachlan high order schemes

In (McLachlan, 1995a), the schemes coefficients w_i are the coefficients for a symmetric composition of second order steps. We give in table E.1 the corresponding coefficients a_i and b_i for the schemes that we used $\mathcal{ABA}(6*)$ and $\mathcal{ABA}(8*)$. McLachlan provides 20 significant digits so we made the computation in quadruple precision and truncated to the appropriate precision.

Table E.1 – Coefficients of the schemes used in this article. The values are computed from (McLachlan, 1995a).

Scheme	Order	Stages	a_i	b_i
$\mathcal{ABA}(6*)$	6	7	$a_1 = 0.39225680523877863191$ $a_2 = 0.51004341191845769875$ $a_3 = -0.471053385409756436635$ $a_4 = 0.068753168252520105975$	$b_1 = 0.78451361047755726382$ $b_2 = 0.23557321335935813368$ $b_3 = -1.17767998417887100695$ $b_4 = 1.3151863206839112189$
$\mathcal{ABA}(8*)$	8	15	$a_1 = 0.370835182175306476725$ $a_2 = 0.166284769275290679725$ $a_3 = -0.109173057751896607025$ $a_4 = -0.191553880409921943355$ $a_5 = -0.13739914490621317141$ $a_6 = 0.31684454977447705381$ $a_7 = 0.324959005321032390205$ $a_8 = -0.240797423478074878675$	$b_1 = 0.74167036435061295345$ $b_2 = -0.409100825800031594$ $b_3 = 0.19075471029623837995$ $b_4 = -0.57386247111608226666$ $b_5 = 0.29906418130365592384$ $b_6 = 0.33462491824529818378$ $b_7 = 0.31529309239676659663$ $b_8 = -0.79688793935291635398$

Bibliography

- Albouy, A. (2002). *Lectures on the Two-Body Problem*. Princeton University Press.
- Andoyer, H. (1923). *Cours De Mécanique Céleste*. Paris, Gauthier-Villars et cie, 1923–26.
- Arnold, V. I. (1979). *Mathematical Methods of Classical Mechanics*. Moscow Izdatel Nauka.
- Arnold, V. (1963). Small Denominators and Problems of Stability of Motion in Classical and Celestial Mechanics. *Russian Mathematical Surveys*, 18, pp. 85–191.
- Barnes, R. and Greenberg, R. (2006). Stability Limits in Extrasolar Planetary Systems. *The Astrophysical Journal Letters*, 647, pp. L163–L166.
- Barnes, R. and Raymond, S. N. (2004). Predicting Planets in Known Extrasolar Planetary Systems. I. Test Particle Simulations. *The Astrophysical Journal*, 617.1, pp. 569–574.
- Batygin, K. and Morbidelli, A. (2013). Analytical Treatment of Planetary Resonances. *Astronomy & Astrophysics*, 556, A28–A28.
- Batygin, K. and Laughlin, G. (2008). On the Dynamical Stability of the Solar System. *The Astrophysical Journal*, 683.2, pp. 1207–1216.
- Batygin, K., Morbidelli, A. and Holman, M. J. (2015). Chaotic Disintegration of the Inner Solar System. *The Astrophysical Journal*, 799.2, pp. 120–120.
- Batygin, K., Bodenheimer, P. H. and Laughlin, G. P. (2016). In Situ Formation and Dynamical Evolution of Hot Jupiter Systems. *The Astrophysical Journal*, 829.2, p. 114.
- Benz, W. (2000). Low Velocity Collisions and the Growth of Planetesimals. *Space Science Reviews*, 92.1, pp. 279–294.
- Bitsch, B. *et al.* (2019). Formation of Planetary Systems by Pebble Accretion and Migration: Growth of Gas Giants. *Astronomy & Astrophysics*,
- Blanes, S. *et al.* (2013). New Families of Symplectic Splitting Methods for Numerical Integration in Dynamical Astronomy. *Applied Numerical Mathematics*, 68, pp. 58–72.
- Blanes, S. and Iserles, A. (2012). Explicit Adaptive Symplectic Integrators for Solving Hamiltonian Systems. *Celestial Mechanics and Dynamical Astronomy*, 114.3, pp. 297–317.
- Bode, J. (1772). Anleitung Zur Kentniss Des Gestirnten Himmels.
- Boué, G., Laskar, J. and Farago, F. (2012). A Simple Model of the Chaotic Eccentricity of Mercury. *Astronomy & Astrophysics*, 548, A43–A43.
- Brouwer, D. (1937). On the Accumulation of Errors in Numerical Integration. *The Astronomical Journal*, 46, p. 149.
- Chambers, J (2001). Making More Terrestrial Planets. *Icarus*, 152.2, pp. 205–224.
- Chambers, J. E. (1999). A Hybrid Symplectic Integrator That Permits Close Encounters between Massive Bodies. *Monthly Notices of the Royal Astronomical Society*, 304.4, pp. 793–799.
- Chambers, J. (2013). Late-Stage Planetary Accretion Including Hit-and-Run Collisions and Fragmentation. *Icarus*, 224.1, pp. 43–56.

- Chambers, J., Wetherill, G. and Boss, A. (1996). The Stability of Multi-Planet Systems. *Icarus*, 119.2, pp. 261–268.
- Chiang, E. and Youdin, A. (2010). Forming Planetesimals in Solar and Extrasolar Nebulae. *Annual Review of Earth and Planetary Sciences*, 38.1, pp. 493–522.
- Chirikov, B. V. (1979). A Universal Instability of Many-Dimensional Oscillator Systems. *Physics Reports*, 52.5, pp. 263–379.
- Cumming, A., Marcy, G. W. and Butler, R. P. (1999). The Lick Planet Search: Detectability and Mass Thresholds. *The Astrophysical Journal*, 526.2, p. 890.
- Cumming, A. *et al.* (2008). The Keck Planet Search: Detectability and the Minimum Mass and Orbital Period Distribution of Extrasolar Planets. *Publications of the Astronomical Society of the Pacific*, 120.867, p. 531.
- Dawson, R. I. and Fabrycky, D. C. (2010). Radial Velocity Planets De-Aliased: A New, Short Period for Super-Earth 55 Cnc e. *The Astrophysical Journal*, 722.1, pp. 937–953.
- Dawson, R. I. and Johnson, J. A. (2018). Origins of Hot Jupiters. *Annual Review of Astronomy and Astrophysics*, 56.1, pp. 175–221.
- Deck, K. M., Payne, M. and Holman, M. J. (2013). First Order Resonance Overlap and the Stability of Close Two Planet Systems. *The Astrophysical Journal*, 774.2, pp. 129–129.
- Delaunay, C (1860). Théorie Du Mouvement De La Lune. Volume 28 and 29. *Mémoires de l'Académie des Sciences, Paris*,
- Delisle, J.-B. *et al.* (2012). Dissipation in Planar Resonant Planetary Systems. *Astronomy & Astrophysics*, 546, A71–A71.
- Delisle, J.-B., Laskar, J. and Correia, A. C. M. (2014). Resonance Breaking Due to Dissipation in Planar Planetary Systems. *Astronomy & Astrophysics*, 566, A137–A137.
- Deprit, A. (1969). Canonical Transformations Depending on a Small Parameter. *Celestial mechanics*, 1.1, pp. 12–30.
- Duncan, M., Quinn, T. and Tremaine, S. (1989). The Long-Term Evolution of Orbits in the Solar System: A Mapping Approach. *Icarus*, 82.2, pp. 402–418.
- Duncan, M. J., Levison, H. F. and Lee, M. H. (1998). A Multiple Time Step Symplectic Algorithm for Integrating Close Encounters. *The Astronomical Journal*, 116.4, pp. 2067–2077.
- Eggenberger, A. *et al.* (2010). Probing the Impact of Stellar Duplicity on the Frequency of Giant Planets: Final Results of Our Vlt/Naco Survey. *Proceedings of the International Astronomical Union*, 6.S276, pp. 409–410.
- Fabrycky, D. C. *et al.* (2014). Architecture of Kepler's Multi-Transiting Systems. II. New Investigations with Twice as Many Candidates. *The Astrophysical Journal*, 790.2, pp. 146–146.
- Fang, J. and Margot, J.-L. (2012). Architecture of Planetary Systems Based on Kepler Data: Number of Planets and Coplanarity. *The Astrophysical Journal*, 761.2, pp. 92–92.
- Fang, J. and Margot, J.-L. (2013). Are Planetary Systems Filled to Capacity? A Study Based on Kepler Results. *The Astrophysical Journal*, 767.2, pp. 115–115.
- Farrés, A. *et al.* (2013). High Precision Symplectic Integrators for the Solar System. *Celestial Mechanics and Dynamical Astronomy*, 116.2, pp. 141–174.
- Ferraz-Mello, S. (2007). *Canonical Perturbation Theories*. Vol. 345. Astrophysics and Space Science Library. New York, NY: Springer New York.
- Figueira, P. *et al.* (2012). Comparing HARPS and Kepler Surveys. *Astronomy & Astrophysics*, 541, A139–A139.
- Fressin, F. *et al.* (2013). The False Positive Rate of Kepler and the Occurrence of Planets. *The Astrophysical Journal*, 766.2, p. 81.

- Georgakarakos, N. (2008). Stability Criteria for Hierarchical Triple Systems. *Celestial Mechanics and Dynamical Astronomy*, 100.2, pp. 151–168.
- Giorgilli, A. *et al.* (1989). Effective Stability for a Hamiltonian System Near an Elliptic Equilibrium Point, with an Application to the Restricted Three Body Problem. *Journal of differential equations*, 77.1, pp. 167–198.
- Giorgilli, A., Locatelli, U. and Sansottera, M. (2017). Secular Dynamics of a Planar Model of the Sun-Jupiter-Saturn-Uranus System; Effective Stability in the Light of Kolmogorov and Nekhoroshev Theories. *Regular and Chaotic Dynamics*, 22.1, pp. 54–77.
- Gladman, B. (1993). Dynamics of Systems of Two Close Planets. *Icarus*, 106.1, pp. 247–263.
- Gladman, B., Duncan, M. and Candy, J. (1991). Symplectic Integrators for Long-Term Integrations in Celestial Mechanics. *Celestial Mechanics and Dynamical Astronomy*, 52, pp. 221–240.
- Goldreich, P. and Tremaine, S. (1979). The Excitation of Density Waves at the Lindblad and Corotation Resonances by an External Potential. *The Astrophysical Journal*, 233, p. 857.
- Goldstein, H. (1950). *Classical Mechanics*. Mass.: Addison-Wesley Press.
- Graner, F. and Dubrulle, B. (1994). Titius-Bode Laws in the Solar System. 1: Scale Invariance Explains Everything. *Astronomy and Astrophysics*, 282, pp. 262–268.
- Greenberg, R. *et al.* (1978). Planetesimals to Planets: Numerical Simulation of Collisional Evolution. *Icarus*, 35.1, p. 1.
- Grimm, S. L. *et al.* (2018). The Nature of the Trappist-1 Exoplanets. *Astronomy & Astrophysics*, 613, A68.
- Hadden, S. and Lithwick, Y. (2018). A Criterion for the Onset of Chaos in Systems of Two Eccentric Planets. *arXiv:1803.08510 [astro-ph]*.
- Hansen, B. (2009). Formation of the Terrestrial Planets from a Narrow Annulus. *The Astrophysical Journal, Volume 703, Issue 1, pp. 1131–1140 (2009)*, 703, pp. 1131–1140.
- Hartmann, L. *et al.* (1998). Accretion and the Evolution of T Tauri Disks. *The Astrophysical Journal*, 495.1, pp. 385–400.
- Hénon, M. and Petit, J.-M. (1986). Series Expansions for Encounter-Type Solutions of Hill's Problem. *Celestial Mechanics*, 38.1, pp. 67–100.
- Henrard, J. and Lemaitre, A. (1983). A Second Fundamental Model for Resonance. *Celestial Mechanics*, 30.2, pp. 197–218.
- Henrard, J. *et al.* (1986). The Reducing Transformation and Apocentric Librators. *Celestial Mechanics*, 38.4, pp. 335–344.
- Hernández-Mena, C. and Benet, L. (2011). Statistics and Universality in Simplified Models of Planetary Formation. *Monthly Notices of the Royal Astronomical Society*, 412.1, pp. 95–106.
- Hill, G. W. (1913). Motion of a System of Material Points Under the Action of Gravitation. *The Astronomical Journal*, 27, pp. 171–182.
- Holman, M. J. and Murray, N. W. (2005). The Use of Transit Timing to Detect Terrestrial-Mass Extrasolar Planets. *Science*, 307.5713, pp. 1288–1291.
- Izidoro, A. *et al.* (2019). Formation of Planetary Systems by Pebble Accretion and Migration: Hot Super-Earth Systems from Breaking Compact Resonant Chains. *arXiv:1902.08772 [astro-ph]*,
- Johansen, A. and Lambrechts, M. (2017). Forming Planets via Pebble Accretion. *Annual Review of Earth and Planetary Sciences*, 45.1, pp. 359–387.
- Johansen, A. *et al.* (2007). Rapid Planetesimal Formation in Turbulent Circumstellar Disks. *Nature*, 448.7157, pp. 1022–1025.

- Johansen, A. *et al.* (2012). Can Planetary Instability Explain the Kepler Dichotomy? *The Astrophysical Journal*, 758.1, p. 39.
- Jontof-Hutter, D. *et al.* (2015). The Mass of the Mars-Sized Exoplanet Kepler-138 B from Transit Timing. *Nature*, 522.7556, pp. 321–323.
- Jurić, M. and Tremaine, S. (2008). Dynamical Origin of Extrasolar Planet Eccentricity Distribution. *The Astrophysical Journal*, 686.1, pp. 603–620.
- Kahan, W. (1965). Pracniques: Further Remarks on Reducing Truncation Errors. *Commun. ACM*, 8.1, pp. 40–.
- Kepler, J. (1596). *Mysterium Cosmographicum*.
- Kepler, J. (1609). *Astronomia Nova*.
- Kepler, J. (1619). *Harmonices Mundi*.
- Kinoshita, H., Yoshida, H. and Nakai, H. (1991). Symplectic Integrators and Their Application to Dynamical Astronomy. *Celestial Mechanics and Dynamical Astronomy*, 50.1, pp. 59–71.
- Kokubo, E. and Genda, H. (2010). Formation of Terrestrial Planets from Protoplanets Under a Realistic Accretion Condition. *The Astrophysical Journal*, 714.1, pp. L21–L25.
- Kokubo, E., Kominami, J. and Ida, S. (2006). Formation of Terrestrial Planets from Protoplanets. I. Statistics of Basic Dynamical Properties. *The Astrophysical Journal*, 642.2, pp. 1131–1139.
- Kolmogorov, A. N. (1954). On Conservation of Conditionally Periodic Motions for a Small Change in Hamilton's Function. *Dokl. Akad. Nauk SSSR*, 98, pp. 527–530.
- Kopparapu, R. K. (2013). A Revised Estimate of the Occurrence Rate of Terrestrial Planets in the Habitable Zones around Kepler M-Dwarfs. *The Astrophysical Journal*, 767.1, p. L8.
- Koseleff, P. V. (1993). “Relations among Lie Formal Series and Construction of Symplectic Integrators”. In: *Applied Algebra, Algebraic Algorithms and Error-Correcting Codes*. Ed. by G. Cohen, T. Mora and O. Moreno. Lecture Notes in Computer Science. Springer Berlin Heidelberg, pp. 213–230.
- Lagrange, A.-M. *et al.* (2009). A Probable Giant Planet Imaged in the β Pictoris Disk - VLT/NACO Deep L'-Band Imaging. *Astronomy & Astrophysics*, 493.2, pp. L21–L25.
- Lambrechts, M. and Johansen, A. (2012). Rapid Growth of Gas-Giant Cores by Pebble Accretion. *Astronomy & Astrophysics*, 544, A32.
- Lambrechts, M. *et al.* (2019). Formation of Planetary Systems by Pebble Accretion and Migration: How the Radial Pebble Flux Determines a Terrestrial-Planet or Super-Earth Growth Mode. *arXiv:1902.08694 [astro-ph]*,
- Laplace, P. (1796). *Exposition Du Système Du Monde*. Cercle Social, Paris.
- Laskar, J. (1989). A Numerical Experiment on the Chaotic Behaviour of the Solar System. *Nature*, 338.6212, p. 237.
- Laskar, J. (1990a). “Manipulation Des Séries.” In: *Les Méthodes Modernes de La Mécanique Céleste. Modern Methods in Celestial Mechanics*, pp. 89–107.
- Laskar, J. (1990b). The Chaotic Motion of the Solar System: A Numerical Estimate of the Size of the Chaotic Zones. *Icarus*, 88.2, pp. 266–291.
- Laskar, J. (1991). “Analytical Framework in Poincare Variables for the Motion of the Solar System”. In: *Predictability, Stability, and Chaos in N-Body Dynamical Systems SE - 7*. Ed. by A. Roy. Vol. 272. NATO ASI Series. Springer US, pp. 93–114.
- Laskar, J. (1993). Frequency Analysis for Multi-Dimensional Systems. Global Dynamics and Diffusion. *Physica D Nonlinear Phenomena*, 67, pp. 257–281.
- Laskar, J. (1994). Large-Scale Chaos in the Solar System. *Astronomy and Astrophysics*, 287, pp. L9–L12.

- Laskar, J. (1997). Large Scale Chaos and the Spacing of the Inner Planets. *Astronomy and Astrophysics*, 317, pp. L75–L78.
- Laskar, J. (2000). On the Spacing of Planetary Systems. *Physical Review Letters*, 84.15, pp. 3240–3243.
- Laskar, J. (2008). Chaotic Diffusion in the Solar System. *Icarus*, 196.1, pp. 1–15.
- Laskar, J. and Gastineau, M (2009). Existence of Collisional Trajectories of Mercury, Mars and Venus with the Earth. *Nature*, 459.7248, pp. 817–819.
- Laskar, J. et al. (2011). Strong Chaos Induced by Close Encounters with Ceres and Vesta. *Astronomy and Astrophysics*, 532, p. L4.
- Laskar, J. (1996). Large Scale Chaos and Marginal Stability in the Solar System. *Celestial Mechanics and Dynamical Astronomy*, 64.1-2, p. 115.
- Laskar, J. (2013). “Is the Solar System Stable?” In: *Chaos: Poincaré Seminar 2010*. Ed. by B. Duplantier, S. Nonnenmacher and V. Rivasseau. Progress in Mathematical Physics. Basel: Springer Basel, pp. 239–270.
- Laskar, J. (2017). Andoyer Construction for Hill and Delaunay Variables. *Celestial Mechanics and Dynamical Astronomy*, 128.4, pp. 475–482.
- Laskar, J. and Marchal, C. (1984). Triple Close Approach in the Three-Body Problem - a Limit for the Bounded Orbits. *Celestial Mechanics*, 32.1, p. 15.
- Laskar, J. and Petit, A. C. (2017). AMD-Stability and the Classification of Planetary Systems. *Astronomy & Astrophysics*, 605, A72–A72.
- Laskar, J. and Robutel, P. (1995). Stability of the Planetary Three-Body Problem. *Celestial Mechanics & Dynamical Astronomy*, 62.3, pp. 193–217.
- Laskar, J. and Robutel, P. (2001). High Order Symplectic Integrators for Perturbed Hamiltonian Systems. *Celestial Mechanics and Dynamical Astronomy*, 80.1, pp. 39–62.
- Lehmann, E. L. and Romano, J. P. (2006). *Testing Statistical Hypotheses*. Springer Science & Business Media.
- Lin, D. N. C. and Papaloizou, J. (1986). On the Tidal Interaction Between Protoplanets and the Protoplanetary Disk. Iii. Orbital Migration of Protoplanets. *The Astrophysical Journal*, 309, p. 846.
- Lissauer, J. J. et al. (2011). Architecture and Dynamics of Kepler’s Candidate Multiple Transiting Planet Systems. *The Astrophysical Journal Supplement Series*, 197.1, pp. 8–8.
- Lissauer, J. J. et al. (2013). All Six Planets Known to Orbit Kepler-11 Have Low Densities. *The Astrophysical Journal*, 770.2, p. 131.
- Lovis, C. et al. (2010). The HARPS Search for Southern Extra-Solar Planets. XXVII. up to Seven Planets Orbiting Hd 10180: Probing the Architecture of Low-Mass Planetary Systems.
- Marchal, C. and Bozis, G. (1982). Hill Stability and Distance Curves for the General Three-Body Problem. *Celestial Mechanics*, 26.3, pp. 311–333.
- Marchal, C. and Saari, D. G. (1975). Hill Regions for the General Three-Body Problem. *Celestial Mechanics*, 12.2, pp. 115–129.
- Marchal, C., Yoshida, J. and Yi-Sui, S. (1984a). A Test of Escape Valid Even for Very Small Mutual Distances I. the Acceleration and the Escape Velocities of the Third Body. *Celestial Mechanics*, 33.3, pp. 193–207.
- Marchal, C., Yoshida, J. and Yi-Sui, S. (1984b). Three-Body Problem. *Celestial Mechanics*, 34.1-4, pp. 65–93.
- Marcy, G. W. et al. (2014). Masses, Radii, and Orbits of Small Kepler Planets: The Transition from Gaseous to Rocky Planets. *The Astrophysical Journal Supplement Series*, 210.2, p. 20.

- Marois, C. *et al.* (2010). Images of a Fourth Planet Orbiting HR 8799. *Nature*, 468.7327, pp. 1080–1083.
- Masset, F. and Snellgrove, M. (2001). Reversing Type II Migration: Resonance Trapping of a Lighter Giant Protoplanet. *Monthly Notices of the Royal Astronomical Society*, 320.4, pp. L55–L59.
- Mayor, M. *et al.* (2011). The HARPS Search for Southern Extra-Solar Planets XXXIV. Occurrence, Mass Distribution and Orbital Properties of Super-Earths and Neptune-Mass Planets. *eprint arXiv:1109.2497*,
- Mayor, M. and Queloz, D. (1995). A Jupiter-Mass Companion to a Solar-Type Star. *Nature*, 378, pp. 355–359.
- McLachlan, R. (1995a). On the Numerical Integration of Ordinary Differential Equations by Symmetric Composition Methods. *SIAM Journal on Scientific Computing*, 16.1, pp. 151–168.
- McLachlan, R. I. (1995b). Composition Methods in the Presence of Small Parameters. *BIT Numerical Mathematics*, 35.2, pp. 258–268.
- Michtchenko, T. A., Beaugé, C. and Ferraz-Mello, S. (2008). Dynamic Portrait of the Planetary 2/1 Mean-Motion Resonance – I. Systems with a More Massive Outer Planet. *Monthly Notices of the Royal Astronomical Society*, 387.2, pp. 747–758.
- Mikkola, S. (2008). “A Brief History of Regularisation”. In: *Dynamical Evolution of Dense Stellar Systems*. Vol. 246, pp. 218–227.
- Mikkola, S. (1997). Practical Symplectic Methods with Time Transformation for the Few-Body Problem. *Celestial Mechanics and Dynamical Astronomy*, 67.2, pp. 145–165.
- Mikkola, S. and Innanen, K. (1999). Symplectic Tangent Map for Planetary Motions. *Celestial Mechanics and Dynamical Astronomy*, 74.1, pp. 59–67.
- Mikkola, S. and Tanikawa, K. (1999). Explicit Symplectic Algorithms for Time-Transformed Hamiltonians. *Celestial Mechanics and Dynamical Astronomy*, 74.4, pp. 287–295.
- Mogavero, F. (2017). Addressing the Statistical Mechanics of Planet Orbits in the Solar System. *Astronomy and Astrophysics*, 606, A79.
- Moorhead, A. V. *et al.* (2011). The Distribution of Transit Durations for Kepler Planet Candidates and Implications for Their Orbital Eccentricities. *The Astrophysical Journal Supplement Series*, 197.1, pp. 1–1.
- Morbidelli, A. *et al.* (2012). Building Terrestrial Planets. *Annual Review of Earth and Planetary Sciences*, 40.1, pp. 251–275.
- Morbidelli, A. *et al.* (2015). The Great Dichotomy of the Solar System: Small Terrestrial Embryos and Massive Giant Planet Cores. *Icarus*, 258, pp. 418–429.
- Morbidelli, A. *et al.* (2016). Fossilized Condensation Lines in the Solar System Protoplanetary Disk. *Icarus*, 267, pp. 368–376.
- Morbidelli, A. (2002). *Modern Celestial Mechanics: Aspects of Solar System Dynamics*. Taylor & Francis.
- Morbidelli, A. and Giorgilli, A. (1995). Superexponential Stability of KAM Tori. *Journal of Statistical Physics*, 78.5-6, pp. 1607–1617.
- Morbidelli, A. and Raymond, S. N. (2016). Challenges in Planet Formation.
- Möser, J (1962). On Invariant Curves of Area-Preserving Mappings of an Annulus. *Nachr. Akad. Wiss. Göttingen, II*, pp. 1–20.
- Murray, C. D. and Dermott, S. F. (1999). *Solar System Dynamics*. Cambridge University Press.
- Mustill, A. J. and Wyatt, M. C. (2012). Dependence of a Planet’s Chaotic Zone on Particle Eccentricity: The Shape of Debris Disc Inner Edges. *Monthly Notices of the Royal Astronomical Society*, 419.4, pp. 3074–3080.

- Mustill, A. J., Davies, M. B. and Johansen, A. (2018). The Dynamical Evolution of Transiting Planetary Systems Including a Realistic Collision Prescription. *Monthly Notices of the Royal Astronomical Society*, 478.3, pp. 2896–2908.
- Nekhoroshev, N. N. (1977). An Exponential Estimate of the Time of Stability of Nearly-Integrable Hamiltonian Systems. *Uspekhi Matematicheskikh Nauk*, 32.6, pp. 5–66.
- Nesvorný, D. *et al.* (2013). KOI-142, the King of Transit Variations, Is a Pair of Planets Near the 2:1 Resonance. *The Astrophysical Journal*, 777.1, p. 3.
- Newton, I. (1687). *Philosophiae Naturalis Principia Mathematica*.
- Nieto, M. M. (1972). *The Titius-Bode Law of Planetary Distances: Its History and Theory*. Pergamon Press.
- Obertas, A., Van Laerhoven, C. and Tamayo, D. (2017). The Stability of Tightly-Packed, Evenly-Spaced Systems of Earth-Mass Planets Orbiting a Sun-Like Star. *Icarus*, 293, pp. 52–58.
- O’Brien, D. P., Morbidelli, A. and Levison, H. F. (2006). Terrestrial Planet Formation with Strong Dynamical Friction. *Icarus*, 184.1, pp. 39–58.
- Orosz, J. A. *et al.* (2012). Kepler-47: A Transiting Circumbinary Multiplanet System. *Science*, 337.6101, pp. 1511–1514.
- Orosz, J. A. *et al.* (2019). Discovery of a Third Transiting Planet in the Kepler-47 Circumbinary System. *The Astronomical Journal*, 157.5, p. 174.
- Paardekooper, S.-J. and Mellema, G. (2006). Halting Type I Planet Migration in Non-Isothermal Disks. *Astronomy & Astrophysics*, 459.1, pp. L17–L20.
- Papaloizou, J. C. B. and Larwood, J. D. (2000). On the Orbital Evolution and Growth of Protoplanets Embedded in a Gaseous Disc. *Monthly Notices of the Royal Astronomical Society*, 315.4, pp. 823–833.
- Petigura, E. A., Howard, A. W. and Marcy, G. W. (2013). Prevalence of Earth-Size Planets Orbiting Sun-Like Stars. *Proceedings of the National Academy of Science*, 110.48, p. 19273.
- Petit, A. C., Laskar, J. and Boué, G. (2017). AMD-Stability in the Presence of First-Order Mean Motion Resonances. *Astronomy and Astrophysics*, 607, A35.
- Petit, A. C., Laskar, J. and Boué, G. (2018). Hill Stability in the AMD Framework. *Astronomy & Astrophysics*, 617, A93.
- Pierens, A. and Nelson, R. P. (2008). On the Formation and Migration of Giant Planets in Circumbinary Discs. *Astronomy and Astrophysics*, 483.2, p. 633.
- Poincaré, H. (1892). *Les Méthodes Nouvelles De La Mécanique Céleste*. Gauthier-Villars, Paris.
- Poincaré, H. (1905). *Leçons De Mécanique Céleste, Tome I*. Gauthier-Villars. Paris.
- Pollack, J. B. *et al.* (1996). Formation of the Giant Planets by Concurrent Accretion of Solids and Gas. *Icarus*, 124.1, pp. 62–85.
- Preto, M. and Tremaine, S. (1999). A Class of Symplectic Integrators with Adaptive Time Step for Separable Hamiltonian Systems. *The Astronomical Journal*, 118.5, p. 2532.
- Pu, B. and Lai, D. (2019). Low-Eccentricity Formation of Ultra-Short Period Planets in Multi-Planet Systems. *arXiv e-prints*, arXiv:1901.08258.
- Pu, B. and Wu, Y. (2015). Spacing of Kepler Planets: Sculpting by Dynamical Instability. *The Astrophysical Journal*, 807.1, pp. 44–44.
- Quillen, A. C. (2011). Three-Body Resonance Overlap in Closely Spaced Multiple-Planet Systems. *Monthly Notices of the Royal Astronomical Society*, 418.2, pp. 1043–1054.
- Ramos, X. S., Correa-Otto, J. A. and Beaugé, C. (2015). The Resonance Overlap and Hill Stability Criteria Revisited. *Celestial Mechanics and Dynamical Astronomy*, 123.4, pp. 453–479.

- Raymond, S. N. *et al.* (2014). “Terrestrial Planet Formation at Home and Abroad”. In: *Protostars and Planets VI*. University of Arizona Press.
- Raymond, S. N., Quinn, T. and Lunine, J. I. (2006). High-Resolution Simulations of the Final Assembly of Earth-Like Planets I. Terrestrial Accretion and Dynamics. *Icarus*, 183.2, pp. 265–282.
- Raymond, S. N., Barnes, R. and Mandell, A. M. (2008). Observable Consequences of Planet Formation Models in Systems with Close-in Terrestrial Planets. *Monthly Notices of the Royal Astronomical Society*, 384.2, pp. 663–674.
- Rein, H. and Liu, S.-F. (2012). REBOUND: An Open-Source Multi-Purpose N-Body Code for Collisional Dynamics. *Astronomy and Astrophysics*, 537, A128.
- Rein, H. and Spiegel, D. S. (2015). IAS15: A Fast, Adaptive, High-Order Integrator for Gravitational Dynamics, Accurate to Machine Precision over a Billion Orbits. *Monthly Notices of the Royal Astronomical Society*, 446.2, p. 1424.
- Rein, H. and Tamayo, D. (2015). WHFAST: A Fast and Unbiased Implementation of a Symplectic Wisdom-Holman Integrator for Long-Term Gravitational Simulations. *Monthly Notices of the Royal Astronomical Society*, 452.1, p. 376.
- Rein, H. *et al.* (2019). Hybrid Symplectic Integrators for Planetary Dynamics. *arXiv:1903.04972 [astro-ph]*,
- Safronov, V. S. (1972). *Evolution of the Protoplanetary Cloud and Formation of the Earth and the Planets*.
- Schneider, J. *et al.* (2011). Defining and Cataloging Exoplanets: The Exoplanet.Eu Database. *Astronomy & Astrophysics*, 532, A79–A79.
- Sessin, W. and Ferraz-Mello, S. (1984). Motion of Two Planets with Periods Commensurable in the Ratio 2:1 Solutions of the Hori Auxiliary System. *Celestial Mechanics*, 32.4, pp. 307–332.
- Shabram, M. *et al.* (2016). The Eccentricity Distribution of Short-Period Planet Candidates Detected by Kepler in Occultation. *The Astrophysical Journal*, 820.2, pp. 93–93.
- Shakura, N. I. and Sunyaev, R. A. (1973). Black Holes in Binary Systems. Observational Appearance. *Astronomy and Astrophysics*, 24, pp. 337–355.
- Smith, A. W. and Lissauer, J. J. (2009). Orbital Stability of Systems of Closely-Spaced Planets. *Icarus*, 201.1, pp. 381–394.
- Stiefel, E. L. and Scheifele, G. (1971). *Linear and Regular Celestial Mechanics*. Springer, Berlin.
- Stumpff, K. (1962). *Himmelsmechanik, Band I*. VEB Deutscher Verlag der Wissenschaften, Berlin.
- Sundman, K. F. (1912). Mémoire Sur Le Problème Des Trois Corps. *Acta Mathematica*, 36.0, pp. 105–179.
- Sussman, G. J. and Wisdom, J. (1992). Chaotic Evolution of the Solar System. *Science*, 257.5066, pp. 56–62.
- Tamayo, D. *et al.* (2016). A Machine Learns to Predict the Stability of Tightly Packed Planetary Systems. *The Astrophysical Journal*, 832.2, pp. L22–L22.
- Tamayo, D. *et al.* (2017). Convergent Migration Renders TRAPPIST-1 Long-Lived. *The Astrophysical Journal*, 840.2, p. L19.
- Tanaka, H. and Ida, S. (1999). Growth of a Migrating Protoplanet. *Icarus*, 139.2, pp. 350–366.
- Terquem, C. and Papaloizou, J. C. B. (2007). Migration and the Formation of Systems of Hot Super-Earths and Neptunes. *The Astrophysical Journal*, 654.2, pp. 1110–1120.
- Titius, J. (1766). Betrachtung Über Die Natur, Vom Herrn Karl Bonnet. *Johann Friedrich Junius, Leipzig*,

- Tremaine, S. (2015). The Statistical Mechanics Of Planet Orbits. *The Astrophysical Journal*, 807.2, pp. 157–157.
- Veras, D. and Armitage, P. J. (2004). The Dynamics of Two Massive Planets on Inclined Orbits. *Icarus*, 172.2, pp. 349–371.
- Ward, W. R. (1986). Density Waves in the Solar Nebula: Differential Lindblad Torque. *Icarus*, 67.1, pp. 164–180.
- Ward, W. R. (1997). Survival of Planetary Systems. *The Astrophysical Journal*, 482.2, pp. L211–L214.
- Weidenschilling, S. J. (1977). The Distribution of Mass in the Planetary System and Solar Nebula. *Astrophysics and Space Science*, 51.1, pp. 153–158.
- Winn, J. N. and Fabrycky, D. C. (2015). The Occurrence and Architecture of Exoplanetary Systems. *Annual Review of Astronomy and Astrophysics*, 53, p. 409.
- Wisdom, J. (1980). The Resonance Overlap Criterion and the Onset of Stochastic Behavior in the Restricted Three-Body Problem. *The Astronomical Journal*, 85, pp. 1122–1122.
- Wisdom, J. (2006). Symplectic Correctors for Canonical Heliocentric N-Body Maps. *The Astronomical Journal*, 131.4, p. 2294.
- Wisdom, J., Holman, M. and Touma, J. (1996). Symplectic Correctors. *Fields Institute Communications*, 10, p. 217.
- Wisdom, J. (1986). Canonical Solution of the Two Critical Argument Problem. *Celestial Mechanics*, 38.2, pp. 175–180.
- Wisdom, J. and Holman, M. (1991). Symplectic Maps for the N-Body Problem. *The Astronomical Journal*, 102, p. 1528.
- Woillez, É. (2018). *Stochastic Description of Rare Events for Complex Dynamics in the Solar System*. Thesis. Lyon.
- Wright, J. T. et al. (2009). Ten New and Updated Multiplanet Systems and a Survey of Exoplanetary Systems. *The Astrophysical Journal*, 693.2, pp. 1084–1099.
- Wright, J. T. et al. (2012). The Frequency of Hot Jupiters Orbiting Nearby Solar-Type Stars. *The Astrophysical Journal*, 753.2, p. 160.
- Wright, J. T. et al. (2011). The Exoplanet Orbit Database. *Publications of the Astronomical Society of the Pacific*, 123.902, pp. 412–422.
- Wu, Y. and Lithwick, Y. (2011). Secular Chaos and the Production of Hot Jupiters. *The Astrophysical Journal*, 735.2, pp. 109–109.
- Xie, J.-W. et al. (2016). Exoplanet Orbital Eccentricities Derived From LAMOST-Kepler Analysis. *Proceedings of the National Academy of Sciences*, 113.41, pp. 11431–11435.
- Yoshida, H. (1990). Construction of Higher Order Symplectic Integrators. *Physics Letters A*, 150.5, pp. 262–268.
- Youdin, A. N. and Goodman, J. (2005). Streaming Instabilities in Protoplanetary Disks. *The Astrophysical Journal*, 620.1, pp. 459–469.

RÉSUMÉ

L'architecture des systèmes planétaires nous renseigne sur leur formation et de leur histoire. De plus, le grand nombre de découvertes récentes et futures d'exoplanètes permet d'étudier la population de systèmes exoplanétaires. Cependant, l'organisation des systèmes planétaires est fortement affectée par la stabilité dynamique, ce qui rend les études particulièrement difficiles. Étant donné que la dynamique est chaotique, une analyse détaillée entraîne de long temps de calculs.

Dans cette thèse, je développe des critères analytiques de stabilité pour la dynamique des planètes. Dans le système séculaire, la conservation du moment cinétique et des demi-grand axes impliquent la conservation du déficit en moment cinétique (AMD). L'AMD est une mesure pondérée des excentricités et des inclinaisons mutuelles d'un système et agit comme une température dynamique.

Dans le premier chapitre, nous définissons le concept de d'AMD-stabilité. Le critère d'AMD-stabilité permet de faire la distinction entre les systèmes planétaires a priori stables et les systèmes pour lesquels la stabilité n'est pas garantie et nécessite plus d'études. Je montre que l'AMD-stabilité peut être utilisée pour établir une classification des systèmes multiplanétaires afin de différencier les systèmes stables à long terme et ceux qui sont AMD-instables, nécessitant alors une étude dynamique supplémentaire. Nous classons 131 systèmes multiplanétaires de la base de données exoplanet.eu ayant des éléments orbitaux suffisamment connus.

Bien que le critère AMD soit rigoureux, la conservation de l'AMD n'est garantie qu'en l'absence de résonances en moyen mouvement (MMR). Si les îles des MMR se chevauchent, le système devient chaotique et instable. Dans le deuxième chapitre, nous élargissons le critère de stabilité AMD pour prendre en compte le recouvrement de MMR du premier ordre. Je déduis analytiquement un nouveau critère qui unifie ceux précédemment proposés dans la littérature et admet comme cas limite les critères obtenus pour les orbites initialement circulaires et excentriques.

Dans le troisième chapitre, j'explique comment la stabilité de Hill peut être comprise via la notion d'AMD. Largement utilisée, la stabilité de Hill est un critère de stabilité topologique pour le système à trois corps. Cependant, la plupart des études utilisent uniquement l'approximation pour des orbites coplanaire et circulaire. Je montre que le critère général de Hill peut être exprimé en fonction des seuls demi-grand axes, des masses et de l'AMD total du système. Le critère proposé n'est développé que dans le rapport de masse des planètes à l'étoile et non dans les éléments orbitaux.

Lors de l'étude d'un système AMD-instable, le recours aux simulations numériques est nécessaire. Cependant, les grands temps d'évolution dans la dynamique planétaire rendent nécessaire l'utilisation de méthodes symplectiques. Ces méthodes permettent une intégration très précise et rapide lorsqu'un système est stable. Leur inconvénient est qu'elles sont limitées à une intégration à pas de temps fixe, i.e. l'intégrateur peut ne pas résoudre les rencontres proches et devient inexact. Dans le quatrième chapitre, je propose une renormalisation du temps qui permet d'utiliser un intégrateur symplectique d'ordre élevé avec un pas de temps adaptatif aux rencontres proches. L'algorithme est bien adapté aux systèmes de masses de planètes similaires.

Dans le dernier chapitre, je revisite le modèle-jouet de formation planétaire de J. Laskar. Tandis que l'AMD est conservé par la dynamique séculaire, il diminue lors des collisions planétaires. Le modèle de Laskar peut être résolu de manière analytique pour obtenir le résultat moyen et les simulations numériques sont très rapides, ce qui permet de créer une grande population de systèmes. Je montre que ce modèle de formation est en bon accord avec les simulations réalistes récentes de formation, dans lesquelles l'architecture finale résulte d'une phase d'impacts géants.

MOTS CLÉS

Systèmes planétaires, Mécanique céleste, Stabilité, Formation planétaire

ABSTRACT

The architecture of a planetary systems is a signpost of their formation and history. Moreover, the large number of recent and future exoplanets discoveries allows to study the exoplanet system population. Besides, the observations of exoplanet systems has enriched the diversity of planetary system architecture, revealing that the Solar System shape is far from being the norm.

However, the organization of planetary systems is heavily affected by dynamical stability, making individual studies particularly challenging. Since planets dynamics are chaotic, a detailed stability analysis study is computationally expensive.

In this thesis, I develop analytic stability criteria for planet dynamics. In the secular system, the conservation of the total angular momentum and semi-major axes imply the conservation of the Angular Momentum Deficit (AMD). The AMD is a measure of a system's eccentricities and mutual inclinations and act as a dynamical temperature of the system. Based on this consideration, we make the simplifying assumption that the dynamics can be replaced by AMD exchanges between the planets.

In the first chapter we define the concept of AMD-stability. The AMD-stability criterion allows to discriminate between a priori stable planetary systems and systems for which the stability is not granted and needs further investigations. We show how AMD-stability can be used to establish a classification of the multiplanet systems in order to exhibit the planetary systems that are long-term stable because they are AMD-stable, and those that are AMD-unstable which then require some additional dynamical studies to conclude on their stability. We classify 131 multiplanet systems from the exoplanet.eu database with sufficiently well-known orbital elements.

While the AMD criterion is rigorous, AMD conservation is only granted in absence of mean-motion resonances (MMR). If the MMR islands overlap, the system experiences chaos leading to instability. In the second chapter, we extend the AMD-stability criterion to take into account the overlap of first-order MMR.

I derive analytically a new overlap criterion for first-order MMR. This stability criterion unifies the previous criteria proposed in the literature and admits the criteria obtained for initially circular and eccentric orbits as limit cases.

In the third chapter I explain how the Hill stability can be understood in the AMD framework. Widely used, the Hill stability is a topological stability criterion for the three body system. However, most studies only use the coplanar and circular orbit approximation. We show that the general Hill stability criterion can be expressed as a function of only semi-major axes, masses, and total AMD of the system. The proposed criterion is only expanded in the planets-to-star mass ratio and not in the orbital elements.

When studying AMD-unstable system, numerical simulations are mandatory. However the long timescales in planet dynamics make necessary the use of symplectic methods. These methods provide very accurate and fast integration when a system is stable. Their downside is that they are limited to fixed time-step integration. For unstable systems, the integrator may fail to resolve a close encounter and become inaccurate. In the fourth chapter, I propose a time renormalization that allow to use high order symplectic integrator with adaptive time-step at close encounter. The algorithm is well-adapted to systems of few similar masses planets.

In the final chapter, I revisit the planet formation toy model developed by J. Laskar. While the AMD is conserved in the secular dynamics, it decreases during planets collisions. Laskar's model can be solved analytically for the average outcome and numerical simulations are very quick allowing to build large system population. I show that this formation model is in good agreement with recent realistic planet formation simulations where the final architecture results from a giant impact phase.

KEYWORDS

Planetary systems, Celestial mechanics, Stability, Planetary formation